UNIVERSIDADE DE LISBOA
FACULDADE DE CIÊNCIAS

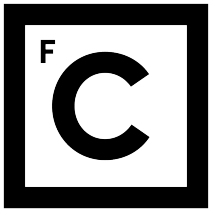

Ciências
ULisboa

# STAR-FORMING GALAXIES' STRUCTURAL EVOLUTION ACROSS COSMIC TIME AND ENVIRONMENT

**Documento Definitivo**

**Doutoramento em Astronomia e Astrofísica**

**Ana Sofia Paulino Afonso**

Tese orientada por:
Doutor David Ricardo Serrano Gonçalves Sobral
Doutor José Manuel Lourenço Coutinho Afonso

Documento especialmente elaborado para a obtenção do grau de doutor

2018

UNIVERSIDADE DE LISBOA
FACULDADE DE CIÊNCIAS

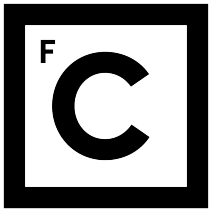

Ciências
ULisboa

# STAR-FORMING GALAXIES' STRUCTURAL EVOLUTION ACROSS COSMIC TIME AND ENVIRONMENT

**Doutoramento em Astronomia e Astrofísica**

**Ana Sofia Paulino Afonso**

Tese orientada por:

Doutor David Ricardo Serrano Gonçalves Sobral

Doutor José Manuel Lourenço Coutinho Afonso

Júri

Presidente:

- Doutor José Manuel de Nunes Vicente Rebordão, Investigador Coordenador, Faculdade de Ciências da Universidade de Lisboa

Vogais:

- Doutora Laura Pentericci, Primo Ricercatore, INAF - Osservatorio Astronomico di Roma
- Doutor Jarle Brinchmann, Investigador FCT de nível "Coordenador", Centro de Investigação em Astronomia/Astrofísica da Universidade do Porto
- Doutor Cirino Pappalardo, Bolseiro de Pós-Doutoramento, Instituto de Astrofísica e Ciências do Espaço
- Doutor Fernando Buitrago Alonso, Professor Auxiliar Convidado, Faculdade de Ciências da Universidade de Lisboa
- Doutor David Ricardo Serrano Gonçalves Sobral, Professor Auxiliar Visitante, Faculdade de Ciências da Universidade de Lisboa

Documento especialmente elaborado para a obtenção do grau de doutor

Trabalho desenvolvido com o apoio da Fundação para a Ciência e a Tecnologia através da bolsa de doutoramento PD/BD/52706/2014 e da bolsa de investigação UID/FIS/04434/2013.

2018

*Ai que prazer*
*Não cumprir um dever,*
*Ter um livro para ler*
*E não o fazer!*
*Ler é maçada,*
*Estudar é nada.*
*O Sol doira sem literatura.*
*O rio corre, bem ou mal,*
*Sem edição original.*
*E a brisa, essa,*
*De tão naturalmente matinal,*
*Como tem tempo não tem pressa.*

*Livros são papéis pintados com tinta.*
*Estudar é uma coisa em que está indistinta*
*A distinção entre nada e coisa nenhuma.*

*Quanto é melhor, quanto há bruma,*
*Esperar por D.Sebastião,*
*Quer venha ou não!*

*Grande é a poesia, a bondade e as danças...*
*Mas o melhor do mundo são as crianças,*
*Flores, música, o luar, e o sol, que peca*
*Só quando, em vez de criar, seca.*

*O mais do que isto*
*É Jesus Cristo,*
*Que não sabia nada de finanças*
*Nem consta que tivesse biblioteca...*

– Fernando Pessoa, in "*Cancioneiro*"

This page intentionally contains only this sentence.

To those that made me a citizen of the word. To those that helped me to become a grown up. To those that made me accountable to someone other than myself and my parents. To those that made me accountable for more than my grades. To those that kept me alive. To my love, Bruno, and to my beloved ones, Isabel, Fernando, Nikharu, Fermi, and Ron.

In memory of Ebony and Petra.

This page intentionally contains only this sentence.

# RESUMO

O estudo da evolução de galáxias ao longo do tempo mostra-nos que estas sofreram muitas alterações que resultam da combinação de vários processos físicos que competem entre si: acreção de gás inter-galáctico; evolução da formação estelar; interações entre galáxias e o ambiente que as rodeia; a reposição de energia e material por supernovas e buracos negros super massivos; entre outros.

Todos estes processos deixam a sua marca na morfologia que observamos nas galáxias e, por isso, esta tese é dedicada ao estudo da evolução morfológica das galáxias ao longo dos últimos 13 mil milhões de anos e ao impacto do ambiente aonde estas se encontram inseridas quer na morfologia quer nas populações estelares que observamos.

Ao estudar uma amostra de galáxias que estão a formar estrelas de forma ativa (selecionadas pela sua emissão em H$\alpha$) desde há 11 mil milhões de anos até aos dias de hoje, eu mostro que as galáxias dobraram ou triplicaram o seu tamanho (de 2 para $4-6$ kpc) mas que, contudo, os seus perfis de luz continuam a se caraterizarem como discos ao longo do mesmo período.

Neste mesmo estudo, eu avaliei também o impacto dos efeitos observacionais (mais concretamente o escurecimento cosmológico e as diferenças entre instrumentos) nas propriedades observadas nas galáxias. Eu mostro que tais efeitos têm um impacto pequeno nos tamanhos (um erro $< 5\%$) mas substancial nos perfis de luz ($\sim 20\%$ nos designados índices de Sérsic). Assim sendo, a evolução que observamos durante este período é real.

Quando comparados os tamanhos medidos na região azul do espetro das galáxias (caraterísticos de traçarem a luz das estrelas jovens) com os medidos na região vermelha (caraterísticos de traçarem a luz de populações estelares mais antigas), eu mostro que a evolução dos tamanhos medidos é diferente. Esta diferença pode ser uma indicação de que as galáxias em estudo têm uma população de estrelas mais antigas na zona central e que intervem numa formação estelar que se dá de dentro para fora da galáxia levando, assim, ao consequente crescimento das regiões aonde se formam estrelas novas.

Para estudar as caraterísticas das galáxias num Universo ainda mais jovem, eu usei outra risca

de emissão que é acessível a partir da Terra: a risca de Ly$\alpha$. Neste caso, eu uso uma amostra de galáxias (genericamente designadas por LAEs) com valores de desvio cosmológico para o vermelho entre 2 e 6 e mostro que a sua morfologia é constante ao longo deste período.

Estas LAEs têm tamanhos típicos de 1 kpc e perfis de luz também caraterísticos de discos. Uma análise visual destas galáxias mostra que elas são na sua maioria ($\sim 60-70\%$) objetos compactos, com $\sim 25\%$ delas com morfologias irregulares e $\sim< 10\%$ com a aparência de discos mais extensos.

Quando comparando a morfologia com as propriedades da risca de emissão de Ly$\alpha$, eu encontro que as galáxias mais pequenas são aquelas com riscas de maior largura equivalente (i.e. de fluxo da risca relativamente à emissão no contínuo) e, quando comparadas com outras populações de galáxias com formação estelar (selecionadas pelo luz ultra-violeta ou pela emissão em H$\alpha$), são sistematicamente mais pequenas, com a diferença a tornar-se mais evidente a partir de desvios cosmológicos para o vermelho $< 4$.

Esta evolução diferencial entre galáxias das duas populações (H$\alpha$ e Ly$\alpha$) é consistente com o cenário em que no Universo jovem a maior fração das galáxias com formação estelar são observadas com emissão em Ly$\alpha$, como é confirmado por diversos estudos feitos nesta área. Isto é uma indicação que a população de LAEs, que não mostra evolução em morfologia num período de 3 mil milhões de anos, está provavelmente a traçar a população mais jovem a cada desvio cosmológico para o vermelho e, assim, a permitir-nos estudar as primeiras fases da evolução da população mais geral de galáxias.

Complementando o estudo anteriormente referido, eu faço também uma breve análise da morfologia das galáxias mais brilhantes em Ly$\alpha$ observadas até hoje, usando para o efeito as imagens de alta resolução disponíveis para os finais da época da reionização (correspondendo a desvios cosmológicos para o vermelho entre 5 e 7). Confirmando a tendência descoberta para desvios cosmológicos para o vermelho mais baixos, estas galáxias são similares a uma população selecionada pela sua luminosidade UV (*Lyman Break Galaxies* - LBGs) com a prevalência de uma morfologia irregular com várias regiões distintas de emissão ("grumos"). A elevada incidência de “grumos” neste tipo de objetos relativamente à população de LBGs é uma possível indicação que a existência de "grumos" de formação estelar facilita o escape de fotões Ly$\alpha$ das galáxias.

Como estudo complementar à evolução temporal das propriedades das galáxias, eu levei ainda a cabo a análise de uma amostra de galáxias com espetroscopia ótica, selecionadas de uma região superdensa observada há 7 mil milhões de anos, com o objetivo de estudar a influência do ambiente na morfologia e na capacidade de formação de estrelas das galáxias.

Com uma amostra completa em massa para galáxias mais massivas que $10^{10}\mathrm{M}_{\odot}$, eu mostro que a fração de galáxias passivas depende da massa estelar e do ambiente em que as galáxias vivem. Para as galáxias mais massivas (acima de $10^{10.75}\mathrm{M}_{\odot}$), o ambiente em que vivem não tem

influência na formação estelar. Para galáxias menos massivas, o ambiente em que vivem é um forte indicador da quantidade de estrelas formadas nas galáxias com a fração de galáxias passivas a crescer dos 10% para os 60% das regiões pouco densas para as regiões mais densas estudadas.

Um estudo mais específico das propriedades das populações estelares das galáxias mostra que as zonas de densidades intermédias são mais propícias para uma formação mais eficiente de estrelas. Nas minhas análises eu mostro que a idade média das estrelas aumenta tanto com a massa estelar como com o ambiente. Nas regiões mais densas, as estrelas têm uma idade média de $6-8$ mil milhões de anos enquanto que nas regiões menos densas são tipicamente mais jovens que mil milhões de anos. Para cada ambiente, as galáxias mais massivas são sempre as mais velhas, com a diferença de idades entre as mais e as menos massivas a ser tanto maior quanto maior for a densidade da região onde as galáxias residem.

Relativamente à morfologia das galáxias, eu mostro que quando consideramos a população como um todo existe uma clara relação entre a densidade e a morfologia das galáxias. Em regiões mais densas existe um maior número de galáxias elípticas enquanto que os discos predominam as regiões de menor densidade, semelhante ao que é observado no Universo local. No entanto, se dividirmos as galáxias pela sua cor, o que é um indicador da sua atividade de formação estelar, entre azuis e vermelhas (ativas e passivas, respetivamente), a morfologia torna-se independente do ambiente em que as galáxias vivem. Mais especificamente, podemos mostrar que a dependência da morfologia da população em relação ao ambiente é uma consequência da dependência da fração de galáxias passivas e isto pode ser uma indicação de que os processos que atuam para suprimir a formação de estrelas nas galáxias em regiões mais densas têm também de afetar a morfologia das mesmas.

O único indicador morfológico que parece variar nas galáxias em função do ambiente é a quantidade de luz que encontramos no bojo (quando comparada com a luz total da galáxia). Eu encontro uma indicação que o bojo das galáxias é maior para galáxias em ambientes de densidade intermédia o que pode estar relacionado uma maior incidência de interações entre galáxias, incluindo acreção de galáxias satélite e disrupção cinemática por forças de maré.

Graças aos espetros de alta resolução, foi possível também estudar as condições do meio inter-estelar das galáxias usando o rácio do fluxo das duas componentes da risca de emissão de [OII] que pode ser usado como um indicador da densidade de eletrões no gás. Mais uma vez, eu mostro que a dependência da densidade do gás com o ambiente depende da massa estelar das galáxias. Para galáxias menos massivas (entre $10^{10}\mathrm{M}_{\odot}$ e $10^{10.75}\mathrm{M}_{\odot}$), a densidade do gás diminui quando as galáxias estão em regiões de maior densidade. Para galáxias mais massivas, encontro a tendência oposta, i.e. o gás a aumentar a densidade em regiões mais densas. Isto pode ser um indicador de que o mecanismo responsável pela emissão de fotões [OII] pode ser diferente em galáxias mais massivas em ambientes densos, i.e. pode não ser devido à formação estelar mas à presença de certos tipos de núcleos ativos de galáxias ou outros mecanismos

mais complexos. Menos provável, mas também possível, será a diferença (de $\sim 2$ ordens de magnitude) na temperatura média do gás em função da massa estelar das galáxias.

Em suma, nesta tese eu compilo o estudo de várias populações de galáxias emissoras com o objetivo de contribuir para uma melhor compreensão de como o tempo e as estruturas têm implicações na evolução galáctica. De uma forma geral podemos dizer que as galáxias com formação estelar ativa são caraterizadas por terem perfis de luz em forma de discos que crescem ao longo do tempo, sendo menos prevalentes em regiões de alta densidade. Claro está que ao usarmos diferentes indicadores de formação estelar podemos estar a observar populações diferentes. Nomeadamente, quando comparamos galáxias selecionadas em UV/H$\alpha$ e Ly$\alpha$ verificamos que estas evoluem de forma diferente com o tempo, sendo apenas indistinguíveis para desvios cosmológicos para o vermelho $> 4$. Os resultados aqui apresentados serão uma importante base para os futuros estudos que contribuirão para melhor compreender a evolução das diferentes populações de galáxias assim como para revelar o que as liga e qual o seu papel na construção de um modelo unificado de formação e evolução galáctica.

**Palavras-chave**: galáxias: evolução – galáxias: formação estelar – galáxias: morfologia – galáxias: Universo distante – estruturas de larga escala do Universo

# ABSTRACT

From early times we find galaxies undergo major transformations which encode the physics of competing processes that shape the galaxy evolution (gas accretion, star formation, mergers, feedback processes, among others).

In this thesis, I study the galaxy structural evolution across cosmic time and environment. By linking the distant and local Universe, I show that the star-forming galaxies (SFGs, selected by their H$\alpha$ emission) have typical disk-like morphologies and grow by a factor of $2-3$ from $z \sim 2$. I also attempt to measure the impact of cosmological dimming on the perceived galaxy evolution and find that it has little-to-no impact on the measured structural parameters.

By tracing Ly$\alpha$-selected galaxies (LAEs), I find that these galaxy population show little-to-no evolution in size ($\sim$ 1 kpc) across a $\sim$ 3 Gyr period in the early Universe ($2 < z < 6$). However, when compared to other SFGs, this population deviates in morphological properties only at $z < 4$. I hypothesize that LAEs and other SFGs trace the dominant galaxy population at earlier times while, later, LAEs only trace the smaller, younger, and less massive star-forming population.

By targeting a region in and around a superstructure at $z \sim 0.8$ in the COSMOS field, I find that both stellar mass and environment impact the galaxy evolution. The environment has a pivotal role in the observed star formation activity in galaxies since one can witness an increase of the quiescent fraction of galaxies towards high-density regions. In the intermediate density regions, there is an increase of the star formation which can be linked with the change of the galaxy morphology from disks to ellipticals from the low- to high-density regions. The electron density decreases from low to high densities for galaxies up to $10^{10.75}$M$_{\odot}$. However, massive galaxies tend to point towards a different and opposite relation for which the possible ionizing mechanisms remain unclear.

**Keywords:** galaxies: evolution – galaxies: high redshift – galaxies: morphology – galaxies: star formation – large scale structure of the Universe

This page intentionally contains only this sentence.

# CONTENTS

This page intentionally contains only this sentence.

# LIST OF FIGURES

# LIST OF TABLES

This page intentionally contains only this sentence.

# PREFACE

The emergence of the study of the celestial bodies outside of our own galaxy can be pinpointed to the middle of the 18th century. On that epoch, Thomas Wright hypothesized about the possibility of some of the nebulae that were observed in the skies might be actually outside of our Milky Way. Some years past and Immanuel Kant came up with the "*island universes*" terminology to refer to these possibly distant objects. Almost a century later, François Arago revived the hypothesis of nebulae outside our own galaxy (Arago & Barral, 1854) thus creating momentum for the idea to take roots in the scientific community. However, since some of those nebulae, first compiled by Messier (1781) with a completely different purpose, were actually part of the Milky Way (such as planetary nebulae or globular clusters) a compilation of new observations had to be made to spread some light on this controversial topic. William Herschel and Lord Rosse both contributed greatly by observing several thousand of sources and by being able to distinguish point sources within the extended nebulae, giving support to the idea of the existence of distant extragalactic sources. Slipher (1915) observed the spectra of some of those nebulae and found that some of them had their lines deviated from their laboratory position towards redder wavelengths, leading to the measurement of their recessive motion relative to the Milky Way at speed greater than the needed to escape from our galaxy.

This problem was finally solved in the 1920s. At the beginning of that decade, Curtis (1920) presented several pieces of evidence on why the Andromeda "*nebula*" – M31 – is a galaxy itself like our own. Opik (1922) estimated its distance from us and put it at 450 kpc away, which is still around two times smaller than its current measurements but far enough to be exterior to the Milky Way. Taking advantage of the large aperture of the Mount Wilson Telescope, Hubble (1925) observed a number of Cepheid stars, whose characteristic variable brightness allows one to compute their absolute magnitude, and using the distance modulus confirmed the large distance of these objects only underestimating their actual value by a factor of three due to calibration offsets. Based on the images of the galaxies he also devised a scheme for classifying them according to their shape – the Hubble (1926) sequence – and stated that the Universe is currently expanding (Hubble, 1929).

The morphological classification divided galaxies in three main groups: ellipticals, spirals, and irregulars (Hubble, 1936). Elliptical galaxies are characterized by having ellipsoidal and smooth light distributions with no obvious features. These galaxies populate a large range in mass, size, and luminosity. The most massive ellipticals are more common in regions with a large concentration of galaxies – galaxy clusters – and those in the core of these dense regions are the largest and massive galaxies that exist in the Universe. On the far side, there are dwarf ellipticals and dwarf spheroidal galaxies which are typically very small and have low stellar masses compared to the Milky Way (from ten to a million times less massive). This class of objects was later found to have red colours (meaning that they are mostly populated by old, low mass stars) and little cold gas to form new stars. Additionally, their stars have mostly random motions around the galactic centre.

Spiral galaxies, named after their beautiful patterns, are the most common population in the local Universe. These galaxies have usually two components: a central bulge surrounded by a large rotating disk with an imprinted spiral pattern. Their bright spiral arms have usually blue colours due to a large population of young, hot, massive stars and large reservoirs of cold gas that allow for the continuous process of forming new stars. Some of these galaxies can also have central bars, which are elongated structures with spiral arms departing from each of its extremities.

Usually smaller systems with no apparent structure are classified as irregulars. These galaxies, thought to be analogous to the galaxies that were forming when the Universe was younger, are typically very young and with lower stellar masses.

The collection of more and more objects obliged a revision of the classification scheme (de Vaucouleurs, 1959; van den Bergh, 1960; Sandage, 1961) to include more information on the existence of rings, bars, and the regularity of spiral patterns in galaxies. One of the most important revisions was the inclusion of a new intermediate class of galaxies named lenticular galaxies (also referred as S0 galaxies, Sandage, 1961), which are between the spirals and ellipticals.

Almost a century later since the existence of galaxies outside our own was established, we have a broader knowledge and even more intriguing questions about the nature and formation of these astronomical objects that permeate the Universe. We are now finding galaxies at a time where the Universe was in its infancy and close to finding the formation of the first population of stars. By compiling observations spanning in time almost the entirety of the observable Universe, we can also depict the evolution from those first objects to the ones that we found in the nearby Universe decades ago. However, as it is the nature of science itself, new discoveries lead to new questions and, in this thesis, I humbly report my findings on the meanders of galaxy evolution across cosmic time.

Esposende, August 2018 Ana Paulino-Afonso

# CHAPTER 1

## INTRODUCTION

*The material of which galaxies are made of - gas, dust, and stars - are constantly interacting. The cold and pristine gas is the fuel from which stars form, and gas and dust return to the interstellar medium once the stars reach their final phases of evolution and enrich the surrounding allowing the formation of new, and more metal-rich, stars and planetary systems. At the same time, the energy from stellar explosions expands and heat the gas preventing the condensation of large gas clouds in the regions. This constant interplay is what regulates the rate at which the formation of stars is done and helps shape the galaxies into the forms that we observe today. Tracing the morphology of galaxies and its relation to star formation and environment over the course of the history of the Universe is crucial to understand how galaxies came to be as they are today. In this chapter, I briefly review the main paradigms of galaxy evolution in the context of modern cosmology and the current status of galaxy morphology studies.*

## 1.1 A Λ-CDM UNIVERSE

The first mathematical description of the Universe was postulated by Albert Einstein at the beginning of the 20th century. It predicted that our Universe should either be expanding or contracting, contrary to the belief of a static Universe at that time. To artificially impose a static Universe, he introduced a quantity named *cosmological constant* that would act as a force to prevent the Universe from deviating from the static solution. This was later proved to be just a misconception of our own Universe, since Hubble (1929) showed galaxies to be receding at a constant velocity (now parametrized as the Hubble constant, $H_0$) and proved the expansion of the Universe.

This led to the adoption of the cosmological models of an expanding Universe that were described by Friedmann (1922) and Lemaître (1927) and the notion that the Universe should be denser and hotter at earlier times.The thermonuclear reactions in the early Universe should be responsible for the formation of the chemical elements (Gamow, 1946; Alpher et al., 1948) and, the required

energy to allow for such reactions, implied a thermal relic that should be observed in our Universe at microwave wavelengths (the cosmic microwave background - CMB - Gamow, 1948). This model for a hot and dense beginning of the Universe was derisively nicknamed hot big bang by one of its opponents, Fred Hoyle, who supported a steady Universe solution. However, the development of the big bang model throughout the decades of the 50s and 60s led to increasing evidence supporting such theory, especially through the prediction of cosmic element abundances (see e.g. Wagoner et al., 1967). Another crucial evidence supporting the big bang model was the first discovery of the relic thermal signal (CMB) with a temperature of $\sim 2.7$ K by Penzias & Wilson (1965) which was in the expected range for the big bang (Dicke et al., 1965).

Since established, the big bang model is the accepted model for cosmology. Despite its early successes, several shortcomings affected its validity. The observed isotropy in the CMB was hard to explain since regions far apart had the same temperature despite not having any causal contact (e.g. Misner, 1968). Another problem was the spatial flatness of the Universe which required a very special set of initial conditions for our Universe to exist as it is (e.g. Dicke & Peebles, 1979). This was later partially solved due to a conceptional breakthrough in the early 80s by Guth (1981, see also Linde 1982 and Albrecht & Steinhardt 1982) that proposed an inflationary period in the early Universe. This inflation scenario proposed an exponential expansion few seconds after the big bang that expanded causally connected regions far apart and allows for the Universe to appear flat due to a curvature radius much larger than the observable Universe.

Alongside the development of the standard model of cosmology, another important component of our current paradigm also was discovered. A dark matter component of the Universe was first proposed by Zwicky (1933, 1937) where he concluded that it was necessary to have a dark mass component to explain the observations. But it was only several decades later that the idea of dark matter was accepted. Papers by Ostriker et al. (1974) and Einasto et al. (1974) argued for the existence of massive halos around galaxies to explain the observed motion of their satellites. This was further supported by observations of the rotation curves of galaxies which showed no sign of the predicted fall-off of velocities at larger radii predicted from the stellar distribution of galaxies (Roberts & Rots, 1973; Rubin et al., 1978, 1980). Several predictions for the nature of such dark matter component have been proposed throughout the years, but it still eludes our observations as of today. Dark matter models were broadly divided into three scenarios: cold, warm, and hot dark matter (CDM, WDM, and HDM, respectively), based on the typical mass of the dark matter particles. Due to the survival of matter fluctuations at the galactic scale, HDM models are excluded from consideration (e.g. Peebles, 1982).

In 1998, a discovery independently made by two teams estimating the distance to supernovae of type Ia showed that our Universe was expanding at an accelerating rate (Perlmutter et al., 1998; Schmidt et al., 1998). This required an additional component in our Universe that would allow for an accelerated expansion that counter-acted gravity at large scales. It was this observational evidence that prompted the return of a cosmological constant, $\Lambda$, that while intrinsically different

from that proposed by Einstein, it nonetheless represents an unseen component of our Universe, dark energy (e.g. Peebles & Ratra, 2003).

It is this set of observational evidence that constitutes the current cosmological paradigm: a ΛCDM Universe. This scenario is supported by a plethora of evidence (e.g. Planck Collaboration et al., 2018a,b, and references therein). Although we now know to better precision the value of matter density ($\Omega_m$), dark energy density ($\Omega_\Lambda$) components as well as the rate of current expansion (Hubble constant, $H_0$), it is still commonly used in galactic studies to use the approximation $H_0$ =70 km s$^{-1}$Mpc$^{-1}$, $\Omega_m$ =0.3 and $\Omega_\Lambda$ =0.7.

## 1.2 A GENERAL OVERVIEW ON GALAXY EVOLUTION

The state of the art studies of galaxies, both in observations and theoretical models, span the cosmological timescale. We have as of now observations of galaxies to an epoch the Universe was $\sim$ 400 Myr old ($z \sim 11.1$ Oesch et al., 2016), a cosmological paradigm that can explain the formation and evolution of structures in the Universe (ΛCDM, see e.g. White & Rees, 1978), and the knowledge of the main physical processes that govern galaxy evolution (see e.g. Somerville & Davé, 2015). The standard model of cosmology states that the Universe began in a very hot and dense state approximately $\sim$ 13.8 billion years ago (Planck Collaboration et al., 2016b). Due to a rapid expansion of the Universe, quantum fluctuations grew to macroscopic scales (see e.g. Kamionkowski & Kovetz, 2016) leading to the small scale perturbations that we see in the cosmic microwave background (CMB, Planck Collaboration et al., 2016a). These perturbations grew with time due to their gravitational instabilities and were the seeds of all structure we see in today's Universe. At some point in time, the perturbations grew to a state where gravitational collapse takes over the expansion and the first astrophysical objects (first stars, black holes, and primitive galaxies) started to form (e.g. Bromm & Yoshida, 2011).

Such objects from through the collapse of gas clouds inside the newly formed dark matter halo that, through effective cooling, becomes dense enough and reaches higher temperatures. During this collapsing process, the cloud fragments into small dense cores that will be the birthplace of stars. Once a group of stars has formed from this initial gas cloud, we find the first visible galaxies in the Universe. We have yet to observe such structures and do not fully grasp many details of this process, but it is generally accepted to be the mechanism through which the first generation of galaxies are born (e.g. Mo et al., 2010).

Since established by Hubble (1926) that two general types of galaxies were observed (spirals and ellipticals) detailed models on the formation of such structures were proposed (see Fig. 1.1). One of the explanations for the difference in structure of these two galaxy types is due to the different cooling times (e.g. Eggen et al., 1962). In this scenario, if the cooling time was short,

gas would collapse very rapidly and form an elliptical galaxy. If the cooling time was slow, gravitational energy would be radiated away via shocks and radiative cooling until eventually the cloud would become rotation supported and form a galactic disk. Another important process that helped shape galaxies are the gravitational interactions among themselves, from tidal forces to merging events (e.g. Toomre & Toomre, 1972). The merging process between two disks is also one of the main mechanisms through which elliptical galaxies are thought to be formed. An alternative and more recent formation scenario invokes the presence of cold gas flows that fuel into the centre and disks of galaxies which leads to disk instabilities or elliptical/bulge formation depending on the smoothness or clumpiness of the gas stream. (e.g. Dekel et al., 2009).

Once galaxies form, and more and more gas in-falls due to its gravitational potential, models expect that star formation occurs efficiently and that most of the baryonic matter eventually collapses into stars due to a very efficient cooling process. However, such predictions fall short of reality, as they over-predict the number of stars that we observe in galaxies. Therefore, there must be at least one physical mechanism that prevents the gas from collapsing and cooling. The currently accepted explanations are based on feedback processes. These may be caused by explosion of giant stars (supernovae) or by the activity linked to the central super massive black hole (the so called active galactic nuclei, AGN) that is found in almost all massive galaxies (e.g. Sparke & Gallagher, 2007; Mo et al., 2010).

Over the last decades, we have significantly improved on our knowledge of how galaxies form and evolve through cosmic history (see reviews by Robertson et al., 2010; Dunlop, 2013; Madau & Dickinson, 2014). A particular aspect of this understanding comes from computing the amount of new stars formed per year across time. This is measured through the star formation rate (SFR) density ($\rho_{SFR}$, computed at a fixed co-moving volume) as a function of redshift. On this topic, various surveys indicate that the cosmic $\rho_{SFR}$ had a peak between redshift 2 and 3 and then declines down to the present day (Madau & Dickinson, 2014, and references therein). This fact implies that most of the stars were formed in our Universe more than $\sim 6$ billion years ago.

Nowadays, the preferred scenario for galaxy formation is based on a $\Lambda$-Cold Dark Matter ($\Lambda$CDM) Universe on which galaxies form and reside inside dark matter halos (see summary by Efstathiou & Silk, 1983; Blumenthal et al., 1984). Current large-scale simulations like EAGLE (Schaye et al., 2015) or Illustris (Vogelsberger et al., 2014) include treatment of all kinds of hydrodynamical processes, including AGN and supernovae feedback, and are able to globally reproduce the observed properties of the galaxy population at $z \approx 0$. However, there are still a number of outstanding problems like the universality of the Initial Mass Function (IMF), the co-evolution of galaxies and their central black holes, the formation of the first stars, the model over-prediction of dwarf satellites and the wrong shape of the core of dark matter halos, and the emergence of the Hubble sequence, the role of feedback in regulating star formation, to name a few.

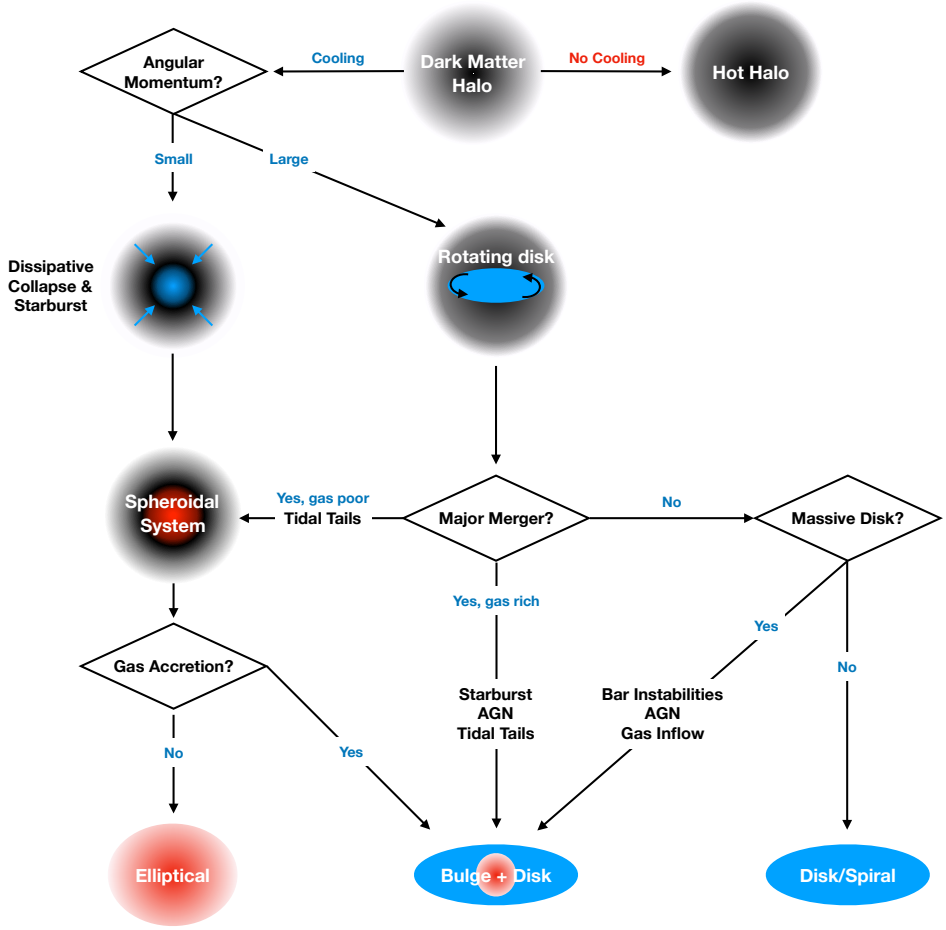


**Figure 1.1** Schematic diagram of galaxy evolution adapted from Mo et al. (2010).

## 1.3 Physical processes affecting galaxy evolution

Once a dark matter halo collapses due to its own gravity and a galaxy forms within this halo, there are several physical mechanisms that shape its evolution to current days (see e.g. Kormendy & Kennicutt, 2004, see also Fig. 1.2). These mechanisms can be broadly grouped in external (involving interactions with other galaxies and/or dark matter halos) or internal (involving interactions between gas, stars, dust within the galaxy itself). Moreover, we can also classify processes as being fast (like galaxy mergers) or slow (like bulge build-up through bars).

One of the key processes that enable galaxy formation is gravity itself. It governs the motions of dark matter, responsible for all structure formation, and allows for the baryonic material to form stars from the collapse of gas clouds within dark matter halos. After galaxies are formed, gravity also plays a crucial role in the rate of merging systems (which affect angular momentum, star formation, morphology among others, see e.g. Conselice, 2014) and their spatial clustering in the Universe.

When gas collapses occur, baryonic matter is increasingly governed by its thermal and hydro-

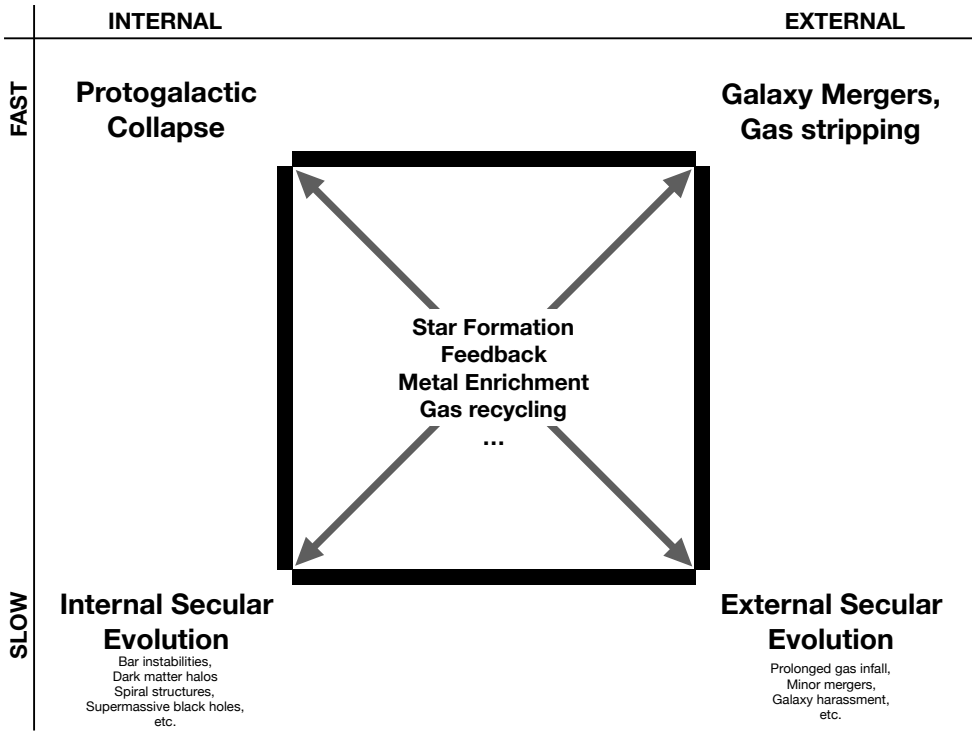


**Figure 1.2** Summary of physical processes affecting galaxy evolution adapted from Kormendy & Kennicutt (2004).

dynamical evolution. There is an increase in gas density, which in turn increases temperature and pressure which can counteract the collapsing strength of gravity. In order for gas clouds to efficiently form dense gas clouds (required for the formation of new stars) one needs a cooling process to radiate away energy, decrease gas pressure, and allow further collapse. Depending on the cooling rates of gas, we can either very rapidly form a proto-galaxy (when cooling times are short) or slowly form quasi-hydrostatic gas halos which cool down. In this scenario, the gas looses pressure until eventually its motion is supported by the angular momentum of the material, giving rise to the formation of galactic disks (e.g. Mo et al., 2010; Somerville & Davé, 2015).

Once gas cools down enough that large molecular gas clouds can form, one has the conditions for the start of star formation. These clouds typically fragment into smaller and denser cores in which the necessary temperatures for nuclear fusion are reached and proto-stars are born (e.g. McKee & Ostriker, 2007; Kennicutt & Evans, 2012; Somerville & Davé, 2015, for reviews on this subject). Alongside star formation, we also need to account for the formation of massive black holes, since they also impact long-term galaxy evolution.

After galaxies are populated by stars and massive black holes, a new mechanism comes into play: feedback. This process is necessary to explain the low fraction of baryons actually locked in stars in our Universe. Otherwise, the very efficient cooling in small halos at high redshift would have formed too many stars by now (e.g. Mo et al., 2010). This led to a number of astrophysical phenomena being called to explain this discrepancy. On one hand, there is feedback from star formation itself, either from strong winds in massive stars or through highly energetic supernovae explosions. One the other hand, large amounts of energy are also transferred to the inter-stellar

medium by the super massive black holes in galaxy centres (e.g. Kereš et al., 2009a; Puchwein & Springel, 2013). Additionally, there are also scenarios in which very massive halos induce gravitational heating of the gas, preventing it from cooling down and forming new stars (e.g. Birnboim et al., 2007).

Subsequent processes influencing galaxy evolution include all dynamical effects that rearrange galactic material after accounting for all intervening forces/components. The most violent events are mergers that can radically alter galactic properties (from star formation to morphology). Less energetic and more common events in the Universe include disk instabilities, cold gas inflows, galactic harassment, successive accretion of small satellites, among others (see e.g. Kormendy & Kennicutt, 2004).

## 1.4 Evolution of galaxy properties across cosmic time

Due to a substantial effort in the past decades we have a broad understanding of the evolution of cosmic star formation, stellar mass, and is relation with halo mass spanning almost the entirety of the Universe history (e.g. Ilbert et al., 2013; Madau & Dickinson, 2014). There is a strong rise in the global star formation and in the assembly of stellar mass from the dark ages down to $z \sim 2$. Since then we have seen a decline of a factor of $\sim$10 in the star formation rate density and a small evolution in the global stellar mass density in galaxies. And, has expected, their morphology also shows a strong evolution that encodes the build-up history of galaxies, and is seen as the transformation of complex/peculiar morphologies at high redshift to the well established Hubble sequence we see in the local Universe (e.g. Delgado-Serrano et al., 2010a; Buitrago et al., 2013; Mortlock et al., 2013; Huertas-Company et al., 2015a). Detailed studies on the build-up of the Hubble sequence show that most morphological changes occurs in the transformation of peculiar/irregular galaxies evolving transforming into disk/spiral galaxies (e.g. Lilly et al., 1998; Delgado-Serrano et al., 2010a; Huertas-Company et al., 2016). The fraction of elliptical/spheroidal galaxies does not change as much since $z \sim 3$ (Mortlock et al., 2013; Huertas-Company et al., 2015a).

In recent years, the wealth of data allowed for the quantification of galaxy morphology with several methods available for the estimation of structural parameters (Conselice, 2014). One of the most commonly studied structural property is the size of galaxies (e.g. Ferguson et al., 2004; Bouwens et al., 2004; Ravindranath et al., 2004; Daddi et al., 2005; Ravindranath et al., 2006; Trujillo et al., 2006a; Akiyama et al., 2008; Franx et al., 2008; Hathi et al., 2008; Tasca et al., 2009; Cassata et al., 2010; Williams et al., 2010; Oesch et al., 2010; Mosleh et al., 2011; Ichikawa et al., 2012; Cassata et al., 2013; Huang et al., 2013; Ono et al., 2013; Stott et al.,

2013a; Morishita et al., 2014; van der Wel et al., 2014; Straatman et al., 2015; Shibuya et al., 2015; Curtis-Lake et al., 2016; Ribeiro et al., 2016). These studies probing a wide range in redshifts and galaxy properties mostly point to the growth of galaxies with cosmic time. It is also widely reported that galaxy sizes depend on stellar mass (e.g. Franx et al., 2008; van der Wel et al., 2014; Morishita et al., 2014) and luminosity (e.g. Grazian et al., 2012; Huang et al., 2013). Although the overall size evolution is the accepted norm there are some instances where sizes are measured to be constant with time, specially at high redshift ($z > 2$, e.g. Law et al., 2007; Curtis-Lake et al., 2016; Ribeiro et al., 2016). Apart from galaxy sizes there are also studies on the evolution of galaxy profiles. There seems to be an overall evolution on the Sérsic index, with larger values at later epochs and the evolution being stronger for spheroidal/quiescent galaxies (Weinzirl et al., 2011; Buitrago et al., 2013; Morishita et al., 2014). And as found in the local Universe, there is also a trend for higher Sérsic indices in spheroidal galaxies with little to no star formation, which dominate the galaxy population at the higher stellar masses ($\log M_\star/M_\odot \gtrsim 10$ Wuyts et al., 2011; Whitaker et al., 2015). A specific branch of galaxy evolution studies at high redshift focus on samples of galaxies selected through Ly$\alpha$ emission (LAEs, e.g. Erb et al., 2006; Gawiser et al., 2006, 2007; Pentericci et al., 2007; Ouchi et al., 2008; Lai et al., 2008; Reddy et al., 2008; Finkelstein et al., 2009; Kornei et al., 2010; Guaita et al., 2011; Nilsson et al., 2011; Acquaviva et al., 2012; Oteo et al., 2015; Hathi et al., 2016; Matthee et al., 2016; Santos et al., 2016; Sobral et al., 2017, 2018b). Regarding their morphology, LAEs have been characterized thoroughly (e.g. Venemans et al., 2005; Pirzkal et al., 2007; Overzier et al., 2008; Taniguchi et al., 2009; Bond et al., 2009, 2011, 2012; Gronwall et al., 2011; Jiang et al., 2013; Kobayashi et al., 2016) and are found to be typically small, often compact objects (half-light radius around 1 kpc), which undergo no evolution in the first 1 to 3 billion years of the Universe ($z \sim 2-6$, e.g Venemans et al., 2005; Malhotra et al., 2012). The different properties of this population with regard to UV-selected samples may be due to their particular selection method, as LAEs are similar to other line-emission selected galaxies at $z \sim 2$ and different from colour-selected galaxies at the same redshifts (e.g. Oteo et al., 2015; Hagen et al., 2016).

From a theoretical perspective, the latest suit of numerical simulations has been producing realistic looking galaxies with morphologies comparable to what is observed in the Universe (e.g. Furlong et al., 2015; Snyder et al., 2015; Clauwens et al., 2018; Dickinson et al., 2018). While it is still a challenge to reproduce the observed sizes in simulated galaxies (e.g. Bottrell et al., 2017; Naab & Ostriker, 2017), there is evidence that matching the observed size distribution of galaxies is key to reproduce galaxy-scaling relations with better agreement with observations (e.g. Ferrero et al., 2017). Clauwens et al. (2018) provided a scenario for galaxy morphology evolution that is mostly dependent on stellar mass of the disk and spheroidal components and not the redshift of formation. The least massive galaxies show irregular morphologies driven by random stellar motions, intermediate stellar mass galaxies grow to spiral disks by in-situ star-formation and the most massive objects are mostly spheroidal that grow through accretion

of stars at large radii.

The evolution of galaxies in time is accompanied by the growth of large scale structure and the emergence of dense and void regions in the Universe (see e.g. Springel et al., 2005; Genel et al., 2014; Schaye et al., 2015). And there was early evidence that galaxy morphology not only evolves with time but also with the environment (e.g. Oemler, 1974; Dressler, 1980, 1984). Cluster galaxies are typically elliptical, red, and massive/quenched while in low density environments the population is dominated by spiral blue star-forming galaxies (SFGs, e.g. Dressler et al., 1997; Balogh et al., 2004; Kauffmann et al., 2004; Baldry et al., 2006; Bamford et al., 2009). The galaxy density (often projected local density, $\Sigma$, or normalised over-density, $\delta$) has also been found to correlate strongly with the star formation rate (SFR) and star-forming fraction ($f_{\rm SF}$, e.g. Lewis et al., 2002; Gómez et al., 2003; Hogg et al., 2004; Best, 2004; Kodama et al., 2004). Observations also imply that most massive galaxies assembled their stellar mass quicker (at earlier times in the Universe, when typical SFRs were much higher than presently) and had their star formation quenched in the past (e.g. Iovino et al., 2010). In what concerns galaxy morphology, there seems to be a correlation with environment at least out to $z \sim 1$ ($z < 1$, e.g. Dressler et al., 1997; van der Wel et al., 2007; Tasca et al., 2009). At higher redshifts the evidence is scarce, but there are hints that from size studies that such differentiation might happen at earlier times (e.g. Grützbauch et al., 2011; Bassett et al., 2013a; Strazzullo et al., 2013; Allen et al., 2015).

The plethora of processes affecting galaxy evolution require different and complementary studies to tackle the topic of galaxy evolution. In this thesis I will present results based on different approaches and complement existing studies with new analysis and samples aimed at unveiling the processes shaping evolution of galaxies across time and space.

## 1.5 This thesis

This thesis presents different approaches to the study of galaxy evolution, with a particular emphasis on galaxy morphology across cosmic time and environments. The structure of this thesis is as follows:

Chapter 2 is dedicated to the study of morphological evolution of star-forming galaxies selected through their H$\alpha$ luminosity in the last 11 Gyr. I establish a comparison between local and the distant Universe by combining the largest H$\alpha$ survey (High-Z Emission Line Survey, Sobral et al., 2013a) with ongoing local IFU surveys (e.g. CALIFA - Sánchez et al. (2012), SAMI - Bryant et al. (2015); MaNGA - Bundy et al. (2015)) and a local reference sample (NYU-VAGC, Blanton et al., 2005c). I address the issue of cosmological surface brightness dimming by implementing an algorithm designed to artificially redshift local galaxies and assess the impact of such effects

on the derived structural properties. I establish an evolution scenario for star-forming galaxies in terms of their sizes and typical profile shapes and also address the evolution of the stellar mass-size relation.

Chapters 3 and 4 focus on the morphological characterization of Ly$\alpha$ emitting galaxies (LAEs) from $2 < z < 6$ and $6 < z < 7$, respectively. This study is based on samples of galaxies selected through narrow- and medium-band imaging data (explored in Sobral et al., 2015a, 2018b; Matthee et al., 2016, 2017a,b; Santos et al., 2016). On the lower redshift sample, we focus on the largest sample of Ly$\alpha$ selected galaxies compiled to date and trace the evolution of the general population of LAEs. In the highest redshift sample (observed at in the epoch of reionization), I focus only on a subset of the most luminous emitters published to date and present my preliminary analysis of their morphological properties.

Chapters 5 through 8 are dedicated to the scientific exploration of the VIS$^3$COS survey (Paulino-Afonso et al., 2018a) which targets a superstructure at $z \sim 0.84$ and contains high resolution spectroscopic data for $\sim 500$ galaxies in and around that structure. Chapter 5 focus on the survey presentation and the study of star formation in different environments. Chapter 6 details the analysis of three spectral features ([OII] emission, the H$\delta$ Balmer line, and $D_n4000$) as a function of stellar mass and environment. Chapter 7 studies the possible existence of a kind of morphology-density relation (see e.g. Dressler, 1980) at $z \sim 0.84$ and its relation to star formation. Finally, Chap. 8 focus on the estimates of galactic electron densities measured from the [OII] line doublet and how it changes with stellar mass and local density.

Finally, in Chap. 9 I summarize the main findings of this thesis. I note that Chap. 2, 3 and 5 are based on articles of which I am first-author and which are already published in peer reviewed journals (Paulino-Afonso et al., 2017, 2018a,b). I also note that the structure of this thesis is done is such a way that each chapter should be self-contained, with similar structure to published scientific articles.

# CHAPTER 2

## THE STRUCTURAL AND SIZE EVOLUTION OF STAR-FORMING GALAXIES OVER THE LAST 11 GYR

*We present new results on the evolution of rest-frame blue/UV sizes and Sérsic indices of Hα-selected star-forming galaxies over the last 11 Gyr. We investigate how the perceived evolution can be affected by a range of biases and systematics such as cosmological dimming and resolution effects. We use* GALFIT *and an artificial redshifting technique, which includes the luminosity evolution of Hα-selected galaxies, to quantify the change on the measured structural parameters with redshift. We find typical sizes of 2 to 3 kpc and Sérsic indices of $n \sim 1.2$, close to pure exponential disks all the way from $z = 2.23$ to $z = 0.4$. At $z = 0$ we find typical sizes of $4-5$ kpc. Our results show that, when using GALFIT, cosmological dimming has a negligible impact on the derived effective radius for galaxies with $< 10$ kpc, but we find a $\sim 20\%$ bias on the estimate of the median Sérsic indices, rendering galaxies more disk-like. Star-forming galaxies have grown on average by a factor of $2-3$ in the last 11 Gyr with $r_e \propto (1+z)^{-0.75}$. By exploring the evolution of the stellar mass-size relation we find evidence for a stronger size evolution of the most massive star-forming galaxies since $z \sim 2$, as they grow faster towards $z \sim 0$ when compared to the lower stellar mass counterparts. As we are tracing the rest-frame blue/UV, we are likely witnessing the growth of disks where star formation is ongoing in galaxies while their profiles remain close to exponential disks, $n \lesssim 1.5$, across the same period.*

adapted from **Paulino-Afonso**, A., Sobral, D., Buitrago, F. & Afonso, J., 2017, MNRAS, 465, 2717

## 2.1 INTRODUCTION

Ever since the first classification schemes based on the visual appearance of galaxies were created (e.g. Hubble, 1926; de Vaucouleurs, 1959), the ways we study galaxy morphology have evolved dramatically. On one hand, we have improved on the quantification of the light distribution in galaxies either using parametric surface brightness profiles (e.g. Caon et al., 1993; Simard, 1998; Peng et al., 2002, 2010a) or non-parametric approaches (e.g. Abraham et al., 1994; Conselice, 2003; Lotz et al., 2004; Law et al., 2007; Freeman et al., 2013). On the other hand, there was the

need to create new classifications as galaxies become more and more irregular towards higher redshift (e.g. Delgado-Serrano et al., 2010b; Huertas-Company et al., 2015a).

Although the observed morphology may not be directly linked with intrinsic properties of the stellar populations and dust/gas content of galaxies (see e.g. Conselice, 2014, and references therein), early studies have shown that rest-frame optical morphology correlates with colour and star-formation activity (e.g. Holmberg, 1958) and there is a marked difference in the prevalence of different morphological populations in different environments (e.g. Dressler, 1980). These effects are seen both in the local (e.g. Ball et al., 2008; Bamford et al., 2009) and in the higher redshift Universe (e.g. Pérez-González et al., 2008; Viero et al., 2012; Bassett et al., 2013b). Additionally, there was significant work regarding correlations between the shape of a galaxy and other physical properties such as stellar populations, mass and star formation (e.g. Roberts & Haynes, 1994; Conselice, 2003; Blanton et al., 2003; Wuyts et al., 2011; Whitaker et al., 2015). Processes such as galaxy mergers, *in-situ* star formation and accretion of inter-galactic gas can be revealed by a detailed structural analysis of galaxy samples.

The peak of star formation in the Universe occurred at $z \sim 2$ ($\sim 11$ Gyr ago, e.g. Madau & Dickinson, 2014, and references therein) and it is also since this peak of activity that most of the structures (disk and spheroidal galaxies) that we observe today have been formed (e.g. Buitrago et al., 2013; Mortlock et al., 2013). However, to understand how the baryonic structures grew between different cosmological epochs it is not only necessary to study morphology, but also couple that with kinematic information.

In the recent years, it has been possible to study the interplay between galaxy morphology and kinematics by making use of the new available Integral Field Unit (IFU) instruments. These allowed for large galaxy surveys either in the local Universe (e.g. CALIFA Sánchez et al. (2012), SAMI Bryant et al. (2015); MaNGA Bundy et al. (2015)) and at high redshift (e.g. KROSS Stott et al. (2016), KMOS$^{3D}$ Wisnioski et al. (2015)), and added valuable information that will provide key insights on the physics that drive galaxy evolution.

Despite the large potential for progress, to connect observed properties across a large span of time we need to account for biases and systematics which can arise either due to selection or instrumental and/or cosmological effects. To overcome these problems we need both large and homogeneous surveys at various cosmic epochs to minimize the impact of cosmic variance and to probe a wide range of galaxy properties and environments. This is now possible when using surveys based on well known and calibrated physical properties over a wide range of redshifts, such as H$\alpha$ in narrow band-surveys (see e.g. Moorwood et al., 2000; Geach et al., 2008; Villar et al., 2008; Sobral et al., 2009; Ly et al., 2011; Sobral et al., 2011) and in spectroscopic/grism surveys (see e.g. McCarthy et al., 1999; Yan et al., 1999; Hopkins et al., 2000; Shim et al., 2009; Atek et al., 2010; van Dokkum et al., 2011).

Nonetheless, even with an ideal, homogeneous sample, we still need to account for all effects

that have a dependence on redshift as they could mimic and/or influence evolutionary trends that we observe. One of the strongest effects that impacts the study of galaxy morphology is the surface brightness dimming (Tolman, 1930). Between $z \sim 0$ and $z \sim 2$ this effect impacts the observed fluxes by two orders of magnitude. The first attempts to describe the impact of the surface brightness dimming on how galaxies would be observed at high redshift if they were as we see them today were conducted by Weedman & Huenemoerder (1985). Later on, studies on the impact on galaxy visual morphology (e.g. Giavalisco et al., 1996; Hibbard & Vacca, 1997) and on the morphology quantifiers (e.g. Trujillo et al., 2007; Barden et al., 2008; Petty et al., 2009; Weinzirl et al., 2011; Mosleh et al., 2013) were also carried out and find no systematics and errors $\lesssim 15\%$ on the derived sizes at $z \sim 1$. Nonetheless, these studies are often limited to small samples and comparison between two distinct epochs (one local and one at high redshift).

There are numerous studies reporting on size and structural evolution of galaxies (e.g. Ferguson et al., 2004; Ravindranath et al., 2004; Trujillo et al., 2006b; Buitrago et al., 2008; Cimatti et al., 2008; Franx et al., 2008; van Dokkum et al., 2010; Wuyts et al., 2011; Mosleh et al., 2011; Ichikawa et al., 2012). For star-forming galaxies (SFGs) in the range $0.5 < z \lesssim 3$ studies find moderate (e.g. $r_e \propto (1+z)^{\alpha}$; Buitrago et al., 2008; van der Wel et al., 2014; Morishita et al., 2014, with $\alpha = -0.82, -0.75, -0.57$, respectively) to negligible size evolution (Stott et al., 2013b) and light profiles close to exponential disks (e.g. Morishita et al., 2014; Shibuya et al., 2015). For $2 < z < 4.5$, it was shown that the trend on size evolution (measured from rest-frame UV) depends on the method used to derive galaxy sizes (Ribeiro et al., 2016). And, at even higher redshifts ($4 < z < 8$), Curtis-Lake et al. (2016), using FUV rest-frame galaxy sizes, show that the derived evolution depends on the statistical estimators one uses. These evolutionary trends of galaxy growth and the relation of sizes with stellar masses are also found in large scale cosmological simulations (e.g. Genel et al., 2014; Furlong et al., 2015). However, we do not know yet if such differences can be explained by different selection methods for the definition of the SFGs samples (e.g. Oteo et al., 2015).

Although there are existing studies on the morphologies of SFGs (e.g. van der Wel et al., 2014; Morishita et al., 2014; Shibuya et al., 2015) and on the quantification of systematic differences of structural properties at low and high redshift (e.g. Barden et al., 2008; Petty et al., 2009; Weinzirl et al., 2011; Mosleh et al., 2013), it is still unclear what the role of potential biases and systematics may be. In this chapter, we take advantage of a unique H$\alpha$ selection, along with the largest IFU samples, to make further progress on the current open questions.

This chapter is organized as follows. In Sect. 2.2 we describe the samples of SFGs that will be used throughout the chapter. We present our methodology to simulate galaxies at high redshift and to study their structural parameters in Sect. 2.3 and 2.4. The results obtained for our low and high redshift SFGs and simulations are reported in Sect. 2.5. We discuss the implications of our results in the context of galaxy evolution in the last $\sim$11 Gyr in Sect. 2.6. Finally, in Section 2.7 we summarize our conclusions. Magnitudes are given in the AB system (Oke & Gunn, 1983).

All the results assume a ΛCDM cosmological model with $H_0$=70.0 km s$^{-1}$Mpc$^{-1}$, $\Omega_m$=0.3 and $\Omega_\Lambda$=0.7 and a Chabrier (2003) initial mass function.

## 2.2 GALAXY SAMPLES

**Table 2.1** Samples studied in this chapter. The median redshift, median stellar mass and median observed aperture corrected (for SAMI, MaNGA, and NYU-VAGC) H$\alpha$ luminosity (in ergs s$^{-1}$) for all samples. The last column shows the ratio of the median observed aperture corrected (for SAMI, MaNGA and NYU-VAGC) H$\alpha$ luminosity to the $L^*_{\rm H\alpha}$ at the median redshift. The value in brackets shows the median values for each subsample after applying the selection criteria defined in Sect. 2.2.

| | Sample | $\tilde{z}$ | $N_{\rm tot}[N_{\rm subsample}]$ | $\log_{10}(M_\star/M_\odot)$ | $\log_{10}(L_{\rm H\alpha})$ | $L_{\rm H\alpha}/L^*_{\rm H\alpha}(z)$ |
|---|---|---|---|---|---|---|
| Local | CALIFA | 0.015 [0.016] | 541 [137] | 10.44 [10.53] | 41.08 [41.22] | 0.16 [0.22] |
| | SAMI | 0.039 [0.049] | 2349 [422] | 10.06 [10.26] | 40.38 [41.22] | 0.03 [0.21] |
| | MaNGA | 0.030 [0.037] | 8492 [1536] | 9.85 [9.91] | 40.25 [41.14] | 0.02 [0.18] |
| | NYU-VAGC | 0.041 [0.041] | 1285 [412] | 9.73 [10.08] | 40.74 [41.05] | 0.07 [0.14] |
| HiZELS | NB921 | 0.400 | 460 [33] | 8.25 [9.83] | 40.39 [41.31] | 0.02 [0.18] |
| | NBJ | 0.840 | 425 [309] | 9.69 [9.96] | 41.43 [41.45] | 0.15 [0.16] |
| | NBH | 1.470 | 313 [250] | 9.65 [9.89] | 42.11 [42.12] | 0.38 [0.38] |
| | NBK | 2.230 | 572 [526] | 9.71 [9.74] | 42.19 [42.19] | 0.21 [0.21] |

The main sample of SFGs that we use in this chapter comes from the High-Z Emission Line Survey (HiZELS, Sobral et al., 2013a). Being the largest H$\alpha$ narrow-band survey at high-redshift it provided targets to be observed with IFU instruments such as VLT/SINFONI (Swinbank et al., 2012a,b) and VLT/KMOS (Sobral et al., 2013b; Stott et al., 2014, 2016). Other samples are selected from the currently on-going IFU surveys in the local Universe (see Sect 2.2.1). However, local samples differ from a simple H$\alpha$ selection as done in HiZELS. To ensure that we are studying comparable populations, we apply simple sample selection based on stellar mass and H$\alpha$ luminosity:

$$\log_{10}(M_\star/M_\odot) > 9 \quad \wedge \quad L_{\rm H\alpha} > 0.1 L^*_{\rm H\alpha}(z), \tag{2.1}$$

where the luminosity cut is taken from the equation for the redshift evolution of $L^*_{\rm H\alpha}$ derived by Sobral et al. (2013a)

$$\log_{10}(L^*_{\rm H\alpha}(z)) = 0.45z + 41.87 \tag{2.2}$$

We choose to focus our study by selecting samples through their H$\alpha$ luminosities since such samples should be representative of the full star-forming population (e.g. Oteo et al., 2015). Note that for the local Universe samples, with the exception of the CALIFA survey, we only

have available H$\alpha$ luminosities measured inside a 3" fibre. We thus apply aperture corrections following e.g. Garn & Best (2010) by computing the flux ratio of the total and fiber magnitudes in the Sloan Digital Sky Survey (SDSS) *r*-band (the filter that contains H$\alpha$) and applying that correction to the observed fibre-based H$\alpha$ luminosity. These correction factors vary from $\sim 1.5$ up to $\sim 40$. Our samples and the selection criteria are shown in Fig. 2.1. For a quick summary we refer the reader to Table 2.1.

### 2.2.1 THE LOW-REDSHIFT SAMPLES

#### 2.2.1.1 THE CALIFA SAMPLE

The Calar Alto Legacy Integral Field spectroscopy Area (CALIFA, Sánchez et al., 2012) survey is a program conducted using the Potsdam Multi-Aperture Spectrophotometer with PMAS fibre PAcK (PMAS/PPAK) integral field spectrophotometer mounted on the 3.5m Calar Alto telescope. The survey aims at observing $\sim 600$ galaxies in the local Universe (redshift range $0.005 < z < 0.03$), which are selected from the SDSS as a sample limited in apparent diameter ($45" < D < 80"$). This constraint assures that galaxies are observed within the large field of view ($\sim 1$ arcmin$^2$) with a large covering fraction and high spectral resolution.

We use the reported values by Catalán-Torrecilla et al. (2015) for the H$\alpha$ luminosities of this sample, which are available for 270 galaxies. By taking the selection criteria defined in Eq. 2.1 we reach a final sample of 137 CALIFA galaxies (see Fig. 2.1).

#### 2.2.1.2 THE SAMI TARGET SAMPLE

The Sydney-AAO Multi-object Integral field spectrograph (SAMI, Bryant et al., 2015) Galaxy survey proposes to target 3400 galaxies with the SAMI instrument mounted on the Anglo-Australian Telescope (AAT). This survey targets galaxies in the redshift range $0.004 < z < 0.095$, SDSS magnitudes $r_{\rm pet} < 19.4$, from low ($10^7 M_\odot$) to high stellar mass ($10^{12} M_\odot$), both isolated, in groups or members of clusters with halo masses of $\sim 10^{15} M_\odot$. Most of the targets (with the exception of few cluster objects) have available SDSS coverage and are selected from the Galaxy and Mass Assembly survey (GAMA, Driver et al., 2009).

We use the GAMA Data Release 2 (Liske et al., 2015) to obtain H$\alpha$ luminosities for the SAMI sample. By taking the selection criteria defined in Eq. 2.1 we reach a final sample of 422 SAMI galaxies (see Fig. 2.1). We note that the SAMI sample is stellar-mass complete for our mass limit only at $z < 0.5$. We include higher redshift galaxies but do not expect it to have a great impact on our derived results.

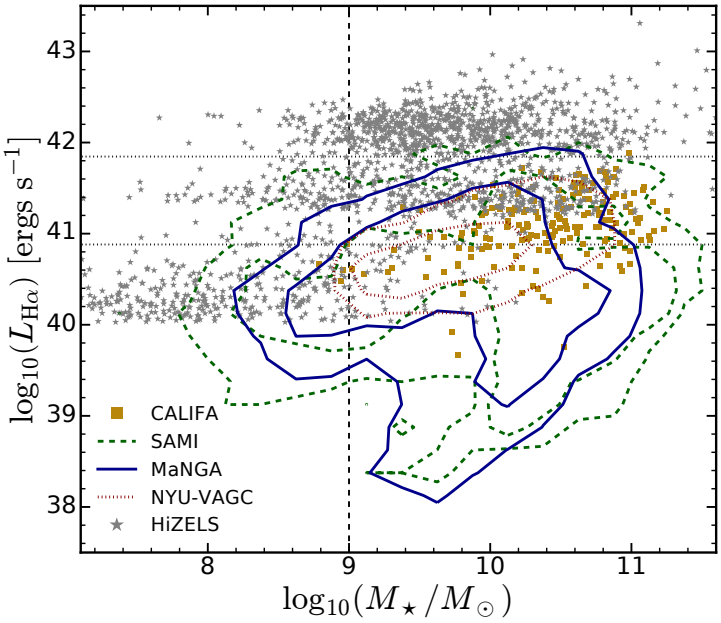


**Figure 2.1** The stellar masses and aperture corrected observed H$\alpha$ luminosities of the parent samples used in this chapter. The contour lines for SAMI, MaNGA, and NYU-VAGC show the limits that contain 68% and 95% of the sample for two-dimensional histograms with 0.25 width bins in both stellar mass and H$\alpha$ luminosity. The vertical dashed line shows the stellar mass cut used for the final sample selection. We see that most our samples are above the stellar mass limit imposed in our selection and that the local redshift samples overlap. The horizontal dotted lines show the H$\alpha$ limits at $z = 0.01$ (lower line) and at $z = 2.23$ (upper line). This shows that the H$\alpha$ luminosity selection as a great impact on the final samples that we study.

#### 2.2.1.3 A MaNGA-LIKE SAMPLE

The Mapping Nearby Galaxies at Apache point observatory (MaNGA, Bundy et al., 2015) survey is part of the SDSS-IV program and aims to study kinematics and internal composition of a sample of $\sim$ 10000 galaxies. It will do so with fiber-bundle IFUs with diameters ranging from $12''$ to $32''$ and will provide spectral information in the full optical range. The MaNGA sample is derived from an extended version of the NASA Sloan-Atlas (NSA), based on the SDSS DR7 Main Galaxy Sample (Abazajian et al., 2009) with the additions and improvements detailed by Blanton et al. (2011)[1]. It will observe galaxies at redshifts $0.01 < z < 0.15$ with stellar masses above $\sim 10^9 M_\odot$ and it will make use of redshift and $i$-band luminosity to achieve a homogeneous radial coverage (see Fig. 8 of Bundy et al., 2015), flat stellar mass distributions and a diversity of environments. An additional selection on colour space will enhance the targeting of rarer galaxies (green valley, low mass red, and massive blue galaxies).

Using the available data from NSA we attempt to mimic the MaNGA selection by applying the selection bands as described in Bundy et al. (2015). We use the published version of the NSA table (restricting our galaxies to $z < 0.055$) and pre-select all galaxies that fall inside the selection bands of Fig. 8 by Bundy et al. (2015). We randomly select $\sim$ 6000 galaxies (with uniform sampling up to $1.5r_e$, primary selection criteria) and $\sim$ 2500 galaxies (with uniform sampling up

[1] http://www.nsatlas.org

to $2.5r_e$, secondary selection criteria) to roughly match the sample numbers of MaNGA (Bundy et al., 2015). We neglect the colour enhanced selection. By taking the selection criteria defined in Eq. 2.1 we reach a final sample of 1536 MaNGA galaxies (see Fig. 2.1).

#### 2.2.1.4 THE NYU-VAGC SAMPLE

This sample is based on the New-York University Value Added Galaxy Catalog (NYU-VAGC, Blanton et al., 2005c). A subset of the catalogue, which was constructed as a volume limited sample with well defined selection criteria (see Blanton et al., 2005b), was chosen as a control sample so that we may inspect if the IFU samples are biased against a magnitude selected sample. To complement the information we matched the catalogue with the Max Planck for Astronomy & Johns Hopkins University Data Release 7 catalogues (MPA-JHU DR7) (Kauffmann et al., 2003; Tremonti et al., 2004; Salim et al., 2007), which have spectroscopic information for SDSS DR7 galaxies (Abazajian et al., 2009).

We first do a pre-selection of SFGs with stellar masses $9 < \log_{10}(M_\star/M_\odot) < 12$ and H$\alpha$ luminosities greater than $L_{\mathrm{H}\alpha} > 10^{39.5}$ergs s$^{-1}$ to exclude both low and high stellar masses and match the HiZELS detection limits. This results in a total of $\sim$ 13000 galaxies. From this sample, we have randomly selected 10% (1285) of all galaxies. This selection was performed by randomly picking galaxies with a probability matched to the magnitude, radius and Sérsic indices distribution available from the NYU-VAGC catalogue. With this method we guarantee that we probe the full morphological parameter space using this subset.

We then restrict our sample to 412 NYU-VAGC galaxies (see Fig. 2.1) with aperture corrected H$\alpha$ luminosities and stellar masses matching our sample selection criteria defined in Eq. 2.1.

### 2.2.2 THE HIGH-REDSHIFT UNIVERSE

By using four narrow-band filters in the $z$, $J$, $H$, and $K$-band, HiZELS (Sobral et al., 2013a) has detected thousands of H$\alpha$ emitters in four distinct redshifts intervals centred at 0.4, 0.84, 1.47, and 2.23. Such large samples, selected in an uniform way, allow one to probe galactic evolution across these slices of our Universe that map the decline since the peak of star formation activity. To ensure that the selection is effective in picking up H$\alpha$ emitters, the observations were conducted on well studied extragalactic fields (UDS, COSMOS, SA22, ELAIS N1, Boötes, and Lockman Hole), where the ancillary broad band data helps at pinpointing H$\alpha$ emitters by means of colour selections and photometric redshifts to allow for the control of the contamination rates (Sobral et al., 2013a).

In this chapter we make use of the list of emitters that are found in the COSMOS field (Sobral

et al., 2013a) for which we have extensive coverage of F814W imaging obtained with the Hubble Space Telescope (Scoville et al., 2007). After applying the selection cuts defined in Eq. 2.1 we reach final samples with 33 galaxies at $z = 0.4$, 309 galaxies at $z = 0.84$, 250 galaxies at $z = 1.47$, and 526 galaxies at $z = 2.23$ (see Table 2.1).

## 2.3 ARTIFICIAL REDSHIFTING GALAXIES

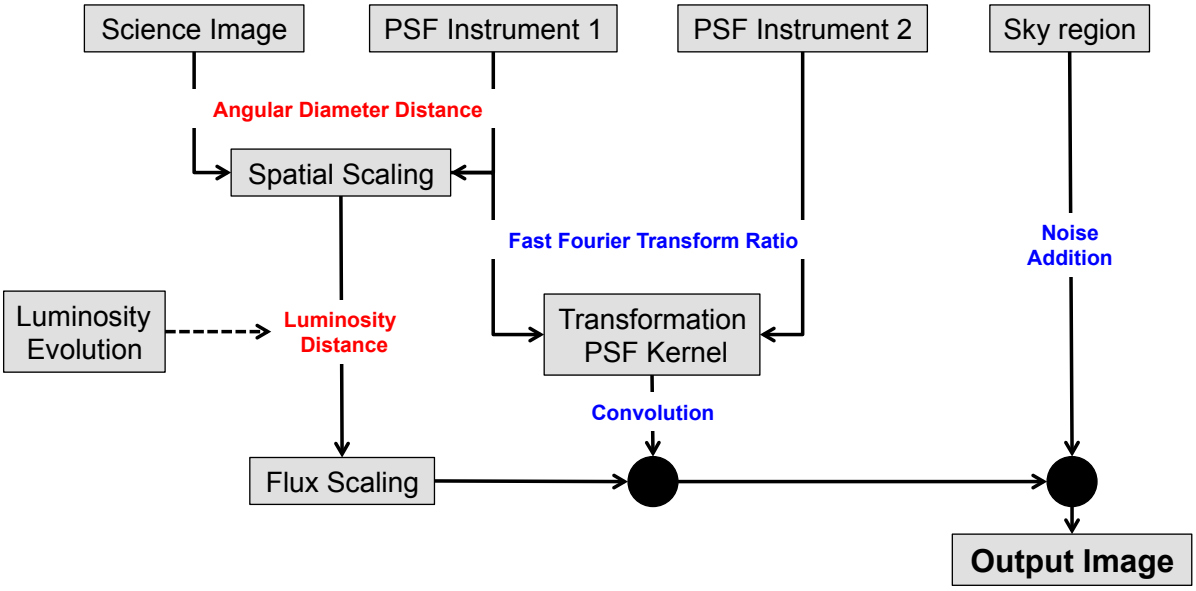


**Figure 2.2** Schematic diagram of the algorithm for artificially redshift galaxies. Each step is described in Sect. 2.3.

To understand how the perceived structural parameters have changed across cosmic time we study how our local galaxies would look like if they were at high redshift. We explore and evaluate the effects of cosmological dimming on various properties of galaxies (e.g. size/shape measurements) taking into account that these are prone to resolution and bandpass issues.

By artificially redshifting galaxy images, we aim to address the biases and systematics of the parent sample and to build a coherent vision of the galaxies' structural evolution. To do that we translate the core algorithm of FERENGI (Barden et al., 2008) into PYTHON and we include a more general treatment of the intrinsic luminosity evolution of galaxies as a function of redshift. This treatment ensures that we are using an artificially redshifted sample that closely matches, in brightness, the sample that we have at higher redshifts. The core of the algorithm is shown as a diagram in Fig. 2.2 and is briefly summarized in the following steps:

1. We re-scale our image (preserving their total flux) to match the pixel-scale of the high redshift observations while preserving the physical scale of the galaxy.

2. We apply a flux correction to the image that is the combination of two factors: the

dimming factor that scales as the inverse of the luminosity distance to the galaxy, and the luminosity evolution factor which account for the average evolution in brightness across different redshifts and is taken from Sobral et al. (2013a). Since we are studying rest-frame blue/NUV, we assume light scales with SFR/H$\alpha$.

3. We compute a transformation PSF following the prescription described by Barden et al. (2008) applied to the PSFs of the used instruments.

4. We convolve the re-scaled image with the PSF computed in the previous step and then we place the image on an empty region of the target high redshift survey.

Note that we study rest-frame blue/NUV light for a sample of galaxies which are star-forming by selection. So, we expect that at these wavelengths the light will be dominated by young stars and we do not expect great differences across the rest-frame wavelengths that we cover (2500 – 5800Å).

As an example, we show the final result of this algorithm applied in 4 different galaxies redshifted into 4 different redshifts is shown in Fig. 2.3. We show that most of the fine substructures at low redshift are suppressed. The galaxies are still visible, albeit at a low surface brightness level, across all redshifts.

## 2.4 Parametric Morphological Analysis

One of the most common ways of characterizing the structure of galaxies is to fit a Sérsic (1968) profile to the surface brightness distribution of galaxy images (e.g. Davies et al., 1988; Caon et al., 1993; Andredakis et al., 1995; Moriondo et al., 1998; Simard, 1998; Khosroshahi et al., 2000; Graham, 2001; Möllenhoff & Heidt, 2001; Trujillo et al., 2001; Peng et al., 2002; Blanton et al., 2003; Trujillo et al., 2007; Wuyts et al., 2011; van der Wel et al., 2014). This profile is characterized by the functional form

$$I(r) = I_e \exp[-\kappa(r/r_e)^{1/n} + \kappa],$$

where the Sérsic index $n$ describes the shape of the light profile, $r_e$ is the effective radius of the profile, $I_e$ is the surface brightness at radius $r = r_e$ and $\kappa$ is a parameter coupled to $n$ such that half of the total flux is enclosed within $r_e$. An index of $n = 1$ corresponds to a typical exponential disk galaxy, whereas $n = 4$ corresponds to the classical de Vaucouleurs profile associated to elliptical galaxies.

To conduct this parametric analysis we make use of GALFIT (Peng et al., 2002, 2010a), which is a public algorithm designed to perform a detailed two-dimensional decomposition of galaxies

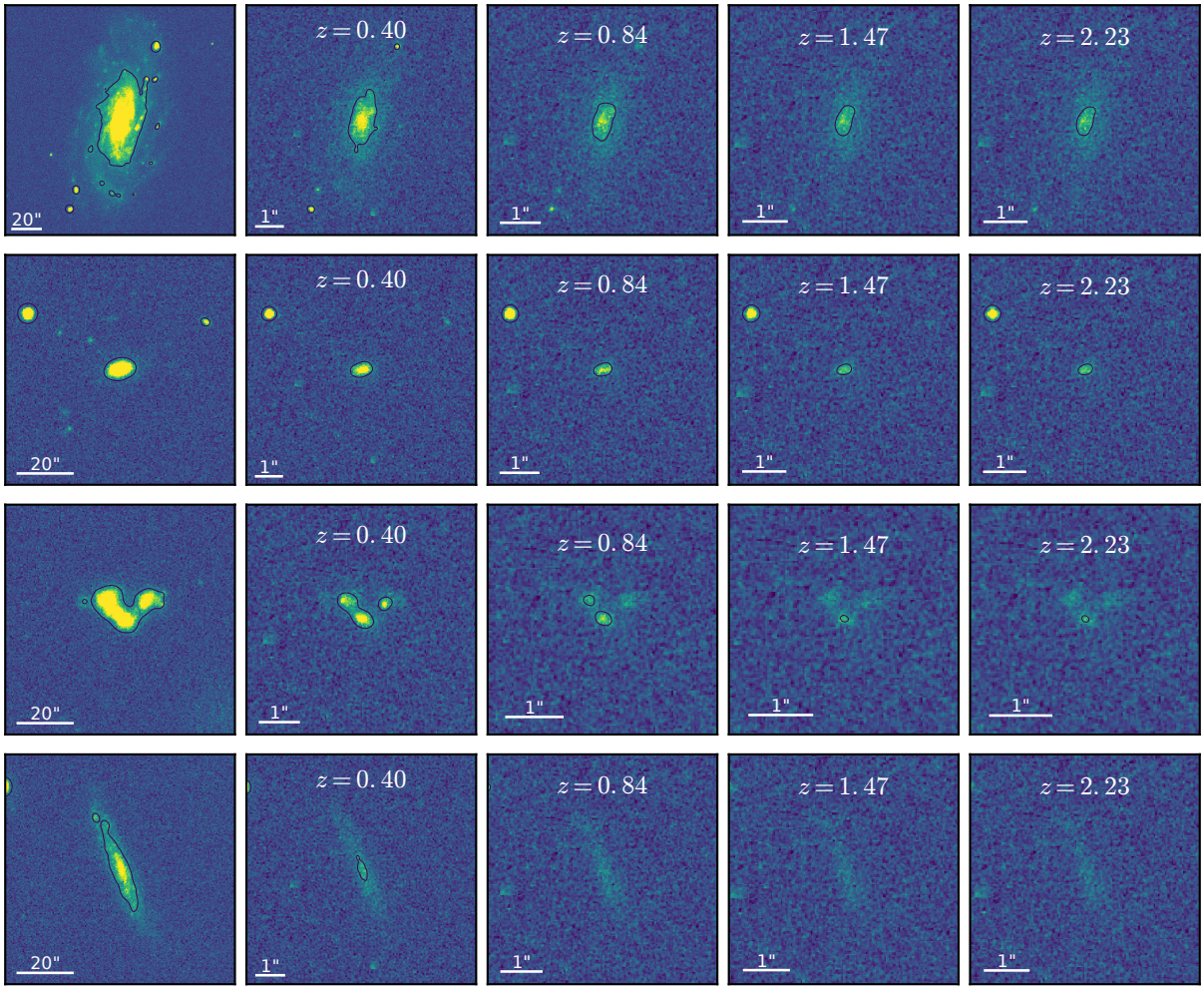


**Figure 2.3** Artificial redshifted examples for 4 galaxies from the samples used in this chapter. The leftmost panel is the original SDSS $g$-band image. The next 4 panels show the effect of artificial redshifting the galaxy to 4 different redshifts, increasing from left to right. The contours show the $3\sigma$ level detection in each image. In each image the colour map ranges from -3$\sigma$ to 10$\sigma$. We observe that the fainter/external regions of the galaxies observed in the local Universe completely disappear as we move towards higher redshifts. All images have the same physical scale. The observed scale is shown for each panel to compare angular sizes at different redshifts.

using mathematical models.

On 2D images, each Sérsic model has potentially seven free parameters: the position of the center, given by $x_c$ and $y_c$, the total magnitude of the model, $m_{tot}$, the effective radius, $r_e$, the Sérsic index, $n$, the axis ratio of the ellipse, $b/a$, and the position angle, $\theta_{PA}$, which refers to the angle between the major axis of the ellipse and the vertical axis and it has the sole purpose of rotating the model to match the galaxy's image.

Since GALFIT requires an initial set of parameters from which to start evaluating the model, it is necessary to provide it with realistic guesses. For that reason, we use the source extraction software SExtractor (Bertin & Arnouts, 1996), which allows one to directly obtain a set of parameters that will serve as input to GALFIT and to find the model that best fits the data faster and with reliable values.

We use 10" $\times$ 10" cut-outs of the HST ACS F814W (Scoville et al., 2007; Koekemoer et al., 2007) centred on each HiZELS galaxy. The cut-outs are downloaded from the COSMOS HST archive. These images have a typical PSF FWHM of $\sim 0.09''$, a pixel scale of $0.03''$/pixel and a limiting point-source depth AB(F814W) = 27.2 (5 $\sigma$). For the low-redshift samples, we use images from SDSS DR9 (Ahn et al., 2012) $g$-band imaging data. These are characterized by a median PSF FWHM of $\sim 1.3''$, a pixel scale of $0.396''$/pixel and a 95% completeness for point sources at a magnitude of $g = 22.2$. For each SDSS image, the cut-out size is proportional to the extent of the galaxy we want to fit in order to accommodate a reasonable amount of sky area (at least 50% of the total region). This is done so that GALFIT can simultaneously fit the residual sky emission.

We masked galaxy neighbours by use of the segmentation map output by SExtractor. All sources that fall outside the galaxy of interest are masked. To account for the instrumental PSF, in the case of SDSS data we use interpolated PSF models (Lupton et al., 2001) reconstructed with *sdss_psfrec.pro*[2]. For HST F814W images, the PSF was one of the TINYTIM (Krist, 1995) models as described by Rhodes et al. (2006, 2007).

Irregular, complex and/or sources detected at low S/N are excluded from the final sample as GALFIT failed to converge on meaningful structural parameters (see Fig. 2.12 and 2.13 for a comparison between those and the full sample). These cases amount from 8% (in the NYU-VAGC sample) up to 40% (in the $z \sim 2.23$ HiZELS sample) of our samples which are distributed in both stellar masses and H$\alpha$ luminosities in the same way as the full sample. Thus, this rate of failure does not introduce any bias against stellar masses or H$\alpha$ luminosities (see Appendix of this chapter).

## 2.5 RESULTS

### 2.5.1 THE IMPACT OF SURFACE BRIGHTNESS DIMMING

We focus our attention on the impact of surface brightness dimming on two structural parameters that are often used to describe the global morphology of galaxies: the effective radius ($r_e$) and the Sérsic index ($n$) (see e.g. van der Wel et al., 2014; Morishita et al., 2014; Shibuya et al., 2015).

We investigate the ratio of fractional error for $r_e$ for all samples described in Sect. 2.2.1 and at the four redshifts slices observed with HiZELS. We show (in Fig. 2.4) that the effective radius is, on average, recovered with success (within an error margin of $\sim$ 10%) for galaxies with $r_{e,z\approx 0} < 10$ kpc. For larger galaxies we reach a saturation value, i.e., galaxies with $r_{e,z\approx 0} > 10$

[2] http://www.sdss.org/dr12/algorithms/read_psf/

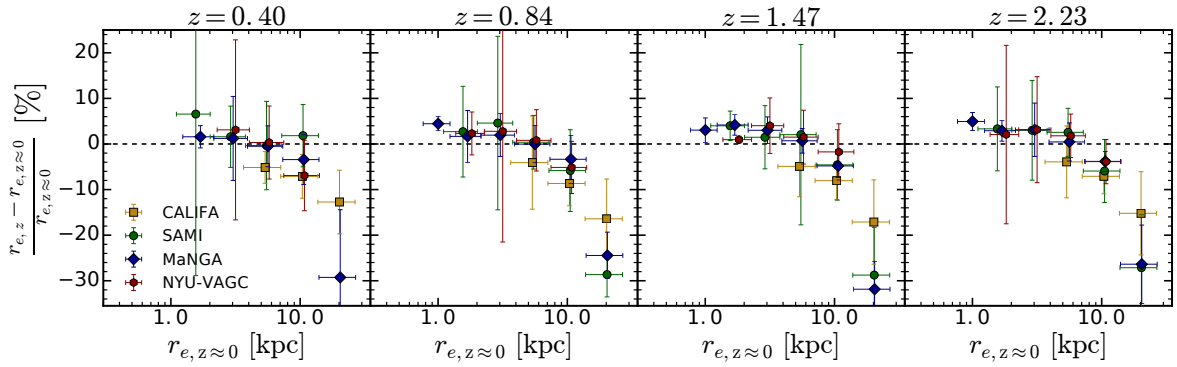


**Figure 2.4** The fraction difference between the recovered and input effective radius, $(r_{e,z} - r_{e,z\approx0})/r_{e,z\approx0}$, for each of the local subsamples and each redshift (one per column). Each symbol represent the median values in bins (with a minimum of 10 galaxies) of width of the horizontal error bar. The vertical error bar shows the error on the median value. The black dashed line pinpoints a fractional difference of 0, i.e., when the recovered effective radius is the same as input. We find the difference to be very small (<10%) up to 10 kpc. Above that value, the size of galaxies is more severely underestimated ($\sim 10-30\%$). Small horizontal offsets were applied to improve the readability of the plot.

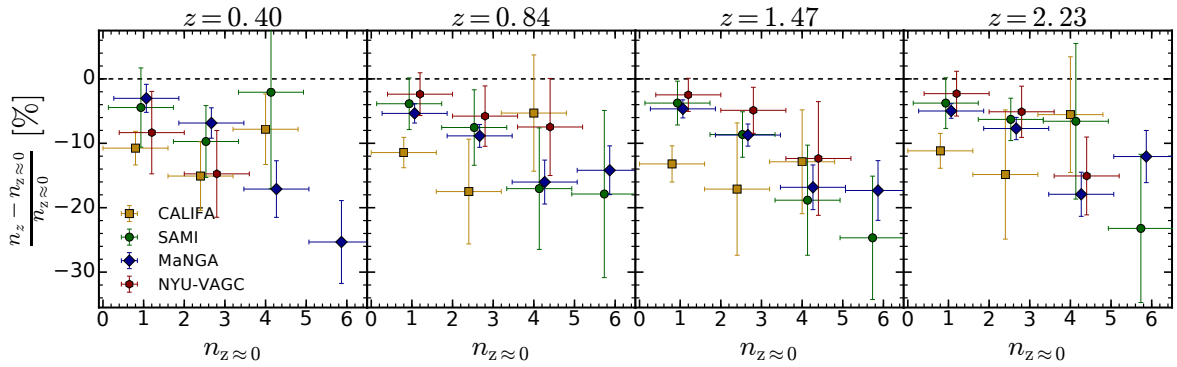


**Figure 2.5** The fraction difference between the recovered and input Sérsic index, $(n_z - n_{z\approx0})/n_{z\approx0}$, for each of the local subsamples and each redshift (one per column). Each symbol represent the median values in bins (with a minimum of 10 galaxies) of width of the horizontal error bar. The vertical error bar shows the error on the median value. The black dashed line pinpoints a fractional difference of 0, i.e., when the recovered effective radius is the same as input. We find that the value of the Sérsic index is always underestimated ($\sim 2-30\%$) in all redshifts and for all four surveys. Small horizontal offsets were applied to improve the readability of the plot.

kpc are recovered, on average, with $r_e \sim 10-20$ kpc (thus the ratio declines for larger radii). This effect is seen on the CALIFA and MaNGA subsamples which are the ones where we have galaxies in this range of sizes. It is also noticeable that for the smaller galaxies we have a higher chance of recovering the value observed at $z \approx 0$.

We also investigate the impact on the derived Sérsic indices. We show in Fig. 2.5 that we recover the value of the Sérsic index at a smaller value (by $\sim 5-20\%$) than the one that is observed at $z \approx 0$. This effect is larger at larger $n_{z\approx0}$ and it shows in all samples at all redshifts. There does not seem to be any systematic offset between different redshifts.

We show in Appendix the impact of dimming on the recovered total magnitudes (corrected for the luminosity evolution) and axis ratio of the profiles of individual galaxies. Our results are consistent with those exploring artificial redshifting up to $z \sim 1$ (Barden et al., 2008; Mosleh

et al., 2013) and also for artificial redshifting of massive galaxies from $z \sim 0$ to $z \sim 2.5$ (Weinzirl et al., 2011).

The success of the recovery of the structural parameters for the highest redshift galaxies is directly linked to the counter-balance of the luminosity evolution and the cosmological surface brightness dimming. We have tested a scenario where galaxies undergo no luminosity evolution and the recovery of galaxies (at the largest radius) is severely affected. This would imply that we would not be able to observe large galaxies at higher redshifts and thus, our distributions would be skewed towards smaller sizes potentially mimicking an evolution scenario.

That impact is explored in Table 2.2 where we compare the median values of the distributions in $r_e$ and $n$ at each redshift compared to the observed median value at $z \approx 0$. As somewhat expected from the comparison of individual galaxies, we observe no systematic trend induced by the cosmological dimming on the recovered median values. For $r_e$ we see that we slightly underestimate sizes for galaxies in the CALIFA sample ($\sim 90\%$ of the original). For the other samples, we get the same median value within $\lesssim 10\%$ at all redshifts. As for the value of $n$, we systematically underestimate the median value at a level of $11-27\%$ of the value observed at $z \approx 0$ with all artificially redshifted samples. This value does not seem to change as a function of redshift.

We discuss the dependence of the fractional error of sizes and Sérsic indexes on the input magnitude in Appendix to this chapter. The reader is also referred to that Appendix for a discussion on the possible explanations for a systematic overestimation of sizes due to dimming.

**Table 2.2** Ratio of the median values, $r_e$ and $n$, for each simulated redshift to the observed values at z≈0. This dimensionless value quantifies the over/under estimation of each parameter as a function of the simulated redshift. The average values derived from the 4 samples are used for correction.

| | $\frac{r_{e,z}}{r_{e,z\approx0}}$ \| $\frac{n_z}{n_{z\approx0}}$ | | | |
|---|---|---|---|---|
| | $z = 0.40$ | $z = 0.84$ | $z = 1.47$ | $z = 2.23$ |
| CALIFA | 0.885 \| 0.805 | 0.918 \| 0.828 | 0.863 \| 0.829 | 0.918 \| 0.839 |
| SAMI | 1.006 \| 0.869 | 1.166 \| 0.763 | 1.096 \| 0.812 | 1.052 \| 0.789 |
| MaNGA | 1.031 \| 0.856 | 1.037 \| 0.848 | 1.039 \| 0.851 | 1.037 \| 0.832 |
| NYU-VAGC | 1.107 \| 0.729 | 1.011 \| 0.841 | 0.989 \| 0.832 | 1.001 \| 0.887 |
| Average | 1.007 \| 0.815 | 1.033 \| 0.820 | 0.997 \| 0.831 | 1.002 \| 0.837 |

### 2.5.2 THE STRUCTURE AND SIZES OF GALAXIES

We plot the histograms of sizes ($r_e$) and Sérsic indices ($n$) in Fig. 2.6 and 2.7 and we summarize the median values in Table 2.3. For the local samples we see that galaxies have, on average, $r_e \sim 9$ kpc for the CALIFA sample and $r_e \sim 4-5$ kpc for the other three samples. We want to

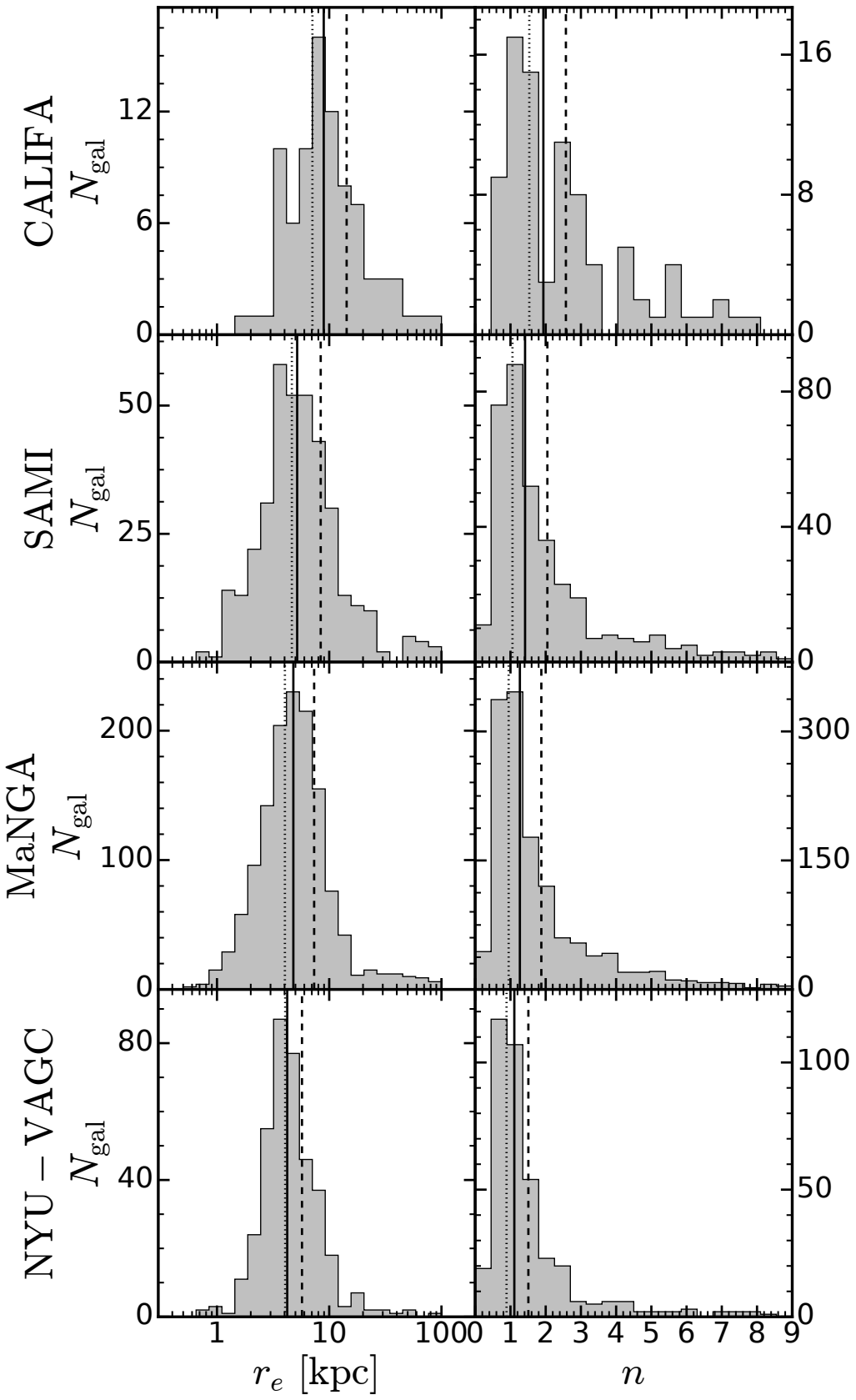


**Figure 2.6** Distributions of sizes ($r_e$) and Sérsic indices ($n$) of the galaxies observed at $z \approx 0$ for the 4 local samples defined in Sect. 2.2. The vertical solid, dashed and dotted lines indicate the median, mean, and modal values, respectively.

**Table 2.3** Median, mean, and modal values for the effective radius ($r_e$) and Sérsic index ($n$) for all samples described in Sect. 2.2. The errors on the median denote the 16th (lower bound) and 84th (upper bound) percentiles of the variables distribution.

| | | $r_e$[kpc] | | | $n$ | |
|---|---|---|---|---|---|---|
| Sample | median | mean | mode | median | mean | mode |
| CALIFA | $8.94^{+11.13}_{-4.60}$ | $14.30 \pm 1.83$ | 7.08 | $1.93^{+2.34}_{-0.85}$ | $2.57 \pm 0.19$ | 1.53 |
| SAMI | $5.18^{+5.54}_{-2.51}$ | $8.40 \pm 0.62$ | 4.65 | $1.41^{+1.89}_{-0.67}$ | $2.05 \pm 0.09$ | 1.06 |
| MaNGA | $4.79^{+3.94}_{-2.24}$ | $7.34 \pm 0.30$ | 4.03 | $1.27^{+1.83}_{-0.56}$ | $1.88 \pm 0.05$ | 0.95 |
| NYU-VAGC | $4.23^{+3.30}_{-1.50}$ | $5.72 \pm 0.34$ | 4.05 | $1.11^{+1.07}_{-0.45}$ | $1.51 \pm 0.07$ | 0.89 |
| $z = 0.40$ | $3.98^{+2.34}_{-1.30}$ | $5.88 \pm 1.49$ | 3.67 | $1.04^{+0.49}_{-0.47}$ | $1.29 \pm 0.23$ | 0.69 |
| $z = 0.84$ | $3.72^{+2.45}_{-1.87}$ | $4.77 \pm 0.35$ | 3.50 | $1.05^{+1.49}_{-0.55}$ | $1.55 \pm 0.08$ | 0.64 |
| $z = 1.47$ | $2.79^{+2.89}_{-1.55}$ | $3.78 \pm 0.25$ | 2.26 | $1.16^{+1.62}_{-0.72}$ | $1.58 \pm 0.11$ | 0.91 |
| $z = 2.23$ | $2.17^{+2.35}_{-1.11}$ | $2.89 \pm 0.16$ | 1.47 | $1.15^{+1.92}_{-0.76}$ | $1.73 \pm 0.10$ | 0.58 |

**Table 2.4** Median values of $\alpha_X$ after fitting through all samples and for fitting only the HiZELS high-$z$ sample.

| Variable | Correction | All samples | High-$z$ only |
|---|---|---|---|
| $\alpha_{r_e}$ | w/o dimm. | $-0.74 \pm 0.20$ | $-0.71 \pm 0.11$ |
| | w/ dimm. | $-0.75 \pm 0.20$ | $-0.70 \pm 0.09$ |
| $\alpha_n$ | w/o dimm. | $-0.25 \pm 0.21$ | $0.15 \pm 0.04$ |
| | w/ dimm. | $-0.07 \pm 0.19$ | $0.12 \pm 0.04$ |

stress that the CALIFA sample is diameter selected to match the diameter of the IFU field of view and that is what is driving the larger sizes with respect to the other samples, which have lesser to no constraints on galaxy size in their selection. As for the values of $n$, we see that the distributions are similar, but peaking at increasing values of $n$ for NYU-VAGC, MaNGA, SAMI and CALIFA, respectively. Again, the CALIFA sample shows an increased fraction of galaxies with high value of $n$, which is likely due to the morphological constraint to cover the entire Hubble diagram.

As we examine the high redshift galaxies from HiZELS (Fig. 2.7) we see that galaxies have increasingly smaller sizes as we move towards higher redshifts with median values ranging from $r_e \sim 2$ kpc at $z = 2.23$ up to $r_e \sim 4$ kpc at $z = 0.40$. As for the values of the Sérsic indices, we see that it is rather stable at these redshifts with median values around $n \sim 1.1$, close to exponential disk profiles characteristic of SFGs in the local Universe. We do not observe an enhancement of the fraction of higher $n$ galaxies at any redshift probed with HiZELS. We note that this is not driven by observational biases.

There are some cases of SFGs with large sizes and/or Sérsic indices seen in Fig. 2.7. However, these generally come from poorly constrained fits, which involve large errors on both $r_e$ and $n$.

### 2.5.3 THE EVOLUTION OF THE STRUCTURE AND SIZES OF GALAXIES

After obtaining the structural parameters of our samples we can see how they compare in terms of their evolution. In Fig. 2.8 we show how the measured sizes and Sérsic indices depend on redshift. We fit the equation

$$X \propto (1+z)^{\alpha_X} \tag{2.3}$$

for $X = r_e, n$ to quantify the rate of change of these quantities across cosmic time. We compute these quantities by considering, or not, the impact of dimming in terms of the overestimate/underestimate average ratios shown in Table 2.2. Theses results are summarized on Table 2.4.

From an overall perspective on the H$\alpha$-selected sample the scenario of size growth is compatible with mild evolution ($\alpha_{r_e} \approx -0.7 \pm 0.11$) between redshifts 2.2 and 0.4. We see in Table 2.4 that considering the entire redshift range (by including the local samples in the fit) increases slightly the value of the slope to $\alpha_{r_e} \approx -0.75 \pm 0.20$, which is fully consistent with the result obtained using only the higher redshift samples from HiZELS. We can also see that including the dimming correction has virtually no impact on the derived value of $\alpha_{r_e}$, as expected from what we see in Table 2.2. These slopes deviate more than $3\sigma$ from the no evolution scenario ($\alpha = 0$) and thus it is very unlikely that galaxies experience no growth across this period.

We also investigate any potential evolution of the median value of the Sérsic index of galaxies where we get slightly different solutions if we look only at the higher redshift samples (decreasing Sérsic index with time, $\alpha_n \approx 0.15 \pm 0.04$) or include all the samples in the fit (increasing Sérsic index with time, $\alpha_n \approx -0.25 \pm 0.21$). However, we note that the slopes are very shallow and point to almost no evolution. These two slightly contrasting scenarios are appeased when we include the impact of dimming in the derived value of $n$ derived in Table 2.2. With that correction we obtain $\alpha_n \approx -0.07 \pm 0.19$ for all samples and $\alpha_n \approx 0.12 \pm 0.04$ when only considering the HiZELS samples. Considering the full range in redshifts, our derived evolution encompasses the value $\alpha = 0$ within the $1\sigma$ error. This supports a scenario where SFGs maintain their surface brightness distribution close to pure exponential disks at all times.

### 2.5.4 THE SIZE-MASS RELATION ACROSS COSMIC TIME

The other aspect to retain from the morphological analysis is the relation of the structural parameters with the stellar mass, which is displayed in Fig. 2.9 and 2.10. There, we show the median values in bins of stellar mass and their dispersion on the stellar mass-size relation

alongside with the individual measurements for all galaxies. In order to parametrize this relation we use the functional form

$$r_e \propto M_\star^{\alpha_{M_\star}} \tag{2.4}$$

which is over plotted as a red solid line in those figures. The slopes of this relation are summarized in Table 2.5.

To fit the stellar mass-size relation we perform a Monte Carlo Markov Chain simulation (using the *emcee* package, Foreman-Mackey et al., 2013) where all individual galaxies are considered for the fit. The first guess is computed from a simple fit to the binned points. We use a total of 50 chains with initial guesses randomly deviated from the simple fit. Each chain then runs for 2000 steps and we exclude the first 500 steps for each chain to erase the influence of the initial first guesses. The reported errors on the slope are the width of the posterior distribution.

**Table 2.5** Slope of the stellar mass-size relation for all the samples described in Sect. 2.2.

| Sample | $\alpha_{M_\star}$ |
|---|---|
| CALIFA | $0.05 \pm 0.17$ |
| SAMI | $0.37 \pm 0.07$ |
| MaNGA | $0.44 \pm 0.05$ |
| NYU-VAGC | $0.32 \pm 0.09$ |
| $z = 0.40$ | $0.15 \pm 0.36$ |
| $z = 0.84$ | $0.11 \pm 0.11$ |
| $z = 1.47$ | $-0.03 \pm 0.14$ |
| $z = 2.23$ | $0.05 \pm 0.11$ |

We show that for the local samples, apart from CALIFA, there is a more evident correlation of sizes with stellar masses as that measured from the HiZELS samples. Again, for the CALIFA sample, the marked difference against the other local Universe samples is related to the size constraint imposed for the parent selection of CALIFA. This results in a flatter stellar mass-size relation as galaxies were chosen to have similar sizes within the sample and stresses the importance of sample selection whenever we study a galaxy population. Due to this selection effect, we disregard the CALIFA sample when establishing comparisons between local and high-redshift morphologies. Nonetheless, despite the apparent inversion of the relation for $z = 1.47$, we observe that on average the most massive galaxies are larger than their lower mass counterparts.

We compare our best fit relations with those found in the literature for SFGs and find that in the local Universe the CALIFA sample is the one that deviates the most from what is found in SDSS by Shen et al. (2003) and Guo et al. (2009). This deviation from CALIFA is expected since it is a size-selected sample and thus a flatter correlation with stellar mass is unsurprising.

As we move towards higher redshifts, we observe that the HiZELS sample changes its slope to shallower values. This is in contrast with the apparent constancy in the stellar mass-size relation slopes found by van der Wel et al. (2014) and Morishita et al. (2014). We note that their selection of SFGs is based on a colour-colour diagram, and not on H$\alpha$. On top of that, we measure our relation on bluer wavelengths than those studies which are based on rest-frame optical data on smaller areas of the sky.

We go further in the investigation of the evolution of this stellar mass-size relation across cosmic time and plot the values of the slope as a function of redshift in Fig. 2.11. Again, if one excludes CALIFA sample (due to its selection bias), the relation is becoming steeper as we move towards the local Universe. We note also that the steepening appears to occur mostly between $z = 0.4$ and $z \approx 0$ as when we look only at the HiZELS samples the rate of change on the value of $\alpha_{M_\star}$ is smaller. We have attempted to improve the robustness of our fits by relaxing the H$\alpha$ luminosity cut and down to $0.01L^*_{\mathrm{H}\alpha}$ for $z = 0.4$. We have 95 galaxies in this scenario and derive a slope of $\alpha_M = 0.17 \pm 0.26$, consistent with what we have but with a slightly smaller error.

By using the fits derived in Eq. 2.4 it is possible to derive the effective radius at a given stellar mass for all the samples we are studying in this chapter. We have computed the sizes of galaxies at $\log_{10} M_\star/M_\odot = 10, 10.5$ and find that they follow a similar trend as displayed in Fig. 2.8 and Table 2.3. The evolution one would derive from this quantity is similar to that of using the median sizes for the galaxy population. Additionally one can see that the more massive galaxies tend to grow faster with cosmic time as the differences between consecutive redshift slices is larger at $\log_{10} M_\star/M_\odot = 10.5$ than at $\log_{10} M_\star/M_\odot = 10$.

### 2.5.5 Impact of cosmological dimming on the stellar-mass-size relation

We attempt to quantify the impact that dimming may have on the derived stellar mass-size relations by exploring the dependence of the fractional error on the effective radius on the stellar mass of the input galaxy. In Fig. 2.18 we see that there is no strong correlation between the two quantities. However, we do find that galaxies at the highest masses ($\log_{10}(M_\star/M_\odot) \gtrsim 10.5$) are more likely to have their sizes underestimated at a level of $\lesssim 20\%$. We do not find any dependence on the effect of dimming with simulated redshift slice. These two results imply that it is unlikely that the shallow slopes that we observe for our stellar mass-size relations are caused by the cosmological dimming.

Thus, we believe that the differences we observe are due to our selection based on H$\alpha$ and to the weaker correlation between rest-frame UV light and stellar mass which is measured mostly from rest-frame NIR.

## 2.6 DISCUSSION

In order to infer the true evolution of galaxies we need to account for any observational bias that may affect our observed results. Regarding morphology, and its evolution with redshift, the strongest bias could come from cosmological surface brightness dimming. The impact of this dimming was already extensively explored out to $z \sim 1-2.5$ by Barden et al. (2008) (see also Trujillo et al., 2007; Franx et al., 2008; Weinzirl et al., 2011; Mosleh et al., 2013), where they find that to have little impact on GALFIT based measurements in this redshift range. Nevertheless due to the strong dependence of dimming on redshift and the luminosity evolution of galaxies with redshift, any evolutionary trend must be taken with care. For instance, Ichikawa et al. (2012) found a small evolution on galaxy sizes in optical rest-frame, but consistent with the expected effect from cosmological dimming. We show in Sect. 2.5 that indeed the cosmological dimming has a small impact on the derived sizes and it is more important on the derived Sérsic indices.

As for the local samples we find galaxies that are 2-3 times larger, depending on the local sample we consider, when compared to other studies based on late-type galaxies in SDSS. For example, Shen et al. (2003) find values of the half-light Petrosian radius $r_{50} \sim 2.5$ (3.2) kpc at stellar masses of $\log_{10}(M_\star/M_\odot) = 10$ (10.5). Guo et al. (2009) study central galaxies in SDSS, and find that late-type galaxies have $\sqrt{b/a}r_e \sim 2.45$ (4.78) kpc at stellar masses of $\log_{10}(M_\star/M_\odot) = 10$ (10.5).

The differences that we find in the typical sizes of galaxies are a reflection of differences in the overall stellar mass-size relation. Shen et al. (2003) fitted a double power law and finds slopes of $\alpha_{M_\star} = 0.14$ for $\log_{10}(M_\star/M_\odot) < 10.6$ and $\alpha_{M_\star} = 0.39$ for $\log_{10}(M_\star/M_\odot) > 10.6$. Note that we use the major axis effective radius in all our plots to be comparable to those reported by the literature at high-redshift, namely the values from Stott et al. (2013b). However, the values reported by Shen et al. (2003) refer to the circularized effective radius. When using this size estimate we get a much better agreement between our results and those reported by Shen et al. (2003), especially on the control NYU-VAGC sample. We do, however, still find a bias that IFU samples have slightly larger galaxies at high masses. This small bias may be perceived as an attempt to maximize the covering factor of IFU instruments. We computed the absolute difference between between our best fit model and the quoted best fit by Shen et al. (2003) in the stellar mass interval $9 < \log(M_\star/M_\odot) < 11.5$ we find that difference to be a factor of $2-3$ smaller when using the circularized effective radius.

Guo et al. (2009) finds a steeper slope of the stellar mass-size relation with $\alpha_{M_\star} = 0.47 \pm 0.03$, which is slightly higher but statistically compatible with our observed slopes for the local samples. We note that our SFGs are lying in between the slopes that are found but have larger sizes at the same stellar masses. However, we stress that the selection of late-type galaxies in SDSS is different than what we have applied (see Sect. 2.2). They are based in either visual inspection

(Guo et al., 2009) and structural separation (using the concentration $c < 2.86$ and $n < 2.5$, Shen et al., 2003). We also exclude low mass galaxies from the fit ($\log(M_\star/M_\odot) < 9$), which influence the stellar mass-size relation by Shen et al. (2003). We are also missing very massive galaxies ($\log(M_\star/M_\odot) \gtrsim 11$), which could influence our slopes to shallower values if they populate a lower size than what is predicted from our fits. We note however that we agree with the results from the literature at a $\sim 2\sigma$ level and that our shallower slopes could be driven by our smaller sample size or that we are measuring sizes in the blue-NUV rest-frame region.

As for the size evolution our derived trends are consistent with the slopes found by van der Wel et al. (2014), $\alpha_{r_e} = -0.75$ and slightly steeper than what was found by Morishita et al. (2014), $\alpha_{r_e} = -0.57$. Both these studies target SFGs selected from the $UVJ$ diagram (Williams et al., 2009) at redshifts $z < 3.0$. They also focus on the stellar mass-size relation and find a consistent slope of $\alpha_{M_\star} = 0.22$ (van der Wel et al., 2014) and $\alpha_{M_\star} \sim 0.2$ (Morishita et al., 2014) at all redshifts. This slopes are within the errors of the slope found at $z < 0.84$, but we find consistently shallower slopes at higher redshifts and a possible hint of evolution with increasingly shallow slopes as we move to higher redshifts.

These shallow slopes are more consistent with those derived by Stott et al. (2013b), using the same HiZELS sample but measuring sizes in rest-frame ground-based optical images. They do not find any evolution at the same redshifts and find remarkably constant sizes with $r_e(M_\star = 10^{10} M_\odot) \sim 3.6$ kpc in the same redshifts we probe here. The small change in sizes found by Stott et al. (2013b) may seem contradictory to the evolution we find which is mostly anchored on the larger difference in sizes observed at $z = 2.23$. We believe that the different findings may be caused by a different sample selection but more importantly by the different resolution and rest-frame bands that we use. Stott et al. (2013b) use of $K$ band imaging data (covers the region $6800 - 15700$Å rest-frame) and can be less prone to a morphological $k$-correction than the use of F814W which covers the region $2500 - 5800$Å rest-frame). This is especially true for galaxies with a strong $D_n4000$Å break and for galaxies with spatially disparate young and old stellar populations. However, for strong SFGs, the break is expected to be small (e.g. figure 2 of Li et al., 2015, and references therein). Additionally, it has been shown that for galaxies with dominant star-forming population the morphological $k$-correction is small (e.g. Conselice et al., 2000b; Windhorst et al., 2002; Taylor-Mager et al., 2007). Nonetheless, it is possible that we are seeing a different path of evolution for the young star-forming regions when compared to the older underlying stellar population. This points to a scenario where star formation happens from inside-out and we are witnessing the star formation activity extending to the outer regions of the galactic disk (see e.g. Hagen et al., 2016).

van der Wel et al. (2014) finds that late-type galaxies are smaller at longer wavelengths and that this trend is stronger for the most massive galaxies. This trend is weaker as we move towards higher redshifts. When applied to the HiZELS sample, where the provided corrections can be applied, these two effects combined could contribute to shallower stellar mass-size relation

slopes as the most-massive, lower redshift galaxies would be the ones with the largest decrease in size. However, we already find shallower slopes than those reported by other studies and these effects would only contribute to a more consistent, no-evolution scenario, of the slope of the stellar mass-size relation which would then be consistent with what is found by Stott et al. (2013b).

We can also compare our results to other typical selections of high-redshift galaxies, namely those based on the Lyman Break Galaxies (LBGs, Steidel et al., 1996). For example, (Ferguson et al., 2004; Mosleh et al., 2011; Shibuya et al., 2015) find stronger evolution of these populations with slopes $\alpha_{r_e} < -1$. Mosleh et al. (2011) also finds steeper slopes for galaxies with UV bright selections. This hints at the fact that despite tracing part of a star-forming population, the LBG selection misses the global picture of star-forming galaxies that should be the dominant population at high redshifts.

There are also studies using galaxies selected by their photometric redshift (e.g Trujillo et al., 2006b, 2007; Buitrago et al., 2008; Franx et al., 2008) and they find a global size evolution scaling with $\alpha_{r_e} = -0.40$, $-0.82$,$\sim -0.59$ at $0 < z \lesssim 3$, respectively, and also a stronger size evolution going from low to high mass galaxies. However, they have not specifically targeted the star-forming population at these redshifts.

## 2.7 Conclusions

We present the morphological characterization of SFGs selected through their H$\alpha$ luminosity and we compare their evolution across the last 11 Gyr of the Universe ($z < 2.23$). We compare the correlation of the structural parameters with the stellar mass and derive evolutionary trends for galaxy sizes (parametrized as the effective radius) and Sérsic indices including the effect of cosmological dimming in the analysis. Our main results are:

- Cosmological surface brightness dimming (when using GALFIT) has a negligible impact ($\lesssim 10\%$) on the derived effective radius for all galaxies with $r_e < 10$ kpc. We show that it impacts the derivation of the Sérsic index, where we find a systematic underestimation of $\sim 20\%$ at the higher redshifts in the artificially redshifted samples compared to the ones observed at $z \approx 0$. This underestimation does not change the fact that the observed galaxies have surface brightness profiles similar to exponential disks.

- Effective radii of SFGs show moderate evolution ($\alpha_{r_e} \approx 0.7 \pm 0.2$) from $z = 2.23$ down to $z \approx 0$. They have a range of galaxy sizes that grow from $\sim 2$ kpc at $z = 2.23$ up to $4-9$ kpc at $z \approx 0$.

- We find that SFGs have typically disk-like profiles with a median value of $n \sim 1.2$. Their

Sérsic indices show negligible evolution ($\alpha_n$ is consistent with 0) across the same period with a median value of $1 < n < 1.5$, close to exponential disk profiles.

- The stellar mass-size relation becomes steeper as we move towards lower redshifts. This hints at a stronger size evolution of the most massive SFGs when compared to the lower mass counterparts.

We use 4 different samples in the local Universe, 3 of them based on ongoing IFU surveys and one selected from SDSS as a control sample, to compare local to high redshift morphologies. Due to its diameter selected sample, the SFGs in the CALIFA survey are the most biased against a dynamic range in galaxy sizes. This limits the interpretations of the results if it is to be used as a local counterpart to the high-redshift samples being gathered with near-infrared IFU instruments. As for the SAMI and MaNGA samples, they seem to provide a representative morphological range of the local Universe, when compared to our NYU-VAGC control sample and, therefore, are more suitable for such comparisons.

Our results reveal that cosmological dimming plays a negligible role in the derivation of evolutionary trends on galaxy morphology for SFGs (and when using GALFIT). We show that SFGs grow in size, as seen from blue to UV rest-frame regions, by a factor of 2-3 since $z \sim 2.23$ while their profile shapes remain the same (close to exponential disks). Interestingly, this growth is not observed in the same sample as seen from red-NIR regions (Stott et al., 2013b) and the observed differences are not due to sampling issues. This can also be linked to a scenario of inside-out star-formation as seen by Nelson et al. (2016). Although selection effects may play a role, it is possible that we are witnessing two distinct evolution paths for active star-forming regions and the underlying older stellar population across these redshifts. Alternatively, investigating new non-parametric size measurements, which fully account for cosmological surface brightness dimming (Ribeiro et al., 2016), might provide new hints at size evolution trends. Moreover, our results put into perspective the galaxy morphologies of ongoing local IFU surveys and serve as a reference for future comparisons of local and high redshift IFU galaxy surveys.

## ACKNOWLEDGEMENTS

We thank the anonymous referee for the thorough review, positives comments, and constructive remarks which greatly improved the quality and clarity of this work. We also thank J. Stott for sharing their size measurements that were used in the making of this study. This work was supported by Fundação para a Ciência e a Tecnologia (FCT) through the research grant UID/FIS/04434/2013. APA, PhD::SPACE fellow, acknowledges support from the FCT through the fellowship PD/BD/52706/2014. DS acknowledges financial support from the Netherlands Organisation for Scientific research (NWO) through a Veni fellowship and from FCT through a

FCT Investigator Starting Grant and Start-up Grant (IF/01154/2012/CP0189/CT0010).

Funding for SDSS-III has been provided by the Alfred P. Sloan Foundation, the Participating Institutions, the National Science Foundation, and the U.S. Department of Energy Office of Science. The SDSS-III web site is http://www.sdss3.org/. SDSS-III is managed by the Astrophysical Research Consortium for the Participating Institutions of the SDSS-III Collaboration including the University of Arizona, the Brazilian Participation Group, Brookhaven National Laboratory, Carnegie Mellon University, University of Florida, the French Participation Group, the German Participation Group, Harvard University, the Instituto de Astrofisica de Canarias, the Michigan State/Notre Dame/JINA Participation Group, Johns Hopkins University, Lawrence Berkeley National Laboratory, Max Planck Institute for Astrophysics, Max Planck Institute for Extraterrestrial Physics, New Mexico State University, New York University, Ohio State University, Pennsylvania State University, University of Portsmouth, Princeton University, the Spanish Participation Group, University of Tokyo, University of Utah, Vanderbilt University, University of Virginia, University of Washington, and Yale University.

The HiZELS sample used in this work is publicly available from Sobral et al. (2013a).

This work was only possible by the use of the following PYTHON packages: NumPy & SciPy (Walt et al., 2011; Jones et al., 2001); Matplotlib (Hunter, 2007), and Astropy (Astropy Collaboration et al., 2013).

# APPENDIX

## FAILURE RATE OF CONVERGENCE OF GALFIT

We summarize in Fig. 2.12 and 2.13 the impact of the GALFIT failures to converge on the final stellar mass and H$\alpha$ luminosities distributions, respectively. It is evident that there is no bin in either in stellar mass or H$\alpha$ luminosity that is preferentially affected by a large failure rate when compared to other bins. This means that excluding galaxies for which GALFIT failed to converge from our final samples, from which we derive median structural parameters, does not introduce any additional bias in both stellar masses or H$\alpha$ luminosities.

## FURTHER REMARKS ON THE IMPACT OF COSMOLOGICAL DIMMING

We show in Fig. 2.14 the impact of the artificial redshift on the derived total magnitude of each galaxy. We compare absolute magnitudes and not the direct result from GALFIT, the apparent

magnitudes, because it is the only way to compare magnitudes across different redshifts. We note that for comparison of the two quantities we correct the output absolute magnitude for the luminosity evolution that we impose for each redshift following the fit by Sobral et al. (2013a). We show that the impact is close to zero ($< 1\%$), which makes it the more stable parameter against cosmological dimming. As for the axis ratio of galaxies (Fig. 2.15) we recover, on average, the observed value at $z \approx 0$, within an error of $\lesssim 5\%$. We observe a slight trend of overestimation of the axis ratio at smaller $(b/a)_{z\approx0}$ and underestimation of the axis ratio at higher $(b/a)_{z\approx0}$.

We investigate further the impact of cosmological dimming by comparing our fractional errors on the effective radius and Sérsic index to the input galaxy magnitude. In Fig. 2.16 we show that the brightest local galaxies are the ones most likely to have their sizes underestimated. The largest galaxies are the ones for which our sizes are not being recovered accurately as shown in Fig. 2.4 and they are also more likely to be the brightest galaxies in our sample which helps to explain partly our results. The size overestimation that we observe on the faint end is possibly explained due to the likelihood of local galaxies having a bulge+disk structure which can prevent a single Sérsic profile to estimate the total extent of the galaxy. As we move the galaxy to higher redshifts the substructures tend to no-longer be resolved by the instrument PSF and GALFIT can more successfully measure sizes for the entire galaxy, hence estimating a larger size than the one measured at low redshift for the same galaxy. On the other hand, if the bulge-to-total light ratio is large, it may imply that we completely loose the disk component of the galaxy and end up underestimating the size of the galaxy. This latter effect is expected to happen on the brighter galaxies since those are the ones we expected to have more likely experienced at least one major merger which induces the formation of a prominent central bulge.

Since both effective parameters are linked through the same equation, we expect that a failure to reproduce the original effective radius leads in turn to a large error on the Sérsic index of the corresponding profile. And since the Sérsic index is the most unstable parameter of the profile we are likely witnessing in Fig. 2.17 a simple consequence of the results shown before for the effective radius.

We have further separated the sample in two axis ratio bins (below and above $b/a = 0.5$) and re-did Fig. 2.17 and 2.17. The results we find in these case are qualitatively the same and so we conclude that the axis ratio as no major impact on our ability to recover sizes and Sérsic indexes.

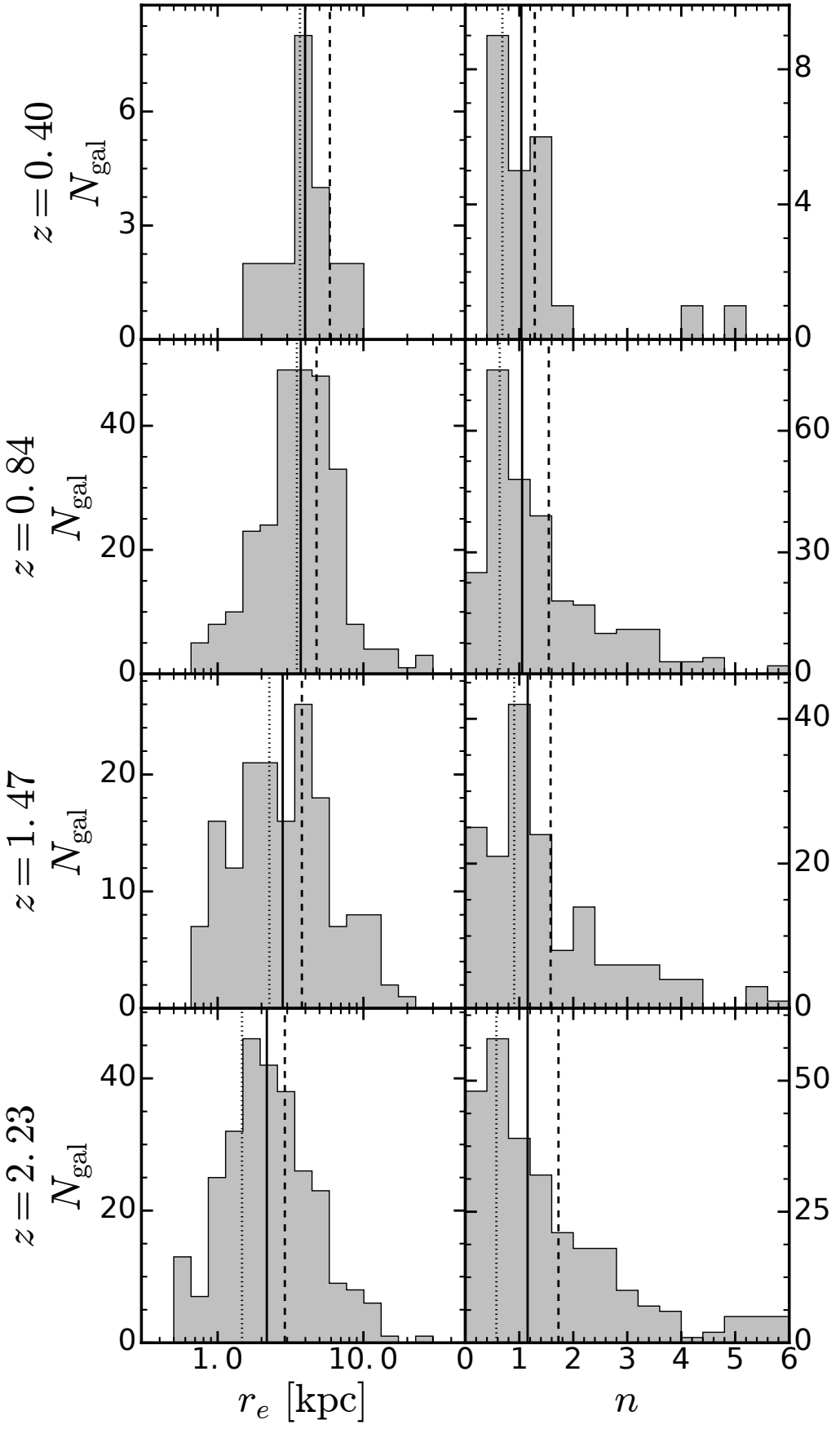


**Figure 2.7** Distributions of sizes ($r_e$) and Sérsic indices ($n$) of the galaxies observed at high redshift from HiZELS. The vertical solid, dashed and dotted lines indicate the median, mean, and modal values, respectively. The distributions are based on the observed values without any correction.

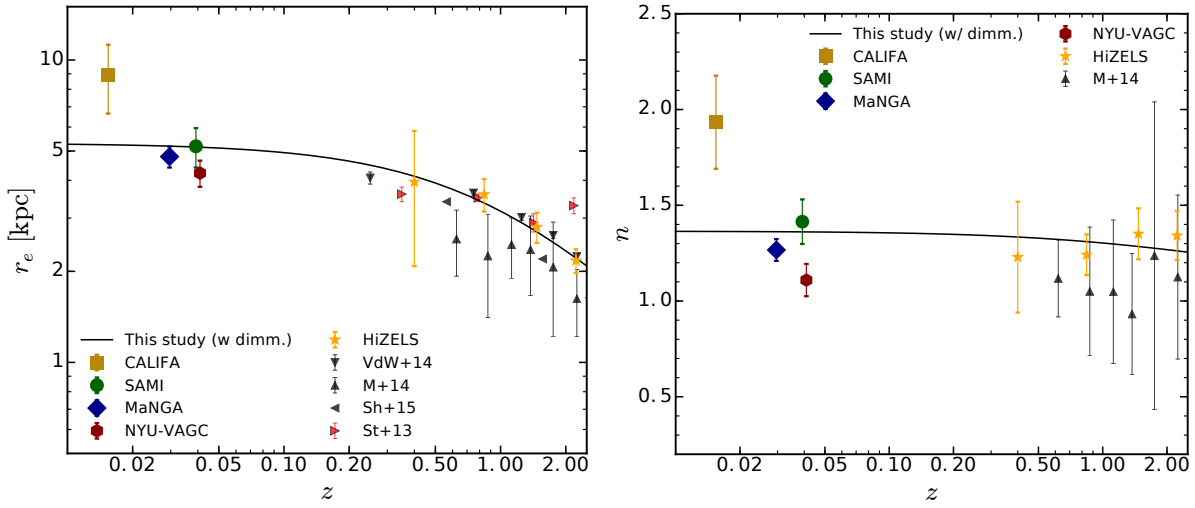


**Figure 2.8** Structural evolution of SFGs as parametrized by Sérsic profiles. Left: the evolution of galaxies' median (observed) effective radius as a function of the median redshift. Right: same as left but for the galaxies' median Sérsic index. The coloured points show the values (after dimming correction for HiZELS) derived from this study. The triangles show reported values from Stott et al. (2013b); van der Wel et al. (2014); Morishita et al. (2014); Shibuya et al. (2015). The points from Stott et al. (2013b) have been horizontally offset for viewing purposes. The solid line shows the fit to Eq. 2.3 after dimming correction.

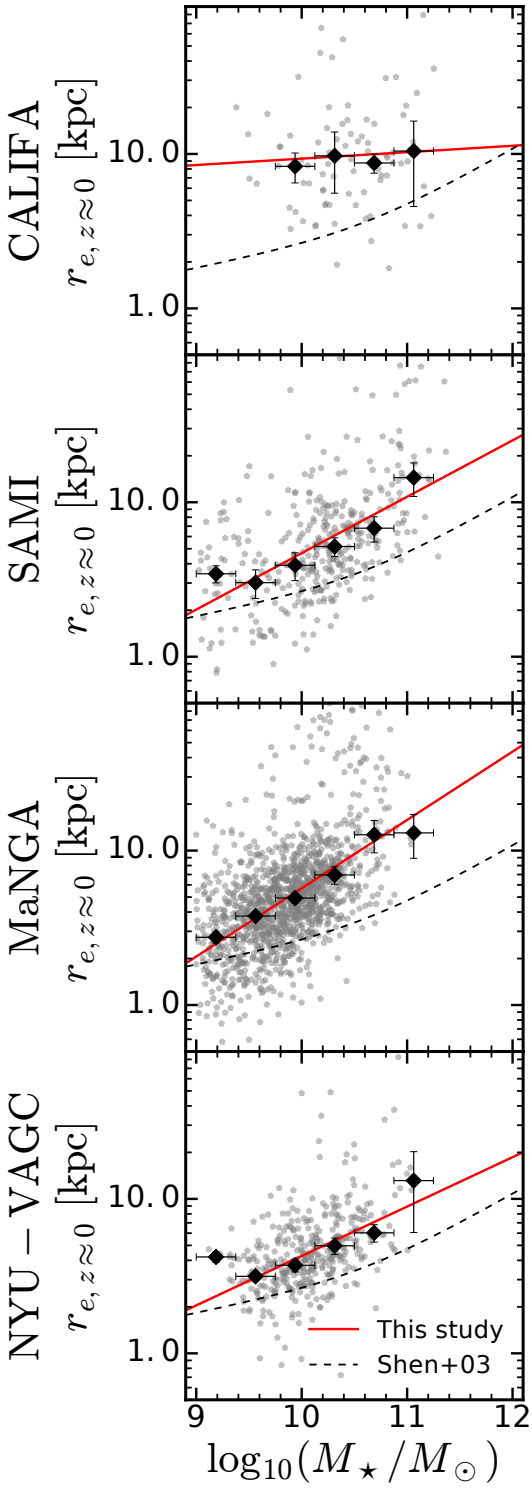


**Figure 2.9** The stellar mass-size relation for the local Universe samples described in Sect. 2.2. Each grey pentagon represents an individual galaxy, the large black diamonds are the median values in a stellar mass bin of width indicated by the horizontal error bar. The vertical error bar denotes the error on the median. The red solid line shows the best fit of Eq. 2.4 to the data (see also Table 2.5). We include the fits from Shen et al. (2003) as a solid dashed line. We note that the reason for the differences between our fits and those by Shen et al. (2003) is mainly due to the use of different size estimator. We use the major axis effective radius and they use the circularized effective radius. When using the latter in our data we find a better agreement. See Sect. 3.6 for more details.

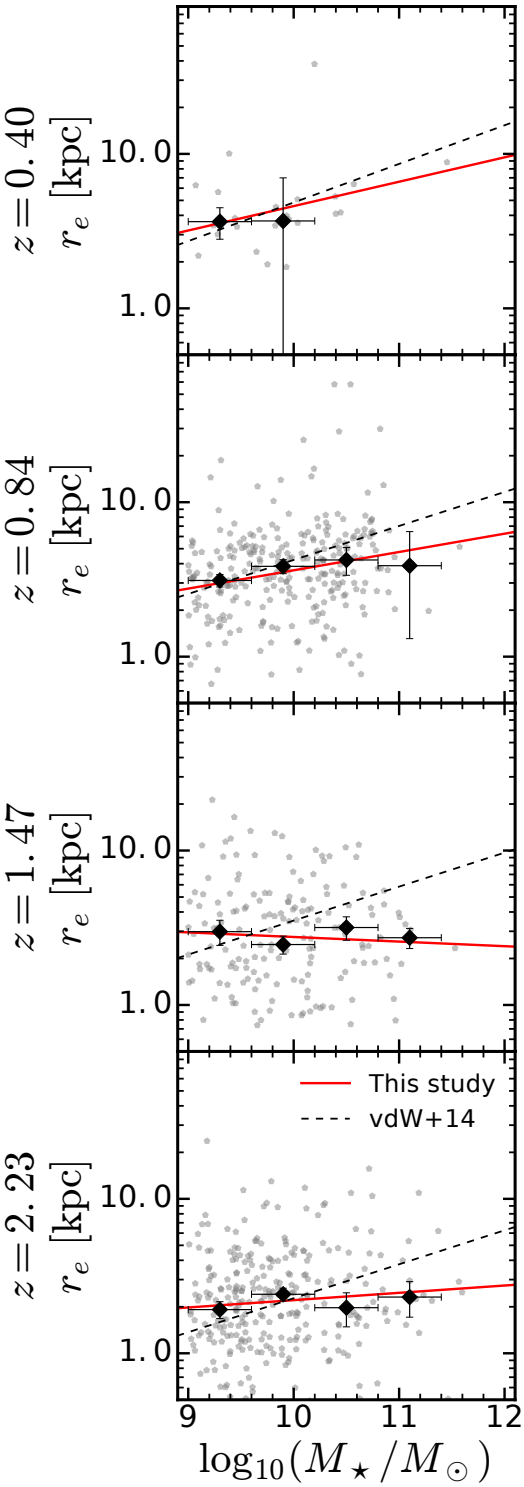


**Figure 2.10** The stellar mass-size relation for 4 redshifts probed by HiZELS. Each grey pentagon represents an individual galaxy, the large black diamonds are the median values in a stellar mass bin of width indicated by the horizontal error bar. The vertical error bar denotes the error on the median. The red solid line shows the best fit of Eq. 2.4 to the data (see also Table 2.5). We include the fits from van der Wel et al. (2014) as a solid dashed line (from top to bottom, the redshift bins from that chapter are: $0.0 < z < 0.5$, $0.5 < z < 1.0$, $1.0 < z < 1.5$, and $2 < z < 2.5$).

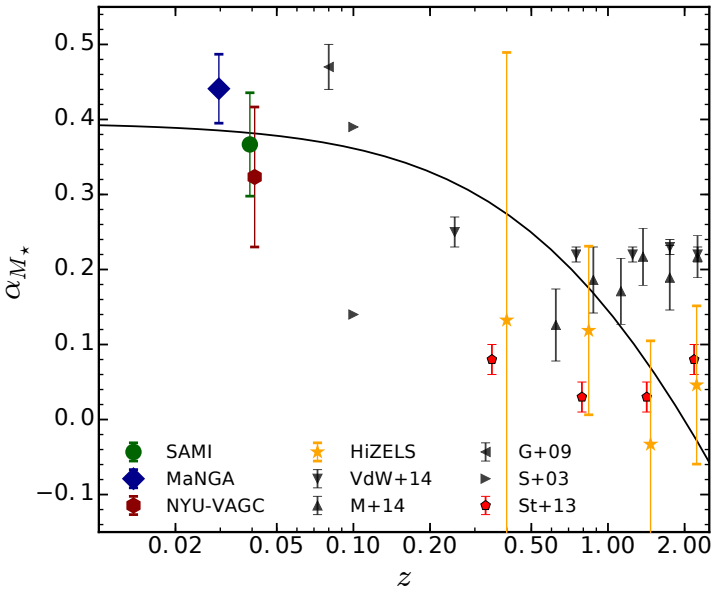


**Figure 2.11** The value of the slope of the stellar mass-size relation as a function of the median redshift of each sample. Larger full coloured symbols are for the samples studied in this chapter. The semi-transparent triangles are from other reports from the literature: Shen et al. (2003); Guo et al. (2009); van der Wel et al. (2014); Morishita et al. (2014). Shen et al. (2003) symbols correspond to the low (0.14 at $< 10^{10.6} M_{\odot}$) and high (0.39 at $> 10^{10.6} M_{\odot}$) stellar mass end. Values from Stott et al. (2013b) are shown as red pentagons and a horizontally shift was applied for viewing purposes. The solid line shows the best fit through our data points of $\alpha_{M_\star} = A \log_{10}(1+z) + B$, with $A = 0.8 \pm 0.2$ and $B = 0.40 \pm 0.05$.

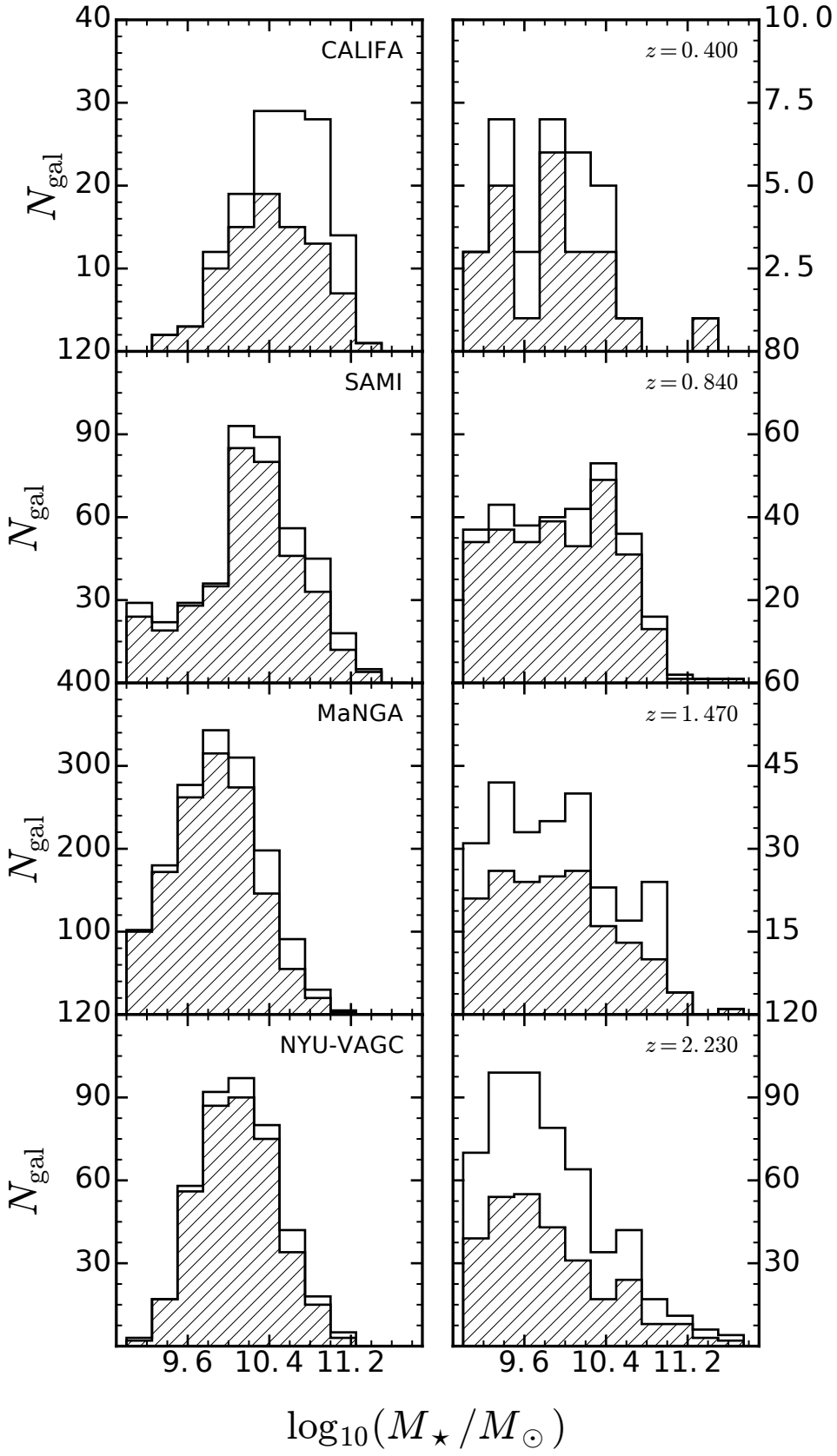


**Figure 2.12** The distribution of galaxies for which GALFIT converged (as diagonally hatched histogram) compared to the total sample (solid black line) that was analysed as a function of their stellar mass.

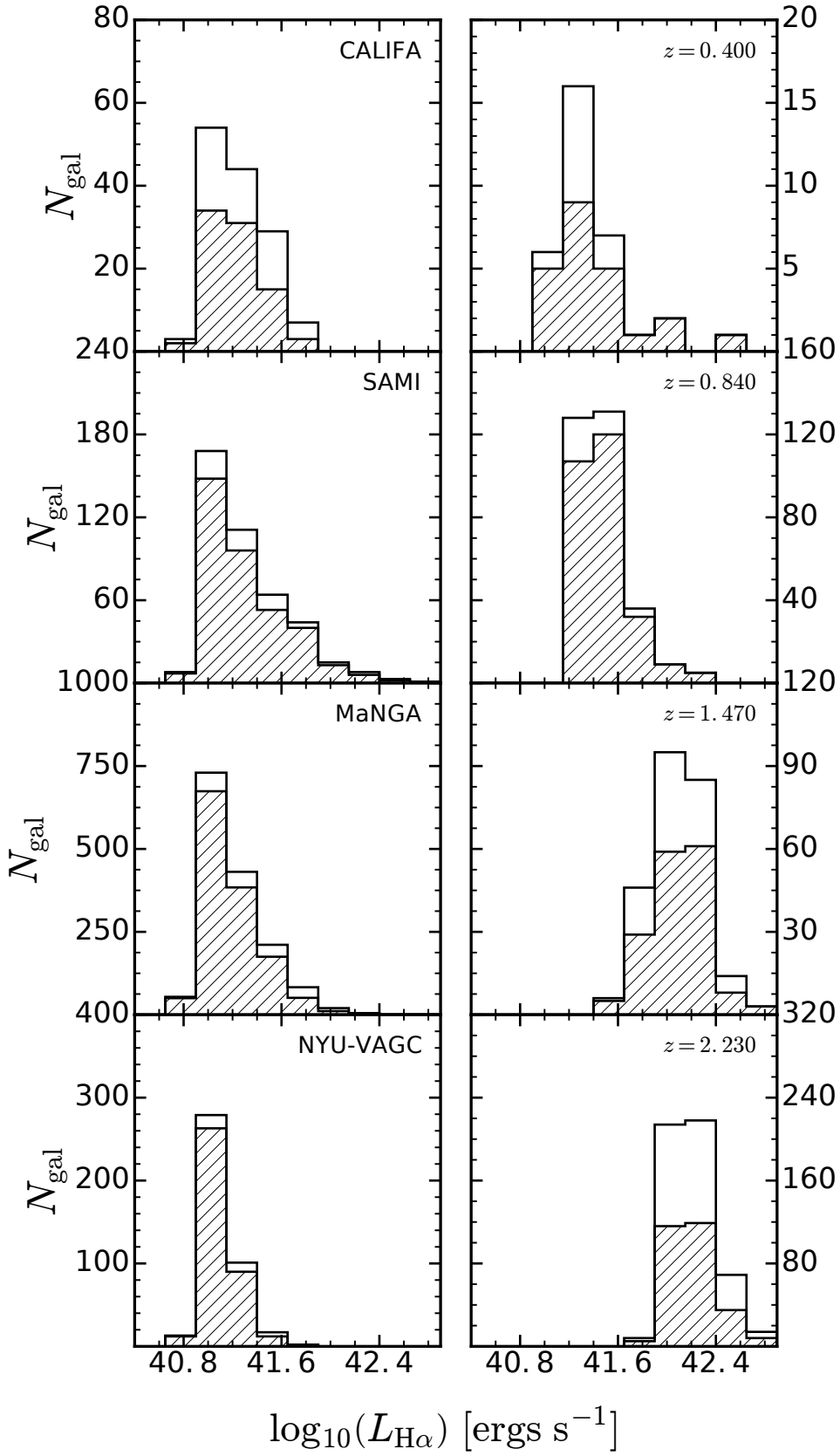


**Figure 2.13** The distribution of galaxies for which GALFIT converged (as diagonally hatched histogram) compared to the total sample (solid black line) that was analysed as a function of their H$\alpha$ luminosity.

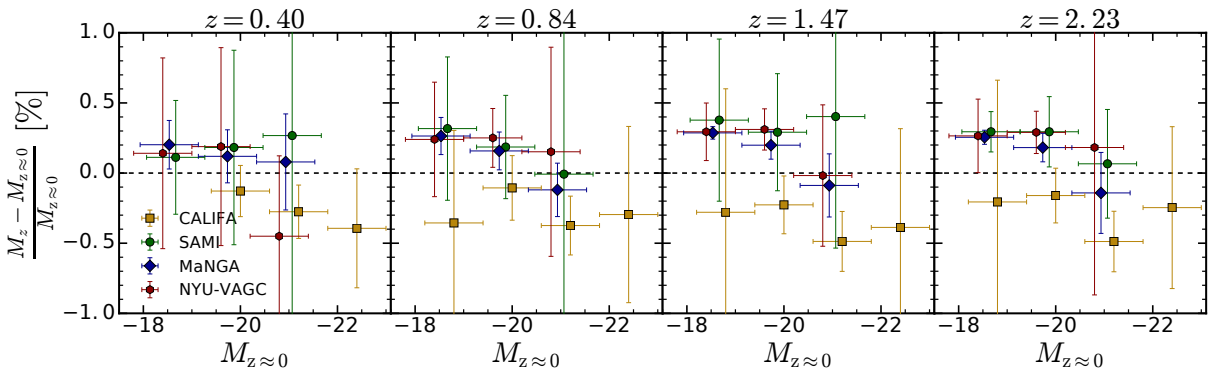


**Figure 2.14** Variable difference, $(M_z - M_{z\approx0})/M_{z\approx0}$, for each of the local subsamples and each redshift (one per column). Each symbol represent the median values in bins (with a minimum of 10 galaxies) of width of the horizontal error bar. The vertical error bar shows the error on the median value $\sigma/\sqrt{N_{\rm gal,bin}}$. The black dashed line pinpoints the accurate recovery. The recovered absolute magnitude is corrected for the luminosity evolution term of equation $\log_{10}[L(z)] = 0.45z + 41.87$. The impact on this parameter is tiny ($\lesssim 1\%$) at all redshifts. Small horizontal offsets were applied to improve the readability of the plot.

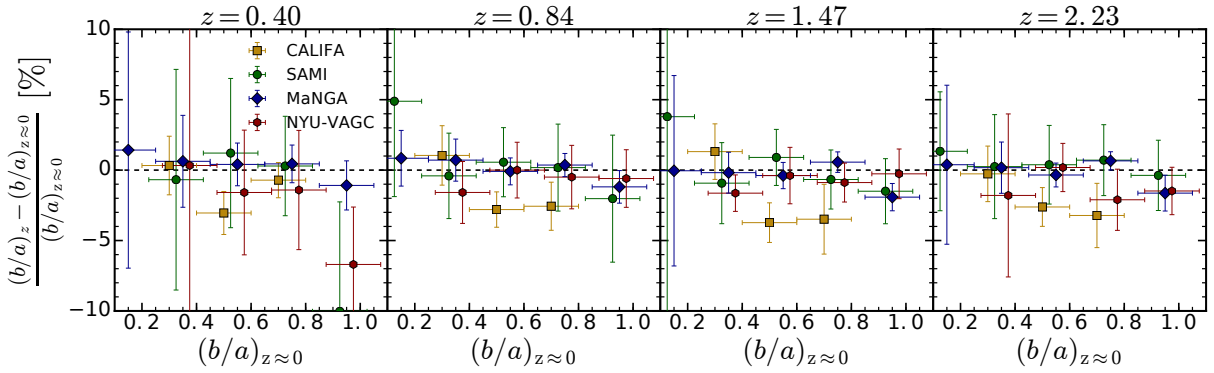


**Figure 2.15** Variable difference, $((b/a)_z - (b/a)_{z\approx0})/(b/a)_{z\approx0}$, for each of the local subsamples and each redshift (one per column). Each symbol represent the median values in bins (with a minimum of 10 galaxies) of width of the horizontal error bar. The vertical error bar shows the error on the median value $\sigma/\sqrt{N_{\rm gal,bin}}$. The black dashed line pinpoints the accurate recovery. The impact on this parameter is small ($\lesssim 5\%$) at all redshifts, with a slight tendency to overestimate at smaller $(b/a)$ and underestimate at higher $(b/a)$. Small horizontal offsets were applied to improve the readability of the plot.

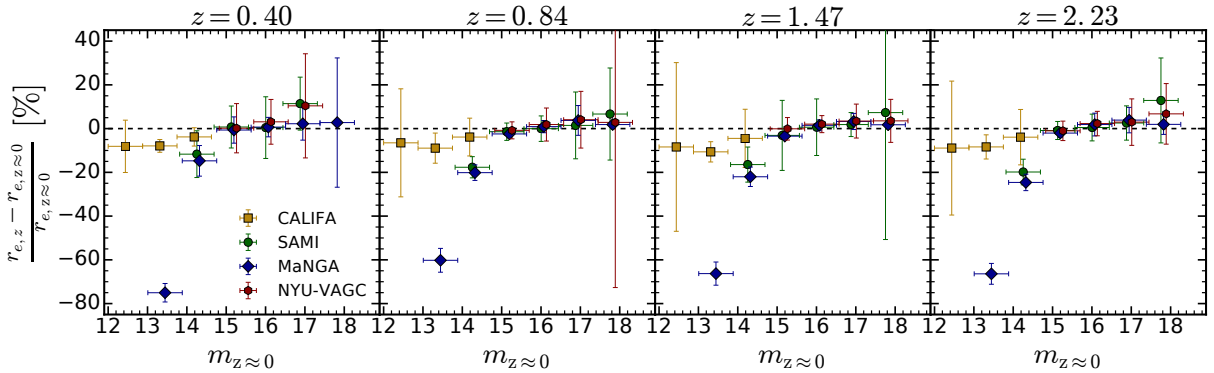


**Figure 2.16** The fraction difference between the recovered and input effective radius, $(r_{e,z} - r_{e,z\approx0})/r_{e,z\approx0}$, for each of the local subsamples and each redshift (one per column) as a function of input magnitude. Each symbol represent the median values in bins (with a minimum of 10 galaxies) of width of the horizontal error bar. The vertical error bar shows the error on the median value $\sigma/\sqrt{N_{\rm gal,bin}}$. The black dashed line pinpoints the accurate recovery. Small horizontal offsets were applied to improve the readability of the plot.

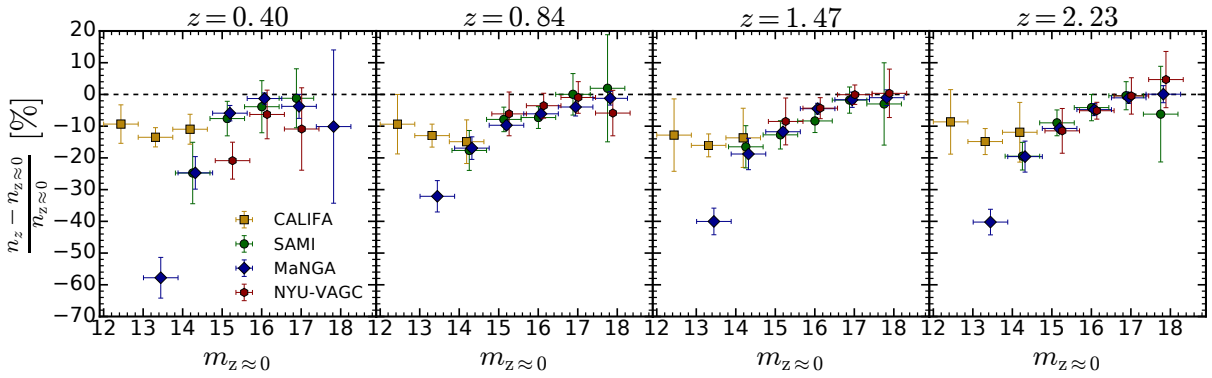


**Figure 2.17** The fraction difference between the recovered and input Sérsic index, $(n_z - n_{z\approx0})/n_{z\approx0}$, for each of the local subsamples and each redshift (one per column) as a function of input magnitude. Each symbol represent the median values in bins (with a minimum of 10 galaxies) of width of the horizontal error bar. The vertical error bar shows the error on the median value $\sigma/\sqrt{N_{\rm gal,bin}}$. The black dashed line pinpoints the accurate recovery. Small horizontal offsets were applied to improve the readability of the plot.

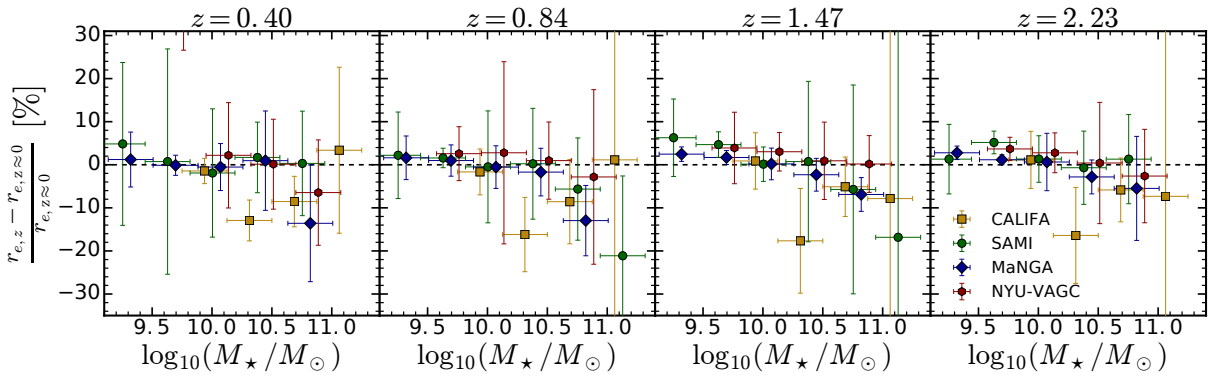


**Figure 2.18** The fraction difference between the recovered and input effective radius, $(r_{e,z} - r_{e,z\approx0})/r_{e,z\approx0}$, for each of the local subsamples and each redshift (one per column) as a function of input stellar mass. Each symbol represent the median values in bins (with a minimum of 10 galaxies) of width of the horizontal error bar. The vertical error bar shows the error on the median value. The black dashed line pinpoints a fractional difference of 0, i.e., when the recovered effective radius is the same as input. We do not observe a strong trend of fractional error deviation as a function of stellar mass. Nonetheless, the most massive galaxies are expected to have their sizes underestimated at a level of $\lesssim 20\%$. Small horizontal offsets were applied to improve the readability of the plot. On the $z = 0.40$ panel there is one point from the SAMI survey at $(r_{e,z} - r_{e,z\approx0})/r_{e,z\approx0} \sim 40\%$ for $\log_{10}(M_\star/M_\odot) \sim 9.75$ that was excluded for visualization purposes.

This page intentionally contains only this sentence.

# CHAPTER 3

## ON THE UV COMPACTNESS AND MORPHOLOGIES OF TYPICAL LYMAN-$\alpha$ EMITTERS FROM $Z \sim 2$ TO $Z \sim 6$

*We investigate the rest-frame UV morphologies of a large sample of Lyman-$\alpha$ emitters (LAEs) from $z \sim 2$ to $z \sim 6$, selected in a uniform way with 16 different narrow- and medium-bands over the full COSMOS field. We use 3045 LAEs with HST coverage in a stacking analysis and find that they have $M_{\rm UV} \sim -20$, below $M^*_{\rm UV}$ at these redshifts. We also focus our analysis on a subsample of 780 individual galaxies with $i_{\rm AB} < 25$ for which GALFIT converges for 429 of them. The individual median size ($r_e \sim 1$ kpc), ellipticities (slightly elongated with $(b/a) \sim 0.45$), Sérsic index (disk-like with $n \lesssim 2$) and light concentration (comparable to that of disk or irregular galaxies, with $C \sim 2.7$) of LAEs show mild evolution from $z \sim 2$ to $z \sim 6$. LAEs with the highest rest-frame equivalent widths (EW) are the smallest/most compact ($r_e \sim 0.8$ kpc, compared to $r_e \sim 1.5$ kpc for the lower EW LAEs). When stacking our samples in bins of fixed Ly$\alpha$ luminosity and Ly$\alpha$ EW we find evidence for redshift evolution in n and C, but not in galaxy sizes. The evolution seems to be stronger for LAEs with $25 < EW < 100$ Å. When compared to other SFGs, LAEs are found to be smaller at all redshifts. The difference between the two populations changes with redshift, from a factor of $\sim 1$ at $z \gtrsim 5$ to SFGs being a factor of $\sim 2-4$ larger than LAEs for $z \lesssim 2$. This means that at the highest redshifts, where typical sizes approach those of LAEs, the fraction of galaxies showing Ly$\alpha$ in emission (and with a high Ly$\alpha$ escape fraction) should be much higher, consistent with observations.*

adapted from **Paulino-Afonso**, A., Sobral, D., Ribeiro, B. et al. 2018, MNRAS, 476, 5479

## 3.1 INTRODUCTION

In the $\Lambda$-Cold Dark Matter framework, galaxies form through the coalescence of small clumps of material (see e.g. Somerville & Davé, 2015, and references therein). This means that the first objects which can be called galaxies are to be young, small and with low stellar mass content. The search for these building blocks of current day galaxies has been pursued intensively in the past decades (see e.g. Bromm & Yoshida, 2011; Stark, 2016).

Because of its intrinsic brightness, this search usually explores the presence of the Lyman-$\alpha$ (Ly$\alpha$) emission line (e.g. Partridge & Peebles, 1967; Schaerer, 2003). This line can be observed in the optical and near-infrared when emitted from $2 < z \lesssim 8$ sources and it is proven to be a successful probe to identify and confirm high-redshift galaxies. From narrow-band surveys (e.g. Rhoads et al., 2000; Ouchi et al., 2008, 2010; Matthee et al., 2016, 2017a; Sobral et al., 2017) to spectroscopic detection and confirmation of high-redshift candidates (e.g. Martin & Sawicki, 2004; Cassata et al., 2011; Ono et al., 2012; Bacon et al., 2015; Le Fèvre et al., 2015; Wisotzki et al., 2016), we have now access to large samples of young galaxies in the early Universe.

The physical properties of Ly$\alpha$ emitting galaxies (LAEs) have been intensively studied (e.g. Erb et al., 2006; Gawiser et al., 2006, 2007; Pentericci et al., 2007; Ouchi et al., 2008; Lai et al., 2008; Reddy et al., 2008; Finkelstein et al., 2009; Kornei et al., 2010; Guaita et al., 2011; Nilsson et al., 2011; Acquaviva et al., 2012; Kusakabe et al., 2015; Oteo et al., 2015; Hathi et al., 2016; Matthee et al., 2016). Some works find them to be typically young, with low stellar masses and scarce dust presence (e.g. Erb et al., 2006; Gawiser et al., 2006, 2007; Pentericci et al., 2007; Oteo et al., 2015), while others indicate a more diverse population (e.g. Shapley et al., 2003; Lai et al., 2008; Reddy et al., 2008; Finkelstein et al., 2009; Kornei et al., 2010; Nilsson et al., 2011; Acquaviva et al., 2012; Kusakabe et al., 2015; Hathi et al., 2016). The different properties of this population may be due to their particular selection method, as LAEs are similar to other line-emission selected galaxies at $z \sim 2$ and different from colour-selected galaxies at the same redshifts (e.g. Oteo et al., 2015; Hagen et al., 2016). Evolution can also play a role in the different observed properties of LAEs with more evolved galaxies having Ly$\alpha$ emission driven by different mechanisms than those that dominate LAEs at higher redshifts. For e.g., Sobral et al. (2018a) show a strong increase in the fraction of Active Galactic Nuclei (AGN) in luminous LAEs from $z \sim 4-5$ to $z \sim 2-3$.

A possible explanation to the diverse nature of LAEs is linked to the complicated nature of the radiative transfer process itself. To escape the region it originated from, Ly$\alpha$ photons are frequently scattered (with random walks up to several kpc) before they escape towards our line of sight (e.g. Zheng et al., 2011; Dijkstra & Kramer, 2012; Lake et al., 2015; Gronke et al., 2015, 2016). This recurrent scattering increases the chance of the photon to be destroyed through dust absorption (e.g. Neufeld, 1991; Laursen et al., 2013). This picture also means that the particular orientation of the emission path relative to the geometrical distribution of gas and dust in the emitting region is important to consider whether or not we are able to observe the line in emission. Some simulations of isolated disk galaxies have shown that the likelihood of observation of Ly$\alpha$ is correlated with the disk inclination relative to our line of sight (Verhamme et al., 2012; Behrens & Braun, 2014). From an observational perspective, the Ly$\alpha$ escape fraction (ratio of observed to intrinsic flux in emission) is loosely correlated with the galaxies' star formation rate (SFR) and dust attenuation (e.g. Hayes et al., 2010, 2011; Atek et al., 2014; Matthee et al., 2016; Trainor et al., 2016; Oyarzún et al., 2017). The column density of HI seems to be another

physical quantity that determines the rate of escape of Ly$\alpha$ photons (e.g. Shibuya et al., 2014a,b; Henry et al., 2015). It also correlates with equivalent width (EW, Sobral et al., 2017; Verhamme et al., 2017) and outflow velocity (e.g. Hashimoto et al., 2015).

The complex process of Ly$\alpha$ escape naturally means that obtaining a complete census of the galaxy population at a given epoch is challenging. To understand the mechanisms that allow Ly$\alpha$ photons to escape it may be important to correlate the morphology of star-forming regions traced by UV continuum emission of young stars with the observed from Ly$\alpha$ photons. This will allow one to constrain the geometry requirements for Ly$\alpha$ to escape from galaxies and further our knowledge of population bias when using selections solely based on this emission line. To gain insight on the mechanisms of Ly$\alpha$ escape it is thus crucial that we characterize the morphology of these sources.

Several samples of LAEs have been studied in terms of their rest-frame UV morphologies at $z > 2$ (e.g. Venemans et al., 2005; Pirzkal et al., 2007; Overzier et al., 2008; Taniguchi et al., 2009; Bond et al., 2009, 2011, 2012; Gronwall et al., 2011; Jiang et al., 2013; Kobayashi et al., 2016). In the local Universe, where rest-frame UV observations are scarce, there is one study based on the Ly$\alpha$ Reference Sample (LARS, Östlin et al., 2014, though the sample is H$\alpha$ selected), that characterizes the morphology of these sources (Guaita et al., 2015). Observations show that LAEs are typically small, often compact objects (half-light radius around 1 kpc), which undergo no evolution in the first 1 to 3 billion years of the Universe ($z \sim 2-6$, e.g Venemans et al., 2005; Malhotra et al., 2012). This scenario is in stark contrast with the stronger evolution in galaxy sizes observed in other populations observed at similar epochs such as Lyman-break galaxies (LBGs) and other star-forming galaxies (e.g. Ferguson et al., 2004; Bouwens et al., 2004; van der Wel et al., 2014; Morishita et al., 2014; Shibuya et al., 2016; Paulino-Afonso et al., 2017). This can potentially be explained due to the low stellar mass nature of LAEs when compared to other galaxies. However, most studies on SFGs explore the size evolution in stellar mass bins and find stronger size evolution nonetheless (e.g. van der Wel et al., 2014).

One interesting property of LAEs is that the Ly$\alpha$ emission region is often found to be more extended (in a diffuse halo) than the stellar UV continuum emission (e.g. Rauch et al., 2008; Matsuda et al., 2012; Momose et al., 2014; Matthee et al., 2016; Wisotzki et al., 2016; Sobral et al., 2017; Xue et al., 2017). The process responsible for such observations is thought to be the scattering of photons by neutral HI gas around galaxies at high redshift (e.g. Zheng et al., 2011), but could also be due to cooling, satellites and fluorescence (e.g. Mas-Ribas et al., 2017). Additionally, there are evidences for a correlation between Ly$\alpha$ line luminosity and galaxy UV continuum size (e.g. Hagen et al., 2014).

It is still unclear whether LAEs are a special subset of galaxies, if they rather just trace an early phase of galaxy formation or if they are a consequence of different orientation angles from which Ly$\alpha$ photons peer through. To make progress, we have to look at their morphological properties

**Table 3.1** The full sample of Ly$\alpha$ emitters selected with the 16 narrow- and medium-bands used in this work. The $< z >$ column shows the average redshift for the LAEs that fall in the filter. The $N_{\rm LAE}$ column shows the total number of LAEs detected in the NB/IB images. The $N_{\rm HST}$ column shows those who are covered by the HST/ACS F814W imaging survey. The $N_{\rm HST,i_{AB}<25}$ column shows the number of LAEs with available HST data brighter than $i_{\rm AB} < 25$. The $N_{\rm GALFIT,i_{AB}<25}$ column shows the number of bright LAEs for which GALFIT has converged. The $M_{\rm F814W}$ [stack] column shows the absolute magnitude in the $i$-band of the median stacks (see Sect. 3.3.4) which should closely trace $M_{\rm UV}$. The $\log_{10}\left(L_{\rm Ly\alpha}\right)$ shows the median Ly$\alpha$ luminosity of each sample (values derived by Matthee et al., 2016; Santos et al., 2016; Sobral et al., 2017, see also Sobral et al. (2018b)).

| Band | Instrument | $< z >$ | $N_{\rm LAE}$ | $N_{\rm HST}$ | $N_{\rm HST,i_{AB}<25}$ | $N_{\rm GALFIT,i_{AB}<25}$ | $M_{\rm F814W}$ [stack] | $\log_{10}\left(L_{\rm Ly\alpha}\right)$ |
|---|---|---|---|---|---|---|---|---|
| NB392 | INT/WFC | 2.23 | 159 | 109 | 50 | 26 | $-18.3\pm0.4$ | $42.6\pm0.3$ |
| NB501 | INT/WFC | 3.12 | 45 | 41 | 17 | 6 | $-19.7\pm0.2$ | $42.9\pm0.2$ |
| NB711 | Subaru/Suprime-CAM | 4.85 | 78 | 59 | 9 | 4 | $-20.0\pm0.1$ | $42.8\pm0.2$ |
| NB816 | Subaru/Suprime-CAM | 5.72 | 192 | 146 | 4 | 1 | $-19.4\pm0.1$ | $42.8\pm0.2$ |
| IA427 | Subaru/Suprime-CAM | 2.51 | 741 | 591 | 144 | 83 | $-19.2\pm0.2$ | $42.6\pm0.2$ |
| IA464 | Subaru/Suprime-CAM | 2.82 | 311 | 236 | 96 | 45 | $-19.8\pm0.1$ | $42.9\pm0.2$ |
| IA484 | Subaru/Suprime-CAM | 2.98 | 711 | 563 | 137 | 73 | $-19.5\pm0.1$ | $42.8\pm0.2$ |
| IA505 | Subaru/Suprime-CAM | 3.16 | 483 | 375 | 108 | 65 | $-19.8\pm0.1$ | $42.9\pm0.2$ |
| IA527 | Subaru/Suprime-CAM | 3.34 | 641 | 506 | 98 | 54 | $-19.7\pm0.1$ | $42.9\pm0.2$ |
| IA574 | Subaru/Suprime-CAM | 3.72 | 98 | 77 | 26 | 20 | $-20.2\pm0.1$ | $43.0\pm0.2$ |
| IA624 | Subaru/Suprime-CAM | 4.14 | 142 | 111 | 14 | 10 | $-19.9\pm0.1$ | $43.0\pm0.1$ |
| IA679 | Subaru/Suprime-CAM | 4.59 | 79 | 65 | 23 | 16 | $-20.5\pm0.1$ | $43.3\pm0.1$ |
| IA709 | Subaru/Suprime-CAM | 4.84 | 81 | 59 | 20 | 12 | $-20.7\pm0.1$ | $43.2\pm0.1$ |
| IA738 | Subaru/Suprime-CAM | 5.07 | 79 | 61 | 21 | 10 | $-20.5\pm0.1$ | $43.2\pm0.2$ |
| IA767 | Subaru/Suprime-CAM | 5.31 | 33 | 24 | 9 | 3 | $-20.7\pm0.1$ | $43.4\pm0.2$ |
| IA827 | Subaru/Suprime-CAM | 5.81 | 35 | 22 | 4 | 1 | $-20.0\pm0.2$ | $43.4\pm0.1$ |
| Total | | | 3908 | 3045 | 780 | 429 | | |

across cosmic time. In addition to that, it is necessary to compare to other galaxy populations (e.g. LBGs, HAEs, SFGs) for an understanding on how these populations are linked.

In this chapter, we analyse in a consistent way, from sample selection to analysis, a large sample of LAEs probing the early phases of galaxy assembly from the end of re-ionization ($z \sim 6$) to the peak of the cosmic star-formation history ($z \sim 2$). We use data from 16 narrow- and medium-band images in the COSMOS field (Sobral et al., 2018b) to quantify the evolution of galaxy structure (sizes, light profile shapes, elongations and concentrations). With this large data set we can investigate with unprecedented accuracy the evolution of LAEs sizes and connect that to the evolution (or lack thereof) in other morphological properties and contextualize our results within recent results from the literature on morphology of high redshift galaxies.

The chapter is organized as follows. In Sect. 3.2 we describe the data used for the detection and characterization of LAEs that are the object of study in this work. We present our methodology to study the structural parameters of high redshift galaxies in Section 3.3. The results obtained for the LAEs samples are reported in Sect. 3.4. We discuss the implications of our results in the context of early galaxy assembly in Sect. 3.6. Finally, in Sect. 3.7 we summarize our conclusions.

Magnitudes are given in the AB system (Oke & Gunn, 1983). All the results assume a $\Lambda$-CDM

cosmological model with $H_0$=70.0 km s$^{-1}$Mpc$^{-1}$, $\Omega_m$=0.3 and $\Omega_\Lambda$=0.7.

## 3.2 The sample of Ly$\alpha$ emitters at $z \sim 2-6$

The use of narrow-band images to target the Ly$\alpha$ line at specific redshift windows has been widely used in recent years (e.g. Rhoads et al., 2000; Ouchi et al., 2008; Matsuda et al., 2011; Konno et al., 2014, 2016; Trainor et al., 2016; Santos et al., 2016; Matthee et al., 2016; Sobral et al., 2017). In this chapter we use a dataset obtained with the Wide Field Camera at the Isaac Newton Telescope (WFC/INT) and with the Suprime-Cam at Subaru Telescope that cover the full COSMOS field (see Scoville et al., 2007).

We analyse a sample of ∼4000 Ly$\alpha$-selected galaxies spanning a wide redshift range of $z \sim 2-6$ (SC4K, Santos et al., 2016; Sobral et al., 2017, and see also Sobral et al. (2018b)). The sources were detected using a compilation of 16 narrow- and medium-band images taken with the Subaru and the Isaac Newton telescopes. Briefly, sources were classified as Ly$\alpha$ emitters if they satisfied all the following conditions: 1) significant detection in a narrow/medium band with rest-frame equivalent width cuts of 25/50Å, respectively; 2) presence of a Lyman break blue-ward of the respective narrow/medium band; 3) no strong red colour in the near-infrared, which is typical of a red star or lower redshift interlopers. For the full selection criteria we refer the reader to Sobral et al. (2018b).

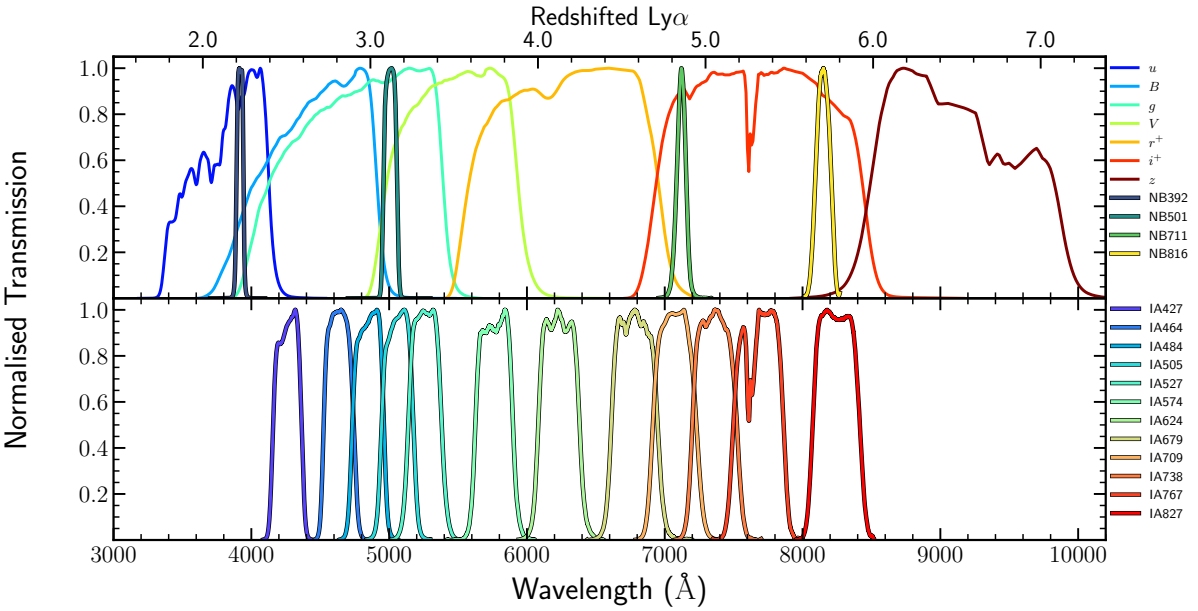


**Figure 3.1** Filter profiles for all NB (top) and IB (bottom) samples, along with BB filters(top) used for the selection of LAEs in this study.

To assess the potential contamination within our sample of LAE candidates we have compiled a set of spectroscopic redshifts from three catalogues - 56 from COSMOS (Ilbert et al., 2013),

83 from VUDS (private communication, Le Fèvre et al., 2015) and 4 from MOSDEF (Kriek et al., 2015) - of which 7 objects overlap. We have computed $\delta z = z_{\rm NB} - z_{\rm spec}$ and find that $\sim$15% (20 out of 133) of our candidates have $|\delta z| > 0.15$ (meaning $\sim$85% are spectroscopically confirmed LAEs, in agreement with Sobral et al., 2017). We find no significant dependence of the contamination rate on redshift, Ly$\alpha$ luminosity or Ly$\alpha$ equivalent width.

### 3.2.1 Sample properties

We summarize in Appendix of this Chapter the general sample properties plotting the individual band distributions in Ly$\alpha$ luminosity, $EW_0$(Ly$\alpha$), and $i_{\rm AB}$. We have a total of 3908 LAE candidates over a contiguous area of 2 deg$^2$ in the COSMOS field. These emitters have Ly$\alpha$ luminosities of $10^{42-44}$erg s$^{-1}$ (see Figure 3.15). We note that due to the relatively constant flux limit, the Ly$\alpha$ luminosity limit becomes higher with redshift and we can only detect galaxies above $10^{43}$erg s$^{-1}$ for $z \gtrsim 4$ in the medium bands and $10^{42.5}$erg s$^{-1}$ for the narrow bands. Despite narrow and intermediate bands having different equivalent width cuts (25 and 50Å, respectively), we show in Fig. 3.16 that both methods yield similar distributions and the majority of narrow-band selected sources are found at $EW_0$(Ly$\alpha$) $> 50$Å. To get reliable individual morphological measurements in the rest-frame UV we require a sufficiently bright magnitude in the F814W band and we show in Fig. 3.17 the $i_{\rm AB}$ distribution of each sample. We note that we miss a significant fraction of LAEs ($\sim$75% of those with HST images) by imposing a cut at $i_{\rm AB} < 25$, resulting in a UV-bright LAE sample of 780 candidates.

### 3.2.2 INT/WFC

We use data from the recent CAlibrating LYMan-$\alpha$ with H$\alpha$ survey (CALYMHA, Matthee et al., 2016; Sobral et al., 2017). This survey aims at detecting LAEs at $z = 2.2$ and $z = 3.1$ (but also allows the study of other emission lines, see e.g. Stroe et al., 2017a,b). The observations were made with specially designed filters (NB392, $\lambda_c = 3918$ & $\Delta\lambda = 52$ and NB501, $\lambda_c = 5008$ & $\Delta\lambda = 100$) mounted on the Wide Field Camera (WFC) in INT at the Observatorio Roque de los Muchachos on the island of La Palma. To perform the detection of LAEs we use the $U$- and $B$-band images from COSMOS (Capak et al., 2007a) for continuum estimation. Along with the WFC/INT data, we registered the images to the referential frame of HST/ACS survey in COSMOS (Scoville et al., 2007). The images were then matched in both spatial resolution ($0.33''$/pixel) and their Point Spread Function (PSF, which ranges from $1.8 - 2.0''$). Fluxes are computed in $3''$ circular apertures. Candidate Ly$\alpha$ emitters are selected to have rest-frame equivalent widths (EW$_0$) greater than 25Å (Sobral et al., 2017; Matthee et al., 2017a). We perform an additional colour selection aimed at excluding potential interlopers at the redshifts

we are probing (see Sobral et al., 2017; Matthee et al., 2017a, with respect to NB392 and NB501 colour selections, respectively). We further exclude one additional source based on recent spectroscopic observations (Sobral et al., in prep.). In the end, our WFC/INT sample has a total 159 LAEs at $z = 2.2$ and 45 LAEs at $z = 3.1$ in the COSMOS region (see Table 3.1).

### 3.2.3 SUBARU/SUPRIME-CAM

We explore deep data obtained with Subaru Suprime-Cam (Miyazaki et al., 2002) in the COSMOS field. We have reduced and analysed archival data of 2 narrow-band and 12 medium-band filters that are listed in Table 3.1. The reduction procedure is that described by Matthee et al. (2015) and Santos et al. (2016). The extraction of LAEs from the reduced data follows closely the method described in Sect. 3.2.2 using the appropriate broad band filter data corresponding to each filter for continuum estimation (optical and near-infrared images/catalogues described by Taniguchi et al. 2007, 2015 and Capak et al. 2007a). We note that the selection criteria for narrow-band detected LAEs impose a rest-frame equivalent widths $\mathrm{EW}_0 > 25$Å (Santos et al., 2016). For medium-band filters, the rest-frame equivalent width cut is at $\mathrm{EW}_0 > 50$Å. The number of detected LAEs for each processed narrow- and medium-band is shown in Table 3.1.

### 3.2.4 HST IMAGE DATA

High-resolution observations are required to study the rest-frame UV morphological properties of galaxies at high redshift. Thus, we limit our analysis to where HST/ACS F814W images are available (COSMOS survey, Scoville et al., 2007; Koekemoer et al., 2007). We use $10'' \times 10''$ cut-outs of the HST/ACS F814W band images centred on each LAE. These images have a typical PSF FWHM of $\sim 0.09''$, a pixel scale of $0.03''$/pixel and a limiting point-source depth AB(F814W) = 27.2 ($5\sigma$) and probe the near to far UV for the sources in our sample (on average $\sim$2000Å rest-frame).

Since the LAEs coordinates are measured from narrow/medium band images at a poorer resolution than HST, we are prone to astrometric errors on the centroid estimate. To mitigate this effect we associate to each LAE candidate the closest detected source in the image within $1''$ radius of the LAE position. If no such source is found, we assume the LAE has no continuum emission in the F814W images (we nevertheless use them in our stacking analysis, see Sect. 3.3.4).

## 3.3 METHODOLOGY

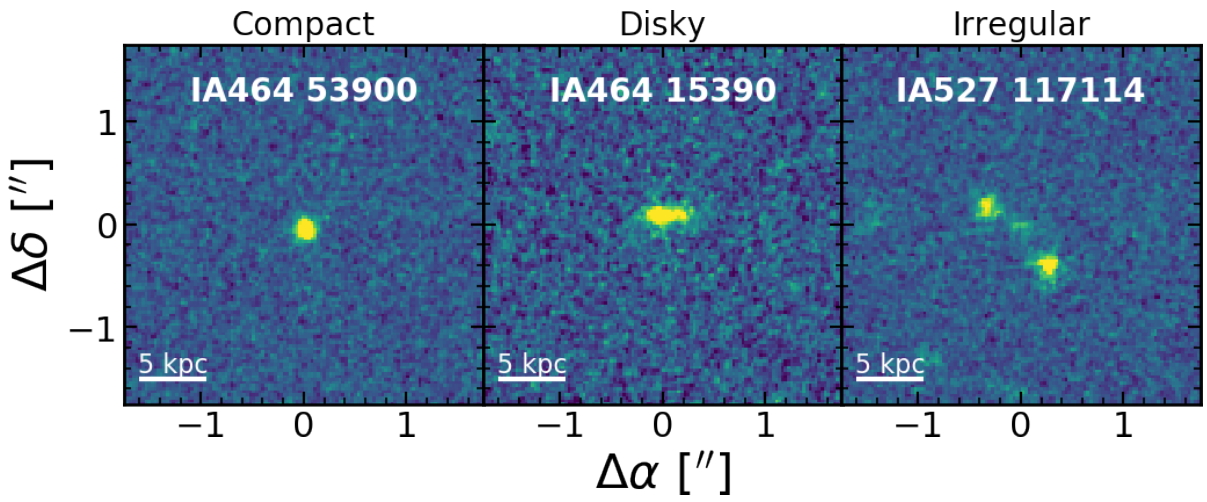


**Figure 3.2** Examples of LAEs at $z \sim 3$ for each of the morphological classes that we have defined for this study. The classes are displayed from left to right in terms of decreasing compactness: 1) bright round sources with compact profiles, 2) disk-like sources and 3) irregular/mergers/clumpy sources.

To quantify the morphological properties of any given source it is common to fit a parametric model to the observed light profile. In the particular case of galaxy modelling, the Sérsic (1968) profile is the most common model assumed (e.g. Davies et al., 1988; Caon et al., 1993; Andredakis et al., 1995; Moriondo et al., 1998; Simard, 1998; Khosroshahi et al., 2000; Graham, 2001; Möllenhoff & Heidt, 2001; Trujillo et al., 2001; Peng et al., 2002; Blanton et al., 2003; Trujillo et al., 2007; Wuyts et al., 2011; van der Wel et al., 2014; Shibuya et al., 2016) and which is also used to model LAEs (e.g. Pirzkal et al., 2007; Bond et al., 2009; Gronwall et al., 2011). The Sérsic model can be described as

$$I(r) = I_e \exp[-\kappa(r/r_e)^{1/n} + \kappa], \tag{3.1}$$

where the Sérsic index $n$ describes the shape of the light profile, $r_e$ is the effective radius of the profile, $I_e$ is the surface brightness at radius $r = r_e$ and $\kappa$ is a parameter coupled to $n$ such that half of the total flux is enclosed within $r_e$. This profile assumes two characteristic models for specific values of $n$ : exponential disk, if $n = 1$, and a de Vaucouleurs (1948) profile, if $n = 4$, best suited for elliptical galaxies and galactic bulges.

An alternative method, relying solely on the observed properties of each object, is to use a non-parametric approach to the morphological characterization (see e.g. Abraham et al., 1996; Bershady et al., 2000; Conselice et al., 2000a; Conselice, 2003; Lotz et al., 2004). These methods offer reliable estimates even in the case of extremely irregular objects, but fail to account for instrumental effects (such as PSF broadening) and are more susceptible to biases induced by low S/N conditions.

### 3.3.1 STRUCTURAL PARAMETER ESTIMATION

The retrieval of structural parameters based on Sérsic profiles is done using the publicly available GALFIT (Peng et al., 2002, 2010a), a stand-alone program aimed at two dimensional decomposition of light profiles through model fitting. In addition to the parameters described in Eq. 3.1[1], 2D models need 4 additional quantities: the model central position, $x_c$ and $y_c$, the axis ratio of the isophotes, $b/a$ and respective position angle, $\theta_{PA}$, i.e. the angle between the major axis of the ellipse and the vertical axis.

To run GALFIT effectively, it is necessary that we provide an initial set of parameters. To speed up convergence and minimize the occurrence of unrealistic solutions, it is important that these first guesses provide a good approximation of the light profile. To do so, we use the source extraction software SEXTRACTOR (Bertin & Arnouts, 1996), which can be tuned to produce the parameter set that will be used as input to GALFIT. To fit our galaxies, we use cut-outs centred on each target. The size of the cut-outs was chosen so that we achieve good speed performance and to allow GALFIT to simultaneously fit the residual sky emission.

To account for the instrumental PSF effects on the observed light profile, we provide PSF images associated with each individual galaxy. We use the HST/ACS PSF profiles that were created with TINYTIM (Krist, 1995) models and described by Rhodes et al. (2006, 2007). The PSF model accounts for pixel-to-pixel variation inside the CCD and the different telescope focus value for each COSMOS tile observation. We used the segmentation map produced by SEXTRACTOR at the time of the estimation of the initial parameters to create a mask image that flagged all pixels belonging to neighbouring galaxies, preventing them to influence the model of the object of interest. We mask all sources at a distance greater than $1.5''$ from the target RA, DEC ($\sim$10-13 kpc). We use a morphological dilation (kernel of $3 \times 3$ pixels) to smooth the individual masked regions and include in the same mask lower flux pixels in the outskirts that are below the SEXTRACTOR detection threshold.

Irregular, complex and/or sources detected at low S/N are excluded from the final sample as GALFIT failed to converge on meaningful structural parameters. Note, however, that we also visually classify all sources (see Sect. 3.3.3).

### 3.3.2 LIGHT CONCENTRATION

As not all our sources are well fit with a symmetric model ($\sim$45%), we opted to estimate the light concentration, $C$, of each source by using a non-parametric approach (Conselice et al., 2000a;

[1] In GALFIT, the $I_e$ parameter is computed internally. We use instead the model total magnitude as an input parameter.

Conselice, 2003). We used SExtractor 20% and 80% light radius (defined with the parameter PHOT_FLUXFRAC) and directly computed the value as

$$C = 5\log_{10}\left(\frac{r_{80}}{r_{20}}\right), \tag{3.2}$$

where $r_{80}$ and $r_{20}$ are the 80% and 20% light radius, respectively. This parameter measures the rate of decay of the light profile of galaxies in concentric elliptical apertures and allows us to understand if galaxies have lower or higher surface density of stellar emission in the near- and far-UV. Such measure can be linked to the type of star-formation occurring in LAEs which would, in turn, shed some light on the mechanisms linked to the formation of new stars that may boost the escape of Ly$\alpha$ photons.

### 3.3.3 Visual classification

We complemented the quantification of LAE morphology with the visual classification of the rest-frame UV shapes for all sources with $i_{\rm AB} < 25$ and HST coverage. We visually classify galaxies in a simple numerical scheme from 0 to 4 in terms of decreasing compactness: 0) corresponding to faint point-like sources, 1) slightly more extended/bright round/not extended sources, 2) disk-like sources and 3) irregular/mergers/clumpy sources (see Fig. 3.2). Each object was classified independently by three different team members and we combined the final classification by averaging over all classifications. For simplicity, we group classes 0 and 1 as compact sources, 2 as disky and 3 as irregular/clumpy/mergers.

### 3.3.4 Stacks of Ly$\alpha$ emitters

The major goal of stacking is to get measurements of the typical galaxy while not being biased by the ones that are brightest in F814W. We have stacked all detected LAEs with available HST/ACS F814W images (a total of 3045 galaxies from all bands) using the median flux per pixel centred at Ly$\alpha$ detection. We have also performed an image shift (typically $\lesssim 0.5''$on the detected sources) since the image coordinates are measured on ground based images and we observe some deviations when seeing them at HST resolution. The resulting stacks, in specific ranges of redshift, Ly$\alpha$ equivalent width and Ly$\alpha$ luminosity are shown in Fig. 3.3 (see also 3.14).

We show in Table 3.1 the absolute magnitude of these stacks as observed in HST/ACS F814W. These have typical values of $\sim$26 and correspond to absolute magnitudes, in F814W, ranging from $M_{\rm i,NB392} = -18.3$ (at low redshift) up to $M_{\rm i,IA827} = -20.0$ (at high redshift). These magnitudes

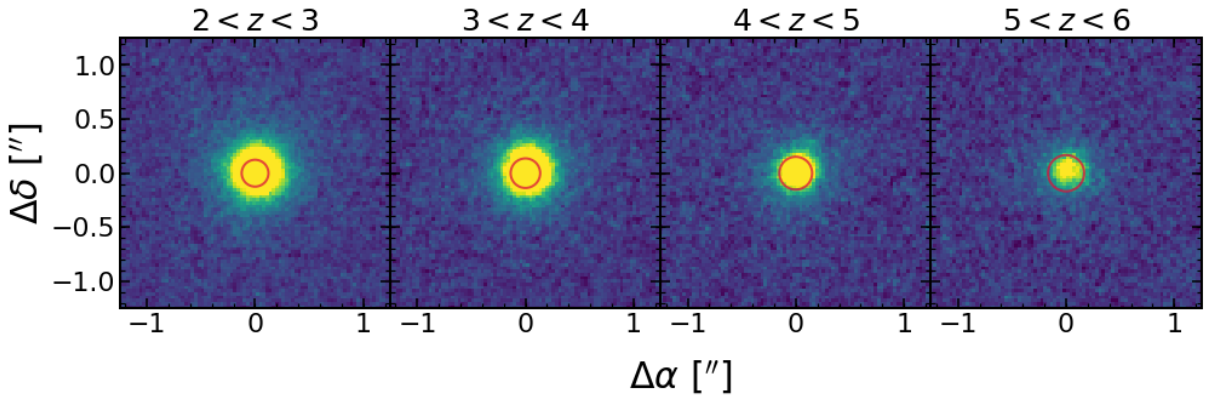


**Figure 3.3** Examples of LAE stacks for each of the bins that we use in this study in terms of redshift. In each panel, the intensity levels range from -3$\sigma_{\rm sky}$ to 15$\sigma_{\rm sky}$, where $\sigma_{\rm sky}$ is the sky rms. The red circle in each panel has a physical radius of 1 kpc.

are typically 1 to 2 magnitudes lower than $M^*_{\rm UV}$ at all redshifts (e.g. Reddy & Steidel, 2009; Bouwens et al., 2015; Finkelstein et al., 2015; Parsa et al., 2016; Alavi et al., 2016).

One of the quantities that is affected by the uncertainties on the astrometry of LAEs and a possible mismatch between the peak of Ly$\alpha$ emission and the UV emission (see e.g. Shibuya et al., 2014b) is the size of the produced light profiles. As we combine astrometric errors from a large number of sources, the profile tends to enlarge. To correct for this, we have used the subset for which we have UV detections in HST ($i_{\rm AB} < 25$) to compute the difference when using or not a centring algorithm prior to the image stacking. We find that when we do not use a centring algorithm, we produce stacks with an effective radius $\sim$1.1-1.5 times larger. We have computed individual corrections for each of the stacks and morphological quantities $r_e$, $n$, $C$ and applied to all values reported in this work (see e.g. Fig. 3.13).

## 3.4 Morphological properties of LAEs

In total, we have full individual morphological information on 429 LAEs across $2 \lesssim z \lesssim 6$ due to GALFIT convergence issues on low S/N galaxies and bright near-perfect point-like objects. However, for visual classification and light concentration parameters, we have results for the 780 LAEs with HST images and $i_{\rm AB} < 25$. To take full advantage of our large sample, the stacking analysis was done using all 3045 LAEs within the HST footprint. In the next subsections we will detail the rest-frame UV morphological properties of each sample and compare it to the strength of the Ly$\alpha$ emission. We stress that all our results presented in the next subsection are limited to LAEs with $i_{\rm AB} \leq 25$. For a summary of our findings, see Table 3.2. We have excluded X-ray detected AGNs from the sample (see Calhau et al., in prep. for details on AGN selection).

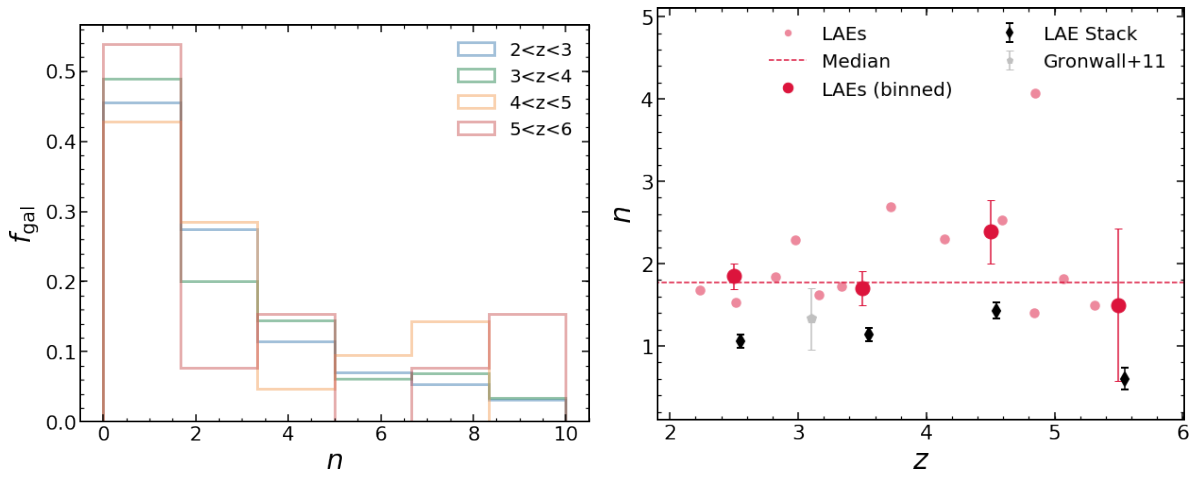


**Figure 3.4** Sérsic index median values of LAEs at $2 \lesssim z \lesssim 6$. On the left panel we show the Sérsic index distribution of LAEs for each redshift bin considered. On the right panel we plot the evolution of the median Sérsic index of the distribution (our results in semi-transparent red circles for intermediate/narrow bands and large opaque red circles after binning in redshift) and compare our values to those reported by Gronwall et al. (2011, grey pentagon). The red dashed line marks the median Sérsic index for individual LAEs at any redshift. The black diamonds show the Sérsic index of the stacked LAEs.

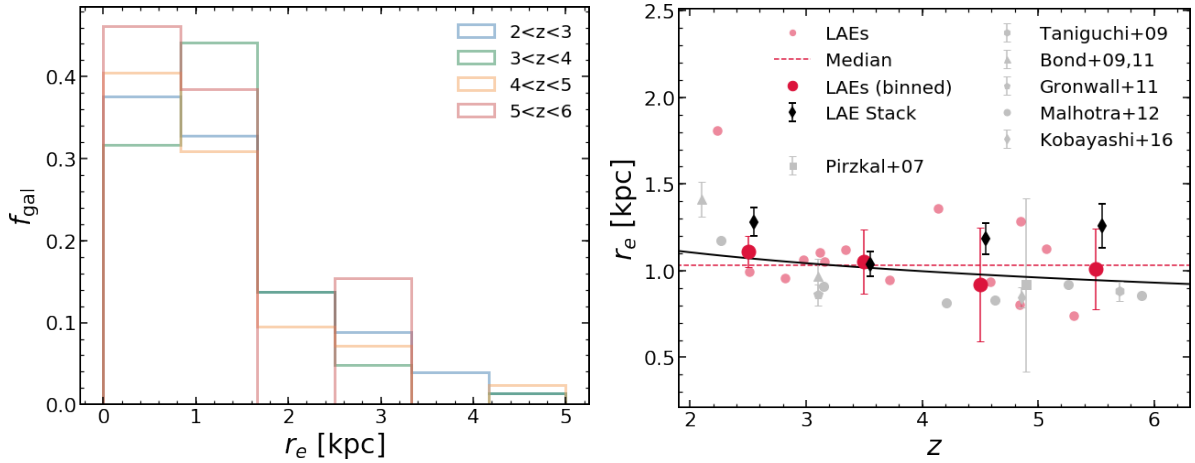


**Figure 3.5** Size properties of LAEs at $2 \lesssim z \lesssim 6$. On the left panel we show the size distribution of LAEs for each redshift bin considered. On the right panel we plot the evolution of the median size of the distribution (our results in semi-transparent red circles for intermediate/narrow bands and large opaque red circles after binning in redshift) and compare our values to those reported in the literature (in grey): square (Pirzkal et al., 2007), hexagon (Taniguchi et al., 2009), triangles (Bond et al., 2009, 2011), pentagon (Gronwall et al., 2011), circles (Malhotra et al., 2012) and diamond (Kobayashi et al., 2016). The black solid line shows the best fit of $r_e \propto (1+z)^{\alpha}$. The red dashed line marks the median effective radius for individual LAEs at any redshift. The black diamonds show the effective radius of the stacked LAEs.

### 3.4.1 Sérsic indices and sizes

In Fig. 3.4 we show the distribution of Sérsic indices and corresponding median of the population. It is readily noticeable that most LAEs have disk-like profiles ($n < 1.5$) with fractions ranging from $\sim 39\%$ at $4 < z < 5$ up to $\sim 54\%$ at $5 < z < 6$ (at $2 < z < 3$ and $3 < z < 4$ the fractions are of 45% and 49%, respectively). We note that there are LAEs with high values of the Sérsic index. Such cases can be related to galaxies with evident interactions, asymmetric morphologies

or compact spheroidal object which we can check with our visual morphological classification. We parametrize the redshift evolution as

$$X = \beta(1+z)^{\alpha} \tag{3.3}$$

with $\alpha, \beta$ being the parameters to be fit and $X$ the dependent variable, $n$ in this case. We find that $n \propto (1+z)^{-0.78\pm0.71}$ for the median of the LAE population, which is consistent (at the $\sim 1\sigma$ level) with a scenario of no evolution in the light profiles of LAEs. We find that for the lower redshift bins, our reported median values for the Sérsic index are in good agreement with those reported by Gronwall et al. (2011). We find systematically lower Sérsic indices for measurements of stacks of LAEs than for individual detections. These difference are related to the smoothing of the central region of the light profile caused by uncertainties on the astrometry (in random directions) and Ly$\alpha$-UV offset which dilute the light and make the profile shallower. Nonetheless, the reported trend is also consistent with little evolution with redshift.

We show in Fig. 3.5 the overall properties of the LAE population in 4 bins spanning the redshift range $2 \leq z \leq 6$. One of the first results is that LAEs have similar size distributions at all redshifts, with most galaxies having effective radii smaller than 1.5 kpc and with $\sim 20\%$ as extended sources with $r_e$ from 2-5 kpc. This similarity extends to the evolution on the median population sizes from $z \sim 6$ to $z \sim 2$, where we observe that LAEs are consistent with little to no evolution scenario in terms of their extent. These results are in agreement with previous results in the literature based on narrow-band selected LAEs (see e.g. Venemans et al., 2005; Pirzkal et al., 2007; Taniguchi et al., 2009; Bond et al., 2009, 2011; Gronwall et al., 2011; Malhotra et al., 2012; Kobayashi et al., 2016). For the evolution of effective radius we find that $r_e \propto (1+z)^{-0.21\pm0.22}$. This roughly translates to a growth by a factor of $\sim 1.2 \pm 0.2$ for LAEs from $z \sim 6$ to $z \sim 2$ (consistent with no evolution within $1\sigma$), which compares to a factor of $\sim 2.3 \pm 0.15$ for a more general star forming population (see e.g. van der Wel et al., 2014; Ribeiro et al., 2016).

We find systematically higher values of the effective radius of measurements of stacks of LAEs than for individual detections. We believe that this is in part due to the centring errors mentioned above but for which we have tried to correct. When deriving size evolution from the stacked profiles, we find that $r_e \propto (1+z)^{-0.01\pm0.25}$ is perfectly consistent with the lack of evolution that we find for the median population evolution.

We have tested the influence of our choice of binning in the derived parameters and we find that when shuffling the bins we get a variation in the slope $\alpha$, which is always smaller than the reported errors.

### 3.4.2 ELLIPTICITIES

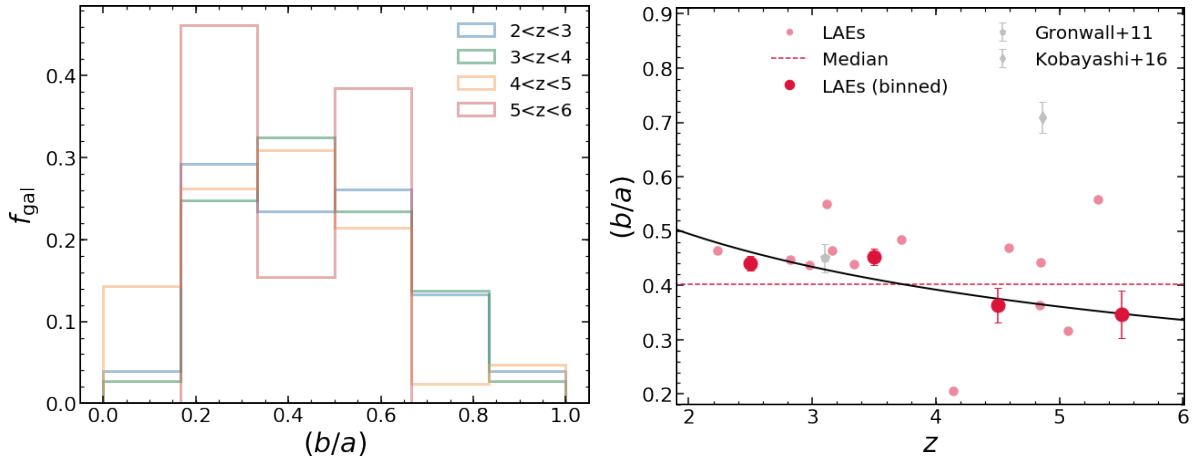


**Figure 3.6** Axis-ratio median values of LAEs at $2 \lesssim z \lesssim 6$. We plot the evolution of the median axis-ratio of the distribution (our results in semi-transparent red circles for intermediate/narrow bands and large opaque red circles after binning in redshift) and we compare our values to those reported in the literature (in grey): pentagon (Gronwall et al., 2011) and diamond (Kobayashi et al., 2016). The black solid line shows the best fit of $(b/a) \propto (1+z)^{\alpha}$. The red dashed line marks the median axis-ratio for all LAEs at any redshift.

The ellipticity of a source is defined as $e = 1 - (b/a)$. We show in Fig. 3.6 the results for the derived axis-ratio for the sources in our sample. Our ellipticities have an average uncertainty of 0.07. This is possible due to the use of the HST PSF to convolve with the Sérsic model before comparing to the data when running GALFIT. We find that LAEs have no clear preference for an ellipticity value, with most of our sources lying at intermediate values $0.2 < (b/a) < 0.8$. This implies that the detected LAEs do not have to be of a particular shape, which is expected given the randomness of the line-of-sight alignments that determine the 2D shape of each galaxy when viewed through an image. On a more interesting note, this also tells us that a specific alignment of the source with our line-of-sight is not required for it to be detected as a Ly$\alpha$ emitter. These results are in good agreement with measurements at $3 < z < 5$ by Gronwall et al. (2011). Given the constant Sérsic indices and the small sizes, our results thus hint that the high Ly$\alpha$ escape fractions of our sources are more of a consequence of their sizes and not orientation effects.

In terms of the median population values for this quantity and its evolution with redshift, we show in the bottom panel of Fig. 3.6 that the values of $(b/a)$ are slightly rising with redshift (median value of $(b/a) = 0.40$) and in excellent agreement with those reported by Gronwall et al. (2011). However, there is a large discrepancy with the mean value reported by Kobayashi et al. (2016) at $z \sim 4.86$. We believe that this difference is mostly due to the method used, as they use SExtractor to measure ellipticities that does not account for any PSF broadening which in the case of small galaxies, such as is typical of LAEs, it is natural that the shape is dominated by the PSF in its core, artificially lowering the ellipticity. Using the parametrization of Eq. 3.3 we find that $b/a \propto (1+z)^{-0.46 \pm 0.16}$, which is marginally consistent with a constant ellipticity scenario (within $3\sigma$). This mild evolution reinforces the idea that the galaxy orientation is not a

main factor in driving the escape fraction for LAEs.

### 3.4.3 CONCENTRATION

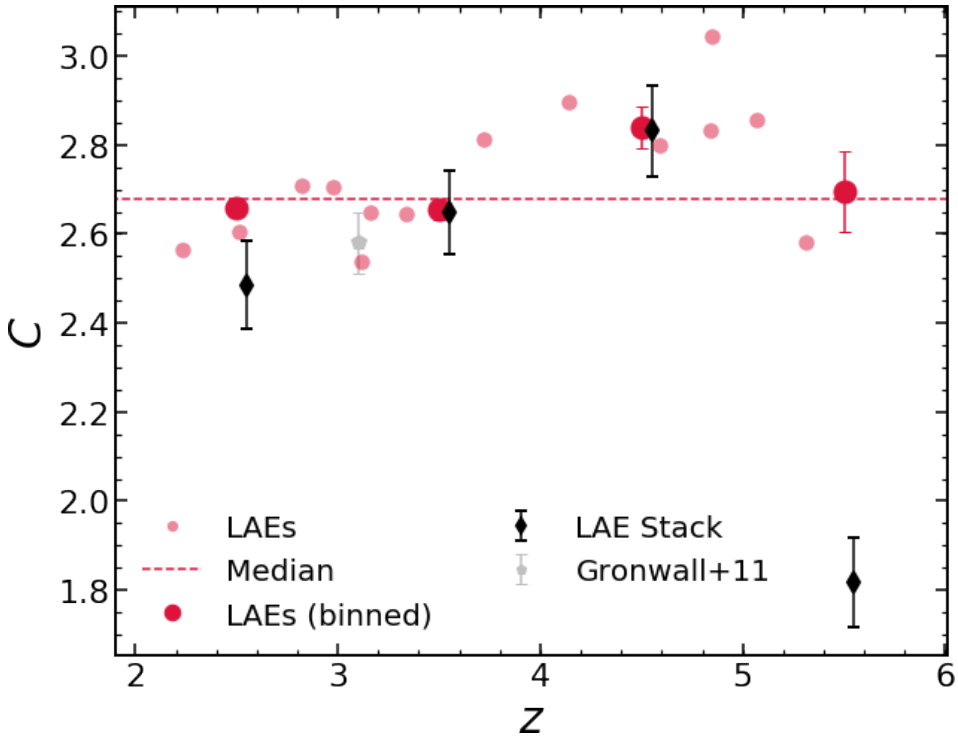


**Figure 3.7** Concentration median values of LAEs at $2 \lesssim z \lesssim 6$. We plot the evolution of the median concentration of the distribution (our results in semi-transparent red circles for intermediate/narrow bands and large opaque red circles after binning in redshift) and compare our values to those reported by Gronwall et al. (2011, grey pentagon). The red dashed line marks the median concentration for individual LAEs at any redshift. The black diamonds show the concentration of the stacked LAEs. The higher value of concentration for the stacked profiles is likely linked to the combination of the compact nature of these objects and the stacking method we use (see Sect. 3.4.3 for more details).

In Fig. 3.7 we investigate any evolution in terms of the light concentration of galaxies. It is rather stable at $C \sim 2.7$ with the exception of the value at $4 < z < 5$. The fact that this parameter is strikingly similar, in its median evolution, with the Sérsic index is a possible indication that the galaxies we are probing are rather symmetrical in nature. Both parameters provide a measure of the surface brightness concentration and, in the case of a symmetrical Sérsic profile, it can be shown that $C$ has a monotonic relation with $n$ (e.g. Graham & Driver, 2005). We find that our results are also in good agreement with the findings by Gronwall et al. (2011). Using the parametrization of Eq. 3.3 we find that $C \propto (1+z)^{0.04 \pm 0.09}$ is fully consistent with a constant light concentration across the entire redshift range. We observe a rise in light concentration for sources at $z \sim 4-5$, which is possibly related to an increase on the number of irregular galaxies that we observe. We note that the value at $4 < z < 5$ is also potentially related to a shallower depth of the images for detection of Ly$\alpha$ (NB711 and IA709), which are more likely to pick

sources with higher surface densities and thus higher values of $C$ are to be expected.

The values we find for the concentration of the stacked profiles are consistent with those we find for the median of the population. At the highest redshift, we find much lower concentrations which is potentially related to the higher number of undetected sources that populate this bin allied to the fact that this is also the bin with the fewer galaxies in the stack.

**Table 3.2** Median population and stack values as a function of redshift for the morphological quantities presented in this work.

| | variable | $2 < z < 3$ | $3 < z < 4$ | $4 < z < 5$ | $5 < z < 6$ |
|---|---|---|---|---|---|
| Population | $r_e$ [kpc] | $1.1 \pm 0.1$ | $1.1 \pm 0.2$ | $0.9 \pm 0.3$ | $1.0 \pm 0.2$ |
| | $n$ | $1.8 \pm 0.2$ | $1.7 \pm 0.2$ | $2.5 \pm 0.4$ | $1.5 \pm 0.9$ |
| | $(b/a)$ | $0.44 \pm 0.01$ | $0.45 \pm 0.02$ | $0.36 \pm 0.03$ | $0.35 \pm 0.04$ |
| | $C$ | $2.66 \pm 0.02$ | $2.66 \pm 0.02$ | $2.86 \pm 0.05$ | $2.69 \pm 0.09$ |
| Stack | $r_e$ [kpc] | $1.2 \pm 0.1$ | $1.0 \pm 0.1$ | $1.1 \pm 0.1$ | $1.3 \pm 0.1$ |
| | $n$ | $1.0 \pm 0.1$ | $1.1 \pm 0.1$ | $1.3 \pm 0.1$ | $0.6 \pm 0.1$ |
| | $C$ | $2.5 \pm 0.1$ | $2.6 \pm 0.1$ | $2.7 \pm 0.1$ | $1.8 \pm 0.1$ |

### 3.4.4 MORPHOLOGICAL CLASSES

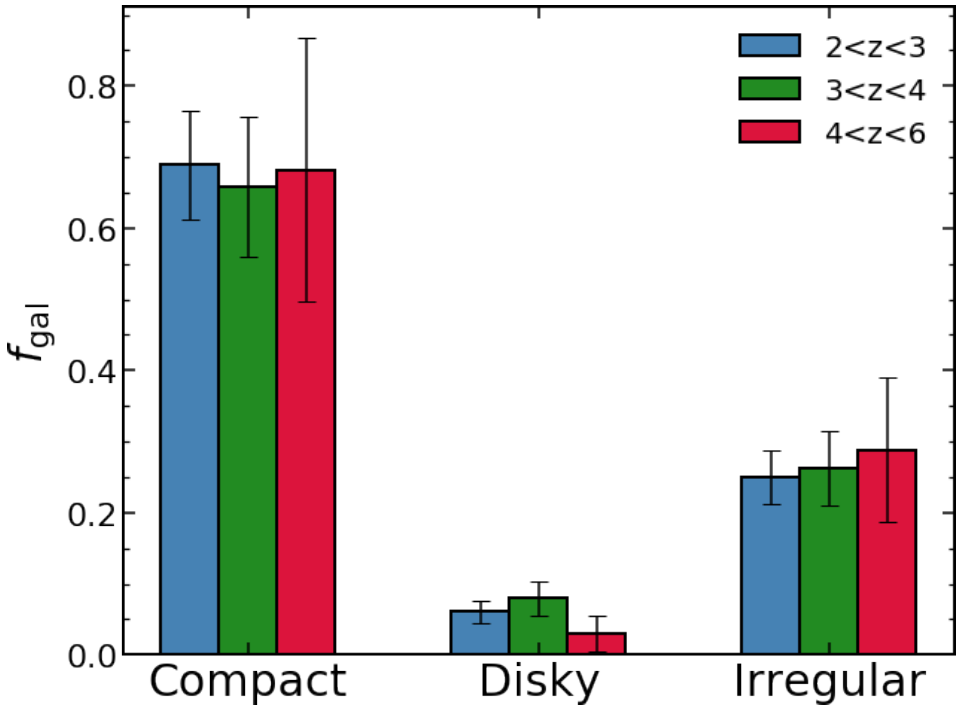


**Figure 3.8** Fraction of galaxies in each of the morphology classes from visual classification of LAEs at $2 \lesssim z \lesssim 6$.

Of the 1092 galaxies with $i_{AB} < 25$ only 780 had good quality images from the HST/ACS archive available. We summarize in Fig. 3.8 the resulting distribution in terms of their visual

classification. We find that the majority of our bright LAEs ($\sim 67\%$) are found to be compact (point-like+elliptical class). Of the other classes, we find that irregular LAEs are $\sim 26\%$ of our sample while disky galaxies amount to only $\sim 7\%$ of the observed LAEs. These fractions are roughly constant, but we observe only a slight rise in the fraction of irregulars towards higher redshifts which can be expected of young galaxies in the earlier Universe (e.g. Buitrago et al., 2013; Jiang et al., 2013; Huertas-Company et al., 2015b; Bowler et al., 2017).

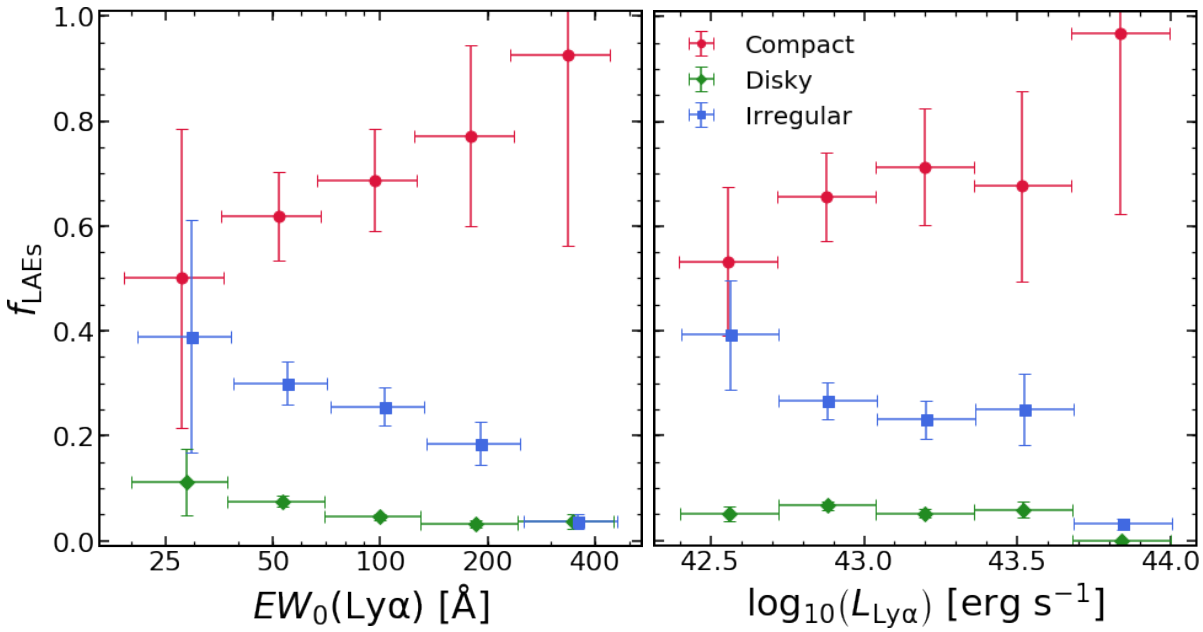


**Figure 3.9** Fraction of LAEs of a given morphological class (compact as red circles, disky as green diamonds and irregulars as blue squares) at $2 \lesssim z \lesssim 6$ as a function of line equivalent width (left) and line luminosity (right).

### 3.4.5 The lack of evolution in individual LAE morphologies

We have shown in the previous sections the general properties of LAEs in the sample that we are studying and find that the morphology of this population of galaxies is rather stable in this $\sim$3 Gyr period. Since we find that there is not any strong evident evolution in all presented parameters, we opt to study the dependence of Ly$\alpha$ emission properties on the rest-frame UV morphology using the entire sample without discriminating between redshifts (with the majority of our sources being at $z \sim 2-3$). This hypothesis will boost the number of sources to inspect such relations and thus uncover more effectively any underlying correlations that may exist.

We are aware that our sample selection is not done in any absolute quantities (such as in Ly$\alpha$ luminosity or $M_{\rm UV}$) and thus we may introduce some biases in our interpretation of the redshift evolution of the presented quantities. We have tested our hypothesis of selection by comparing our results using selections on $\log_{10}(L_{\rm Ly\alpha}) > 43$ and $M_{\rm I} < -20.5$, ($M_{\rm I}$ is the absolute magnitude of the observed I band) independently. We can report that the lack of evolution in the reported

morphological quantities is observed in these smaller subsets from our main sample thus we opt to keep the apparent magnitude cut as our main selection.

### 3.4.6 Morphology dependence on Ly$\alpha$ luminosity and equivalent width

After summarizing our findings on the morphological properties across cosmic time for the LAEs in our sample, we now turn to the influence of morphology on the observed properties of the Ly$\alpha$ emission itself (line equivalent width and luminosity).

We show in Fig. 3.9 the fraction of each morphological class as a function of line equivalent width and line luminosity. We find that we have no disky galaxies at the highest equivalent widths and that the irregular galaxies are less common at higher equivalent widths. These trends are accompanied by a slight rise in the fraction of compact galaxies with line equivalent width. We also find that the brightest emitters are tendentiously more likely to be compact than their lower luminosity counterparts. We observe a decline in the fraction of irregular galaxies with line luminosity and a rather stable fraction of disky galaxies at all luminosities that we are probing.

Our results on the relations between morphological quantities and Ly$\alpha$ emission properties are summarized in Fig. 3.10 and in Table 3.3.

In Fig. 3.10 (first panel, left column), we show the dependence of the equivalent width of Ly$\alpha$ on the observed extent of the UV emission. We observe a trend where higher equivalent width LAEs tend to have smaller sizes. This sort of correlation is seen in other studies (see e.g. Taniguchi et al., 2009; Law et al., 2012; Kobayashi et al., 2016), where they find that there is a lack of large galaxies with large equivalent widths and thus the median sizes are naturally smaller at higher equivalent widths. For low equivalent width galaxies, the dispersion on galaxy sizes is larger, spanning the entire interval of measured sizes in the sample. Since Ly$\alpha$ emitters are selected typically with an EW cut then this is likely related with the small sizes of LAEs. Interestingly, this relation may be connected to the physics of Ly$\alpha$ escape since studies have shown that Ly$\alpha$ equivalent width traces the Ly$\alpha$ escape fraction (e.g. Sobral et al., 2017; Verhamme et al., 2017). We highlight that the trend is also observed for the stacked profiles.

**Table 3.3** Linear fits shown in Fig. 3.10. Each line represents a morphological quantity and in the second and third columns we show the parameters from the best fit for Ly$\alpha$ equivalent width and luminosity, respectively.

| y-variable | $x = EW_0(\mathrm{Ly}\alpha)$ | $x = \log_{10}\left(L_{\mathrm{Ly}\alpha}\right)$ |
|---|---|---|
| $r_e$ | $(-3.5 \pm 1.2) \times 10^{-3} x + (1.5 \pm 0.2)$ | $(-0.51 \pm 0.2) x + (23.0 \pm 8.5)$ |
| $n$ | $(-3.3 \pm 2.3) \times 10^{-3} x + (2.4 \pm 0.3)$ | $(1.8 \pm 0.63) x + (-74.8 \pm 27.2)$ |
| $(b/a)$ | $(5.2 \pm 2.2) \times 10^{-4} x + (0.4 \pm 0.05)$ | $(8.5 \pm 5.6) \times 10^{-2} x + (-3.2 \pm 2.4)$ |
| $C$ | $(1.6 \pm 5.5) \times 10^{-4} x + (2.7 \pm 0.1)$ | $(5.2 \pm 0.72) \times 10^{-2} x + (0.4 \pm 0.3)$ |

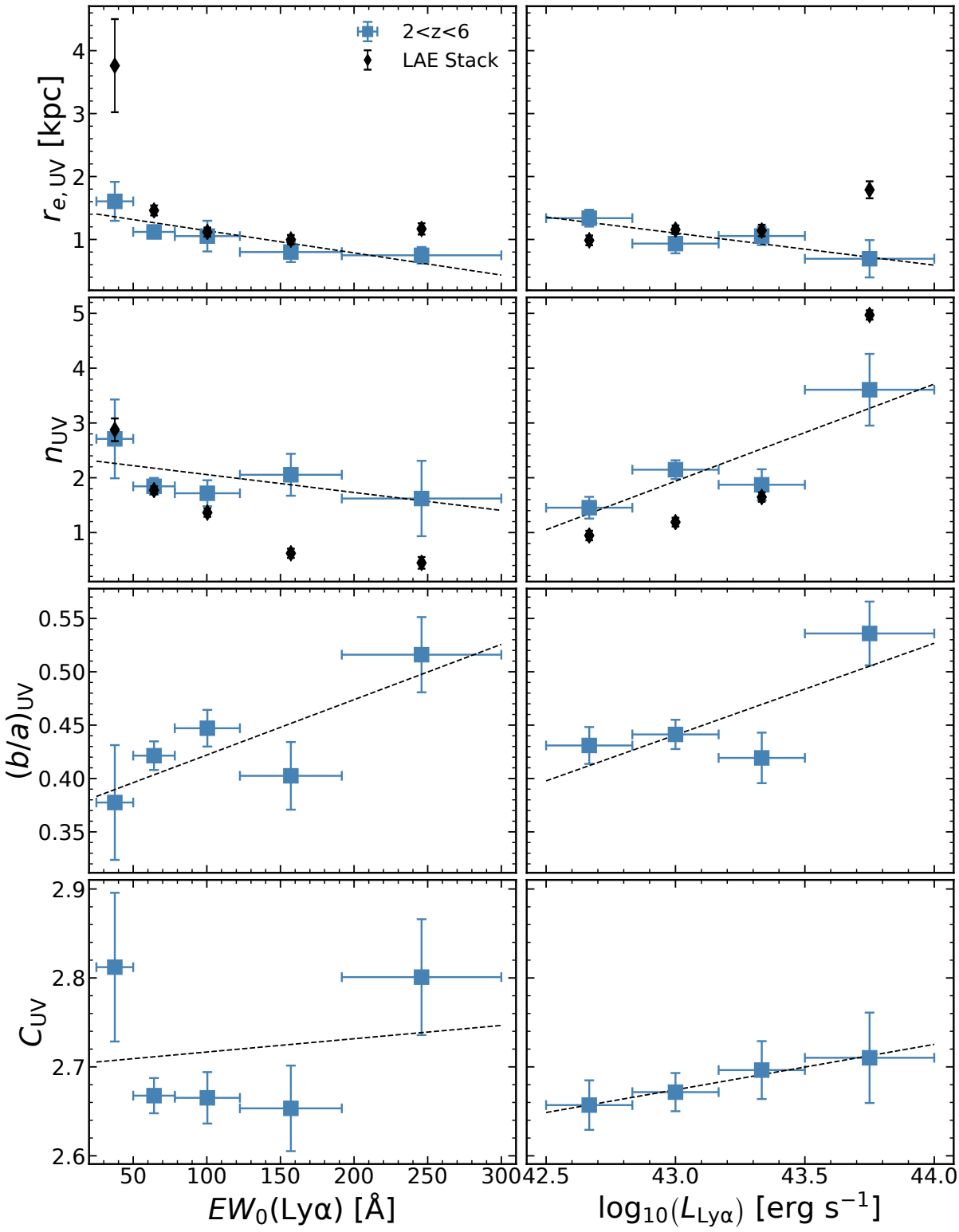


**Figure 3.10** Morphology as a function of line equivalent width (left column) and line luminosity (right column) of LAEs at $2 \lesssim z \lesssim 6$. From top to bottom we show the results for galaxy size, Sérsic index, axis-ratio and light concentration. The median values are shown as blue squares and the stacked LAEs properties are represented by the black diamonds. We note that for galaxies with $25 < EW_0(Ly\alpha) < 50$ we only have LAEs detected in the narrow-band surveys, which severely impacts our statistics and give us higher uncertainties in that bin. Black dashed lines show the best linear fits, which have their best parameters shown in Table 3.3.

We plot in Fig. 3.10 (second panel, left column) the relation between Sérsic index and Ly$\alpha$ equivalent width and find that there is a slight sign of a correlation between these two quantities. Our data suggests that at higher equivalent widths ($EW_0(\mathrm{Ly}\alpha) > 200$Å) we are more likely to have shallower profiles. This trend is also seen from the stacked profiles albeit at systematically lower values of $n$ (see Sect. 3.4.1).

A stronger correlation that we find is between the axis-ratio of the emission and the measured line equivalent width. In Fig. 3.10 (third panel, left column) we find that the strongest emitters (the ones with the largest equivalent width) tend to have rounder shapes (higher axis-ratios, lower ellipticities). These findings are in agreement with those reported by Kobayashi et al. (2016) at $z \sim 4.86$. If we assume that the axis-ratio is a good proxy for galaxy inclination, we can explain the observed trend as a simple effect of geometry due to the inclination of the disk with respect to our line of sight (see e.g. Verhamme et al., 2012; Behrens & Braun, 2014). However, one must be cautious when comparing observations directly with simulations since the latter assume that the galaxy is a perfect flat disk and the former assumes that galaxies are symmetrical enough to be well fit by a parametric model and either assumption has its drawbacks.

We finally explore the correlation between light concentration and Ly$\alpha$ in Fig. 3.10 (fourth panel, left column). Much like the case we presented for the Sérsic index, we cannot infer conclusively about any correlation between these two quantities. We may tentatively say that galaxies with higher equivalent widths ($EW_0(\mathrm{Ly}\alpha) > 200$Å) are to be more concentrated in term of the rest-frame UV emission when compared to their lower equivalent width counterparts. The higher concentration value we have for the lower equivalent width bin is explained due to the lower number statistics of that bin. As stated in Sect. 3.2, galaxies with $25 < EW_0(\mathrm{Ly}\alpha) < 50$Å are only from narrow band data.

We attempt at a similar exercise as above and explore the possible correlations between the galaxy morphology and its observed Ly$\alpha$ line luminosity.

Concerning galaxy sizes there is an apparent downward trend for galaxies with $10^{42.5} \lesssim L_{\mathrm{Ly}\alpha} \lesssim 10^{44}$erg s$^{-1}$ with galaxies being smaller at higher luminosities (see Fig. 3.10, first panel, right column). This trend is not clear since there are some bin-to-bin variations that are mainly due to our small number of objects as well as the loose correlation that exists between these two quantities (for any luminosity bin there is a large spread in galaxy sizes). Interestingly we find an opposite trend when considering the sizes of the stacked profiles. We find this can be explained by an underlying $i_{\mathrm{AB}}$ - Ly$\alpha$ line luminosity where the brightest galaxies on our sample in rest-frame UV are also the ones with the highest Ly$\alpha$ line luminosity. When stacking a large number of bright galaxies, we are more likely to pick up extended lower surface brightness regions and thus get larger sizes.

We find a similar scenario for the Sérsic index (see Fig. 3.10, second panel, right column), with higher luminosity LAEs hinting at a higher value of a Sérsic index. We believe again that the

large dispersion on the observed data is likely an indication of the loose correlation between these two quantities. Nevertheless, it is remarkable that the brightest LAEs have such high Sérsic index ($n \sim 3.5$), corresponding to more classical elliptical profiles. This is a consequence of bright, small and compact objects that are more likely to possess such profiles. We find the same response when looking at the values of the stacked LAEs, with high luminosity LAEs ($L_{\mathrm{Ly}\alpha} \sim 10^{43.75}$erg s$^{-1}$) having higher values of $n \sim 4$. We find the same trend when considering the stacked profiles, albeit at a shallower slope and systematically lower values of $n$ (see Sect. 3.4.1).

When estimating the median axis ratio as a function of Ly$\alpha$ line luminosity (see Fig. 3.10, third panel, right column) we find the same trend as compared to the relation with line equivalent width. In this case, galaxies at higher luminosities show less elongated shapes than their lower luminosity counterparts.

Finally, we show in Fig. 3.10 (fourth panel, right column) that there is a small but steady increase of the light concentration for our luminosity bins. This trend is less broken that what is reported for the equivalent width of the Ly$\alpha$ line, but still points to a scenario where the brightest Ly$\alpha$ emitters are more likely to have high light concentration in their profiles (as also seen in the Sérsic index).

## 3.5 The dependence of morphology on Ly$\alpha$

To investigate the dependence of UV morphology of LAEs on redshift, Ly$\alpha$ luminosities and Ly$\alpha$ EWs independently we have stacked different subsamples probing individually each parameter. The resulting stacked images are shown in Fig. 3.18-3.20. We followed the methodology detailed in Sect. 3.3.4 and obtained individual morphological parameters for each subsample. We summarize the results in Fig. 3.11. We did not perform similar analysis on the median of the population since we only have individual measurements on 429 galaxies. Doing so would result in a highly diluted sample over the 27 bins that we need to probe independently the correlations (3 bins per independent variable). We note however that due to scarcity of sources with $i_{\mathrm{AB}} < 25$ we are not able to compute the corrections described in Appendix to this Chapter. We then use the average redshift correction we derive and apply it to all Ly$\alpha$ luminosities and Ly$\alpha$ EW bins.

### 3.5.1 Galaxy sizes

When considering the evolution in LAEs sizes we find that independently probing in Ly$\alpha$ luminosities and Ly$\alpha$ equivalent width yields interesting results. Overall, we find no significant

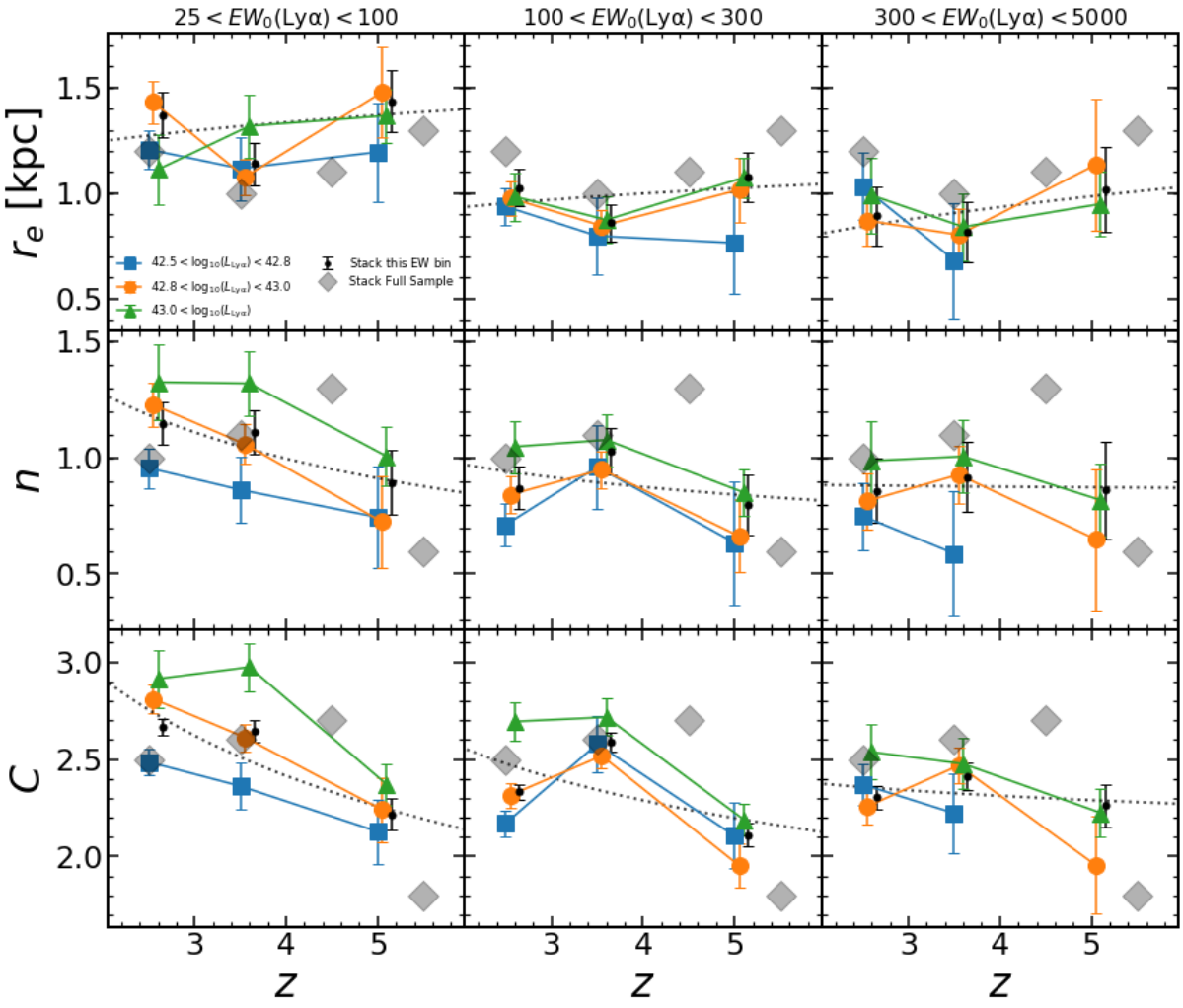


**Figure 3.11** Morphological evolution results for LAE stacks binned in redshift, Ly$\alpha$ luminosities and Ly$\alpha$ equivalent widths independently. Each row shows a different Ly$\alpha$ equivalent width bin and each line a different Ly$\alpha$ luminosity bin. We also compare those with the stack of the full sample binned in redshift and the stack for a specific EW bin. The dotted black line shows the $X \propto (1+z)^{\alpha}$ fit to the EW bin. Overall we find that galaxy sizes grow with cosmic time for all luminosities and equivalent width bins. We find a similar increase in Sérsic index and light concentration, from high to low redshift in all redshift bins. We find the strongest evolution in galaxy sizes, Sérsic index and light concentration in the lower Ly$\alpha$ equivalent width galaxies.

size evolution in any of the bins that we probe. To quantify the evolution trends that we find we fit Eq. 3.3 to each EW bin defined. We find that the slopes to be $\alpha = -0.11 \pm 0.42$ for $25 < EW < 100$ Å stacked LAEs, $\alpha = -0.11 \pm 0.41$ for $100 < EW < 300$ Å stacked LAEs and $\alpha = 0.27 \pm 0.31$ for $EW > 300$ Å stacked LAEs. These slopes are all perfectly consistent with no evolution as we have derived when considering all galaxies (see Fig. 3.5). In addition to that, galaxies with the lowest Ly$\alpha$ EWs are also the largest at any redshift (similar to what is found in e.g. Law et al., 2012). This is the same trend as we already find in Fig. 3.10 when considering the entire LAE population. We find larger galaxies for low EW LAEs.

The luminosity of Ly$\alpha$ seems not to have such a strong influence on the measured sizes (as already indicated by contrary trends in Fig. 3.10). It is true that we have small indications that higher luminosity galaxies can, on average, be larger but that is only marginally true for

the intermediate line equivalent width subsamples ($100 < EW < 300$ Å). At lower and higher equivalent widths the picture is not so clear and we get different size-luminosity trends at different redshifts.

We nevertheless stress that we may be affected by measurement errors on low S/N stacked images, as we have fewer galaxies at high redshift to stack from. We show in Fig. 3.18-3.20 that at $4 < z < 6$ we have faint surface brightness for low and intermediate luminosity bins. We would need larger samples and/or deeper high resolution surveys to probe the morphology of the LAE population.

### 3.5.2 Sérsic index and light concentration

In highly symmetrical profiles, such as those produced by stacking a large number of galaxies with random orientations in the sky, it is normal that the light concentration index, $C$, correlates with the Sérsic index, $n$. In that sense, the results that we find for both are qualitatively the same and can be interpreted from the same perspective. We find an overall increase of both morphological indexes with redshift. We also observe an increase of both indexes with Ly$\alpha$ luminosity and a decrease with Ly$\alpha$ equivalent width. In summary, we expect that the light concentration would be higher for high Ly$\alpha$ luminosity, low Ly$\alpha$ equivalent width and low redshift and lower light concentration for low Ly$\alpha$ luminosity, high Ly$\alpha$ equivalent width and high redshift.

These results are in good agreement with the more general trends that we find in Fig. 3.10, where we also see similar relations when looking at the whole population. It also reinforces the idea that the trends in Ly$\alpha$ luminosities and Ly$\alpha$ equivalent widths are valid in the redshift bins that we probe here. However, we find more interesting trends concerning the evolution with redshift which are slightly more pronounced when separating the galaxies in different regions of the Ly$\alpha$ luminosity and Ly$\alpha$ equivalent width parameter space.

## 3.6 Discussion

### 3.6.1 The evolution in LAE morphology between $z \sim 2-6$

Our results regarding galaxy morphology as a function of redshift (see Sect. 3.4) indicate that LAEs have the same typical shape across the period we probe ($z \sim 2-6$). This is reflected by the little to no variation in size, Sérsic index, axis-ratio and light concentration parameters

which is seen both in the median of the population as well as in the stacked profiles. This lack of evolution relates only to the general LAE population taken as whole. As we show in Fig. 3.11, we are maybe seeing some redshift evolution in Sérsic indexes and light concentration when separating our sample in different Ly$\alpha$ luminosity and Ly$\alpha$ EW bins (but no evidence of that for galaxy sizes). The strongest redshift evolution that we find is for low Ly$\alpha$ equivalent width galaxies. This is likely because typical SFGs and/or LBGs with Ly$\alpha$ emission are mostly populated with low Ly$\alpha$ equivalent widths (see e.g. Hathi et al., 2016) and thus we can expect that these subsamples would have similar properties to that population. We note, however, that the lowest equivalent width LAEs (which are those brighter in UV and likely the most massive within our sample) are not the dominant population and that is the main reason why we do not see strong evolution in morphology of the LAE population from $z \sim 2$ to $z \sim 6$.

### 3.6.2 LAE SIZES AT $z \sim 2-6$

Finally, in Fig. 3.12 we show our results for the evolution in rest-frame UV sizes of LAEs across cosmic time and compare our findings to previous studies (e.g. Taniguchi et al., 2009; Bond et al., 2011, 2012; Gronwall et al., 2011; Guaita et al., 2015; Kobayashi et al., 2016). Our median effective radius are in agreement with other size estimates of LAEs in the literature. At $z \gtrsim 4$ we find typical sizes of $r_e \sim 0.9$ kpc and at $z \sim 2.2$ we find slightly larger galaxies with average sizes of $r_e = 1.1$ kpc. We have attempted to fit a relation to our data points and find that $r_e \propto (1+z)^{-0.21\pm0.22}$ (see Sect. 3.4.1). This scenario, however, predicts slightly larger sizes at $z \sim 0$ than what have been reported for the LARS sample in the local Universe (Guaita et al., 2015) but within their reported dispersion. This scenario points to a lack of evolution on the sizes of LAEs since $z \sim 6$. However, this reasoning hinges on the single point that we have at $z \sim 0$ and which is derived from a heterogeneous sample of 14 galaxies only. To fully understand if LAEs evolve in size as hinted by the data at $z \sim 2.5$ one would need larger samples between $z = 0-2$, which are currently out of the scope of any instrument apart from HST/COS.

### 3.6.3 RELATIONS BETWEEN LAEs, HAEs AND UV-SELECTED GALAXIES

When compared to the typical sizes of star-forming galaxies (selected as H$\alpha$ emitters, HAEs) that have been studied in a previous work (Paulino-Afonso et al., 2017), we immediately see that the two populations are not alike in terms of their extent. Despite having only one common period with observations of both populations (at $z = 2.23$), where HAEs are almost two times larger than LAEs, our prediction of LAEs sizes at lower redshifts are consistently lower that what we report for the HAE population. This is even more contrasting if we include the sample

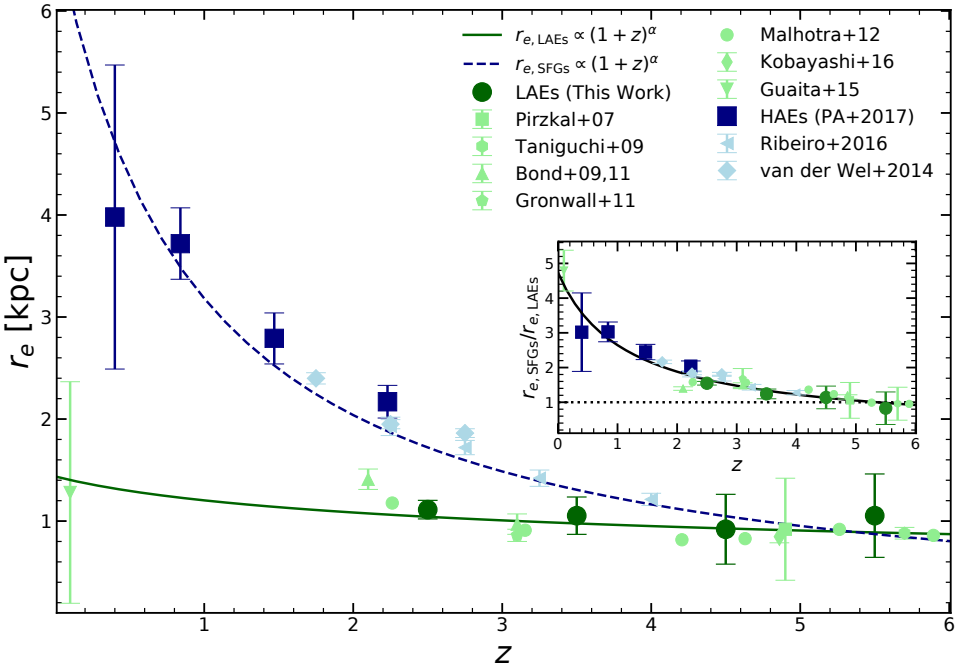


**Figure 3.12** Size properties of LAEs at $2 \lesssim z \lesssim 6$. We plot the evolution of the median size of the distribution (our results in large green circles) and compare our values to those reported in the literature (in light green): square (Pirzkal et al., 2007), hexagon (Taniguchi et al., 2009), triangles (Bond et al., 2009, 2011), circles (Malhotra et al., 2012), diamond (Kobayashi et al., 2016) and inverted triangle (Guaita et al., 2015). We show as blue squares the median size for a sample of HAEs selected at lower redshift using the same narrow band technique (Paulino-Afonso et al., 2017). We complement this figure with results for UV-selected star-forming galaxies from the literature (in light blue): large diamond (van der Wel et al., 2014) and left-facing triangle (Ribeiro et al., 2016). Finally, we show the derived size evolution of LAEs (green solid line) and SFGs (blue dashed line). The inset plot shows the estimated size ratio between SFGs and LAEs. Estimates point to SFGs being $\sim 5$ times larger at $z \sim 0$ and of the same size as LAEs at $z \sim 5.5$. We hypothesize that Ly$\alpha$ selected galaxies are small/compact throughout cosmic time likely linked with the physical processes that drive Ly$\alpha$ escape. At higher and higher redshifts, typical SFGs start to have the typical sizes of Ly$\alpha$ emitters, which can be seen as an alternative explanation for the rise of the Ly$\alpha$ emitting fraction of SFGs/LBGs into $z \sim 6$.

at $z \sim 0$, where almost no evolution is expected for the LAEs population. This is potentially corroborated by the existence of green pea galaxies (Cardamone et al., 2009; Izotov et al., 2011) which are compact in nature and found to have Ly$\alpha$ detections and high Ly$\alpha$ escape fractions (e.g. Henry et al., 2015; Yang et al., 2016; Verhamme et al., 2017).

We also use two recent and comprehensive studies on the evolution of UV-selected star-forming galaxies (van der Wel et al., 2014; Ribeiro et al., 2016, see also Shibuya et al. 2015) that overlap both HAEs and LAEs that we have studied to complement our observations. These confirm our findings that at $z \sim 2$ the typical star-forming population is larger in size than the LAEs population (by a factor of $\sim 3$). However, we see that this difference fades away and, by $z \sim 5$, the two populations are indistinguishable from one another, in what their median extent is concerned. These results are in agreement with previous findings where both populations are compared (e.g. Malhotra et al., 2012; Jiang et al., 2013).

Our results are consistent with a scenario where a Ly$\alpha$ emitter is a phase through which galaxies

may go through in the early stages of their life. From the size evolution perspective, this means that at some point in a galaxy life, when the star-formation is confined to $\lesssim 1$ kpc, there are conditions to boost the escape of Ly$\alpha$ photons to our line-of-sight so that we observe the galaxy as a LAE. As time progresses, each galaxy grows in size (along with stellar mass, dust content, metallicity and star formation evolution) and we tend to observe less and less Ly$\alpha$ in emission and observe large galaxies, which are still actively forming stars but do not contribute to the global budget of the observed Ly$\alpha$ emission of the Universe. This decoupling of the two populations with respect to their median size occurs roughly $\sim$1 Gyr after the first galaxies are born. By arguing that the distinction between the two populations happens at the time where a galaxy has evolved for long enough not to be observed as a LAE any more, we can hypothesise that the life cycle of the Ly$\alpha$ emission of a galaxy is typically of the same scale. This means that we may expect on average every galaxy to be observed in Ly$\alpha$ emission for the first $\sim$1 Gyr of its life.

We are aware that our scenario is grossly simplistic, but it finds support by other studies where LAEs are found to be of low mass and low dust content (e.g. Gawiser et al., 2007; Pentericci et al., 2007; Lai et al., 2008, see also Erb et al. 2006; Kornei et al. 2010; Hathi et al. 2016). However, there are a number of other studies that report conflicting evidence (e.g. Finkelstein et al., 2009; Nilsson et al., 2011, see also Reddy et al. 2008). The large diversity of results indicate a more intricate nature of LAEs, pointing to a scenario with possibly recurrent phases of Ly$\alpha$ emission throughout a galaxy's life cycle.

We nonetheless reinforce our findings that LAEs are clearly the most compact population of the two which is consistent with their naturally higher escape fraction of Ly$\alpha$ with respect to an average SFG. At the highest redshifts, the conditions in the Universe were markedly distinct, with most galaxies being very small ($r \lesssim 1$ kpc) which in turn renders them more likely to be observed as a LAE, as a consequence of Ly$\alpha$ escaping more easily in smaller galaxies. In the early Universe, typical SFGs have sizes comparable to Ly$\alpha$ emitters, which offers an alternative explanation for the rising fraction of the Ly$\alpha$ emitting SFGs/LBGs up to $z \sim 6$ (e.g. Hayes et al., 2011; Stark et al., 2011; Mallery et al., 2012; Cassata et al., 2015).

### 3.6.4 Visual morphology of LAEs

We show in Fig. 3.9 that bright LAEs and high line equivalent width LAEs are more likely to be found with a compact shape. By relating the visual morphology with the structural parameters that we have computed (see Sect. 3.3) we can find some corroborating signs. Galaxies at the bright end of our LAE sample are found to be smaller, with higher Sérsic indices, rounder (higher axis-ratio) and with higher light concentrations. These characteristics are relatable to a classical small and round elliptical galaxy which would be classified as compact given our classification scheme. Apart from the discrepancy on the Sérsic index, we see the same aforementioned trends

in the relation of structural parameters with line equivalent width.

### 3.6.5 THE GEOMETRIC NATURE OF LY-$\alpha$ EMISSION

We found some evidence to support that there are some geometric requirements for the successful escape of Ly$\alpha$ photons. In summary, compact and rounded objects are more likely to harbour conditions for such occurrence. This does not invalidate that there are other processes which contribute significantly to such event. The hinted correlations that we find are far from being a definite conclusion on this matter and certainly the existence of outflows, asymmetric or lack of gas and dust distributions can contribute as well to the observation of Ly$\alpha$ in emission.

This assertion is supported by the relations that we find between light concentration and galaxy axial ratio with Ly$\alpha$ line equivalent width. As found by Sobral et al. (2017) the escape fraction of Ly$\alpha$ photons correlates with the Ly$\alpha$ rest-frame equivalent width. Our results are pointing to the fact that galaxies that are rounder and with higher concentrations of their light profile have potentially higher escape fractions. These results are in line with predictions from simulations (e.g Verhamme et al., 2012), if we assume the axis-ratio is a good proxy for galaxy inclination with respect to our line of sight. However, a scenario of compact objects with higher volume density of stars can reproduce similar results without the need to invoke galaxy inclination to explain the observations. We believe the latter scenario is more likely the explanation for our results, since we do not expect the majority of our galaxies to have had the time to converge in a rotation supported disk for which the inclination would play a more prevalent role in the perceived escape fraction from our line of sight.

## 3.7 CONCLUSIONS

We present the morphological characterization of a large sample of $\sim$4000 LAEs and quantify their evolution in the first $\sim$3 Gyr of the Universe ($2 \lesssim z \lesssim 6$). We study the correlation between the rest-frame UV morphology and the strength of the Ly$\alpha$ emission as a probe to the understanding of the mechanisms underlying the escape of Ly$\alpha$ photons from its host galaxy. Our results can be summarized as:

- UV sizes of LAEs are constant from $z \sim 2$ to $z \sim 6$ with sizes of $r_e \sim 1.0 \pm 0.1$ kpc. We observe a rise in sizes towards lower redshifts ($z \sim 2$), but the trend is shallow. The little to no evolution seems to hold even down to $z \sim 0$.
- At redshifts $z \lesssim 5$, LAEs have sizes that are consistently smaller than those reported for normal SFGs. The difference between the two populations gets more pronounced as we

move towards lower redshifts, going from a factor of $\sim$1 at $z \gtrsim 5$ to SFGs being a factor of $\sim 2-4$ larger than LAEs for $z \lesssim 2$. We hypothesize that the small/compact nature of LAEs is potentially linked to physical escape mechanisms of Ly$\alpha$ photons. In the early Universe, typical SFGs have sizes comparable to Ly$\alpha$ emitters which offers an alternative explanation for the rising fraction of the Ly$\alpha$ emitting SFGs/LBGs up to $z \sim 6$.

- The profiles of LAEs as seen from the rest-frame UV are remarkably constant from $z \sim 2$ up to $z \sim 6$ with $n \sim 1.7$ being slightly steeper than a pure exponential disk. The same scenario is seen in the evolution of the light concentration and axis ratio of LAEs.
- When looking at subsamples of fixed Ly$\alpha$ luminosity and fixed Ly$\alpha$ equivalent width we find a more pronounced evolution with redshift for Sérsic indexes and light concentration (but not for galaxy sizes). LAEs with the lowest EWs (which are the brightest in UV within our sample) are those who show a stronger evolution. This is likely happening because low EW LAEs are those more similar to regular LBGs/SFGs (e.g. Hathi et al., 2016), which show some evolution of their light profiles (e.g. Morishita et al., 2014).
- We find that most LAEs in our sample are compact in their morphology. The fraction of compact LAEs is larger at high line equivalent widths and also at high Ly$\alpha$ luminosity.
- Ly$\alpha$ equivalent width seems to correlate stronger with the axis ratio and size of galaxies than any other morphological parameter we have tested. Strong LAEs are found more likely in small and rounder galaxies ($r_e \sim 0.8$ kpc and $b/a \sim 0.5$).
- The results that we report as the median properties of the population are corroborated by the morphological properties of the stacked profiles of LAEs. This means that even when the image depth is increased, we find no difference with respect to the detected LAEs and discard the existence of an extended lower surface brightness region around UV-bright LAEs.

In broad terms, our results provide a global picture on the rest-frame UV morphology of LAEs in the early Universe. We find that this particular population of galaxies does not evolve significantly in the first 3 Gyr of the Universe and that it departs from the evolution of normal star-forming galaxies for $z < 4$, in what galaxy sizes is concerned.

## ACKNOWLEDGEMENTS

We are grateful to the referee's useful and constructive comments and suggestions which improve this work. This work was supported by Fundação para a Ciência e a Tecnologia (FCT) through the research grant UID/FIS/04434/2013. APA, PhD::SPACE fellow, acknowledges support from the FCT through the fellowship PD/BD/52706/2014. DS acknowledges financial support from

the Netherlands Organisation for Scientific research (NWO) through a Veni fellowship and from Lancaster University through an Early Career Internal Grant A100679. The authors acknowledge the award of time from programmes: I13AN002, I14AN002, 088-INT7/14A, I14BN006, 118-INT13/14B, I15AN008 on the Isaac Newton Telescope (INT). INT is operated on the island of La Palma by the Isaac Newton Group in the Spanish Observatorio del Roque de los Muchachos of the Instituto de Astrofisica de Canarias. We are grateful to the CFHTLS, COSMOS-UltraVISTA, UKIDSS, SXDF and COSMOS survey teams. Without these legacy surveys, this research would have been impossible. We thank the VUDS team for making available spectroscopic redshifts from data obtained with VIMOS at the European Southern Observatory Very Large Telescope, Paranal, Chile, under Large Program 185.A-0791.

This work was only possible by the use of the following PYTHON packages: NumPy & SciPy (Walt et al., 2011; Jones et al., 2001), Matplotlib (Hunter, 2007), and Astropy (Astropy Collaboration et al., 2013).

# APPENDIX

## LY$\alpha$ EMITTERS STACKS

To correct for the possible biases on morphological parameters induced by combining astrometric errors and Ly$\alpha$-UV mismatch (see Sect. 3.3.4) we have computed image stacks using only a subset of galaxies with $i_{\rm AB} < 25$ and compare that to the full sample. Then we compute the corrections to be applied to the measured stack values as the ratio between these two quantities. We show in Fig. 3.13 the values we get for three different morphological quantifiers in the case of the full sample and the $i_{\rm AB} < 25$ sample.

## GENERAL PROPERTIES OF INDIVIDUAL SAMPLES

We show in Fig. 3.15-3.17 the distribution of Ly$\alpha$ luminosities, Ly$\alpha$ equivalent widths and $i_{\rm AB}$ continuum magnitudes for each individual sample present in this chapter. In terms of Ly$\alpha$ luminosity, we see a clear dependence of the minimum detected luminosity with redshift as expected by a constant line flux limit that is imposed by the observations. In terms of Ly$\alpha$ equivalent width all bands probe nearly the same region. We note however that for NB samples we are able to go down to $EW > 25$ Å while for IB samples we have the lower limit at $EW > 50$ Å. Finally, for $i_{\rm AB}$ we find a similar trend as for the Ly$\alpha$ luminosity with fainter galaxies observed at higher redshifts.

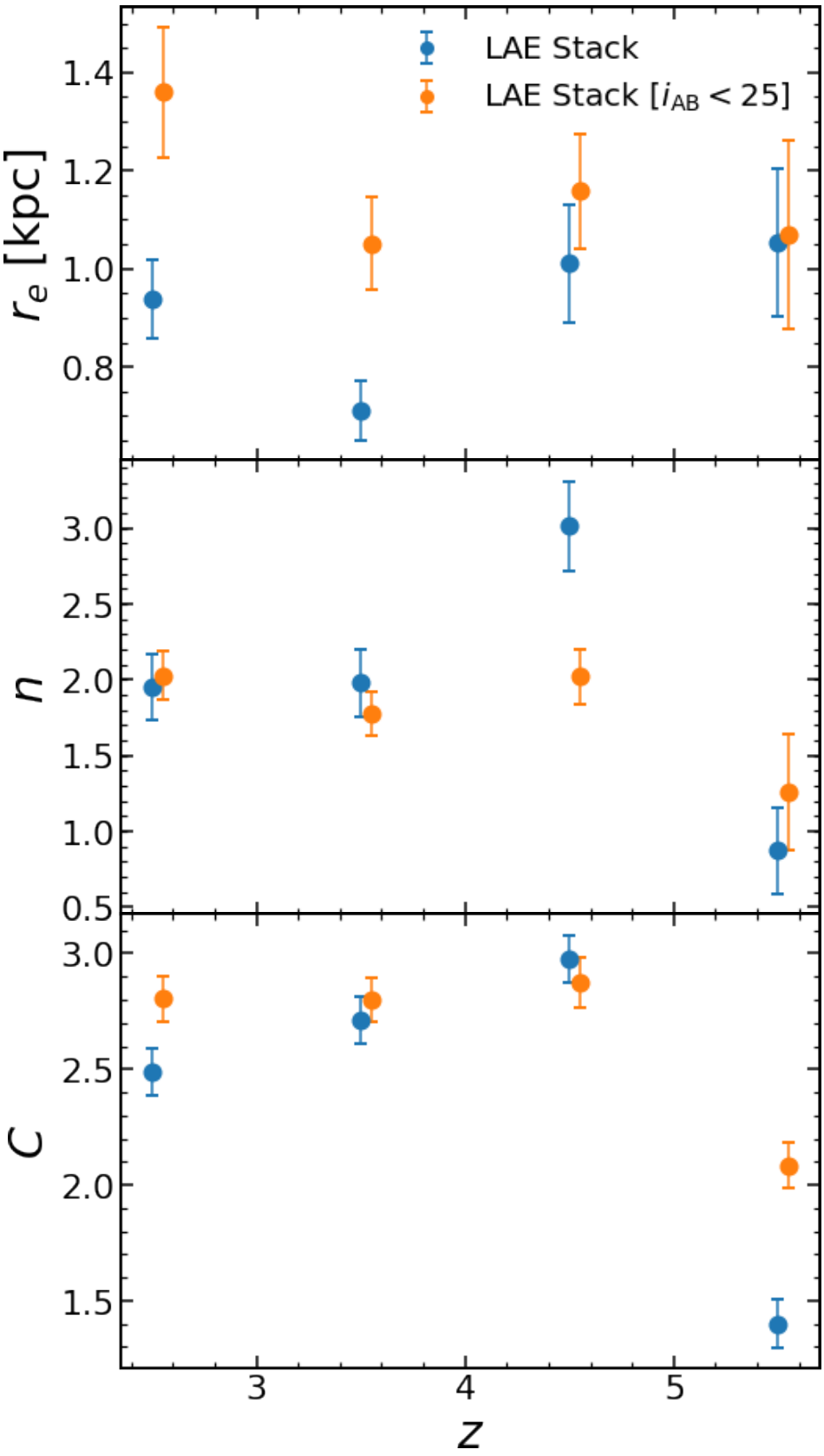


**Figure 3.13** LAE values for different stack samples at $2 \lesssim z \lesssim 6$. From top to bottom we show the derived values for the stack of the full sample (in blue) and the stack of the $i_{AB} < 25$ sample (in orange).

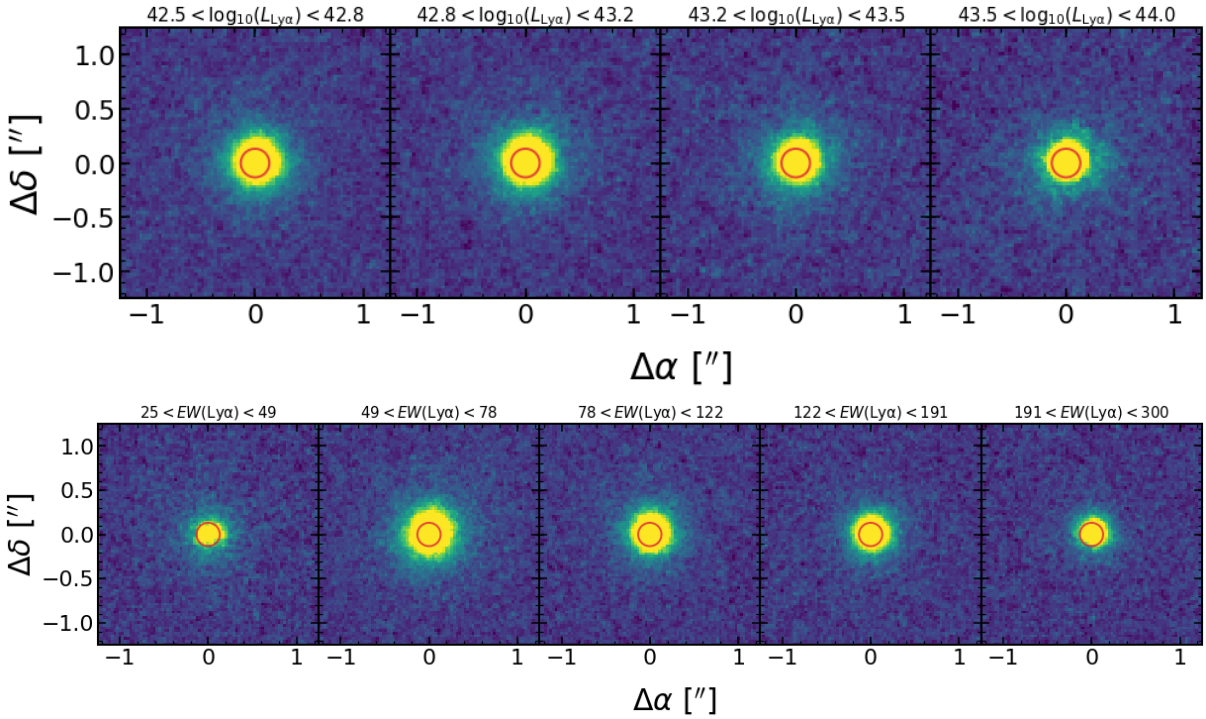


**Figure 3.14** Examples of LAE stacks for each of the bins that we use in this study in terms of Ly$\alpha$ luminosity (top) and Ly$\alpha$ equivalent width (bottom). In each panel, the intensity levels range from -3$\sigma_{sky}$ to 15$\sigma_{sky}$, where $\sigma_{sky}$ is the sky rms. The red circle in each panel has a physical radius of 1 kpc.

## LAE STACKS FOR A MULTI-PARAMETER EXPLORATION

This section contains images showing the resulting stacks for studying independently the redshift, Ly$\alpha$ luminosity and Ly$\alpha$ equivalent width dependence of rest-frame UV LAE morphology (Fig. 3.18-3.20).

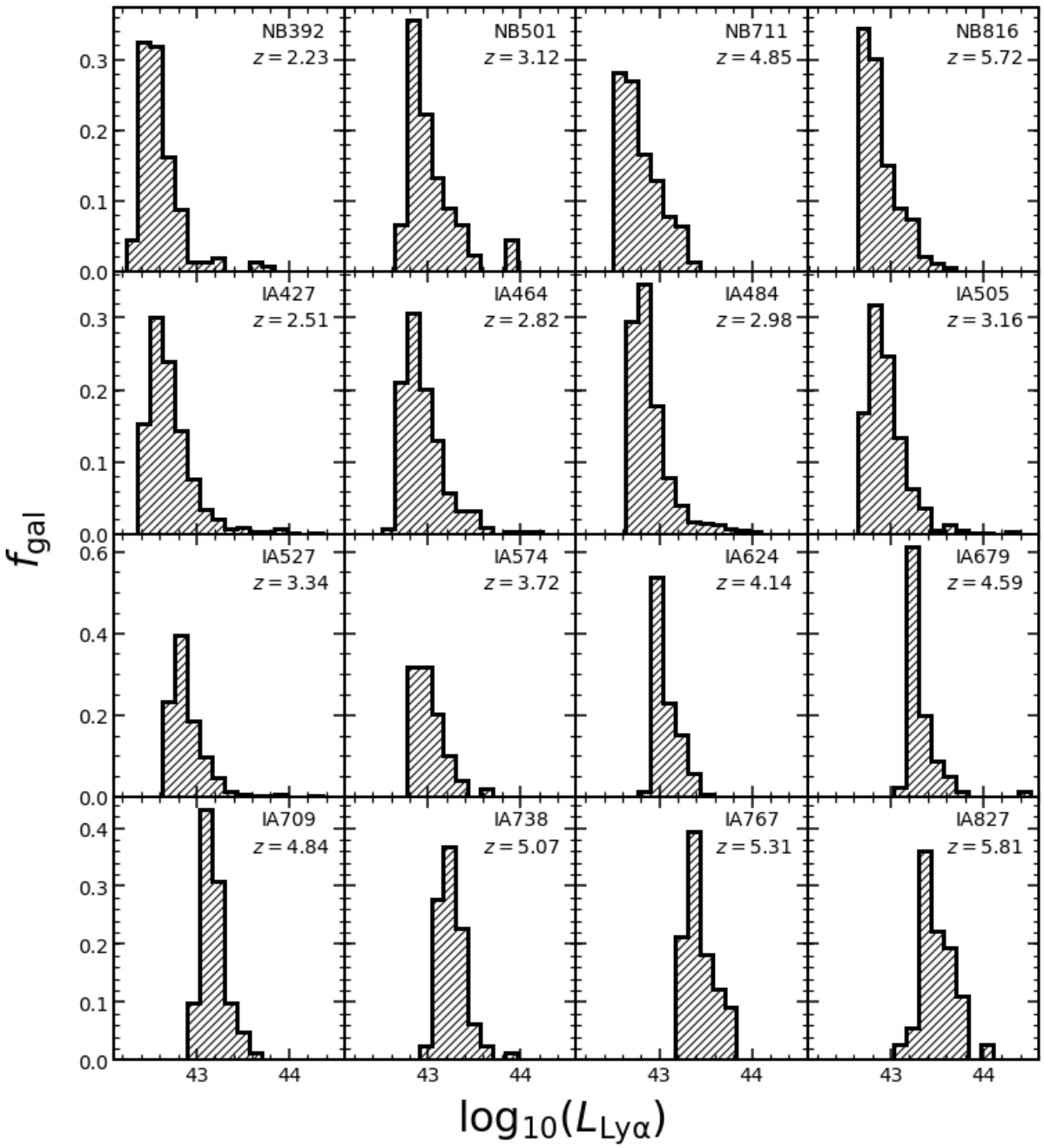


**Figure 3.15** Distribution of Ly$\alpha$ luminosities for all LAE candidates in our samples. NB samples are shown in the top row and IB samples in the other three rows. We find higher Ly$\alpha$ luminosities with increasing redshift and that NB samples probe fainter LAEs when compared to IB samples at similar redshifts.

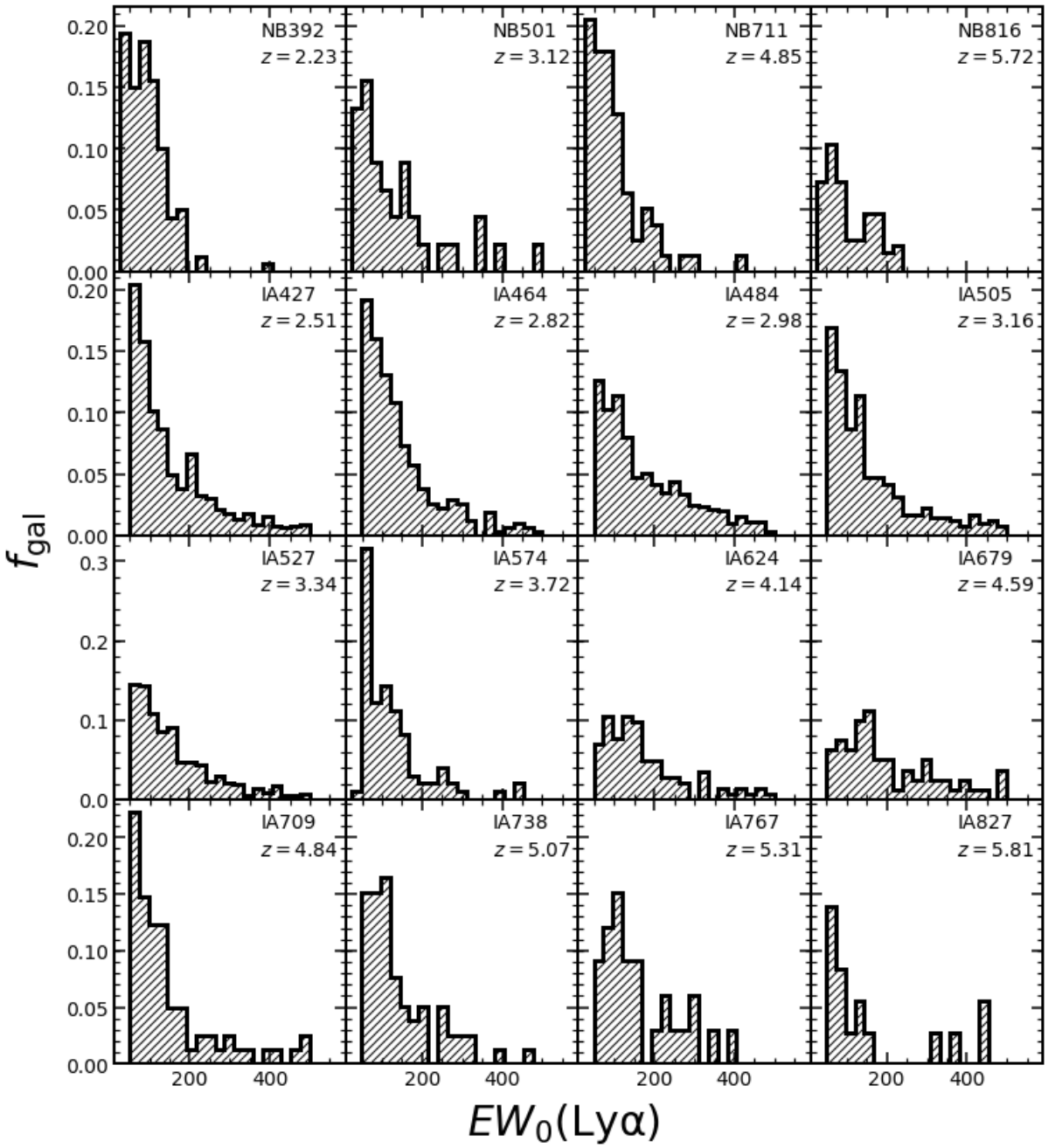


**Figure 3.16** Distribution of Ly$\alpha$ equivalent widths for all LAE candidates in our samples. NB samples are shown in the top row and IB samples in the other three rows. Despite the different line equivalent width cuts for NB and IB samples, we find similar distributions for all bands independent of the redshift.

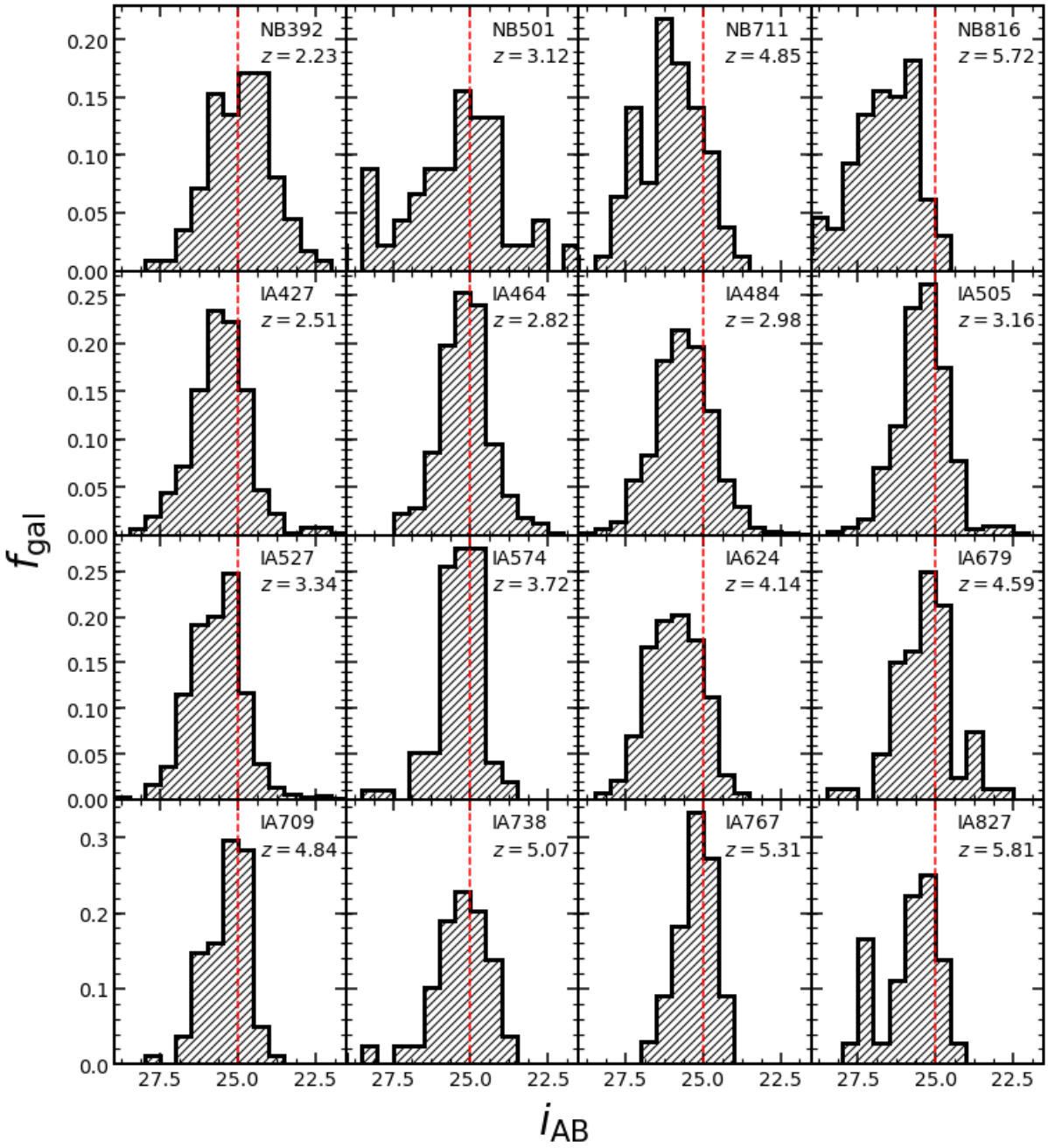


**Figure 3.17** Distribution of $i_{\rm AB}$ for all LAE candidates in our samples. NB samples are shown in the top row and IB samples in the other three rows. The vertical red dashed line highlights the $i_{\rm AB} = 25$ limit that we use in this chapter. There is a large fraction of LAEs fainter than our imposed limit and this is more severe when considering the higher redshift samples.

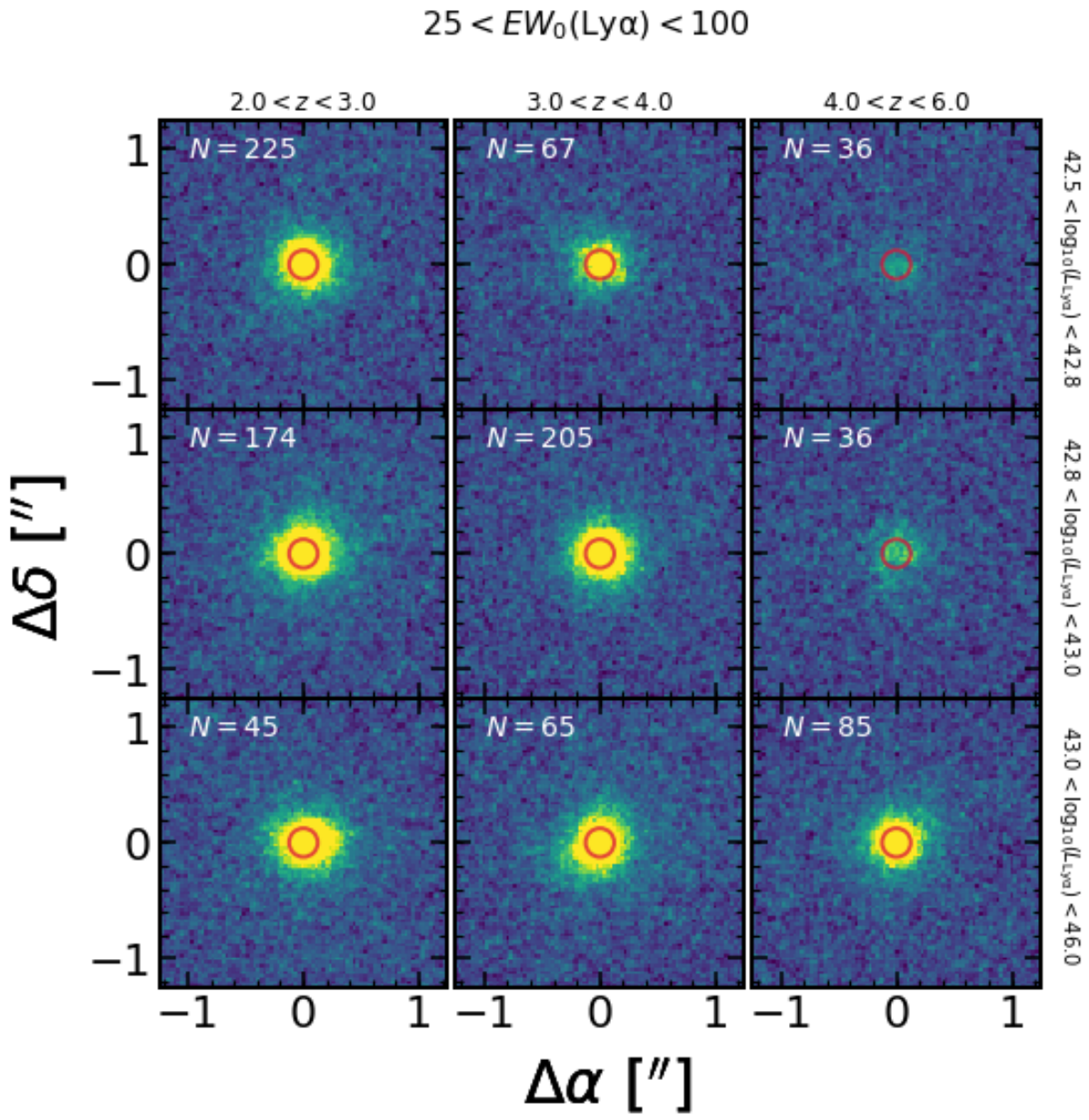


**Figure 3.18** Individual stacks for multi-parameter exploration with $25 < EW_0(\mathrm{Ly}\alpha) < 100$ Å. Each column represents a different redshift bin and each row a different luminosity bin. The red circle has a 1 kpc radius at the median redshift of each bin.

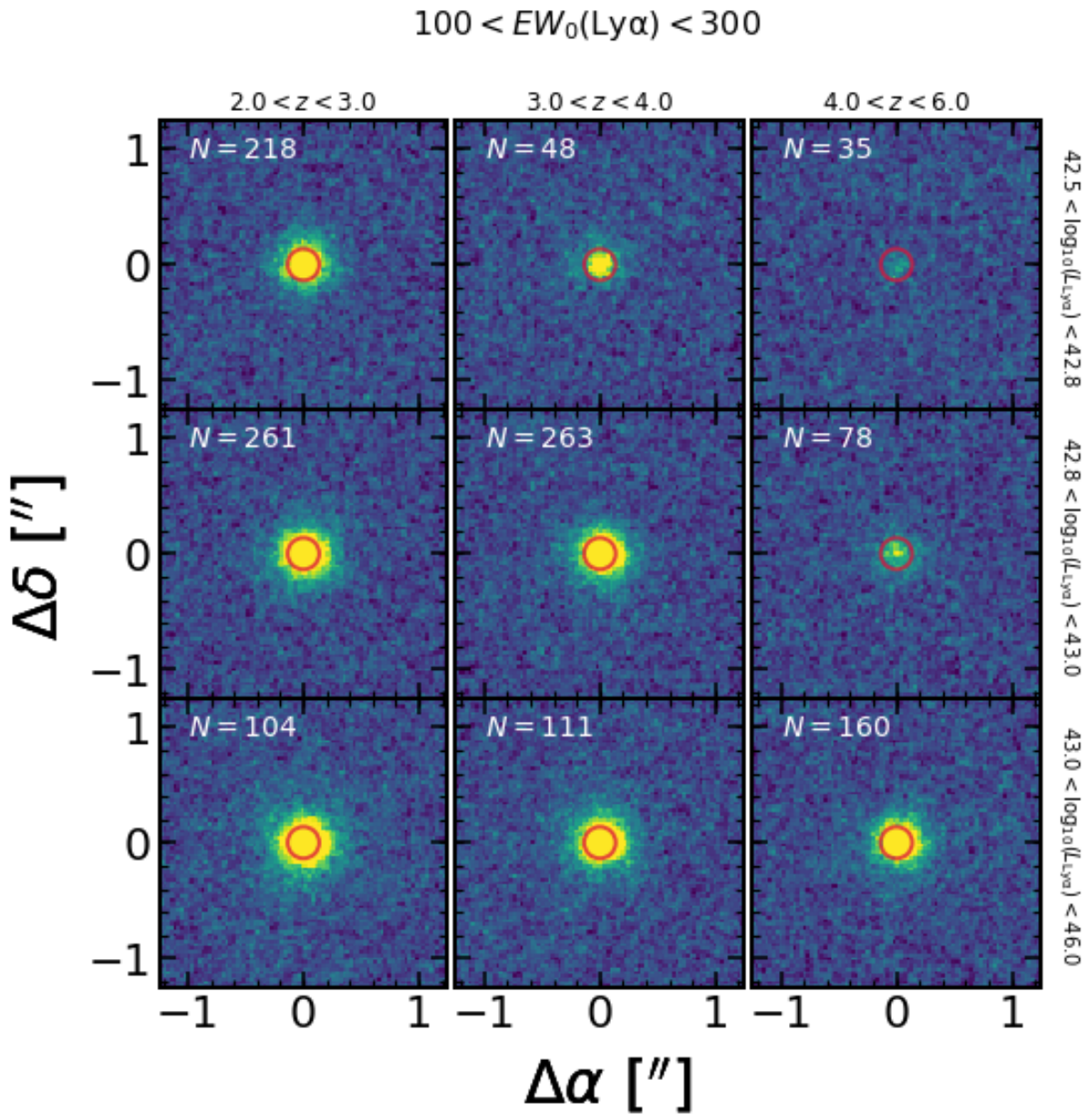


**Figure 3.19** Individual stacks for multi-parameter exploration with $100 < EW_0(\mathrm{Ly}\alpha) < 300$ Å. Each column represents a different redshift bin and each row a different luminosity bin. The red circle has a 1 kpc radius at the median redshift of each bin.

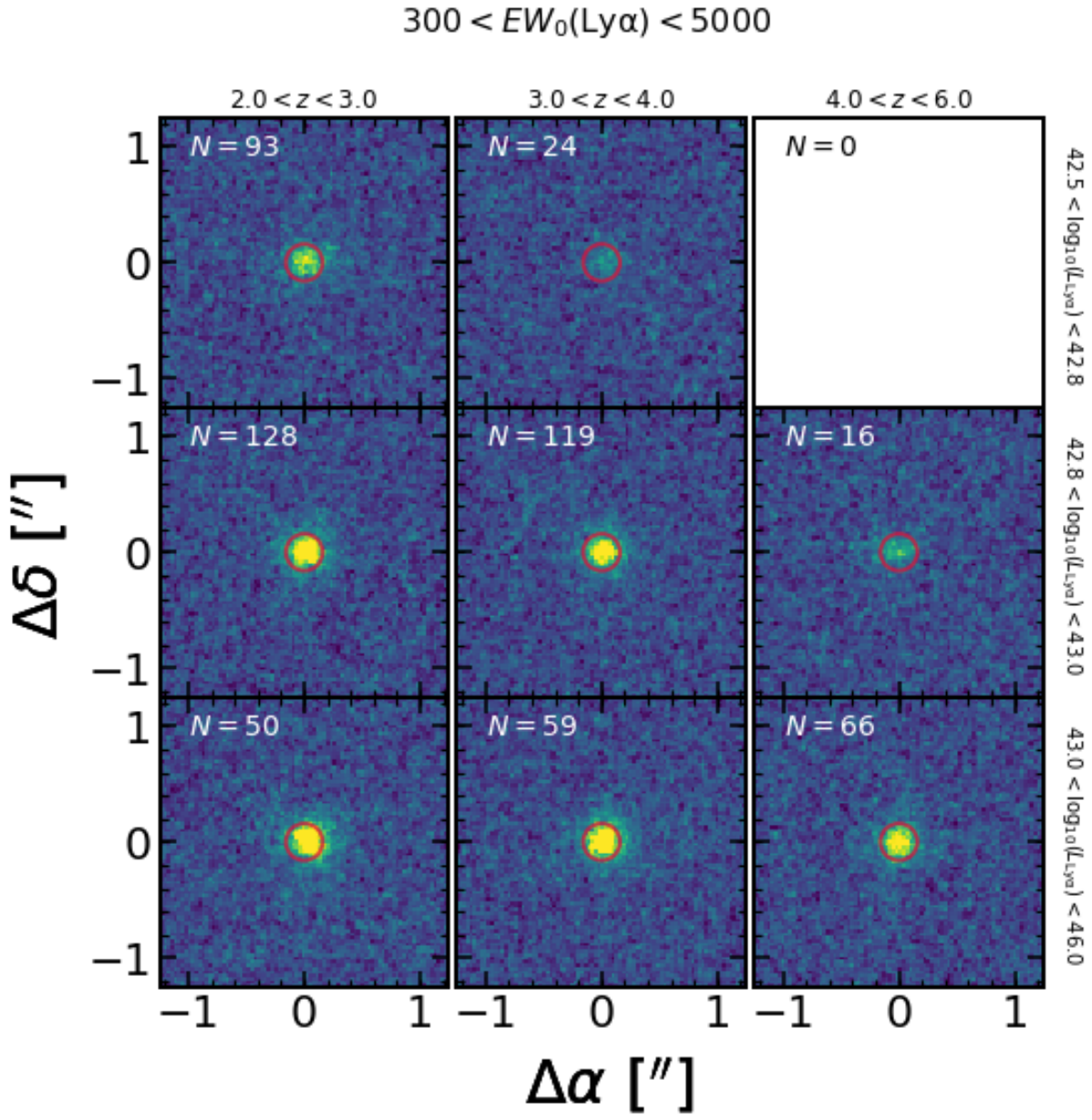


**Figure 3.20** Individual stacks for multi-parameter exploration with $300 < EW_0(\mathrm{Ly}\alpha) < 5000$ Å. Each column represents a different redshift bin and each row a different luminosity bin. The red circle has a 1 kpc radius at the median redshift of each bin. The empty slot in the upper right corner is due to a lack of galaxies in our sample occupying that bin.

This page intentionally contains only this sentence.

# CHAPTER 4

## THE UV SIZES AND CLUMPINESS OF THE BRIGHT LAES IN THE EPOCH OF REIONIZATION

*In this chapter we investigate the rest-frame UV morphology of a sample of the brightest Ly$\alpha$ emitters detected in the epoch of reionization. We use ancillary data and newly obtained images from HST to estimate the sizes and clumpiness of these sources. We find that bright LAEs are similar in size and luminosities to a sample of UV-bright LBGs at similar redshifts. In terms of their clumpiness we estimate that 4(5) out of 6 galaxies have multiple (possible) detected clumps. This fraction is higher than that reported for LBGs and may hint that a clumpy star-formation is required for Ly$\alpha$ to easily escape the galaxy. We further note that the only confirmed non-clumpy galaxy is found at $z < 6$, but larger samples with be required to test a possible transition in the morphology of bright LAEs from during to after the reionization.*

adapted from **Paulino-Afonso**, A., Sobral, D. & Matthee, J., in prep.

## 4.1 INTRODUCTION

To unveil the nature of early galaxy evolution one can use observations of high redshift galaxies. One very successful technique to build large samples of such young galaxies has been identifying them through their Ly$\alpha$ emission (e.g. Rhoads et al., 2000; Ouchi et al., 2008, 2018; Matthee et al., 2016; Sobral et al., 2017, 2018b). On a complementary note, large surveys based on colour selections targeted at the Lyman-break in the spectral energy distribution of galaxies (LBGs, e.g. Steidel et al., 1999; Bouwens et al., 2015; Bowler et al., 2017).

Surveys studying galaxy morphology at $z \gtrsim 6$ are usually restricted to small areas and target the faint galaxy population (sub-$L^*$). These galaxies are found to be compact (sizes below 1 kpc Oesch et al., 2010; Ono et al., 2013; Kawamata et al., 2015; Shibuya et al., 2015; Curtis-Lake et al., 2016) and there are hints of a size-UV luminosity relation in place at these redshifts (Grazian et al., 2012; Huang et al., 2013; Ono et al., 2013; Kawamata et al., 2015; Shibuya et al., 2015). The study of brighter sources selected from larger area ground surveys has hinted that

UV-bright galaxies were larger (confirming the trends of the size-luminosity relation, e.g. Willott et al., 2013; Bowler et al., 2015) which was later confirmed by Bowler et al. (2017) with HST follow-up 25 UV-bright galaxies.

The measurement of galaxy sizes gives an important insight into the growth of galaxies through cosmic time. However, detailed analysis of galaxy morphology provides additional insight into the physical processes at play that shape galaxy evolution. For example, the disturbance in the galaxy shape is usually associated with mergers or tidal interactions in the local Universe (Conselice, 2014, and references therein). However, at higher redshift and due to increase gas content and density in galaxies, clumpy morphologies are naturally produced through gas disk instabilities (e.g. Dekel et al., 2009; Dekel & Krumholz, 2013; Bournaud et al., 2014; Bournaud, 2016). On the observational side, there is a high prevalence of observed clumpy morphologies at $z > 2$ (e.g. Elmegreen et al., 2004; Genzel et al., 2008; Guo et al., 2015; Shibuya et al., 2016; Ribeiro et al., 2017). By $z \sim 6$, there are several reported values with the clumpy fraction varying between $\sim$20% to $\sim$60% (depending on the method, e.g. Shibuya et al., 2016; Ribeiro et al., 2017) and this fraction seems to be higher for the most UV-luminous galaxies when compared to their lower luminosity counterparts (Willott et al., 2013; Jiang et al., 2013; Bowler et al., 2017).

Recently, a number of Ly$\alpha$ bright sources have been found in the epoch of reionization (Ouchi et al., 2009; Sobral et al., 2015a; Matthee et al., 2017b). These sources are potentially galaxies where Ly$\alpha$ can more freely escape the galaxy, with some of them having escape fractions $\gtrsim$ 100% under standard assumptions (Matthee et al., 2017b). This property makes them excellent targets to study the impact of geometry (or galaxy morphology) on the escape of Ly$\alpha$. If one particular morphology distinguished them from other populations (e.g. LBGs, or fainter LAEs), we may gain insights on the preferred geometry to boost Ly$\alpha$ emission from galaxies.

The escape of Ly$\alpha$ photos is a complex process due to the resonance nature and multiple scatterings that they can undergo before reaching the inter-galactic medium (e.g. Zheng et al., 2011; Dijkstra & Kramer, 2012; Lake et al., 2015; Gronke et al., 2017). And the random-walk nature of this process means that the geometry of the inter-stellar medium (ISM) can affect the fraction of escaped Ly$\alpha$ (Verhamme et al., 2012; Duval et al., 2014; Behrens & Braun, 2014; Gronke et al., 2017). Interestingly, there seems to be a correlation between the clumpiness of the ISM and the Ly$\alpha$ properties, with highly clumpy ISM boosting the intensity of Ly$\alpha$ (e.g. Hansen & Oh, 2006; Duval et al., 2014), although Duval et al. (2014) argue that for normal star-forming galaxies the ISM clumpiness is not a determinant factor on the shape of Ly$\alpha$ transmission. However, if the galaxies have an extremely clumpy ISM their observed properties are similar to those explained with simpler shell models assuming an homogeneous ISM (e.g. Gronke et al., 2016, 2017).

In this chapter, we study the UV morphology of 6 bright LAE emitters in the epoch of reionization and link that sample to bright LBGs selected at similar redshifts (Bowler et al., 2017) and to the

general population of LAEs found at later epochs (studied in Chap. 3). This chapter is organized as follows. In Sect. 4.2 we present the imaging data we use. In Sect. 4.3 we describe the methodology to measure galaxy sizes and detect clumps in galaxies. In Sect. 4.4 we highlight the main results of the chapter and summarize our findings in Sect 4.5.

Magnitudes are given in the AB system (Oke & Gunn, 1983). All the results assume a Λ-CDM cosmological model with $H_0$ =70.0 km s$^{-1}$Mpc$^{-1}$, $\Omega_m$ =0.3 and $\Omega_\Lambda$ =0.7.

## 4.2 DATA

This chapter collects a number of previously identified bright Ly$\alpha$ emitters at $z \sim 6-7$. This includes HIMIKO (Ouchi et al., 2009), CR7 and MASOSA (Sobral et al., 2015a), and SR6 and VR7 (Matthee et al., 2017b). We complement previous samples with new HST WFC3 NIR data that allows us to probe the rest-frame NUV morphology of these sources for the first time and gain insights into the geometry of Ly$\alpha$ escape from these strong emitters.

We have collected publicly available HST data for HIMIKO (Ouchi, 2010) and CR7 (two sets of observations Fan, 2016; Forster Schreiber, 2011) from the MAST archive. For the other three sources we have obtained F098M/F140W (for SR6) and F110W/F160W (for MASOSA and VR7) data in a recently approved HST programme (Sobral, 2016). We stacked all available images in the reddest filter available using improved astrometric solutions computed with SCAMP (Bertin, 2006) using the SDSS DR9 catalogue (Ahn et al., 2012) as reference. We then co-added and re-sampled all images to a 0.06″/pixel scale with SWARP (Bertin et al., 2002). An overview of the imaging used for the analysis in this chapter is shown in Fig. 4.2.

## 4.3 MORPHOLOGY MEASUREMENTS

We measure galaxy sizes for this sample of bright LAEs using the parametric method described in Chap. 3. For this specific analysis we did run GALFIT a total of 500 times for each galaxy, varying the initial parameters for the effective radius and Sérsic index from a uniform distribution around the expected value from initial guesses. We then take the median value as the reported size measurement and use the 16th and 84th percentiles of the distribution for an estimate of the error. To account for the broadening of the profile by the PSF, for each galaxy a PSF was built from stacks of 2-6 stars in the same field of view of each source.

To estimate the clumpiness of our sources we use a special segmentation algorithm that we wrote for this purpose. The idea is to select individual groups of pixels (hereafter referred as clumps)

associated with a single local maximum. The algorithm works as follows. For each image, we build a detection image which is composed of a summation of several regular segmentation maps. This step is effectively creating an image based on detection thresholds and removes pixel-to-pixel variations from a galaxy image, as it is composed by a series of discrete maps. These maps are then used to identify local maxima (see Fig. 4.1). Once we have the list of local maxima within the global detection map of a galaxy, we run a watershed segmentation algorithm using those peaks as starting guesses (e.g. Soille & Ansoult, 1990). This produces a list of clumps within the larger galaxy. To remove noisy or low S/N detections we impose a minimum detection area for each clump to be of 20 pixels. We show all detected clumps in a 1.5″ radius around each source on Fig. 4.2. One additional size estimate that is computed as a natural product of this algorithm is the total area corresponding to the galaxy. This size corresponds to the area of all galaxy associated pixels (see e.g. Law et al., 2007; Ribeiro et al., 2016). We can then use a circularized size quantity defined as $r_T = \sqrt{T/\pi}$, where $T$ is the total area of the galaxy in kpc$^2$.

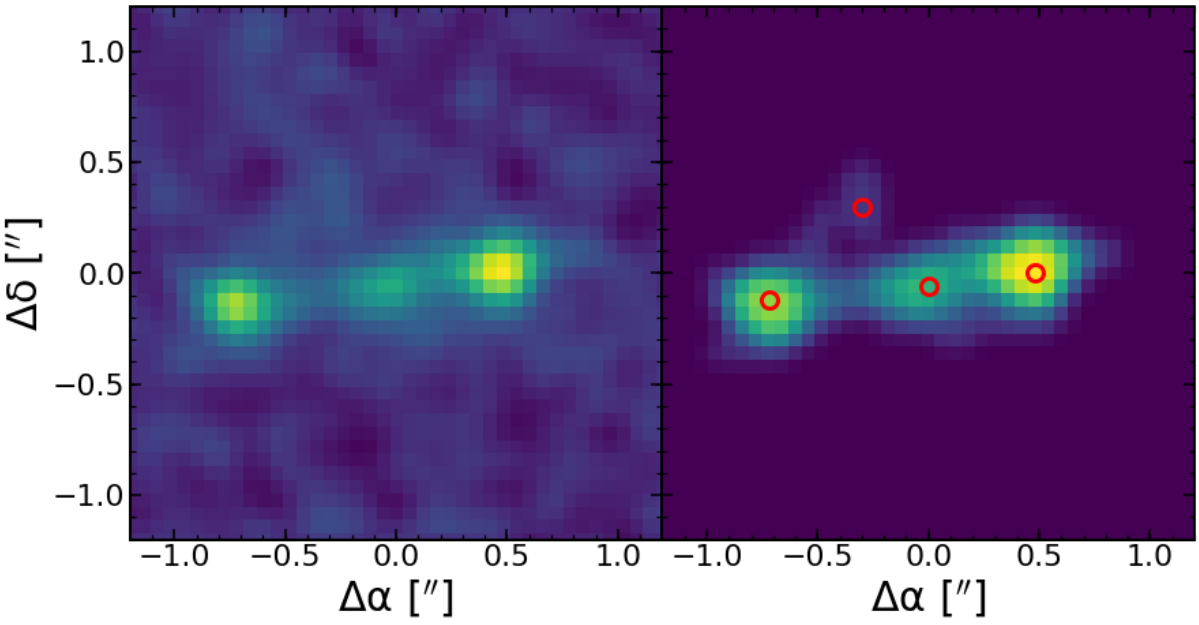


**Figure 4.1** Example of the peak finding algorithm. On the left we have the original image, in this case the F160W image of HIMIKO. On the right I show the detection image which is used to compute local maxima, highlighted by the red circles.

## 4.4 Results

In this chapter we highlight the results on morphological measurements for the sample of bright LAEs with available HST imaging and compare those to lower redshift normal LAE population and a LBG-selected sample at similar redshifts (Bowler et al., 2017). The size measurements for each source are reported in Table 4.1.

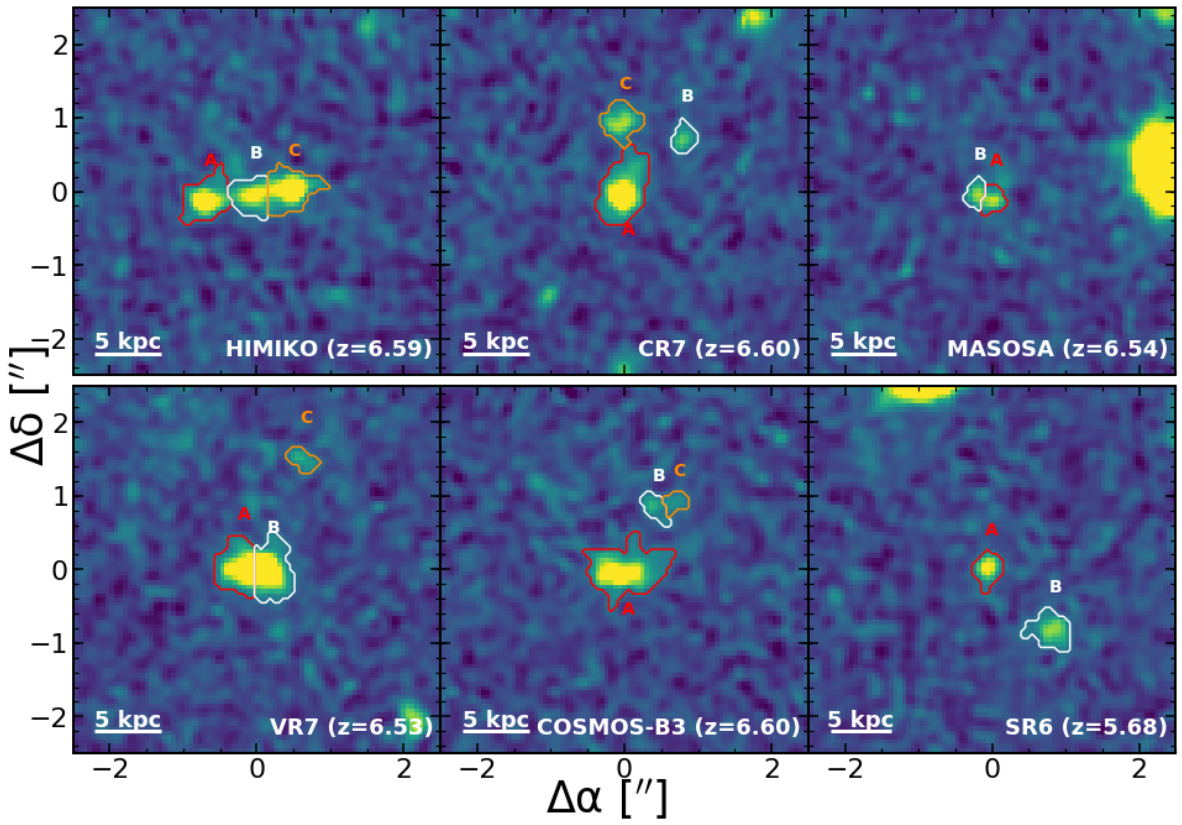


**Figure 4.2** HST rest-frame NUV images of 6 bright LAEs in our sample. In each panel, we highlight in different coloured contours the detected clumps in and around each source. In these image, North is up and East is left.

**Table 4.1** UV and Ly$\alpha$ properties are those reported in the literature: CR7, MASOSA (Sobral et al., 2015a; Matthee et al., 2017b); SR6, VR7 (Matthee et al., 2017b); COLA1 (Matthee et al., 2018); HIMIKO (Ouchi et al., 2009). Size measurements in the last two columns are those derived with GALFIT and from the total extent, respectively.

| Name | RA [deg] | DEC [deg] | z | $M_{\rm UV}$ | $EW_{{\rm Ly}\alpha}$ [Å] | $L_{{\rm Ly}\alpha}$ [$10^{43}$erg s$^{-1}$] | $r_e$ [kpc] | $r_T$ [kpc] |
|---|---|---|---|---|---|---|---|---|
| SR6 | 334.957337 | 0.806639 | 5.68 | $-21.1\pm0.1$ | $802.0\pm155.0$ | $2.5\pm0.3$ | $0.3^{+0.02}_{-0.04}$ | 1.48 |
| CR7 | 150.241708 | 1.804333 | 6.60 | $-22.2\pm0.2$ | $211.0\pm20.0$ | $8.5\pm0.3$ | $0.7^{+0.01}_{-0.01}$ | 2.91 |
| MASOSA | 150.353333 | 2.529261 | 6.54 | $-21.2\pm0.4$ | $206.0\pm0.0$ | $2.4\pm0.3$ | $1.0^{+0.09}_{-0.09}$ | 1.82 |
| COSMOS-B3 | 149.958542 | 1.828533 | 6.60[a] | $-99.0\pm-99.0$ | $210.0\pm0.0$ | $1.9\pm0.3$ | $1.5^{+0.02}_{-0.02}$ | 2.97 |
| VR7 | 334.734833 | 0.135367 | 6.53 | $-22.5\pm0.1$ | $207.0\pm10.0$ | $2.4\pm0.2$ | $1.5^{+0.01}_{-0.01}$ | 2.89 |
| HIMIKO | 34.489845 | -5.145688 | 6.59 | $-22.1\pm0.3$ | $65.0\pm0.0$ | $4.3\pm0.0$ | $4.1^{+0.06}_{-0.04}$ | 3.21 |

[a]Spectroscopic confirmation still required

In Fig. 4.3 (right panel) we compare the size-UV luminosity relation for bright LAEs and bright LBGs at similar redshifts. We find that both samples seem to follow the same relation and are thus indistinguishable in terms of their UV sizes and luminosities. This similarity is in agreement with the expected extrapolation for the lower redshift samples studied in Chap. 3, as LAEs at redshifts greater than 5 are expected to be of comparable sizes to samples based on UV. We also find that bright LAEs at $z\sim6-7$ are on average larger than the lower redshift samples studied in Chap. 3. This seems to be a natural consequence of the size-luminosity relation for LAEs, since the lower redshift samples are derived from wide-field surveys with a much larger population of UV-faint LAEs.

On a technical note regarding size measurements we would like to assess the observed differences regarding the different methods used here and in Bowler et al. (2017). On a first note, by definition the effective radius is smaller than the total extent, as one measures the size containing 50% of the total light while the other is an attempt to estimate the full extent of the galaxy. Secondly, when we are measuring sizes using a single Sérsic profile for galaxies that are markedly clumpy (see Fig. 4.2) one of two things usually happen. In the case of CR7, the size estimate from GALFIT is based on the fit to only clump A, since it is the dominant clump in terms of flux for the entire galaxy and GALFIT tends fit that first when using only a single profile. This alone can explain also the large difference seen when comparing the size derived from GALFIT and the total extent measured for the galaxy (including the three clumps). For the case of HIMIKO, with connected clumps of similar brightness, GALFIT tends to artificially increase the estimated size to encompass the extent of the galaxy while not being able to properly estimate inner part of the profile due to the clumpy nature of the image. In this case, the derived size can be larger than what one estimates from the area associated with the galaxy. For galaxies with marginally distinct clumps (such as VR7 and MASOSA), usually the size estimates are less affected. In the case of SR6, there is only one single clump (clump B is a lower redshift interloper, see Matthee et al., 2017b) and as such the size estimate should be the most robust.

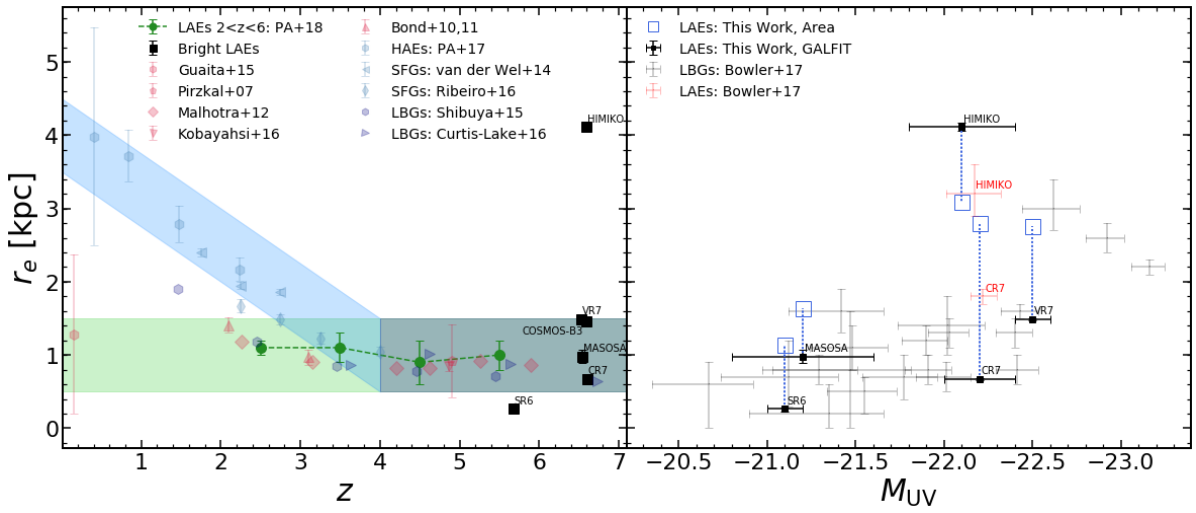


**Figure 4.3** Right: sizes for bright LAEs compared to other samples at lower redshifts. We highlight in blue and green shaded areas the evolution paths of SFGs and LAEs, respectively, above and below $z \sim 4$. Left: size UV-luminosity relation for bright LAEs and LBGs at $z \sim 6-7$.

In Fig. 4.4 we show the dependence of galaxy size on Ly$\alpha$ luminosity and equivalent width. While for the Ly$\alpha$ luminosity relation we find a large scatter in sizes for similar luminosities, with no statistically significant trend, we do seem to confirm a trend for LAE size with Ly$\alpha$ equivalent width. This trend is similar in nature to that found at lower redshift, and also reported by Law et al. (2012), extending it to larger equivalent widths. Considering the galaxies studied in rest-frame NUV, we find a much steeper trend for bright LAEs than what we find in Chap. 3. However, much of this hinges on a single source (HIMIKO), which is far larger than expected from the average of the population.

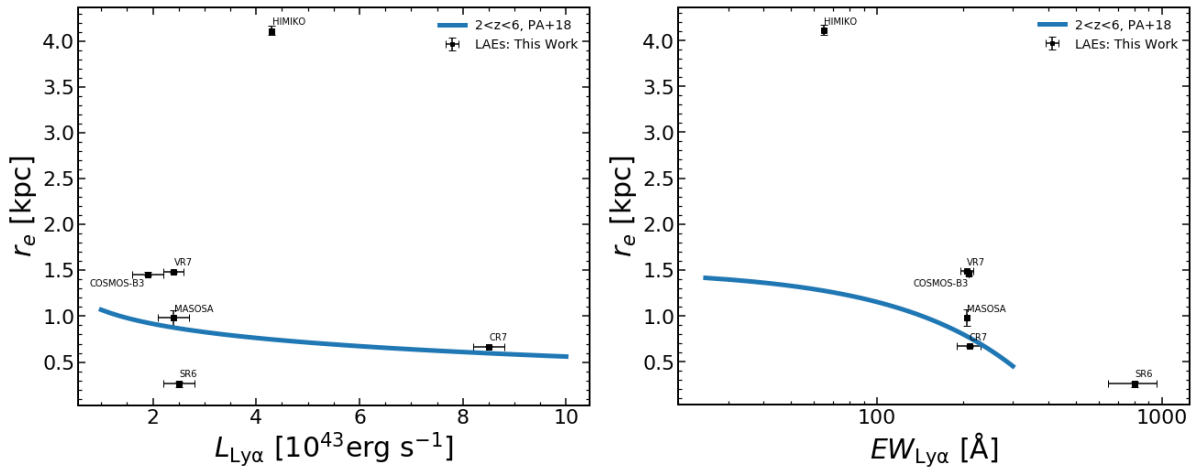


**Figure 4.4** Dependence of size on Ly$\alpha$ equivalent width and luminosity. We show as black symbols the individual measurements of galaxies studied in this chapter. The blue line refers to the relation derived in Sect. 3.4.

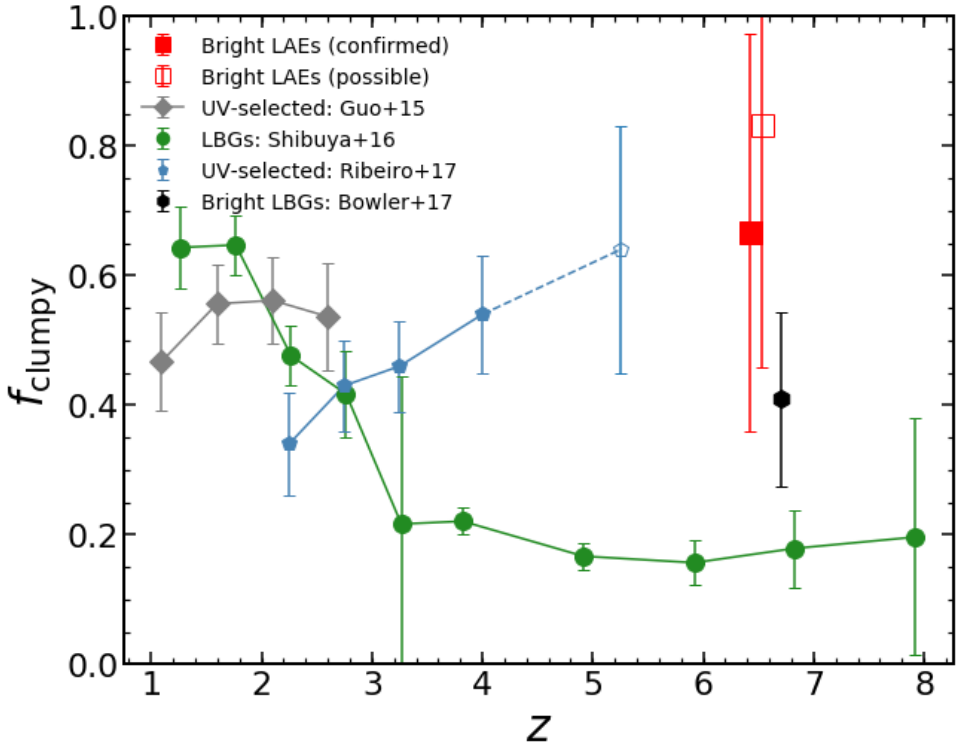


**Figure 4.5** The clumpy fraction of bright LAEs and LBGs (from Bowler et al., 2017) at $z \sim 6-7$. We compare our results with measured clumpy fractions in fainter LBGs by Shibuya et al. (2016) and UV-selected galaxies (Guo et al., 2015; Ribeiro et al., 2017).

Another interesting characteristic of this sample of bright LAEs is that they seem to be dominated by clumpy morphologies. We used the method described in Sect. 4.3 to quantitatively estimate the number of clumps associated with each galaxy. Galaxies HIMIKO and CR7 have been already widely discussed in the literature in terms of their clumpy morphology (Ouchi et al., 2009, 2013; Sobral et al., 2015a; Bowler et al., 2017). For MASOSA, we find that this compact galaxy seems to be composed of two small, connected clumps. VR7 shows an elongated UV morphology with a small degree of asymmetry. This galaxy shows hints of two distinct clumps

marginally detected. In addition, we find a small faint clump $\sim$ 14kpc North-West of the LAE (clump C) which can potentially be linked to VR7, since its Ly$\alpha$ profile extends towards that direction (reaching the edges of clump B, see Matthee et al., 2017b). This can potentially be a galaxy similar to CR7, but a follow-up is required to confirm the association. COSMOS-B3 is also a galaxy similar to CR7 (considering components A+B), with a bright UV component and a fainter clump $\sim$ 5 kpc north-west of it. However, we have on-going observations to spectroscopically confirm this galaxy as a bright LAE and we should be able to pinpoint if those faint clumps are connected to the brighter galaxy. Finally, SR6 is composed of a single clump, with clump B detected at 1.3$''$south-west being a confirmed foreground galaxy (Matthee et al., 2017b).

From this sample of 6 bright LAEs with NUV rest-frame imaging we estimate that between 4/5 sources are clumpy in nature. This translates into a fraction of $67 \pm 30\%$ ($83 \pm 37\%$) for confirmed (possible) clumpy galaxies among bright LAEs. This conservative limit places this fraction slightly above (although within the reported uncertainties) to that reported by Bowler et al. (2017, excluding the 2 LAEs CR7 and HIMIKO). However, if one assumes a more loose criteria, the same required for CR7 to be classified as clumpy given our method, we report an even higher fraction. If this is true, one may confirm the ubiquitous nature of large clumps in bright LAEs which may be linked to the mechanisms of Ly$\alpha$ escape from such bright sources. We further stress that the only bright LAE with no detected clumps is also the only one at $z < 6$. If such trend is confirmed once we collect larger samples of bright Ly$\alpha$ galaxies we might be witnessing a transition in the main mode for Ly$\alpha$ escape during and after the reionization.

When compared to a fainter LBG population studied by Shibuya et al. (2016) we find that bright LAEs are much clumpier. This may be simply a consequence of a dependence of the clumpy fraction on the luminosity of galaxies, as already hinted by the larger fraction of clumpy systems in the UV-bright sample studied by Bowler et al. (2017). Another possible difference might be related to the method used to define a galaxy as clumpy. Shibuya et al. (2016) uses an automated clump finding algorithm which is fundamentally different to the more intuitive, visual-like approach, that we explore in this chapter and also in Bowler et al. (2017). For a detailed discussion of the differences between different methods we refer the reader to the study of Ribeiro et al. (2017).

By assigning a different region to each detected clump (see contours in Fig. 4.2) one can estimate the size (area) and luminosity of each sub-component of the galaxy. We show in Fig. 4.6 the size-luminosity relation for each clump and the global estimate for the entire galaxy for comparison. We find that clumps follow a similar size-luminosity relation as the entire galaxies with some clumps (clump A of CR7, clumps A+B of VR7) being brighter than the smaller galaxies MASOSA and SR6.

In individual terms, we find the HIMIKO as three comparable clumps (in size and luminosity).

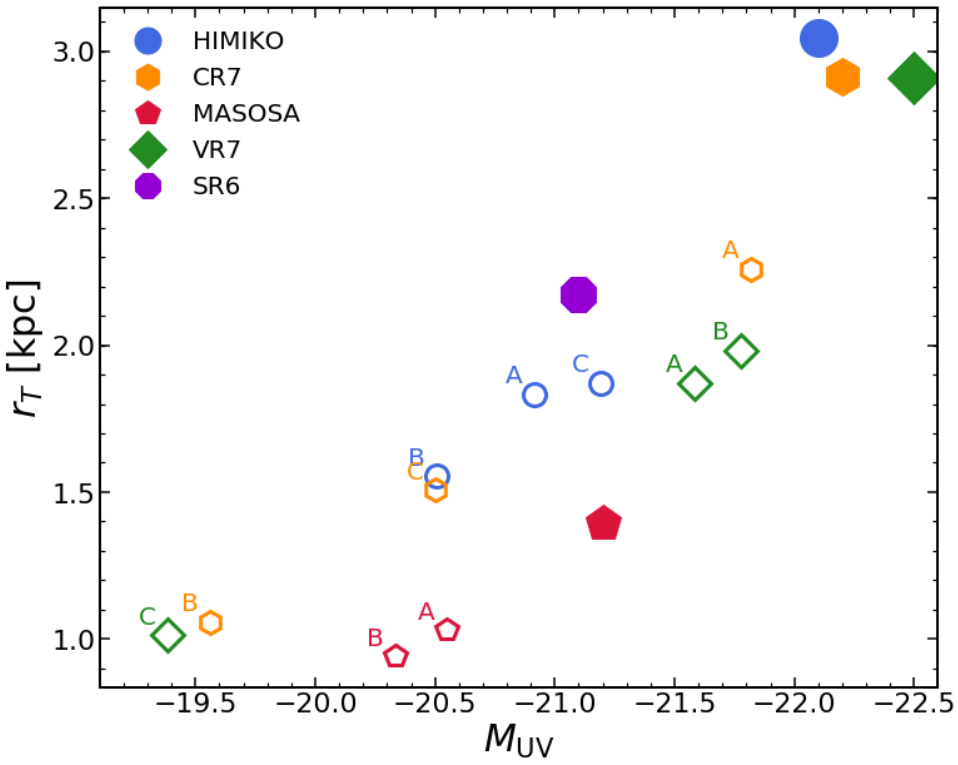


**Figure 4.6** Clump size-magnitude relation for the bright LAEs sample as empty symbols. We show the associated clump identification (as in Fig. 4.2). We also show as comparison the total extent and magnitude of the entire galaxy as filled symbols.

On the other hand, CR7 is largely dominated by the bright clump A (also associated with most of Ly$\alpha$ emission, see Sobral et al., 2015a), with clumps B and C being fainter by $\sim 2.5$ and $\sim 1.5$ magnitudes, respectively. For VR7 and MASOSA we find that the two main detected clumps are also very similar in extent and brightness. The clump C of VR7 (which might or not be connected to the main components) has a similar size and brightness as the faintest clump of CR7, making it possible that it is indeed part of the system.

## 4.5 Summary

After studying the rest-frame NUV morphologies of six bright LAEs in the epoch of reionization, we find that:

- Bright LAEs have typical sizes and luminosities as LBGs for the same redshifts. This links to the results in the previous chapter pointing to LAEs and LBGs having similar sizes at $z \gtrsim 4$.
- We find that UV sizes correlate with Ly$\alpha$ equivalent width and that relation is steeper for the bright LAEs in this sample when compared to the larger population at $2 < z < 6$.

- We find that 4/5 out of the 6 bright LAEs are clumpy (all galaxies at $z > 6$ are potentially clumpy). This high fraction of clumpy galaxies can hint that dynamical interactions or multiple star-forming regions are required to reach such high Ly$\alpha$ luminosities.

The text presented in this chapter is based on a preliminary analysis of 6 bright LAEs. We intend to compliment this study with at least 3 more bright LAE candidates which have public imaging from the CANDELS survey. However, we still do not have spectroscopic measurements of their Ly$\alpha$ profiles and further analysis is required to improve on the statistics.

# CHAPTER 5

## VIS$^3$COS: I. SURVEY OVERVIEW AND THE ROLE OF ENVIRONMENT AND STELLAR MASS ON STAR FORMATION

*We present the VIMOS Spectroscopic Survey of a Supercluster in the COSMOS field (VIS$^3$COS) at $z \sim 0.84$. We use VIMOS high-resolution spectra (GG475 filter) to spectroscopically select 490 galaxies in and around the superstructure and an additional 481 galaxies in the line of sight. We present the redshift distribution, the catalogue to be made public, and the first results on the properties of individual galaxies and stacked spectra ($3500\ \AA < \lambda < 4200\ \AA$ rest-frame). We probe a wide range of densities and environments (from low-density field to clusters and rich groups). We find a decrease in the median star formation rate from low- to high-density environments in all bins of stellar mass and a sharp rise of the quenched fraction (from $\sim 10\%$ to $\sim 40-60\%$) of intermediate-stellar-mass galaxies ($10 < \log_{10}(M_\star/\mathrm{M}_\odot) < 10.75$) from filaments to clusters. The quenched fraction for massive galaxies shows little dependence on environment, being constant at $\sim 30-40\%$. We find a break in the strength of the [OII] emission, with nearly constant line equivalent widths at lower densities ($\sim -11\ \AA$) and then a drop to $\sim -2.5\ \AA$ towards higher densities. The break in the [OII] line strength happens at similar densities ($\log_{10}(1+\delta) \sim 0.0-0.5$) as the observed rise in the quenched fraction. Our results may provide further clues regarding the different environmental processes affecting galaxies with different stellar masses and highlight the advantages of a single dataset in the COSMOS field probing a wide range of stellar masses and environments. We hypothesise that quenching mechanisms are enhanced in high-density regions.*

adapted from **Paulino-Afonso**, A., Sobral, D., Darvish, B., et al. 2018, A& A, in press (arXiv:1805.07371)

## 5.1 INTRODUCTION

In the local Universe, we observe differences in a wide range of galaxy properties (e.g. colours, star formation, morphology) with respect to the environment they reside in (e.g. Oemler, 1974; Dressler, 1980, 1984). Cluster galaxies are typically red and passive, while in low-density environments the population is dominated by blue star-forming galaxies (e.g. Dressler, 1980; Balogh et al., 2004; Kauffmann et al., 2004; Baldry et al., 2006; Bamford et al., 2009). The star

formation rate (SFR) and star-forming fraction ($f_{SF}$) have also been found to correlate strongly with the projected galaxy density (e.g. Lewis et al., 2002; Gómez et al., 2003; Hogg et al., 2004; Best, 2004; Kodama et al., 2004; Peng et al., 2010b; Darvish et al., 2016; Cohen et al., 2017). Observations also imply that the most massive galaxies assembled their stellar mass more quickly and had their bulk of star formation quenched at $z \gtrsim 1$ (e.g. Iovino et al., 2010). While stellar mass and environmental density correlate, it is now possible to disentangle their roles and show that both are relevant for quenching star formation (e.g. Peng et al., 2010b; Sobral et al., 2011; Muzzin et al., 2012; Darvish et al., 2016).

Globally, observations show that the SFR density ($\rho_{SFR}$) peaks at $z \sim 2-3$ and has been declining ever since (e.g. Lilly et al., 1996; Karim et al., 2011; Burgarella et al., 2013; Sobral et al., 2013a; Madau & Dickinson, 2014; Khostovan et al., 2015). However, surprisingly, the decline of $\rho_{SFR}$ with increasing cosmic time is happening in all environments (e.g. Cooper et al., 2008a; Koyama et al., 2013). Recent studies have also shed more light on when the dependency of star-forming galaxies on environment start to become observable (e.g. Scoville et al., 2013; Darvish et al., 2016). However, it is still unclear exactly how the environment affected the evolution of galaxies and how that may have changed across time. In order to properly answer such questions it is mandatory to conduct observational surveys at high redshift (e.g. Tadaki et al., 2012; Koyama et al., 2013; Lemaux et al., 2014; Cucciati et al., 2014; Shimakawa et al., 2018) which can then be used to test theoretical models of galaxy evolution (e.g. Vogelsberger et al., 2014; Genel et al., 2014; Henriques et al., 2015; Schaye et al., 2015; Crain et al., 2015).

There have been a plethora of surveys of clusters and their surroundings at $z \lesssim 1$ (e.g. Treu et al., 2003; Cooper et al., 2008a; Poggianti et al., 2009; Lubin et al., 2009; Cucciati et al., 2010b; Iovino et al., 2010; Li et al., 2011; Muzzin et al., 2012; Mok et al., 2013; Koyama et al., 2013; Lemaux et al., 2014; Cucciati et al., 2014, 2017) with a key focus on the influence of environment on the star formation of galaxies. Emission line surveys of clusters at lower redshifts ($z \sim 0.1-0.5$) targeting either H$\alpha$ (e.g. Balogh et al., 2002; Stroe & Sobral, 2015; Stroe et al., 2017c; Sobral et al., 2016; Rodríguez del Pino et al., 2017) or [OII] (e.g. Nakata et al., 2005) find that star formation is suppressed in cluster environments. This suppression seems to be more effective for early-type galaxies (e.g. Balogh et al., 2002) and to be a slow-acting mechanism that mainly affects the gas component (e.g. Rodríguez del Pino et al., 2017).

By $z \sim 1$, some authors have claimed to have found a flattening, or even a definitive reverse, of the relation between the star formation activity and the projected local density, either studying how the average SFRs of galaxies change with local density (Elbaz et al., 2007) or looking at $f_{SF}$ as a function of density (e.g. Ideue et al., 2009; Tran et al., 2010; Santos et al., 2014). These results would be naturally interpreted as a sign of evolution if other studies (e.g. Patel et al., 2009; Sobral et al., 2011; Muzzin et al., 2012; Santos et al., 2013) had not found an opposite result. The differences found between different clusters may be related to their dynamical state, as merging clusters in the low-redshift Universe can also show reverse trends when compared to

relaxed clusters at similar epochs (e.g. Stroe et al., 2014, 2015, 2017c; Mulroy et al., 2017), but other factors like sample size, active galactic nucleus (AGN) contamination, and environments probed may also play a role (e.g. Darvish et al., 2016). Sobral et al. (2011), probing a wide range of environments and stellar masses, were able to recover and reconcile the previous apparently contradictory results. They attribute the discrepancies to selection effects. If one restricts oneself to similar stellar masses and/or densities, one can find similar trends in different studies. Sobral et al. (2011) also separated the individual roles of mass and environment in galaxy evolution (see also Iovino et al., 2010; Cucciati et al., 2010a; Peng et al., 2010b; Li et al., 2011).

Finding the exact mechanisms of galaxy quenching and their physical agents is still one of the unsolved problems in galaxy evolution. Many internal (e.g. stellar and AGN feedback) and external (e.g. galaxy environment) physical drivers are thought to be linked to the quenching process. One might naively expect a continuous decline in the star formation of galaxies from the field to the dense cores of clusters (e.g. due to a lower amount of available gas or faster gas consumption as galaxies move through denser mediums). However, before galaxies undergo a full quenching process in dense regions, they may experience a temporary enhancement in star formation activity (see e.g. Sobral et al., 2011) which may complicate how observations are interpreted (e.g. ram pressure stripping - Gallazzi et al. 2009; Bekki 2009; Owers et al. 2012; Roediger et al. 2014 - and/or tidal interactions - Mihos & Hernquist 1996; Kewley et al. 2006; Ellison et al. 2008).

When looking in more detail at galaxies in the low to intermediate redshift Universe ($z \lesssim 1$), many properties of star-forming galaxies that are directly or indirectly linked to star formation activity (e.g. SFR, sSFR, emission line equivalent widths and the main sequence of star-forming galaxies) seem to be invariant to their environment (but it is still a debated issue, see e.g. Peng et al., 2010b; Iovino et al., 2010; Wijesinghe et al., 2012; Muzzin et al., 2012; Koyama et al., 2013, 2014; Hayashi et al., 2014; Darvish et al., 2014, 2015a, 2016). Therefore, the main role of the environment seems to be to set the fraction of quiescent/star-forming galaxies (e.g. Peng et al., 2010b; Cucciati et al., 2010a; Sobral et al., 2011; Muzzin et al., 2012; Darvish et al., 2014, 2016) which is likely linked to the reported gas deficit in cluster galaxies (seen in atomic hydrogen, e.g. Giovanelli & Haynes, 1985; Cortese et al., 2010; Serra et al., 2012; Brown et al., 2017). But this is not the picture found when looking at molecular hydrogen which is either independent of environment, or depressed or enhanced in high-density regions dependent on the study (e.g. Boselli et al., 2014; Mok et al., 2016; Koyama et al., 2017). Nevertheless, recent studies are finding that not all characteristics of star-forming galaxies are independent of environment. For example, metallicities have been shown to be a function of environment (e.g. Kulas et al., 2013; Shimakawa et al., 2015b; Sobral et al., 2015b) with studies finding that star-forming galaxies have slightly higher metallicities in high-density environments when compared to lower-density/more typical environments at $z \sim 0.2 - 0.5$ (e.g. Sobral et al., 2015b; Darvish et al., 2015a). Sobral et al. (2015b) study a cluster undergoing a merger and Darvish et al. (2015a) focus on galaxy

filaments, which are both regions of enhanced dynamical activity. Denser environments also seem to boost the dust content of star-forming galaxies (e.g. Koyama et al., 2013; Sobral et al., 2016). The higher dust content seen in high-density regions can be a requirement for galaxies to sustain star formation in such environments, by allowing for dense and compact regions to survive environmental stripping.

Issues related to photometric redshift errors and projection effects can limit our understanding of what is occurring in and around clusters. These issues dilute genuine trends and prohibit us from unveiling the role of the environment in sufficient detail to really test our understanding. Surveys such as EDisCS (e.g. White et al., 2005) have aimed to overcome some of these issues by targeting the densest regions at high redshift with extensive spectroscopic observations. These have made significant progress (Poggianti et al., 2006, 2009; Cucciati et al., 2010a, 2017), but either they target deep and small areas or shallow and wide areas. This limits the study on the role of the larger-scale structure and the densest environments simultaneously. A way to make further progress is to conduct a spectroscopic survey (to avoid projection effects and photometric redshift biases and errors) over a superstructure containing the complete range of environments in a sub-deg$^2$ area at high redshift.

In this Chapter, we present a large spectroscopic follow-up of members of a supercluster in the COSMOS field first detected in X-rays (Finoguenov et al., 2007) and later in H$\alpha$ (see Fig. 5.1, Sobral et al., 2011). We organise this chapter as follows. Section 5.2 discusses the sample and presents the observations with VIMOS/VLT and data reduction. Section 5.3 describes the methods to derive galaxy properties used throughout the chapter. In Sect. 5.4 and Sect. 5.5 we show and discuss the results from both individual and stacked spectral properties. Finally, Sect. 5.6 presents the conclusions. We use AB magnitudes, a Chabrier (Chabrier, 2003) initial mass function (IMF), and assume a $\Lambda$CDM cosmology with $H_0$=70 km s$^{-1}$Mpc$^{-1}$, $\Omega_M$=0.3, and $\Omega_\Lambda$=0.7. The physical scale at the redshift of the superstructure ($z \sim 0.84$) is 7.63 kpc/$''$.

**Table 5.1** Observing log for our observations with VIMOS on the VLT for programmes 086.A-0895, 088.A-0550, and 090.A-0401 (PI: Sobral). The last two columns show the number of targeted objects for each pointing with a spectroscopic redshift and the spectroscopic success rate, respectively.

| Pointing | R.A. (J2000) | Dec. (J2000) | Exp. time (ks) | Dates (2013) | Seeing ($''$) | Sky | Moon | $N_{z_{spec}}$ | % with $z_{spec}$ |
|---|---|---|---|---|---|---|---|---|---|
| COSMOS-SS1 | 10 01 49 | +2 10 00 | 14.4 | Apr 14-16 | 0.9 | Clear | Dark | 133 | 73% |
| COSMOS-SS2 | 10 01 33 | +2 10 00 | 14.4 | Apr 4-5, 8 | 0.8 | Clear | Dark | 116 | 70% |
| COSMOS-SS3 | 10 01 49 | +2 05 30 | 14.4 | Apr 18; May 3-4 | 0.9 | Clear | Dark | 110 | 74% |
| COSMOS-SS4 | 10 01 33 | +2 05 30 | 14.4 | Apr 5, 9, 12 | 0.8 | Clear | Dark | 115 | 71% |
| COSMOS-SS5 | 10 01 49 | +2 00 00 | 14.4 | Apr 15-17 | 0.9 | Clear | Dark | 117 | 71% |
| COSMOS-SS6 | 10 01 33 | +2 00 00 | 14.4 | May 5, 7, 8, 11 | 0.9 | Clear | Dark | 105 | 67% |

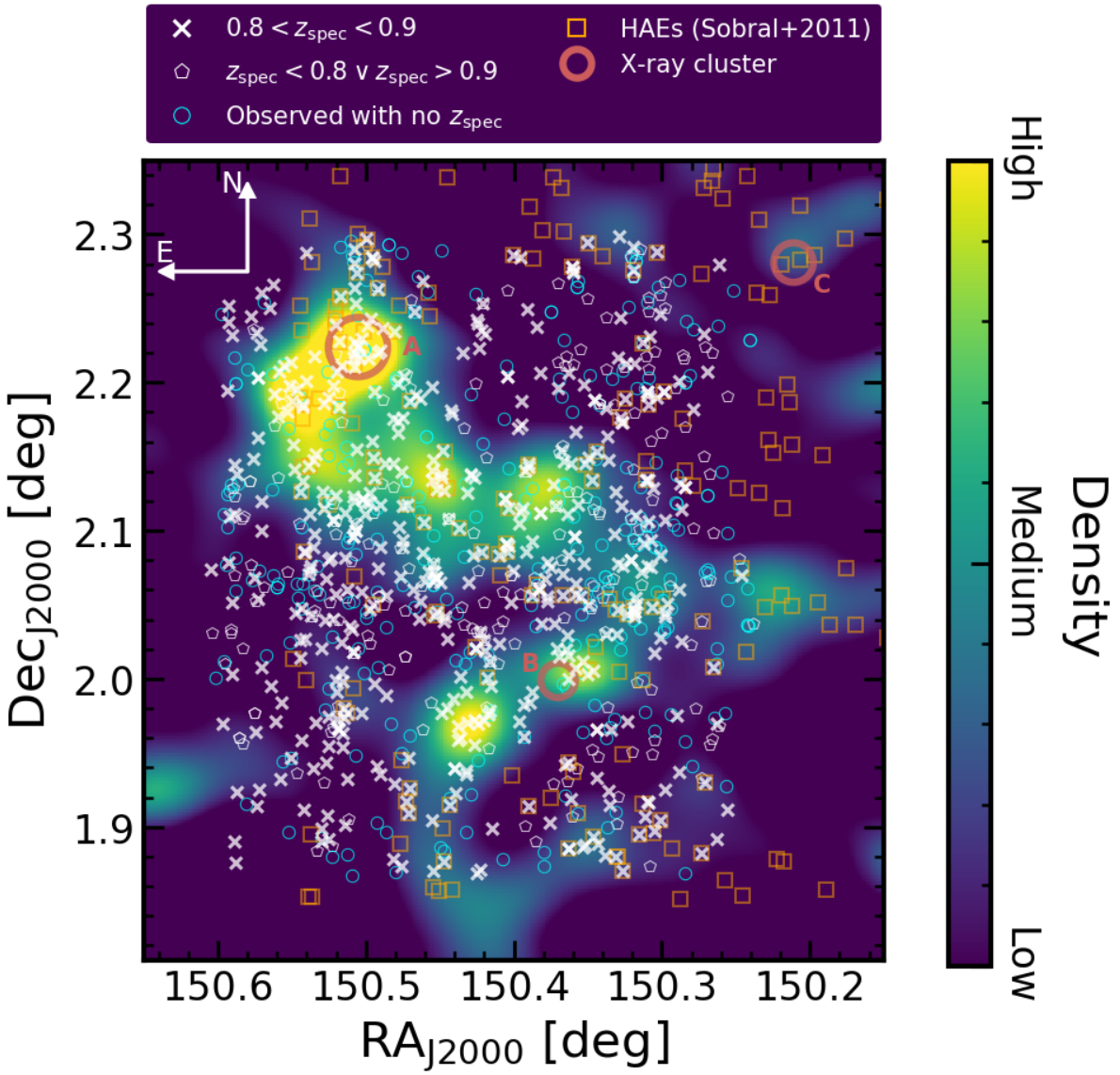


**Figure 5.1** Snapshot of the region targeted by our spectroscopic survey. The colour map encodes the information on the galaxy projected surface density at the redshift slice of interest at $0.8 < z < 0.9$ estimated from the catalogue made public by Darvish et al. (2017). Each thick white cross represents a targeted galaxy with a measured spectroscopic redshift in the same redshift slice. The white pentagons show a targeted galaxy with measured spectroscopic redshift, outside the defined redshift slice. The blue circles show the targeted galaxies for which we have no measured spectroscopic redshift is available. The orange squares show the location of H$\alpha$ emitters studied by Sobral et al. (2011). The large red circles denote the location of X-ray-detected clusters from Finoguenov et al. (2007) at the same redshifts. The size of the circle shows the clusters' estimated X-ray radius $r_{500}$. We see here that we are probing a large range of densities with our survey, in part due to selection effects (e.g. slit placement constraints).

## 5.2 Sample and Observations

### 5.2.1 The COSMOS superstructure at $z \approx 0.84$

By conducting a relatively wide ($\sim 0.8$ square degrees) and deep (down to a flux limit of $8 \times 10^{-17}$erg s$^{-1}$cm$^{-2}$) H$\alpha$ survey at $z = 0.84$ in the COSMOS field, Sobral et al. (2011) found

**Table 5.2** Properties of the clusters in and around the VIMOS target fields (see Fig. 5.1). The cluster coordinates are from the catalogue produced by Finoguenov et al. (2007). The other properties were computed by Balogh et al. (2014). The third column is the median redshift of galaxy members. The fourth column is the intrinsic velocity dispersion. The fifth and sixth columns are the *rms* projected distance of all group members from the centre and corresponding mass of the cluster, respectively.

| Label | R.A. (J2000) | Dec. (J2000) | z | $\sigma_i$ (km/s) | $R_{\rm rms}$ (Mpc) | $M_{\rm rms}$ ($10^{13} M_{\odot}$) |
|---|---|---|---|---|---|---|
| A | 150.505 | 2.224 | 0.84 | $560 \pm 60$ | $0.81 \pm 0.07$ | $17.4 \pm 5.9$ |
| B | 150.370 | 1.999 | 0.83 | $420 \pm 40$ | $0.34 \pm 0.03$ | $4.2 \pm 1.3$ |
| C | 150.211 | 2.281 | 0.88 | $680 \pm 70$ | $0.23 \pm 0.03$ | $7.5 \pm 2.8$ |

a strikingly large over-density of H$\alpha$ emitters within a region that happens to contain three X-ray clusters (first reported in Finoguenov et al. 2007), as shown in Fig. 5.1. Limited spectroscopic observations from zCOSMOS (Lilly et al., 2007) allowed to securely place the most massive cluster in the region at $z = 0.835$, but the full structure seemed to span $z \approx 0.82 - 0.85$ north to south. The H$\alpha$ imaging reveals a strong filamentary structure which seems to be connecting at least three cluster regions, but there are other possible groups/smaller clusters within the region (Sobral et al., 2011). Such structures around a massive cluster are similar to those found in other superstructures at $z \sim 0.5 - 0.8$ (e.g. Sobral et al., 2011; Darvish et al., 2014, 2015a; Iovino et al., 2016). Given the opportunity to study such a range of environments in a single data set, we have designed a spectroscopic survey over this full region.

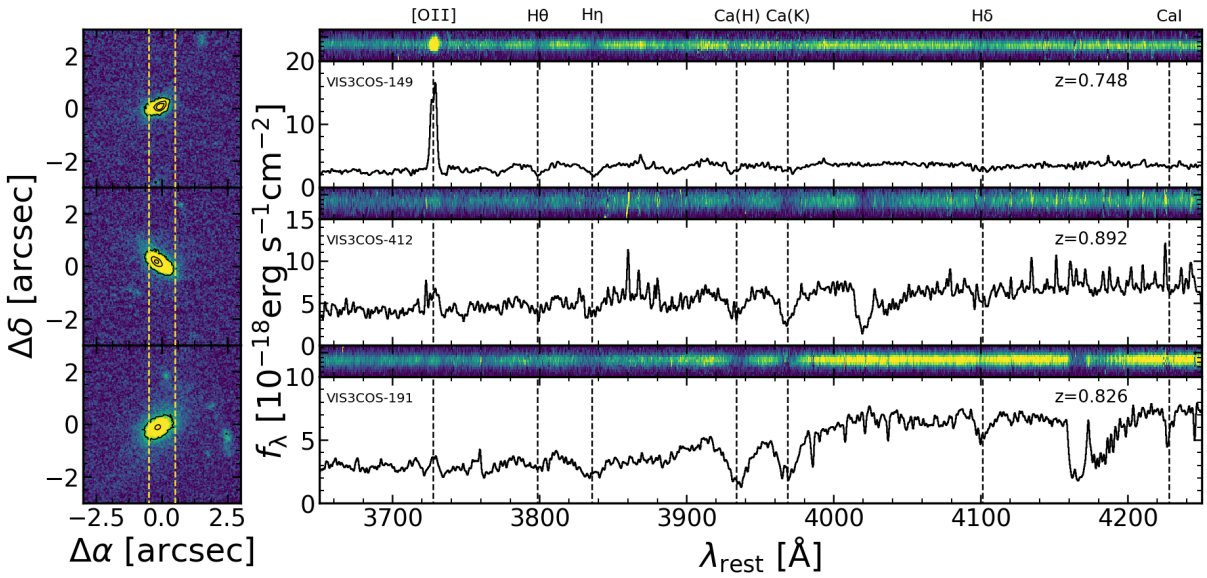


**Figure 5.2** Three individual examples of images and spectra obtained with our survey. Each thumbnail (left panel) shows the HST/ACS F814W image of each target from the COSMOS survey (Koekemoer et al., 2007) with the VIMOS slit overlaid (dashed yellow line). To the right of each stamp we show the corresponding 2D (top) and 1D (bottom) spectrum. We use vertical dashed lines to mark the position of some spectral features present in our spectra.

### 5.2.2 TARGET SELECTION

In order to accurately map the three-dimensional (3D) large-scale structure at $z = 0.84$ and identify the bulk of cluster, group, filament, and field members, we have targeted member candidates (using the VIMOS Mask Preparation Software to maximize the number of targets per mask) down to $I = 22.5$ (corresponding to stellar masses of $\approx 10^{10}\,M_{\odot}$ for older and passive galaxies but much lower for younger galaxies, which have lower M/L ratios - see e.g. Sobral et al. 2011). Our targets are selected by using state-of-the-art photometric redshifts (photo-$z$s) in COSMOS, using up to 30 narrow, medium, and broad bands (c.f. Ilbert et al., 2009). In practice, we use the upper and lower limits of the 99% photo-$z$ confidence interval and select all sources for which such an interval overlaps with $0.8 < z < 0.9$ (including sources best-fit by a quasar/AGN template). We reject all sources that are likely to be stars by excluding those sources for which $\chi^2(\mathrm{star})/\chi^2(\mathrm{galaxy}) < 0.2$ (c.f. Ilbert et al., 2009) or with clear star-like morphologies in high-resolution HST imaging and presenting near-infrared (NIR) vs. optical colours, which clearly classifies them as stars (following e.g. Sobral et al., 2013a).

In order to effectively fill the masks, we introduce galaxies down to $I = 23.0$ and with photo-$z$s of $0.6 < z < 1.1$. We note that we use the 99% photo-$z$ confidence interval instead of the best photo-$z$ to avoid significant bias towards redder and older galaxies (as blue and younger galaxies tend to present the largest scatter in the photometric vs. spectroscopic redshift comparison). We also note that this selection recovers all our blue and star-forming H$\alpha$ emitters (Sobral et al., 2009, 2011). We can therefore fully map the supercluster without major selection biases. In total, out of our entire parent sample of 1015 primary targets and 2257 secondary targets, we have placed 531 ($\sim$55% of the parent primary) slits on primary targets and 440 ($\sim$19% of the parent secondary) on secondary targets. Due to the six pointings targeting the same area, we are not substantially biased against targets in higher densities (see also Sect. 5.6). Observations are described in Sect. 5.2.3. We discuss our sample completeness in terms of spectroscopic success and relative to our parent sample in Appendix and apply corrections whenever completeness effects might bias our results (see example in Sect. 5.4.2).

### 5.2.3 OBSERVATIONS

We have targeted the COSMOS superstructure identified in Sobral et al. (2011) and studied photometrically in Darvish et al. (2014), for example. We have used the High-Resolution Red grism (HR-Red) with VIMOS (Le Fèvre et al., 2003) and the GG475 filter[1]. Our observations are summarised in Table 5.2 and probe the rest-frame $3400-4600$ Å for our main targets (at $z \sim 0.8$) with an observed 0.6 Å pix$^{-1}$ spatial scale, which at $z \sim 0.8$ is $\sim 0.33$ Å pix$^{-1}$ rest-frame. This

[1]This is the same mode used by LEGA-C, see van der Wel et al. (2016) for more details.

allows for a clear separation of the spectral features and very accurate redshift determinations. Spectra cover a key spectral range at $z \approx 0.84$, from [OII] $\lambda$3726,$\lambda$3729 (partially resolving the doublet, as our resolution is $\sim 1$ Å for $z \sim 0.8$ sources) through 4000 Å (allowing us to measure D4000, see Fig. 5.2) to beyond H$\delta$ at high resolution (allowing us to measure many other absorption lines and obtain their widths).

The observations cover a contiguous over-dense region of $21' \times 31'$ ($9.6 \times 14.1$ Mpc, see Fig. 5.1) using 6 VIMOS pointings (chosen to overlap in order to assure both a contiguous coverage and a good target coverage and completeness, particularly for sources located in the densest regions). We have used the VIMOS $1''$ width slit with an average of $9''$ slit length. Our setup allowed us to offset different observing blocks by $\pm 1.3''$ along the slit to guarantee an optimal sky subtraction. Observations were conducted in service mode in April and May 2013 (see Table 5.1) under clear conditions, a new moon and an average seeing of $0.9''$ (ranging from $0.6''$ to $0.95''$). Our pointings, labelled COSMOS-SS1 through COSMOS-SS6, have a total exposure of 4 hours each. Arcs and flats were taken each night. See Table 5.1 for further details.

### 5.2.4 DATA REDUCTION

Data reduction was done using the VIMOS ESO pipeline, version 6.10, through gasgano[2]. The reduction is performed quadrant by quadrant (VIMOS has 4 different quadrants, labelled Q1 to Q4). First, a master bias per night of observations is created by median combining bias frames per quadrant. Appropriate recipes are run in order to create master flats and master arcs for wavelength calibration. The pipeline is used to flag and mask hot pixels and cosmic rays and also to distort correct the observations. We obtain a sky subtracted spectra by estimating the median sky emission in several apertures away from each extracted source. Finally, two-dimensional (2D) spectra are obtained by combining spectra obtained over different observing blocks. The extraction of the one-dimensional (1D) spectra is conducted by collapsing the spectra in wavelength and then extracting along the trace's FWHM. We obtain our 2D and 1D spectra with a relative flux calibration. We are able to extract 1D spectra for 971 sources, with varying levels of signal-to-noise ratio (S/N). See Fig. 5.2 for examples of individual 1D and 2D spectra.

### 5.2.5 FLUX CALIBRATION

Due to the wealth of available well-calibrated photometry for all our sources, we use broad- and medium-band data from COSMOS to test and then scale the flux calibration of our spectra. This allows us to obtain more accurate flux calibrations and to slit correct more appropriately than

[2]http://www.eso.org/sci/software/gasgano.html

using a single standard star for each quadrant. This also allows us to correct for any misalignment in the slit position relative to each source.

Briefly, we use the *I*-band-selected photometric catalogue presented by Ilbert et al. (2009) and start by using the *I*-band magnitudes. We convert *I*-band magnitudes into flux densities for each of our targets and compare those with the integral of the spectra convolved with the *I*-band filter. We then scale each spectra by the appropriate flux normalisation such that the integral within the *I*-band filter equals the flux density derived from photometry. We note that it also allows us to obtain a relatively good slit correction and therefore we do not apply any further slit corrections for our data. For galaxies which are too faint in the *I*-band, we use the median flux calibration for the pointing and quadrant it was observed in. This flux calibration is done under the assumption that galaxies have a homogeneous colour over their extent.

As a further check, we also use the COSMOS medium-band flux densities (see e.g. Ilbert et al., 2009) and check that our flux calibration is valid for the full range of available medium bands. We find very good agreement at all wavelengths within $\pm 10-15\%$ which we interpret as our uncertainty in the flux calibration.

### 5.2.6 Redshift measurements

We use the 1D spectra to measure accurate redshifts using SpecPro (Masters & Capak, 2011) and identify the bulk of the superstructure members. Most redshifts are derived from a combination of H+K absorption and other dominant absorption features such as the G-band for passive galaxies, while for star-forming galaxies we can detect [OII] $\lambda$3726,$\lambda$3729, in addition to absorption features. For a fraction of galaxies, we detect other lines such as H$\delta$ (in either absorption or emission). Redshifts are obtained by visually inspecting all spectra one by one and by searching the features mentioned above. We obtain secure redshifts for 696 sources with high S/N. The redshift distribution for the galaxies in our sample is shown in Fig. 5.3.

### 5.2.7 Final sample

Our final sample is restricted to $0.8 < z < 0.9$ to match our primary selection (see Sect. 5.2.2) and has a total of 490 galaxies spanning a large diversity of environments across several megaparsec that contain three X-ray confirmed galaxy clusters. We are releasing the final catalogue with this chapter and we show in Table 5.3 the first ten entries.

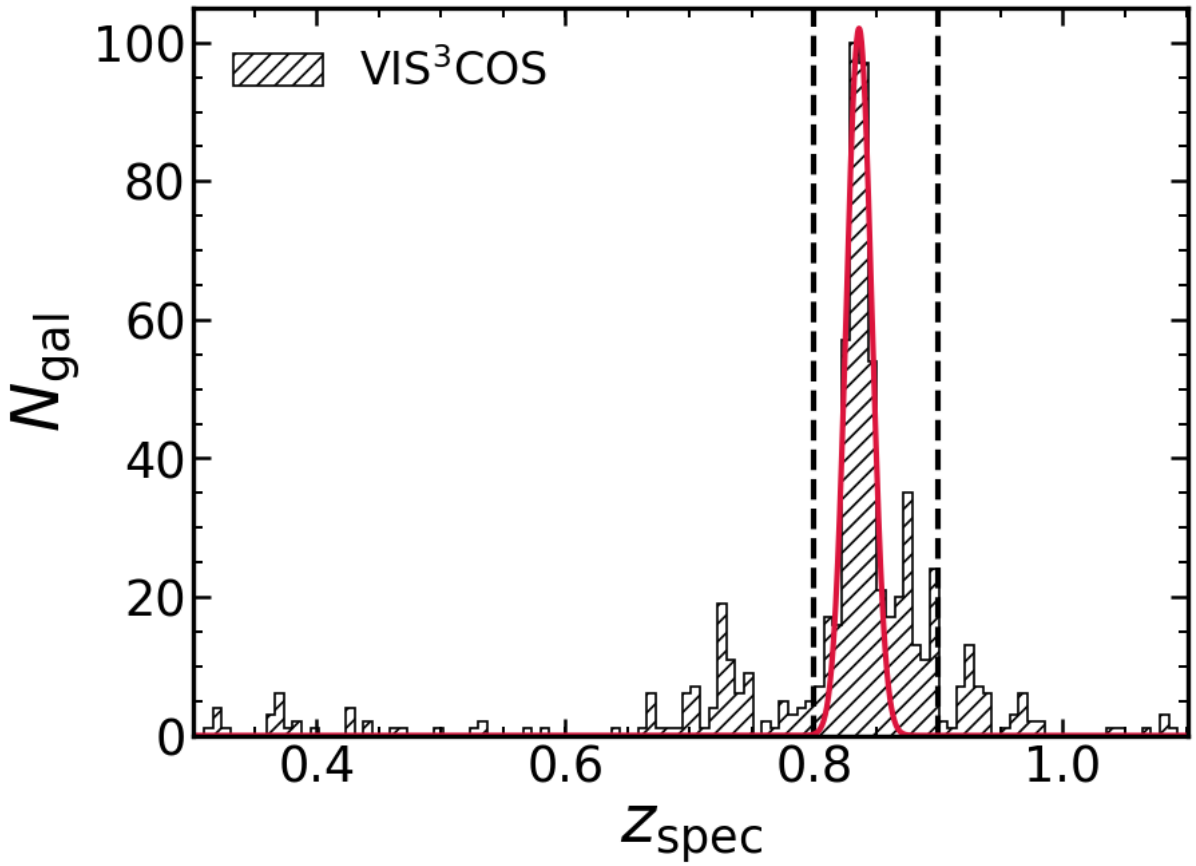


**Figure 5.3** Spectroscopic redshift distribution of the galaxies targeted in our sample as a black histogram. The vertical black dashed lines delimit the redshift selection of the results presented in this chapter. The red line shows our Gaussian fit to the distribution without using rejection algorithms, pinpointing $z = 0.836 \pm 0.008$ as the core redshift of the densest structure we find. The peak at slightly higher redshift ($z \sim 0.88$) is likely produced by members from the north-western cluster C (see Table 5.2 and Fig. 5.1).

## 5.3 Determination of galaxy properties

### 5.3.1 Measurement of [OII] $\lambda$3726,$\lambda$3729 line

To obtain flux measurements of emission lines from our spectra, we interactively iterate through the entire dataset and zoom to a window of 100 Å around [OII] $\lambda$3726,$\lambda$3729. We define two regions of $\sim$ 15 Å (one blue-ward, one red-ward of the line) from which we estimate the median continuum level. Then the local continuum is defined as a straight line that goes through those points. To fit the doublet we use a combination of two Gaussian models through the functional form:

$$f(\lambda) = A_1 \exp\left[-\frac{(\lambda-\lambda_1)^2}{2\sigma^2}\right] + A_2 \exp\left[-\frac{(\lambda-\lambda_2)^2}{2\sigma^2}\right], \tag{5.1}$$

with three free parameters: $A_1$,$A_2$, and $\sigma$. The parameters $A_1$ and $A_2$ are the amplitudes of each

component, and $\sigma$ is the width of each Gaussian component. The centre of each component is fixed at $\lambda_1 = 3726.08 \pm 0.3$Å and $\lambda_2 = 3728.88 \pm 0.3$Å (we allow for a small shift in the line centre that is of the size of the resolution element of the spectra). To estimate the line properties, we use the information on the error spectra and perturb each flux at all wavelengths considered for the fitting by drawing a random number on the observed value and with a width that is equal to its error. We run this exercise 10 000 times and then estimate the errors on the line fit by taking the 16th and 84th percentile of the distribution in each free parameter.

From now on, we only use individual measurements if the S/N is $> 3$. We note that in Sect. 5.3.4 we obtain and measure stacks as a function of environment, allowing us to obtain the median properties of spectral lines for specific subsets of galaxies irrespective of their individual detection. This of course leads to a much higher S/N. We measure the line properties of the stacks with the same procedure described here for individual sources.

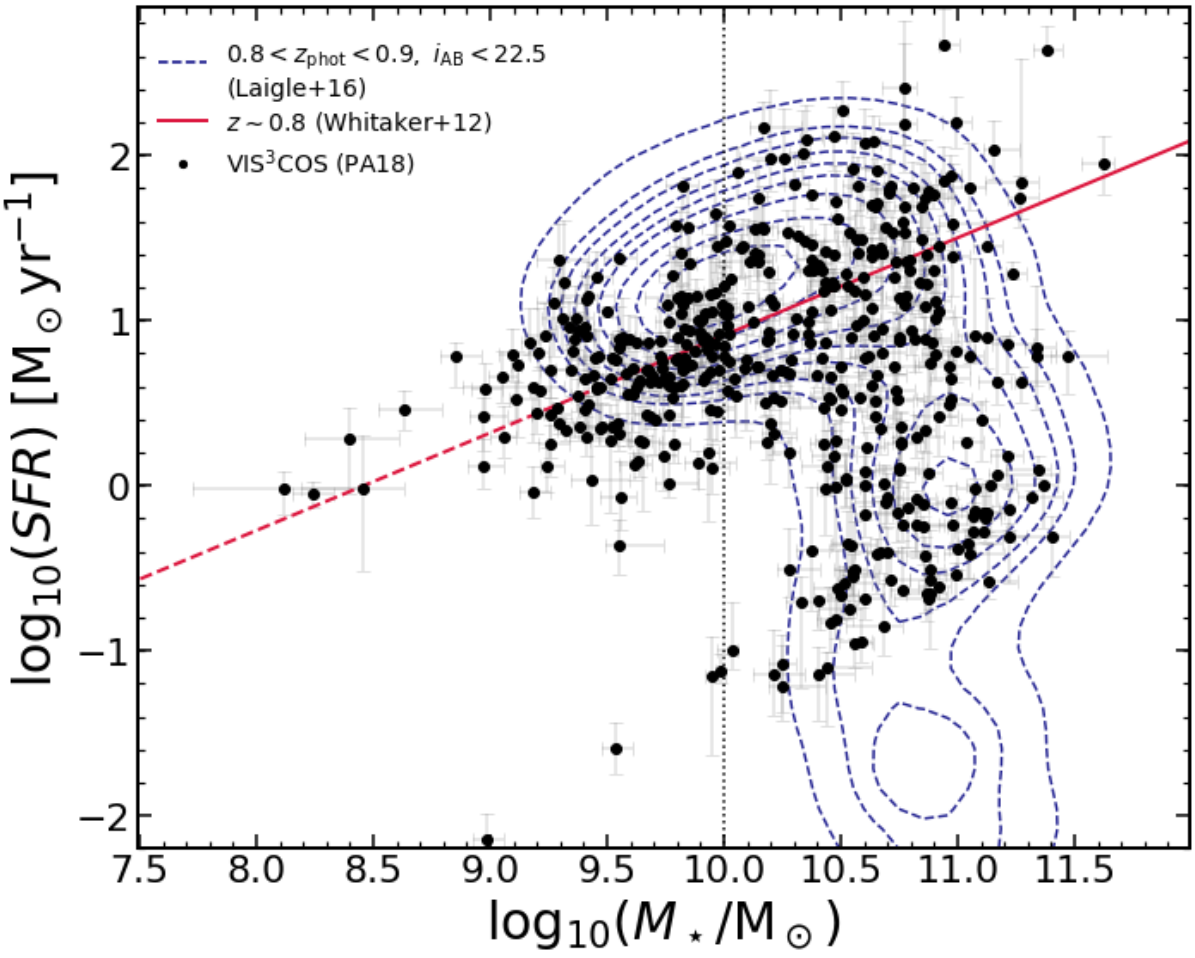


**Figure 5.4** Stellar masses and SFRs derived from SED fitting (see Sect. 5.3.2) in our spectroscopic sample at $0.8 < z < 0.9$. For comparison, we show the derived best-fit relation for star-forming galaxies computed at $z = 0.84$ using the equation derived by Whitaker et al. (2012) over a large average volume in the COSMOS field. The vertical dotted line shows the completeness limit of our survey. The dotted contours show the COSMOS2015 (Laigle et al., 2016) distribution of galaxies with $0.8 < z_{phot} < 0.9$ and $i_{AB} < 23$ from 10% to 95% of the sample in 5% steps. Empty circles highlight the photometric quiescent sample with $\log_{10}(sSFR) < -11$.

### 5.3.2 STELLAR MASSES AND STAR FORMATION RATES

To estimate the stellar masses and SFRs for the galaxies in our sample, we have performed our own SED fitting using MAGPHYS (da Cunha et al., 2008) and our knowledge of the spectroscopic redshift to better constrain the range of possible models. The models were constructed from the stellar libraries by Bruzual & Charlot (2003) using photometric bands from near-ultraviolet (NUV) to NIR (Galex NUV, Subaru uBVriz, UltraVISTA YJHK$_s$, SPLASH-IRAC 3.6$\mu$m,4.5$\mu$m,5.8$\mu$m,8$\mu$m) taken from the COSMOS2015 photometric catalogue (Laigle et al., 2016) and the dust absorption model by Charlot & Fall (2000). We found COSMOS2015 matches for 466 out of the 490 galaxies that are in our selected redshift range $0.8 < z < 0.9$ for which we obtained the physical parameters that we use throughout the chapter (stellar mass and SFRs). If not found in the COSMOS2015 catalogue, we do not obtain any estimate for stellar mass and SFRs through SED-fitting, which happens only for 3% of the sample. These missing sources are serendipitous objects which are faint in the $I$-band and below our completeness limit. We compare our results on stellar mass and SFRs with those provided in the COSMOS2015 catalogue and find a dispersion of $\sim 0.3$ dex for the stellar mass and $\sim 0.7$ dex for the SFRs.

In Fig. 6.1, we present the stellar masses and SFRs in our sample and show that we are probing galaxies with $\log_{10}(M_\star/\mathrm{M}_\odot) \gtrsim 9$ in a wide range of SFRs ($-2 \lesssim \log_{10}(SFR) \lesssim 2$). We see that our sample includes normal star-forming galaxies as well as galaxies that are found well below the SFR MS (see e.g. Noeske et al., 2007; Elbaz et al., 2007; Whitaker et al., 2012), which are characteristic of galaxies in the process of star formation quenching or of those just quenched (e.g. Fumagalli et al., 2014). To select quiescent galaxies within our sample, we impose a specific SFR cut at $\log_{10}(sSFR) < -11$ (see e.g. Ilbert et al., 2010; Carollo et al., 2013) and find a total of 64 galaxies in these conditions.

We also obtain from MAGPHYS the effective optical depth of the dust in the $V$-band, $\tau_V$, which we translate into an average reddening value of $E(B-V) = 1.086\tau_V/R_V$ (assuming $R_V = 3.1$, see e.g. Draine, 2004). We find that our galaxies have an average reddening value of $E(B-V) \sim 0.27 \pm 0.02$. We report here that above $\log_{10}(M_\star/\mathrm{M}_\odot) \gtrsim 10$ there is little dependence of the median extinction with stellar mass with a reddening value of $E(B-V) \sim 0.32 \pm 0.02$ ($\sim 0.37 \pm 0.02$ if we consider star-forming only).

We measure the [OII] line flux by integrating over the best fit model described by Eq. 5.1, which can be solved analytically as $F = \sigma\sqrt{2\pi}(A_1 + A_2)$. We correct the measured [OII] luminosity by the SED extinction value. The corrected luminosity is given by

$$L_{[\mathrm{OII}],\mathrm{corr}} = L_{[\mathrm{OII}]}/e^{-\tau_{[\mathrm{OII}]}}, \tag{5.2}$$

where $\tau_{[\mathrm{OII}]}$ is the optical depth at $\lambda = 3727$Å derived using the dust model used in MAGPHYS (Charlot & Fall, 2000). The effect of extinction on the luminosity of [OII] is displayed in Fig. 5.5

and it can account for the difference that we find when comparing SED and [OII] SFRs using the calibration derived by Kewley et al. (2004) and applying a conversion factor between Salpeter (1955) and Chabrier (2003) IMFs:

$$SFR = \frac{6.58 \times 10^{-42}}{1.7} L_{[\mathrm{OII}],\mathrm{corr}}. \tag{5.3}$$

We find a spread of 0.64 dex, but on average the derived SFRs are consistent with each other (median difference of 0.07 dex. We also show the SFR as derived from H$\alpha$ luminosity (Kennicutt, 1998) from the HiZELS survey, which was used to first pinpoint the existence of this structure (Sobral et al., 2011).

We stress however that [OII] emission can originate from other sources not related to star formation (e.g. AGN, LINERs) and that it is a poor tracer of SFR for red galaxies (e.g. Yan et al., 2006; Kocevski et al., 2011). This tracer is also dependent on the metallicity of the galaxy (Kewley et al., 2004). Those are the reasons for our choice to do our analysis in terms of star formation in galaxies using the quantity derived from SED fitting instead of relying on [OII] emission as a tracer of SFR.

### 5.3.3 Overdensities estimation

The estimate of local over-density was computed as described by Darvish et al. (2015b, 2017) and is based on the photometric redshift catalogue of the COSMOS survey presented by Ilbert et al. (2013, see also Muzzin et al. 2013; Laigle et al. 2016). The density field was computed over an area of $\sim 1.8\,\mathrm{deg}^2$ using a mass-complete sample with accurate photometric redshifts spanning $0.1 < z_{\mathrm{phot}} < 1.2$. The surface density field was computed in 2D slices of redshift of widths $\pm 1.5\sigma_{\Delta z/(1+z)}$ (as suggested by Malavasi et al., 2016). To properly account for the uncertainty on the photometric redshift estimate, the full photo-$z$ PDF of each galaxy is taken into account. Then, at each redshift slice, we select all galaxies which fall in that slice and assigned it a weight corresponding to the percentage of the photo-$z$ PDF contained in that slice. We use all galaxies which have weights greater than 10% in the corresponding slice. The surface density assigned to each point in the density field is (based on adaptive kernel smoothing):

$$\Sigma_i = \frac{1}{\sum_{i=1,}^{N} w_i} \sum_{i=1,}^{N} w_i K(\vec{r}, \vec{r}_i, h_i), \tag{5.4}$$

where $\vec{r}$ is a location in the density field, $\vec{r}_i$ is the position of each galaxy, $w_i$ is the weight assigned to each galaxy, $h_i$ is the kernel width at the position of each galaxy, and $K$ is a 2D Gaussian kernel function.

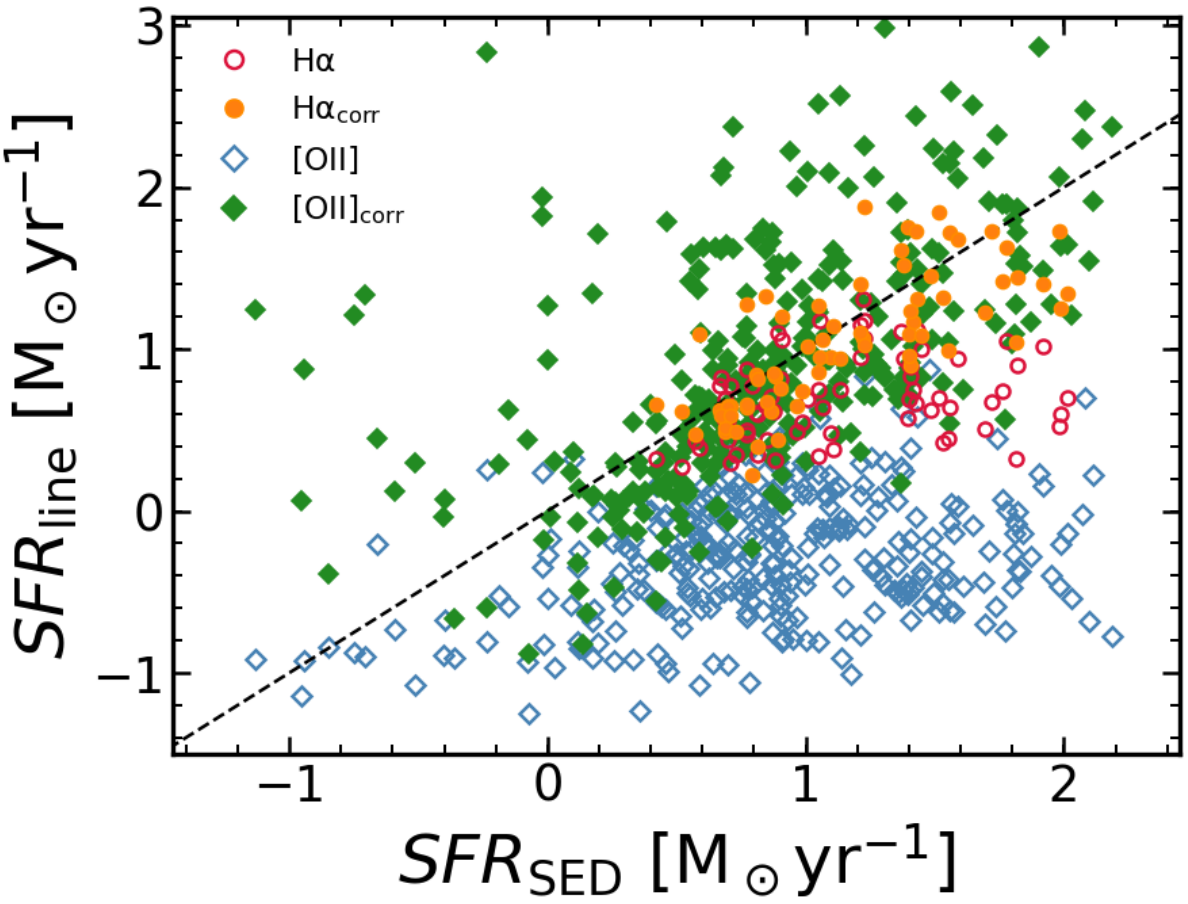


**Figure 5.5** SFR estimates from SED fitting and from [OII] (derived from Eq. 4 of Kewley et al. 2004) of the galaxies in our spectroscopic sample at $0.8 < z < 0.9$. Red circles show the dust uncorrected H$\alpha$ derived star formation rates for the galaxies in our sample and that were measured by Sobral et al. (2011). The subscript *corr* denotes the dust-corrected SFRs derived from each estimate using the optical depth derived through SED fitting (see Sect. 5.3.2).

In these equations, $N$ is the number of galaxies in the slice with weights greater than 10%, $r_i$ is the position of the galaxy, $r_j$ is the position of all other galaxies in the slice, and $h_i$ is the adaptive smoothing parameter for our assumed kernel. The value of $h_i = h\sqrt{G/\Sigma_i}$ Mpc, where $\Sigma_i$ is the initial density estimation at the position of galaxy $i$ using a fixed kernel with a width of 0.5 Mpc, $G$ is the geometric mean of all $\Sigma_i$ at each redshift slice, and $h$ is chosen to have a value around the typical size of X-ray clusters (0.5 Mpc, see e.g. Finoguenov et al., 2007). We then evaluate the density field in a 2D grid with a spatial resolution of 50 kpc at each redshift. We define over-density as:

$$1 + \delta = \frac{\Sigma}{\Sigma_{\rm median}}, \tag{5.5}$$

with $\Sigma$ being the projected local density and $\Sigma_{\rm median}$ being the median of the density field of the redshift slice the galaxy is in. We choose to use number densities instead of mass density estimates (e.g. Wolf et al., 2009) to avoid introducing any bias due to any underlying relation

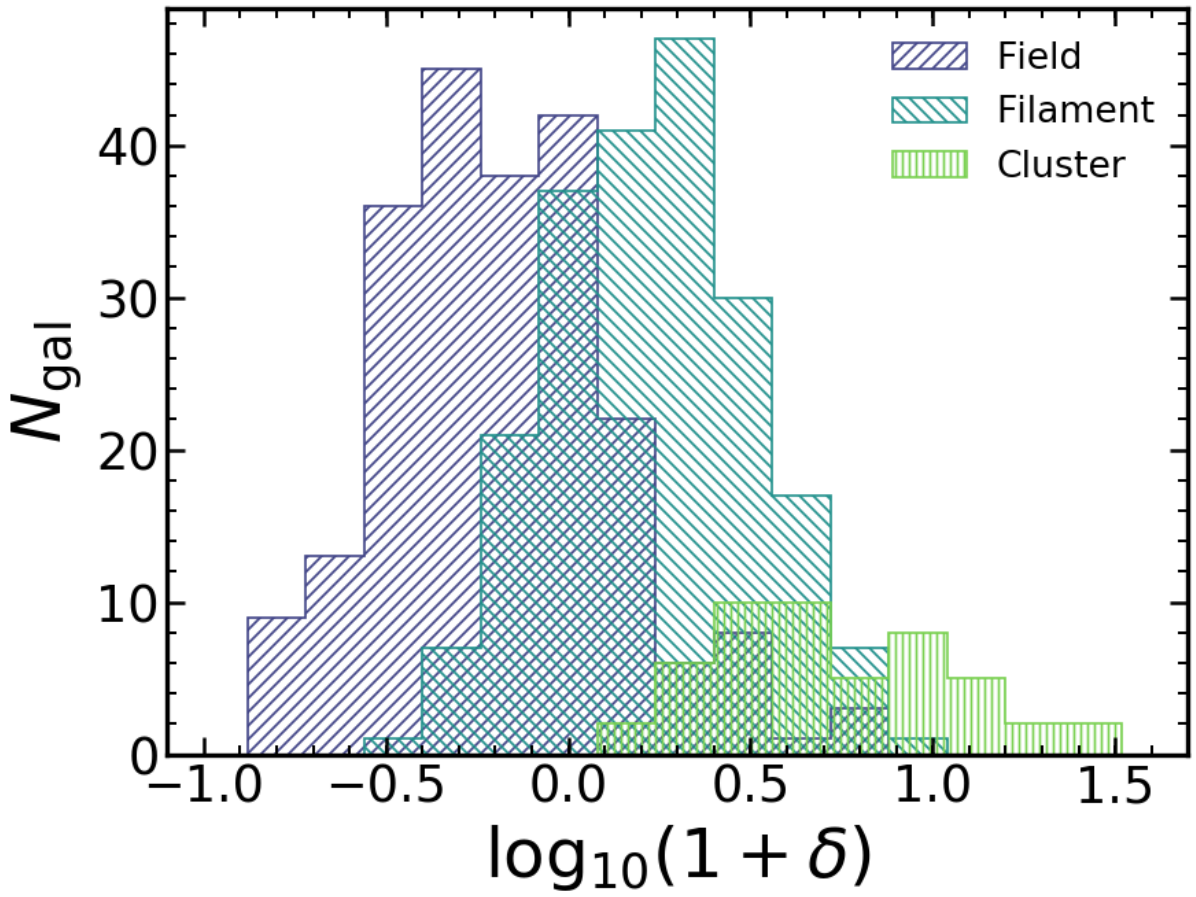


**Figure 5.6** Over-density distribution for the galaxies in our sample with $0.8 < z < 0.9$. We show the different cosmic web environments of galaxies (field, filament, and cluster) according to their classification using the scheme devised by Darvish et al. (2014, 2017).

between stellar mass and density that may exist. For a more detailed description of the method, we refer the reader to Darvish et al. (2014) and Darvish et al. (2015b).

We have computed the value of the over-density for each galaxy by interpolating the density field to their angular position and spectroscopic redshift. We show in Fig. 5.6 the distribution of our galaxies according to their over-density and labelled by the region they are likely to belong to, as defined by the cosmic web measurements computed by Darvish et al. (2014, 2017). We note that when referring to galaxies within our spectroscopic sample in cluster regions, we are mostly referring to either rich groups or the outskirts of massive clusters as our observational setup does not allow for a good sampling of densely populated regions due to slit collision problems.

We note that there is an overlap between the different labelled regions and the measured local over-density in Fig. 5.6. This happens because the region assigned to each galaxy is based on the definition of the strength of the cluster and filament signals, which takes into account the morphology of the density field. That is the reason why a pure density-based definition of the environment of galaxies cannot fully separate them into real physical structures (see e.g. Aragón-Calvo et al., 2010; Darvish et al., 2014). This means for example that we can have dense

filaments (as high-density regions with thread-like morphology, likely in-fall regions of massive clusters) and less dense cluster regions (intermediate density with circular morphology, likely associated with galaxy groups). We refer to Darvish et al. (2014, 2017, see also Aragón-Calvo et al. 2010) for more details.

### 5.3.4 SPECTRAL STACKS

To increase the S/N on the obtained spectra and investigate details on the spectral properties of galaxies as a function of their stellar mass and local density, we have performed stacking of individual galaxy spectra. Our stacking method can be summarised as a median, interpolated, and normalised spectra. For each set of spectra, we start by shifting the spectrum to its rest-frame wavelengths using the redshift we have measured (see Sect. 5.2.6). Then we linearly interpolate the spectra onto a common universal grid (3250-4500 Å, $\Delta\lambda = 0.3$ Å/pixel). We normalise each spectrum to the mean flux measured from 4150-4350 Å. Lastly, we median combine all spectra by taking the median flux at each wavelength. We estimate that our typical errors in the spectroscopic redshift measurements are on the order of $\sim 0.0005$, which translates to an error of $\sim 1$ Å, comparable to our spectral resolution at $z \sim 0.8$. Thus, our stacking should not smear the lines enough to affect the measurements on the [OII] $\lambda$3726,$\lambda$3729 doublet.

## 5.4 RESULTS

Throughout this section, our measure of environment is quantified by $\delta$ (see Eq. 8.1). For a broad comparison between different environments, we defined as lower-density galaxies those residing in $\log_{10}(1+\delta) < 0.1$, and as higher-density galaxies those residing in regions with $\log_{10}(1+\delta) > 0.4$.

### 5.4.1 REDSHIFT DISTRIBUTION

From our first redshift measurements, based on two to three lines, and the dispersion of the measurements, we are able to derive the full redshift distribution of our VIMOS sample. We show the results in Fig. 5.3 which shows a very clear peak at $z \approx 0.84$. By fitting a Gaussian to the redshift distribution at $z \approx 0.8$ we find that the COSMOS superstructure is well characterised by $z = 0.84 \pm 0.01$ with 367 galaxies fully included within this redshift distribution.

We attempt to estimate the mass of the two clusters for which we have coverage (A and B on Table

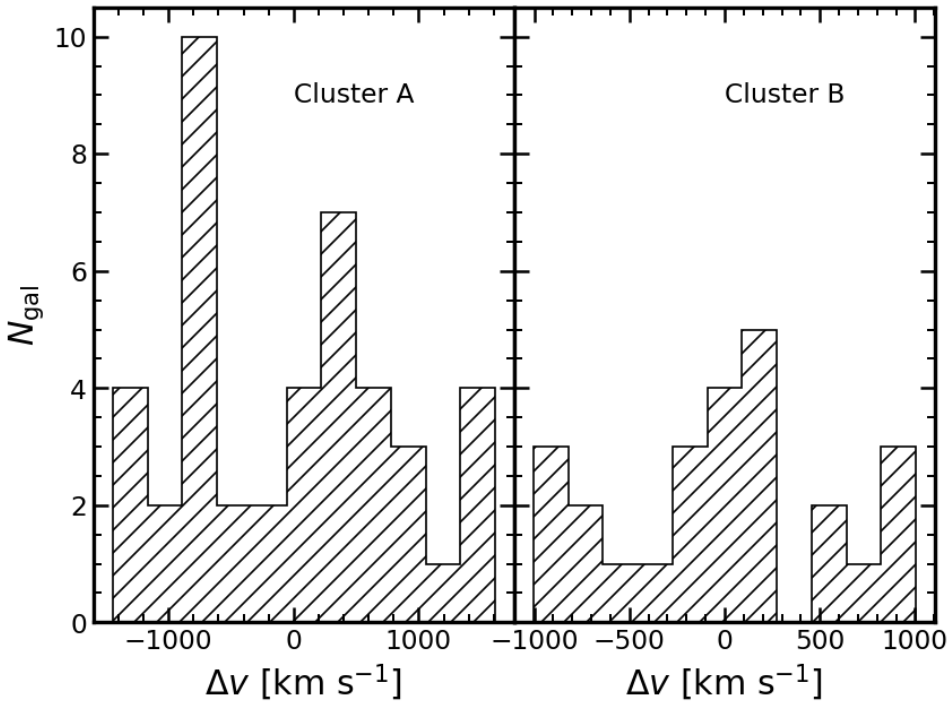


**Figure 5.7** The velocity distribution for clusters A (left) and B (right) of all member galaxies. We note that these structures cannot be described by a single Gaussian shape indicating that these structures are not virialized.

5.2; see also Fig. 5.1) by computing the radial velocity dispersion, $\sigma_r$, of the spectroscopically confirmed galaxies in our sample. We estimate the size of the cluster by computing the root mean square of the distances, $R_{\rm rms}$, to the estimated centre (average position of selected members). We compute the velocity dispersion, $\sigma_r$, using the gapper technique (Beers et al., 1990, see also Balogh et al. 2014). To obtain a final estimate for each cluster, we iterate five times and compute the mean position, $R_{\rm rms}$, and $\sigma_r$ by selecting at each step galaxies within $2R_{\rm rms}$ of the cluster centre and within $2\sigma$ of the median cluster redshift. We start our iteration procedure by assuming an initial guess for $R_{\rm rms} = 0.5$ Mpc.

We find values of $\sigma_r = 875 \pm 179$ km s$^{-1}$ (43 galaxies) and $R_{\rm rms} = 1.1$ Mpc for cluster A and of $\sigma_r = 598 \pm 225$ km s$^{-1}$ (25 galaxies) and $R_{\rm rms} = 1.3$ Mpc for cluster B. Assuming a virial state for each cluster, we can estimate their mass as $M = 3\sigma_r^2 R_{\rm rms}/G$. We find $M = 6 \pm 3 \times 10^{14} {\rm M}_\odot$ and $M = 3 \pm 2 \times 10^{14} {\rm M}_\odot$, respectively. These values are up to an order of magnitude higher than the values reported by Balogh et al. (2014, see Table 5.2) and this difference is mainly driven by our larger derived values of $R_{\rm rms}$. We note here that our measurements are made under the assumption that the clusters are virialized. We hypothesise that when applying a similar criteria for galaxy membership as Balogh et al. (2014), we are likely picking up additional moving substructures (at slightly different redshifts) that are artificially increasing our measured cluster sizes and velocity dispersion. This is supported by the non-Gaussian shape of the velocity distribution histograms of the selected members (see Fig. 5.7).

### 5.4.2 SFR DEPENDENCE ON LOCAL OVER-DENSITY

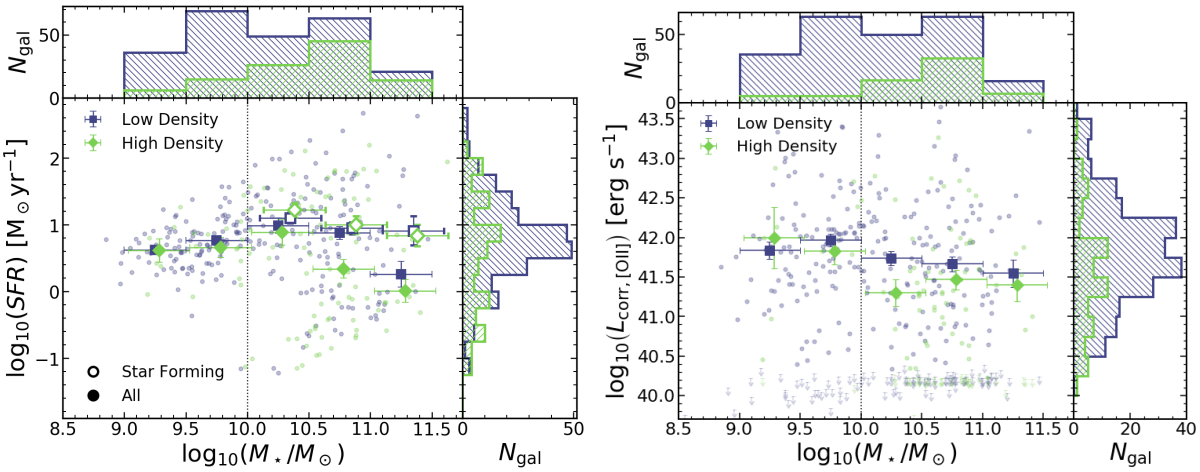


**Figure 5.8** Left: SFR (from SED fitting) distribution as a function of stellar mass. Each small circle represents a single galaxy. Large squares show the median value for the population in stellar mass bins. Error bars show the error on the median of each bin. Higher-density regions are coloured in blue while lower- density galaxies are shown in green colours. The empty symbols represent the bins considering star-forming galaxies only, with $\log_{10}(sSFR) > -11$. The symbols are horizontally shifted for visualisation purposes. The vertical dotted line shows the completeness limit of our survey. Globally, we find that galaxies in higher-density regions have lower SFRs, but only when considering the entire population. When selecting star-forming galaxies, we find no difference between the median SFRs in low- and high-density environments. Right: Dust-corrected [OII] luminosity distribution as a function of stellar mass. We show as small arrows the upper limits on [OII] luminosity for the galaxies for which we have no measure with sufficient S/N. Horizontal lines show three values of SFR = 1, 10, 50 $M_\odot yr^{-1}$ as derived from Eq. 5.3. We typically find no differences between low- and high-density regions in terms of the median dust-corrected [OII] luminosity at all stellar masses probed in our sample.

The upper panel of Fig. 5.8 shows the dependence of SFR on stellar mass and local density. For low-mass galaxies ($\log_{10}(M_\star/M_\odot) \lesssim 10$) we find the same average SFR in both high- and low-density regions, although there are only very few ($\sim$10) low-mass galaxies in our sample in high-density regions and all of them are star-forming (check completeness in Fig. 5.12). At higher stellar masses ($\log_{10}(M_\star/M_\odot) > 10$), we find a stronger dependence of SFR on local density. At $\log_{10}(M_\star/M_\odot) \sim 10.75$, the difference is the highest due to a larger fraction of galaxies at these stellar masses being photometrically defined as quiescent in higher-density regions. At the highest stellar masses ($\log_{10}(M_\star/M_\odot) \gtrsim 11$), there are few star-forming galaxies in both higher- and lower-density regions and we see little dependence of the star formation activity in galaxies on the local density in which they reside. We fit a linear model, $\log_{10}(SFR) = m\log_{10}(M) + b$, to the stellar mass-SFR relation at $\log_{10}(M_\star/M_\odot) > 10$ and find that for lower-density regions the null hypothesis of a flat relation ($m = 0$) is rejected at $\sim 3.3\sigma$ ($m = -0.7 \pm 0.22$) and for higher-density regions is rejected at $\sim 3.5\sigma$ ($m = -0.9 \pm 0.25$).

When looking at the trends, considering star-forming galaxies only (with $\log_{10}(sSFR) > -11$), the difference between low- and high-density regions vanishes. With a similar linear model as described above, we find $m = -0.2 \pm 0.23$ for low-density regions and $m = -0.4 \pm 0.20$ for higher-density regions. These models are less than $2\sigma$ from the null hypothesis. When compared

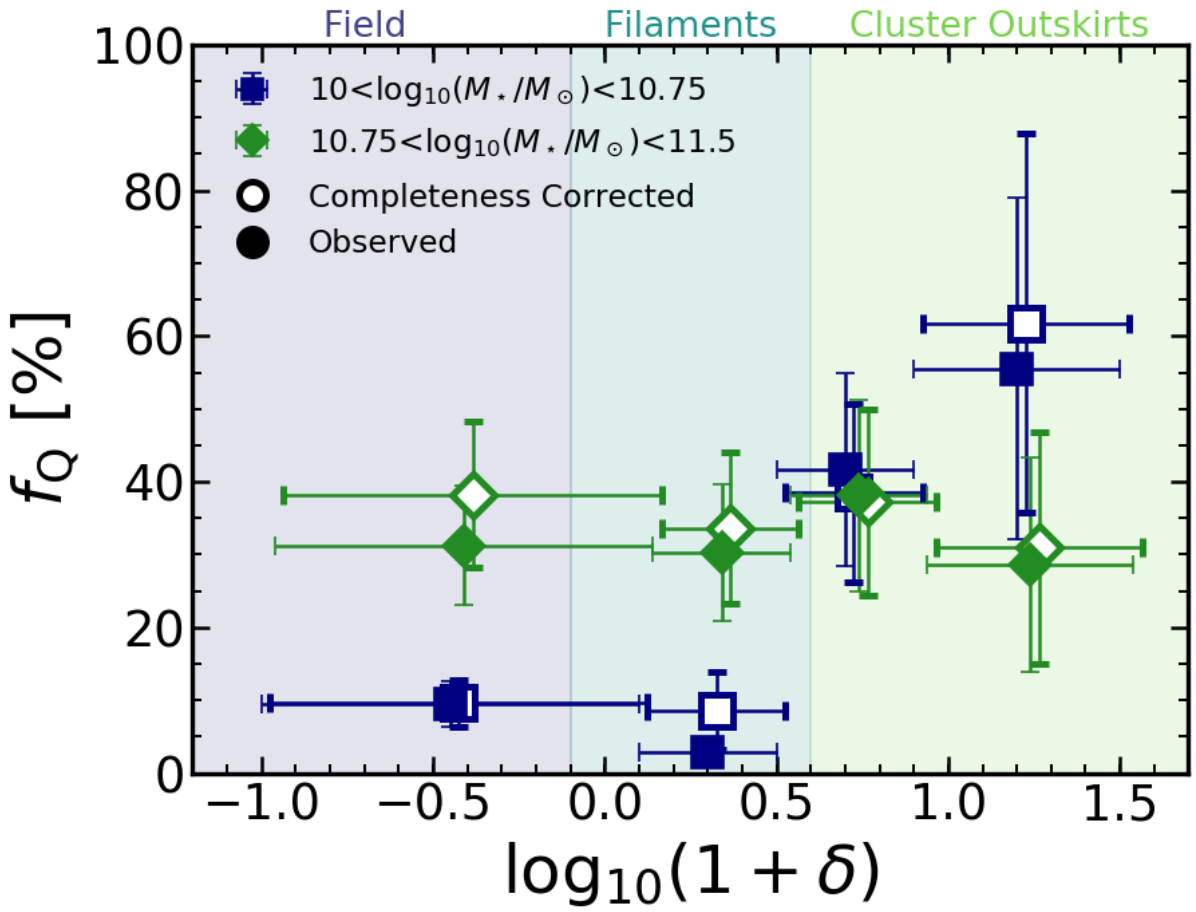


**Figure 5.9** The fraction of quenched galaxies within our sample ($f_{\rm Q}$, with $\log_{10}(sSFR) < -11$) as a function of local density and in two different bins of stellar mass. Open symbols show the same fraction after correcting for our sample completeness. Error bars are computed using Poisson statistics. We find in both cases that the lower-stellar-mass galaxies show a sharp increase for higher-density environments whereas the highest-stellar-mass galaxies show no environmental dependence of $f_{\rm Q}$. Shaded regions provide an approximate estimate of the cosmic web environment given the measured over-density (but see Sect. 5.3.3 for more details).

with the full sample, this suggests that the decline in the median SFR of the full sample in dense regions is mainly driven by the higher fraction of quenched galaxies.

We compute the fraction of galaxies that are defined as quenched in our sample ($\log_{10}(sSFR) < -11$) and show our findings in the Fig. 5.9. Error bars for the fraction of quiescent galaxies are computed using Poisson statistics $\left(\Delta f_Q = f_Q\sqrt{N_Q^{-1} + N_T^{-1} - 2N_Q^{-1}N_T^{-1/2}}\right)$. We inspect the environmental dependence of this fraction on environment for two separate stellar-mass bins. We find that the lower-stellar-mass galaxies ($10 < \log_{10}(M_\star/\mathrm{M}_\odot) < 10.75$) have a nearly constant quenched fraction at low to intermediate densities. We then find a jump from $\sim 10\%$ to $\sim 40-60\%$ towards higher-density regions. When considering the higher-stellar-mass bin ($\log_{10}(M_\star/\mathrm{M}_\odot) > 10.75$), we find no dependence of the quenched fraction on local density, this being nearly constant at $\sim 30\%$. We also show the reported values after correcting for our sample completeness and we find qualitatively the same results (see Appendix for more details on the spectroscopic sample completeness).

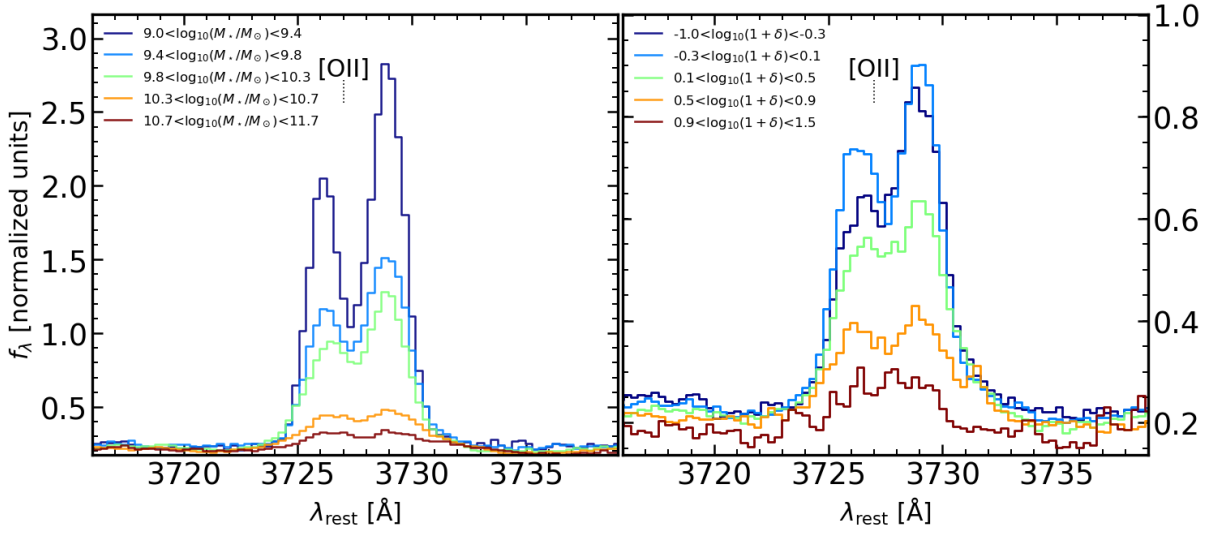


**Figure 5.10** Resulting spectral stacks (normalised by the flux at 4150 Å $< \lambda <$ 4350 Å) around the [OII] doublet in bins of stellar mass (left) and in bins of local density (right). This figure shows the comparison between different stacks (for individual inspection, we refer to Fig. 5.13). We see a strong dependence of the [OII] strength on the stellar mass with higher-stellar-mass galaxies having weaker [OII] emission, as expected since most quenched galaxies are found at higher stellar masses and should have little to no emission. We also find a dependence of the [OII] strength on the local density with high-density regions having galaxies with weaker [OII] emission, again with massive quiescent galaxies dominating at higher densities being the likely cause of this effect.

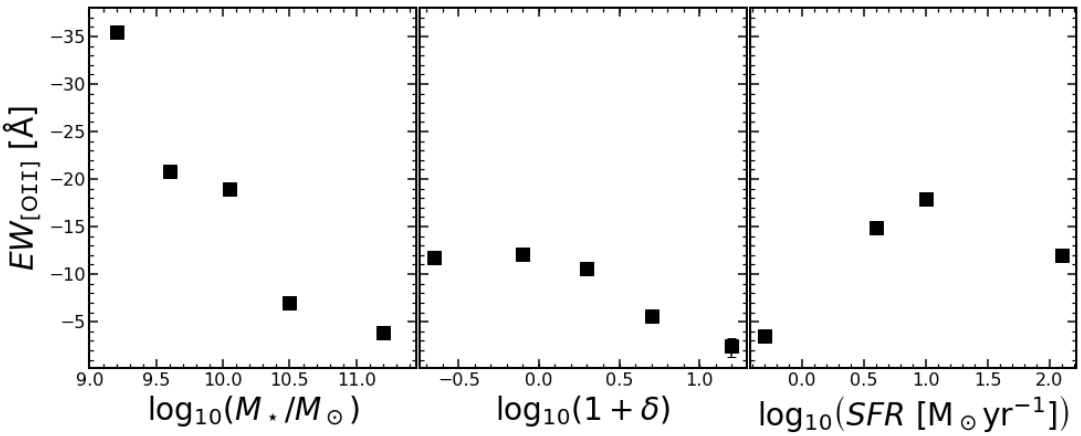


**Figure 5.11** Line equivalent width for the spectral lines in [OII] as a function of the stellar mass range (left) and of the local density range (right) for the stacked spectra. We apply no dust correction to the stacked derived values since we assume spatial coincidence between the continuum and line-emitting regions, and they are affected by dust in a similar manner.

### 5.4.3 [OII] LUMINOSITY DEPENDENCE ON LOCAL OVER-DENSITY

The lower panel of Fig. 5.8 shows the resulting distribution of dust-corrected [OII] luminosity for the sample at $0.8 < z < 0.9$. The bulk of the population has $L_{[\mathrm{OII}]} \sim 10^{41.5}$erg s$^{-1}$ with the brightest in our sample reaching luminosities of $L_{[\mathrm{OII}]} \sim 10^{43}$erg s$^{-1}$.

When looking at galaxies in high- and low-density environments we find no significant difference in the median (excluding upper limits) dust-corrected [OII] luminosity at all stellar masses probed in our study. If we assume that the luminosity of the [OII] emission doublet is correlated

with the galaxy SFR (see e.g Kennicutt, 1998; Kewley et al., 2004; Darvish et al., 2015a), our results on [OII] show that their median luminosity (which traces star formation) is not affected by higher-density environments. This is different from what we show when using SFRs derived from SED fitting. We attribute this discrepancy to the fact that with our observational setup we measure [OII] luminosities more easily for star-forming galaxies than for quiescent galaxies (which are mostly upper limits). The SED fitting results do not suffer from the same problem, meaning that what is likely causing the differences is the quenched fraction as a function of density. Having a higher fraction of quenched galaxies at high densities (see e.g. Fig. 5.9) will result in a lower median SFR value than what we would get from [OII] luminosities because we miss a fraction of that population (upper limits only in Fig. 5.8). If one includes the upper limits in the median calculation, we get qualitatively the same trends as we find for SED-derived SFRs.

We note, however, that differences may also arise if the [OII] emission is originating from other sources than star formation (e.g. AGN, LINERs; see e.g. Yan et al., 2006; Kocevski et al., 2011), but we expect this to be a secondary effect due to the lower overall fraction of this type of object (e.g. Pentericci et al., 2013; Ehlert et al., 2014; Oh et al., 2014).

### 5.4.4 [OII] PROPERTIES IN STACKED SPECTRA

We show in the left panel of Fig. 5.10 (see also Figure 8.5 for individualized panels) the resulting spectra after stacking all galaxies in bins of stellar mass. We observe a strong decrease in [OII] line strength from low to high stellar masses (a factor of $\sim 10$ in flux from the lowest to the highest stellar-mass bin). We also see the relative strength of the two doublet lines is changing with stellar mass. At lower masses, the [OII]$\lambda$3729/[OII]$\lambda$3726 ratio is higher and seems to constantly decrease as we move towards higher masses. This ratio is indicative of the electron density in the interstellar medium (e.g. Seaton & Osterbrock, 1957; Canto et al., 1980; Pradhan et al., 2006; Darvish et al., 2015a; Sanders et al., 2016; Kaasinen et al., 2017) and will be investigated in a subsequent chapter.

In Fig. 5.10 (right panel, see also Fig. 5.14 for individualized panels), we show our findings of the stacked spectra in bins of local density. In terms of the [OII] emission, we find a decreasing line strength from low- to high-density regions. Interestingly, in the three lowest-density bins the difference in [OII] emission strength is appreciably smaller when compared to the two highest-density bins. This decrease at $\log_{10}(\delta) \sim 0-0.5$ hints at a break in star formation around these local over-density values (see e.g. Darvish et al., 2016).

To quantify the properties of each line, we performed a double Gaussian fitting to [OII] using Eq. 5.1. Results of the equivalent widths and fluxes of the [OII] doublet are summarised in Table 5.4 and Fig. 5.11. The qualitative remarks we made on the appearance of the spectral stacks are confirmed by our results after fitting each component.

We find a strong decrease in [OII] strength and line equivalent width with stellar mass (see Fig. 5.11) with a factor of $\sim 10$ between the lowest stellar-mass bin ($9.0 < \log_{10}(M_\star/\mathrm{M}_\odot) < 9.4$) and the highest stellar-mass bin ($\log_{10}(M_\star/\mathrm{M}_\odot) > 10.7$) (similar to results by e.g. Darvish et al., 2015a; Khostovan et al., 2016). Performing the same analysis on the stacked spectra per local density bin, the [OII] line strength and equivalent width show a broken relation with a "break" at $\log_{10}(1+\delta) \sim 0.0 - 0.5$ that translates into a steeper relation at higher densities.

## 5.5 DISCUSSION

The survey presented in this chapter selects galaxies according to their continuum emission and absorption features down to $\log_{10}(M_\star/\mathrm{M}_\odot) \sim 10$ and is able to detect [OII] down to $\sim 5 \times 10^{-18}$ erg s$^{-1}$cm$^{-2}$. Since our sample is based on accurate measurements of redshifts, it is natural that it only selects galaxies at lower stellar masses if they have clear emission lines characteristic of star-forming galaxies. This means that our results on global trends with stellar mass below our completeness limit is biased against low star formation and passive galaxies (see e.g. Fig. 5.4). This fact alone is able to explain an apparent lack of trends in star-formation related quantities (SFR and $L_{[\mathrm{OII}]}$) at stellar masses below $\log_{10}(M_\star/\mathrm{M}_\odot) = 10$, where we see no dependence whatsoever on local over-density. In summary, our results for the lowest-stellar-mass bins (less than $10^{10}\mathrm{M}_\odot$) are likely based only on the star-forming population.

One important aspect to consider when looking for environmental effects on galaxy evolution is to attempt to distinguish between stellar-mass-driven and density-driven mechanisms (e.g. Peng et al., 2010b; Kovač et al., 2014; Darvish et al., 2016). We attempt to address these issues by computing average quantities in different environments as a function of stellar mass (or at different stellar masses as a function of environment).

Considering our results on galaxies with stellar masses above our completeness limit, we find little influence of environment on galaxy SFRs (from SED fitting) and $L_{[\mathrm{OII}]}$. In higher-density regions, galaxies are typically less star-forming (Fig. 5.8; except at the highest stellar masses ($\log_{10}(M_\star/\mathrm{M}_\odot) > 11$) but with comparable [OII] emission. This can easily be explained by the increase of the fraction of quenched galaxies in higher-density regions. These trends support the scenario where environment plays a role in increasing the quiescent fraction of intermediate-stellar-mass galaxies at these redshifts ($z \approx 0.84$). This fits well in the scenario where galaxies already have their star formation suppressed due to environmental effects as early as 7 billion years ago. At higher stellar masses, we see no differences in the average SFR and quiescent fractions, hinting that mass quenching should be effective enough to halt star formation even in low-density regions (see e.g. Peng et al., 2010b) although it is not clear that environmental and stellar mass quenching are fully separable (see e.g. Lee et al., 2015; Darvish et al., 2016;

Kawinwanichakij et al., 2017). This differential effect with stellar mass is a potential indicator that environment acts as a catalyst for star-formation quenching in the sense that we are more likely to see galaxies quench at lower stellar masses if they reside in high-density environments. We stress that for $10 < \log_{10}(M_\star/\mathrm{M}_\odot) < 10.25$, we find no differences in the median SFRs between low- and high-density regions; this is likely caused by a lack of quiescent galaxies close to our completeness limit that drives up the median value of the SFR for that bin. Since we see a rise in the quiescent fraction towards high-density regions on the lowest stellar-mass bin that we probe (see Fig. 5.9 and also Appendix, it is plausible that this is the reason for the observed results in this stellar-mass bin.

Our findings corroborate those reported by Sobral et al. (2011) which probed the same region using H$\alpha$ emitters. They are also consistent with others in the literature which already report a decrease in the star-forming fraction with projected galaxy density at similar redshifts (e.g. Patel et al., 2009; Muzzin et al., 2012). We also see similar trends of star formation with environment in lower-redshift surveys (e.g. Balogh et al., 2002; Rodríguez del Pino et al., 2017). This means that environmental effects are shaping the star formation in individual galaxies in a similar manner in the past 6 Gyr. These effects are readily explained by the number of physical mechanisms (e.g. ram pressure stripping, tidal interactions) capable of stripping gas from galaxies and shutting down any new star formation activity. While we note that these can in fact explain the observed trends in SFR with stellar mass and environment, it is beyond the scope of this chapter to pinpoint the mechanisms responsible for our observations.

### 5.5.1 Halting of star formation in the outskirts of clusters

Overall we find that the average SFR is lower in high-density regions, confirming what was reported by Sobral et al. (2011) when studying H$\alpha$ emitters on the same structure. We report one order of magnitude difference in the average SFR from the lowest- to the highest-density region ($\sim 10$ to $\sim 1$ $\mathrm{M}_\odot \mathrm{yr}^{-1}$). This trend with environment gives strength to the argument of environmentally driven quenching occurring within our superstructure. These signs of environmental quenching of star formation (also seen in e.g. Patel et al., 2009; Sobral et al., 2011; Muzzin et al., 2012; Santos et al., 2013) are distinct from the structures that show a flat or reverse SFR-density relation (e.g. Elbaz et al., 2007; Ideue et al., 2009; Tran et al., 2010; Santos et al., 2014).

One interesting result is the "break" that we find on the relation between [OII] line equivalent width and local over-density that occurs at intermediate densities ($\log_{10}(\delta) \sim 0.0 - 0.5$, see Fig. 5.11 and also e.g. Darvish et al., 2016). We hypothesise that this corresponds to a typical density where environment quenching mechanisms are the most effective. The transition at $\log_{10}(\delta) \sim 0.0 - 0.5$ is consistent with regions of filament-like densities (see transition from filament-

dominated to cluster-dominated galaxies in Fig. 5.6). This result is compatible with intermediate-density regions being the place of enhanced chances for galaxy encounters, promoting galaxy-harassment-related quenching mechanisms (e.g. Moss, 2006; Perez et al., 2009; Li et al., 2009; Tonnesen & Cen, 2012; Darvish et al., 2014; Malavasi et al., 2017). It might also be caused by strong cluster-cluster interactions that are found to enhance star formation as well (e.g. Stroe et al., 2014, 2015). To further reinforce the existence of such a "break", we find that the fraction of quenched galaxies at intermediate stellar masses ($10 < \log_{10}(M_\star/\mathrm{M}_\odot) < 10.75$) increases by a factor of two at the same transition density, being roughly constant below and above. Galaxies at higher stellar masses are likely already quenched due to their own mass (see e.g Peng et al., 2010b) and they are likely not greatly affected by the environment they are in.

## 5.6 Conclusions

We have presented in this chapter an overview of the VIS$^3$COS survey, which targets a superstructure at $z \sim 0.84$ with VIMOS/VLT high-resolution spectra. We report on trends with environment and stellar mass of the SFR and [OII] luminosity. Our main findings are summarised as follows:

- Above our stellar-mass completeness limit ($10^{10}\mathrm{M}_\odot$), galaxies in higher-density regions have lower SFRs at intermediate masses ($10 < \log_{10}(M_\star/\mathrm{M}_\odot) < 10.75$). At the highest masses (above $10^{10.75}\mathrm{M}_\odot$), the star formation activity is similar in low- and high-density environments indicating that mass quenching is probably dominant at high stellar masses.

- We find that the fraction of quenched galaxies ($f_Q$) increases from $\sim 10\%$ to $\sim 40-60\%$ with increasing galaxy over-density, but only for intermediate stellar mass galaxies ($10 < \log_{10}(M_\star/\mathrm{M}_\odot) < 10.75$). The most massive galaxies in our sample (above $10^{10.75}\mathrm{M}_\odot$) have a similar value of $f_Q \sim 30-40\%$ at all densities.

- We find a break in [OII] strength and equivalent width in the stacked spectra in filament-like regions ($\log_{10}(\delta) \sim 0.0-0.5$). We hypothesise that at these densities, quenching mechanisms due to environment play an important role. This is consistent with the increase in the quenched galaxy fraction that we find for intermediate-stellar-mass galaxies.

In summary, the results of this chapter shed some light on the properties of galaxies in and around a superstructure on the COSMOS field. In this chapter, we have focused on the overall properties of the sample in our survey and the general trends that we find on galaxy properties with respect to environment. More detailed studies focusing on the individual star formation activity of galaxies, galaxy morphology, and electron density estimates will be discussed in forthcoming chapters.

# ACKNOWLEDGEMENTS

We thank the anonymous referee for making valuable suggestions, which helped to improve the analysis. This work was supported by Fundação para a Ciência e a Tecnologia (FCT) through the research grant UID/FIS/04434/2013. APA, PhD::SPACE fellow, acknowledges support from the FCT through the fellowship PD/BD/52706/2014. DS acknowledges financial support from the Netherlands Organisation for Scientific research (NWO) through a Veni fellowship and from Lancaster University through an Early Career Internal Grant A100679. BD acknowledges financial support from NASA through the Astrophysics Data Analysis Program (ADAP), grant number NNX12AE20G, and the National Science Foundation, grant number 1716907. PNB is grateful for support from STFC via grant ST/M001229/1. This work was made possible by the use of the following PYTHON packages: NumPy & SciPy (Walt et al., 2011; Jones et al., 2001), Matplotlib (Hunter, 2007), and Astropy (Astropy Collaboration et al., 2013).

# APPENDIX

## SAMPLE COMPLETENESS

We estimate the sample completeness of our spectroscopic observations by comparing the number of sources for which we successfully measured a redshift with the number of possible targets in the parent catalogue (given our selection described in Sect. 5.2.2). We present our results in Fig. 5.12. We will discuss the completeness effects in more detail in a forthcoming work.

We confirm that we are under-sampling denser regions when compared to the lowest density regions, which is expected given the spatial constraints on the positioning of the slits in the VIMOS masks does not allow to target densely populated areas. In terms of star formation activity, we find that our typical completeness is lower for quiescent galaxies ($\sim 30\%$) when compared to star-forming ones ($\sim 40\%$). When taken together, we find that we are most likely missing quiescent galaxies in high-density regions, but that the difference between the two populations is not dramatic in terms of completeness and our derived completeness corrections can tackle this without problems. Therefore we are providing a fair representation of the galaxy population in the regions we are targeting.

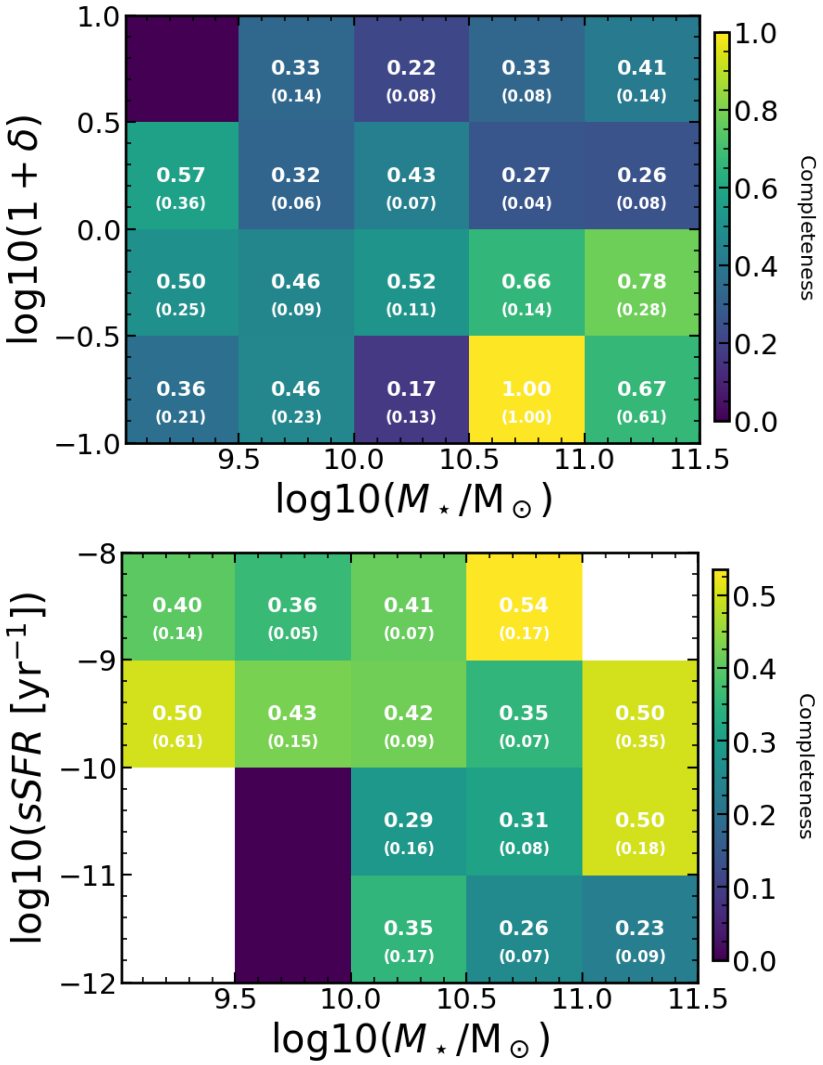


**Figure 5.12** Spectroscopic sample completeness as a function of stellar mass and local overdensity (top) and specific SFR (bottom). In each panel, we indicate the completeness for each bin in white numbers (Poisson errors shown in parenthesis). Bins with no targets are shown in white.

## CATALOGUE OF SUPERSTRUCTURE MEMBERS

We release with this work the VIS$^3$COS catalogue of all targets in and around the superstructure at $z \sim 1$ with spectroscopic redshifts, along with some of their measured properties: SFR, over-density, stellar mass. We present the first ten entries of the full catalogue in Table 5.3.

## INDIVIDUAL STACKS

Since some trends are difficult to see when showing all stacked spectra in a single panel due to line cluttering, here we show all the stacked spectra individually in Figs. 5.13 (in bins of stellar mass) and 5.14 (in bins of over-density). All results are also summarised in Table 5.4.

**Table 5.3** First 10 galaxies in our sample. The first column is our catalogue ID. The second and third columns show the object coordinates from Ilbert et al. (2009). The fourth column is our measured spectroscopic redshift. The fifth column is the $K$-band magnitude from Ilbert et al. (2009). The sixth and seventh columns are the stellar masses and SFRs derived with MAGPHYS. The last column is the local over-density from Darvish et al. (2015b, 2017).

| ID | RA (J2000) | DEC (J2000) | $z_{\rm spec}$ | $K_{\rm AB}$ | $\log_{10}(M_\star)$ $(M_\odot)$ | $\log_{10}(SFR)$ $(M_\odot yr^{-1})$ | $\log_{10}(1+\delta)$ |
|---|---|---|---|---|---|---|---|
| VIS3COS-1 | 150.510640 | 2.035566 | 0.8998 | 20.6 | 10.6 | 0.9 | -0.26 |
| VIS3COS-2 | 150.521776 | 2.040788 | 0.8707 | 21.0 | 10.4 | 0.1 | 0.15 |
| VIS3COS-3 | 150.547778 | 2.044605 | 0.8714 | 20.5 | 11.0 | 0.5 | 0.39 |
| VIS3COS-4 | 150.543696 | 2.047819 | 0.8080 | 21.9 | 9.2 | 0.6 | -0.68 |
| VIS3COS-6 | 150.590194 | 2.051661 | 0.8419 | 20.0 | 10.6 | 1.1 | 0.11 |
| VIS3COS-7 | 150.573302 | 2.053824 | 0.8722 | 21.5 | 10.4 | 1.3 | -0.19 |
| VIS3COS-8 | 150.520207 | 2.057174 | 0.8970 | 21.1 | 10.1 | 1.1 | 0.28 |
| VIS3COS-10 | 150.569219 | 2.062002 | 0.6980 | 19.7 | 11.2 | 1.5 | -0.54 |
| VIS3COS-12 | 150.575212 | 2.068181 | 0.8724 | 99.0 | 10.5 | -0.7 | -0.09 |
| VIS3COS-13 | 150.538943 | 2.070524 | 0.8930 | 20.5 | 10.8 | 0.2 | 0.14 |
| VIS3COS-15 | 150.604440 | 2.074035 | 0.8555 | 21.9 | 9.6 | 0.3 | 0.03 |

**Table 5.4** Summary of [OII] properties from the stacked spectra. The first column shows the stellar mass and environment bins that we consider for the stack. The second column presents the equivalent with of the [OII] doublet. The third column shows the doublet ratio $R$ =[OII]$\lambda$3729/$\lambda$3726.

| Range | EW([OII]) | $R$ |
|---|---|---|
| $9.0 < \log_{10}(M_\star/M_\odot) < 9.4$ | $-35.4^{+0.4}_{-0.4}$ | $1.46^{+0.07}_{-0.07}$ |
| $9.4 < \log_{10}(M_\star/M_\odot) < 9.8$ | $-20.7^{+0.2}_{-0.2}$ | $1.45^{+0.06}_{-0.06}$ |
| $9.8 < \log_{10}(M_\star/M_\odot) < 10.3$ | $-18.9^{+0.2}_{-0.2}$ | $1.43^{+0.06}_{-0.06}$ |
| $10.3 < \log_{10}(M_\star/M_\odot) < 10.7$ | $-6.9^{+0.3}_{-0.2}$ | $1.16^{+0.10}_{-0.10}$ |
| $10.7 < \log_{10}(M_\star/M_\odot) < 11.7$ | $-4.0^{+0.2}_{-0.2}$ | $1.09^{+0.08}_{-0.08}$ |
| $-1.0 < \log_{10}(1+\delta) < -0.3$ | $-11.7^{+0.2}_{-0.2}$ | $1.59^{+0.07}_{-0.07}$ |
| $-0.3 < \log_{10}(1+\delta) < 0.1$ | $-12.8^{+0.2}_{-0.2}$ | $1.26^{+0.05}_{-0.05}$ |
| $0.1 < \log_{10}(1+\delta) < 0.5$ | $-10.4^{+0.4}_{-0.4}$ | $1.23^{+0.08}_{-0.08}$ |
| $0.5 < \log_{10}(1+\delta) < 0.9$ | $-5.6^{+0.3}_{-0.3}$ | $1.15^{+0.09}_{-0.09}$ |
| $0.9 < \log_{10}(1+\delta) < 1.5$ | $-2.5^{+1.1}_{-0.8}$ | $1.31^{+0.47}_{-0.34}$ |

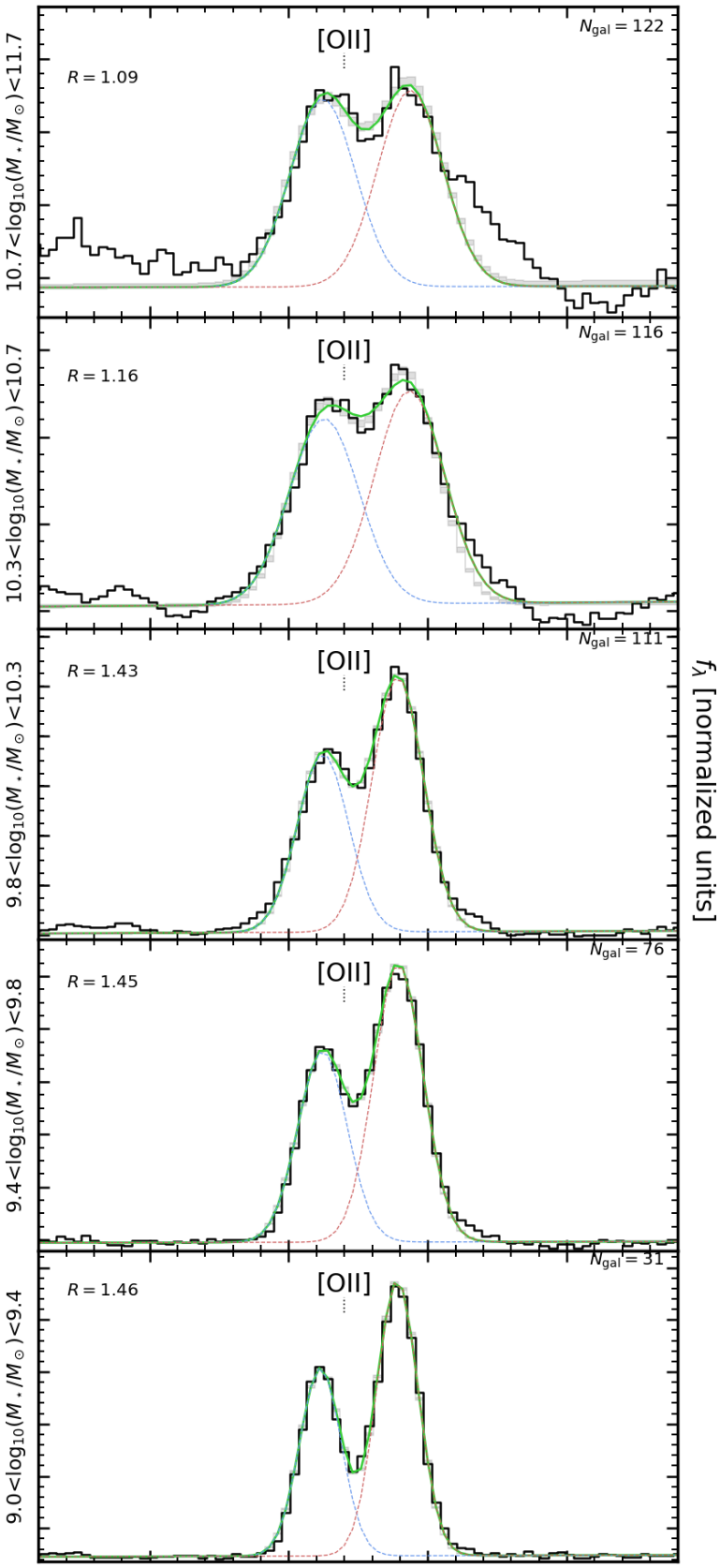


**Figure 5.13** Resulting spectral stacks (solid black line) in bins of stellar mass (high to low stellar mass from top to bottom) around the [OII] doublet. We show in green the best fit doublet model with each component shown as blue and red dashed lines. The shaded grey area represents the typical error on the fit of the spectra at each wavelength computed from the 16th and 84th percentiles of 10 000 realizations of perturbing the spectra by its error. In each panel we show the derived ratio between the two doublet components.

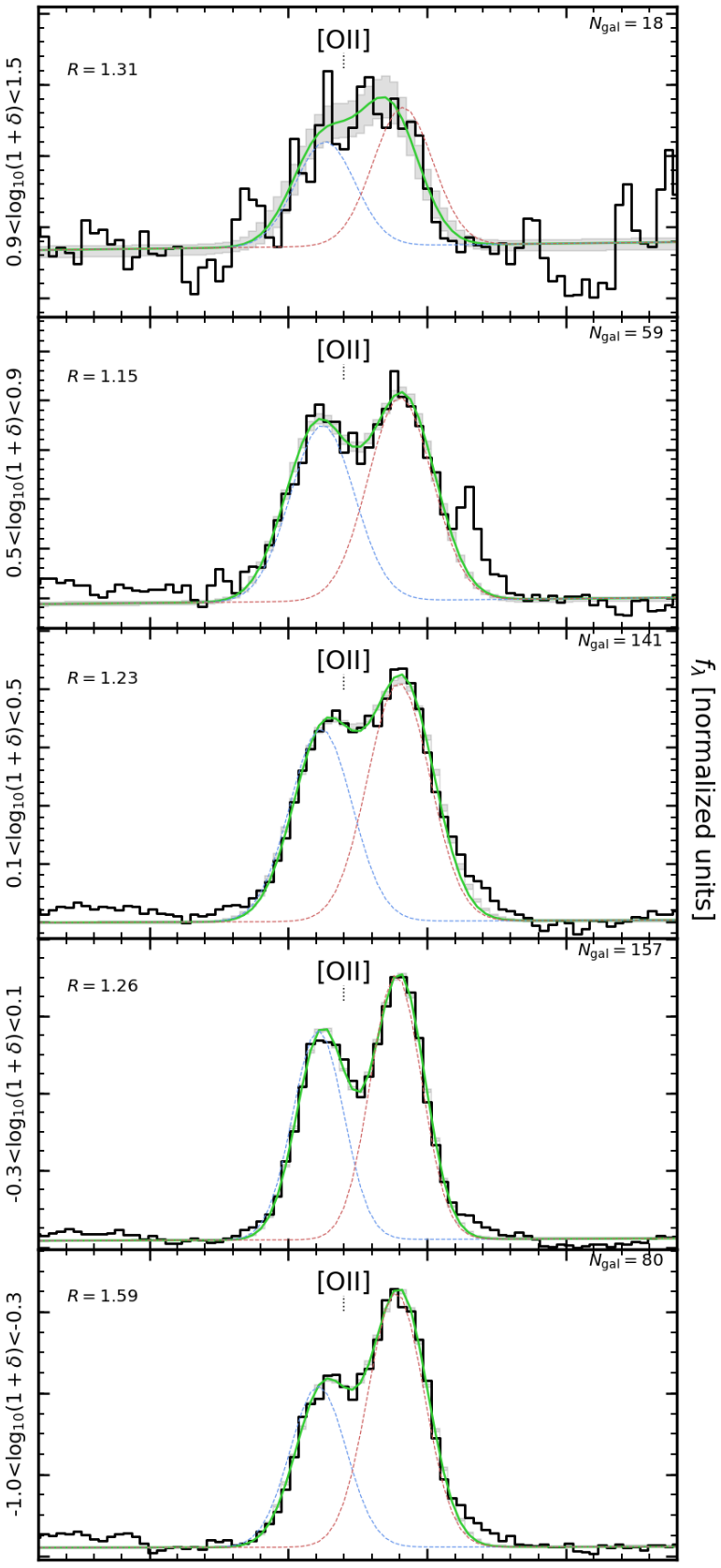


**Figure 5.14** Resulting spectral stacks (solid black line) in bins of over-density (high to low density from top to bottom) around the [OII] doublet. We show in green the best fit doublet model with each component shown as blue and red dashed lines. The shaded grey area represents the typical error on the fit of the spectra at each wavelength computed from the 16th and 84th percentiles of 10 000 realizations of perturbing the spectra by its error. In each panel we show the derived ratio between the two doublet components.

This page intentionally contains only this sentence.

# CHAPTER 6

## VIS$^3$COS: II. ENVIRONMENTAL EFFECTS ON [OII], H$\delta$, AND $D_N4000$ AND THEIR CONSEQUENCE FOR THE STAR FORMATION HISTORIES

*We present spectroscopic results for* 466 *galaxies in and around a superstructure at* $z \sim 0.84$ *targeted with the VIMOS Spectroscopic Survey of a Supercluster in the COSMOS field (VIS$^3$COS). We use [OII]$\lambda$3727, H$\delta$, and* $D_n4000$ *to trace the recent, mid- and long-term star formation histories and investigate how those are impacted by stellar mass and local over-density. By studying trends both in individual and composite galaxy spectra we find that both stellar mass and environment play a role in the observed galactic properties. Low stellar mass galaxies (*$10 < \log_{10}(M_\star/\mathrm{M}_\odot) < 10.5$*) in the field show the strongest H$\delta$ absorption. Similarly, the massive population (*$\log_{10}(M_\star/\mathrm{M}_\odot) > 11$*) shows an increase in H$\delta$ absorption strengths in intermediate-density environments (e.g. filaments). Intermediate stellar mass galaxies (*$10 < \log_{10}(M_\star/\mathrm{M}_\odot) < 10.5$*) have similar H$\delta$ absorption profiles in all environments, but show a hint of enhanced [OII] emission at intermediate-density environments. This hints that low stellar mass field galaxies and high stellar mass filament galaxies are more likely to have experienced a recent burst of star formation, while galaxies of intermediate stellar mass show an increase of star formation at filament-like densities. We also find overall that the median [OII] equivalent width (*$|EW_{[\mathrm{OII}]}|$*) decreases from* $28.4 \pm 0.44$ *Å to* $3 \pm 0.3$ *Å and* $D_n4000$ *increases from* $1.12 \pm 0.01$ *to* $1.52 \pm 0.06$ *with increasing stellar mass (from* $\sim 10^{9.25}$ *to* $\sim 10^{11.35}$ $\mathrm{M}_\odot$*). Concerning its dependence on environment we find that at fixed stellar mass* $|EW_{[\mathrm{OII}]}|$ *is tentatively lower in higher density environments. Regarding* $D_n4000$*, we find that the increase with stellar mass is sharper in denser environments, hinting that such environments may accelerate galaxy evolution. Moreover, we find that* $D_n4000$ *is higher in denser environments at fixed stellar mass which points that galaxies are on average older and/or more metal rich in such dense environments. This set of tracers depicts a scenario where the most massive galaxies have on average the lowest sSFRs (the weakest [OII] equivalent width, a natural consequence of the underlying star-forming main sequence) and the oldest stellar populations (*$\gtrsim 1$ *Gyr, showing a mass-downsizing effect). We also hypothesize that the observed increase in star formation (higher* $EW_{[\mathrm{OII}]}$*, higher sSFR) at intermediate-densities may precede an episode of star formation quenching since we find that the quenched fraction increase sharply from filament to cluster-like regions at similar stellar masses.*

adapted from **Paulino-Afonso**, Sobral, D., Darvish, B. et al., A&A submitted

## 6.1 INTRODUCTION

One of the key tracers of galactic evolution is the rate at which gas is converted into stars, measured as the star formation rate (SFR, e.g. Kennicutt, 1998; Kennicutt & Evans, 2012). Observations show that galaxies were actively forming stars at a rate $\sim 10$ times higher at $z \sim 2$ than at $z \sim 0$ (both the cosmic star formation rate density and typical SFRs decrease during this epoch, see e.g. Madau & Dickinson, 2014; Sobral et al., 2014). One of the fundamental questions of modern Astronomy is to understand the mechanisms responsible for the regulation of star formation in galaxies and find how efficient galaxies are in converting gas into stars (see e.g. Combes et al., 2013; Lehnert et al., 2013).

There are two broad groups of processes, internal and external, that can contribute to the evolution of any given galaxy (e.g. Kormendy, 2013). However, the contribution of each set of processes to regulating star formation in galaxies is still unclear (see e.g. Erfanianfar et al., 2016). Internal processes include dynamical instabilities (e.g. Kormendy, 2013), halo quenching (e.g. Birnboim & Dekel, 2003; Kereš et al., 2005, 2009b; Dekel & Cox, 2006), supernova feedback (e.g. Efstathiou, 2000; Cox et al., 2006), and active galactic nuclei (AGN) feedback (e.g. Bower et al., 2006; Croton et al., 2006; Somerville et al., 2008; Fabian, 2012). External processes include galaxy interactions with other galaxies or the inter galactic medium, specifically ram pressure stripping (e.g. Gunn & Gott, 1972), galaxy strangulation (e.g. Larson et al., 1980; Balogh et al., 2000), galaxy-galaxy interactions and harassment (e.g. Mihos & Hernquist, 1996; Moore et al., 1998), or tidal interaction between the large-scale gravitational potential and the galaxy (e.g. Merritt, 1984; Fujita, 1998). These range of physical processes are thought of being the way through which galaxies regulate and eventually halt the formation of new stars, a phenomenon commonly referred to as galaxy quenching (e.g. Gabor et al., 2010; Peng et al., 2010b).

The way in which each proposed mechanism affects individual galaxies is complex. In internal processes, feedback can either heat or eject the gas from galaxies preventing it from condensing in molecular clouds to form new stars (e.g. Kereš et al., 2009a). Supernova feedback is more important at lower stellar masses and AGN feedback is an important mechanism for quenching at high stellar masses (e.g. Puchwein & Springel, 2013). Halo quenching refers to gravitational heating preventing gas to cool down and form new stars. However, it requires a sustained mechanism to heat the gas (e.g. Birnboim et al., 2007) and cold gas flows might still penetrate the halo into the galactic disk to fuel star formation (e.g. Kereš et al., 2009b).

In external processes, ram pressure stripping can initially compress the gas/dust thus increasing the column density of the gas and dust which is favourable for star formation (e.g. Gallazzi et al., 2009; Bekki, 2009; Owers et al., 2012; Roediger et al., 2014). Tidal galaxy-galaxy interactions can lead to the compression and inflow of the gas in the periphery of galaxies into the central part, feeding and rejuvenating the nuclear activity which results in a temporary enhancement in

star formation activity (e.g. Mihos & Hernquist, 1996; Kewley et al., 2006; Ellison et al., 2008). Of similar nature, galaxy-galaxy encounters can also act as a catalyst for a burst of star formation. Such encounters are more probable when the galaxies do not have high velocities (low-velocity-dispersion environment) and are closer to each other (denser regions). Intermediate-density environments such as galaxy groups, in-falling regions of clusters, cluster outskirts, merging clusters, and galaxy filaments provide the ideal conditions for such interactions (e.g. Moss, 2006; Perez et al., 2009; Li et al., 2009; Sobral et al., 2011; Tonnesen & Cen, 2012; Darvish et al., 2014; Stroe et al., 2014, 2015; Malavasi et al., 2017). This temporary enhancement of star formation is thought to be responsible for the subsequent quenching, since most of the available gas is consumed or expelled through outflows in a short period of time effectively preventing future star formation to occur in the galaxy without further external influence. If those events are ubiquitous, one should observe a temporary rise of star formation in such environments after which galaxies are expected to quench. This has been found in several studies referring to the intermediate-density environments as sites of enhanced star formation rate and obscured star formation activity (e.g. Smail et al., 1999; Best, 2004; Koyama et al., 2008, 2010, 2013; Gallazzi et al., 2009; Geach et al., 2009; Sobral et al., 2011, 2016; Coppin et al., 2012; Stroe et al., 2015, 2017c).

Since many of these mechanisms are linked to regions of increased number density of galaxies, it is natural to look for the impact of the local environment on the observed properties of each object. In the local Universe ($z \sim 0$), the star formation rate (SFR) is typically lower in higher density environments (e.g. Oemler, 1974; Dressler, 1980; Gómez et al., 2003; Kauffmann et al., 2004; Blanton et al., 2005a; Li et al., 2006; Peng et al., 2010b; Darvish et al., 2016, 2018). By separating galaxies into distinct populations (star-forming and quiescent, see e.g. Williams et al., 2009; Ilbert et al., 2010; Arnouts et al., 2013; Carollo et al., 2013), studies find that the quenched fraction is highly dependent on the local density (at least up to $z \lesssim 1$) with the quenched population being more common in high-density regions and a higher fraction of star-forming galaxies found in lower density regions (e.g. Kodama et al., 2001, 2004; Best, 2004; Nantais et al., 2013b; Darvish et al., 2016; Erfanianfar et al., 2016; Cohen et al., 2017). While in the local Universe the picture is clear, with SFR being the lowest in high-density and relaxed cluster regions (e.g. Balogh et al., 2000; Kauffmann et al., 2004), it is still unclear if that holds to higher redshifts. Some studies find a flattening and/or reversal of such relation ($z \sim 1 - 1.5$, e.g. Cucciati et al., 2006; Elbaz et al., 2007; Ideue et al., 2009; Tran et al., 2010; Popesso et al., 2011; Li et al., 2011; Santos et al., 2014), while others find the same trends that we see locally (e.g. Patel et al., 2009; Sobral et al., 2011; Muzzin et al., 2012; Santos et al., 2013; Scoville et al., 2013; Darvish et al., 2016). It is possible that reconciling the different observed trends requires a more detailed analysis on other possible underlying relations, especially with stellar mass (e.g. Peng et al., 2010b; Sobral et al., 2011; Muzzin et al., 2012; Darvish et al., 2016), and also controlling for other properties such as AGN fraction and dust content. An alternative explanation might be

the stochastic nature of the formation of dense environments which can explain the observed differences as natural cosmic variance.

Recent studies in the literature are using spectral indices [OII], H$\delta$, and $D_n4000$ to probe the stellar population of galaxies at intermediate redshifts ($0.5 \lesssim z \lesssim 1.2$) due to their availability in the optical observed frame. The [OII] emission, which traces on-going star formation (timescales of $\sim$10 Myr, e.g. Couch & Sharples, 1987; Poggianti et al., 1999; Kennicutt, 1998; Kewley et al., 2004; Poggianti et al., 2006) and the specific SFR (sSFR, from measuring the line equivalent width), is found to anti-correlate with stellar mass (e.g. Bridge et al., 2015; Cava et al., 2015; Darvish et al., 2015a) with more massive galaxies having weaker [OII] emission. Additionally, higher density environments are found to depress [OII] emission (e.g. Darvish et al., 2015a). The 4000Å break is also found to be stronger for higher stellar mass galaxies (e.g. Muzzin et al., 2012; Vergani et al., 2008; Hernán-Caballero et al., 2013; Siudek et al., 2017; Wu et al., 2018), hinting at their older stellar populations. In terms of local density, Muzzin et al. (2012) found that galaxies in cluster environments have on average stronger breaks than their field counterparts at similar stellar masses, which they argue that can be explained by the different fractions of star-forming and quiescent galaxies in different environments. The H$\delta$ absorption line is mostly used to identify recent starbursts (e.g. Couch & Sharples, 1987; Balogh et al., 1999; Poggianti et al., 1999, 2009; Dressler et al., 2004; Vergani et al., 2010; Mansheim et al., 2017b) due to a dominant population of A stars and a lack of on-going or detectable star formation (e.g. Dressler & Gunn, 1983; Couch & Sharples, 1987; Poggianti et al., 1999). Recently, Wu et al. (2018) found that H$\delta$ equivalent width correlates with stellar mass with more massive galaxies having weaker H$\delta$ absorption lines, but have no study on the impact of environment (see also e.g. Siudek et al., 2017, for a similar result on passive galaxies).

We aim to investigate the influence of environment on the star formation history of galaxies using a number of spectral indicators (e.g. Balogh et al., 1999; Poggianti et al., 1999, 2009; Dressler et al., 2004; Vergani et al., 2010; Mansheim et al., 2017a; Wu et al., 2018). Due to the spectral coverage of the VIMOS Spectroscopic Survey of a Superstructure in the COSMOS field (VIS$^3$COS, Paulino-Afonso et al., 2018a, Chap. 5) we estimate the current and past star formation activity of galaxies using a combination of [OII] (for on-going star formation, $\lesssim$10Myr), H$\delta$ (for probing star-formation on intermediate timescales - 50 Myr to $\sim$1 Gyr prior to observation), and $D_n4000$ (probing the star formation history on longer timescales). We investigate this using spectroscopic observations of $\sim$ 500 galaxies in and around a superstructure at $z \sim 0.84$ in the COSMOS field (Sobral et al., 2011, Chap. 5) by probing a wide range of environments and stellar masses with a single survey.

This chapter is organized as follows: in Sect. 6.2 we briefly explain the survey and give some details on the data used. Section 6.3 details the stacking methods and the spectroscopic measurements. In Sect. 6.4 we present the results from individual and stacked spectral properties. We discuss our findings in Sect. 6.5. Section 6.6 presents the conclusions of the study. We use

AB magnitudes (Oke & Gunn, 1983), a Chabrier (Chabrier, 2003) initial mass function (IMF), and assume a ΛCDM cosmology with $H_0$=70 km s$^{-1}$Mpc$^{-1}$, $\Omega_M$=0.3 and $\Omega_\Lambda$=0.7. The physical scale at the redshift of the superstructure ($z \sim 0.84$) is 7.63 kpc/″.

## 6.2 THE VIS$^3$COS SURVEY

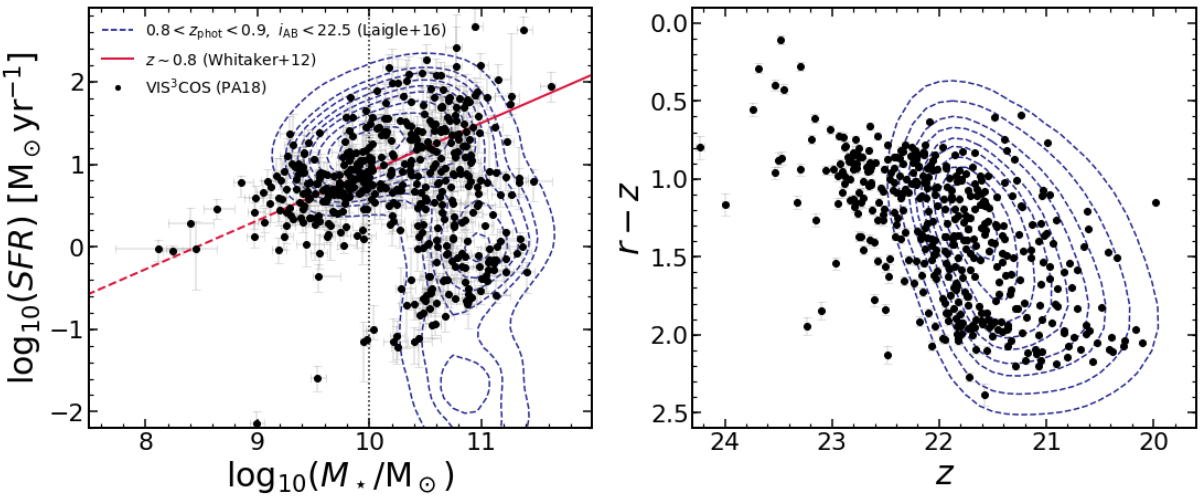


**Figure 6.1** Stellar masses and star formation rates derived from SED fitting in our spectroscopic sample at $0.8 < z < 0.9$ (left). Colour-magnitude diagram for the same sample (right). For comparison we show the derived best-fit relation for star-forming galaxies computed at $z = 0.84$ using the equation derived by Whitaker et al. (2012) over a large average volume in the COSMOS field (the dashed line is an extrapolation below their stellar mass completeness). The vertical dotted line shows the approximate stellar mass completeness limit of our survey. The dotted contours show the COSMOS2015 distribution of galaxies with $0.8 < z_{\rm phot} < 0.9$ and $i_{\rm AB} < 22.5$ from 10% to 90% of the sample in 10% steps. We note that our sample are representative of the larger galaxy population in COSMOS at the same redshifts.

The VIS$^3$COS survey maps a large $z \sim 0.84$ over-density spanning $21' \times 31'$ ($9.6 \times 14.1$ Mpc$^2$) in the COSMOS field (Scoville et al., 2007) with the VIMOS instrument mounted on the VLT/ESO. This structure contains three confirmed X-ray clusters (Finoguenov et al., 2007) and also harbours large scale over-density of H$\alpha$ emitters (Sobral et al., 2011; Darvish et al., 2014). The full description of the data and redshift measurements are presented in Chap. 5 and we briefly describe here some details.

We targeted galaxies selected from Ilbert et al. (2009) catalogue and with $0.8 < z_{\rm phot,l} < 0.9$ (with $z_{\rm phot,l}$ being either the upper or lower 99% confidence interval limit for each source) and $i_{\rm AB} < 22.5$, corresponding to a typical stellar mass of $10^{10}$M$)_\odot$. For the selected targets we obtained high resolution spectra with the VIMOS High Resolution red grism (with the GG475 filter, $R \sim 2500$). This grism covers the $3400 - 4600$Å rest-frame at the redshift of the target superstructure. The observational configuration of the survey was done so we could measure spectral features such as [OII] $\lambda$3726,$\lambda$3729 (partially resolved doublet), the 4000Å break, and H$\delta$ for the superstructure members.

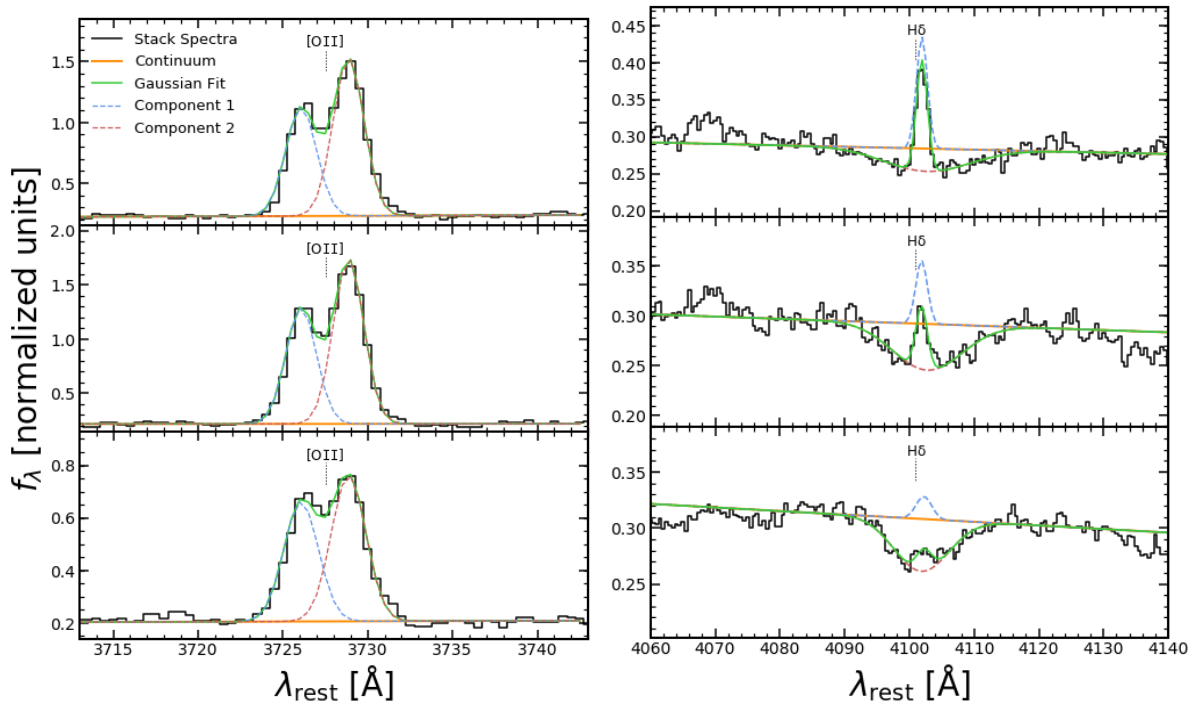


**Figure 6.2** Three examples of the fit to the stacked [OII] emission (left) and the stacked H$\delta$ absorption+emission (right) spectral lines. The solid black line shows the observed spectrum. The green line shows the median fit (after 10 000 realizations) and the orange line the estimated continuum around the line. We also show in red and blue dashed lines the fit of each individual Gaussian component.

We measure the redshifts of our sources using SPECPRO (Masters & Capak, 2011) on the extracted 1D spectra and using a combination of [OII], H+K absorption, G-band, some Fe lines, and H$\delta$. All spectra were visually inspected for the features aforementioned. We obtain secure spectroscopic redshifts for 696 sources with high S/N of which 490 are at $0.8 < z < 0.9$. Spectroscopic failures are related to either low S/N continuum or the lack of obvious features.

With the knowledge of the spectroscopic redshift we improve the estimate of physical parameters that are available in the COSMOS2015 photometric catalogue (Laigle et al., 2016). We ran MAGPHYS (da Cunha et al., 2008) with spectral models constructed from the stellar libraries by Bruzual & Charlot (2003) and using photometric bands from near-UV to near-IR. The dust is modelled following the prescription described by Charlot & Fall (2000). We obtain estimates for the stellar masses and star formation rates for 466 out of the 490 galaxies that are observed at $0.8 < z < 0.9$. Galaxies with no estimates are fainter $I$-band sources with no match in COSMOS2015. We compare our stellar masses and star formation rates with those provided in the COSMOS2015 catalogue and find negligible offsets (median difference of $< 0.05$ dex for both stellar mass and SFR) and a dispersion of $\sim 0.3$ dex for the stellar mass and $\sim 0.7$ dex for the SFR. The scatter is smaller, $\sim$0.15 dex and $\sim$0.6 dex respectively, if we consider galaxies with $|z_{\rm spec} - z_{\rm phot}| < 0.1$. For this study, we use SED derived SFRs since [OII] emission is a poor tracer of SFR for red galaxies and depends on gas-phase metallicity (e.g. Kewley et al., 2004; Yan et al., 2006; Kocevski et al., 2011) and we have no independent way to quantify

dust extinction or measure metallicity from our spectral coverage. We refer to Chap. 5 for a comparison between SED and [OII] derived SFRs.

Our final sample is restricted to be at $0.8 < z < 0.9$ to match our primary selection (see Chap. 5) and has a total of 466 galaxies spanning a large diversity of environments across several Mpc. We show in Fig. 6.1 the colour-magnitude diagram ($r-z$ versus $z$-band) and the stellar mass-SFR relation from our sample and compare it to the parent photometric catalogue. We highlight that our sample is probing a similar parameter space as those of the general population at similar redshifts.

To estimate the local galaxy over-density we use the density fields computed by Darvish et al. (2015b, 2017). These results are based on the photometric redshift catalogue in the COSMOS field provided by Ilbert et al. (2013). The density field was calculated for a $\sim 1.8\,\mathrm{deg}^2$ area using a mass-limited ($\log_{10}(M/\mathrm{M}_\odot) > 9.6$) sample at $0.1 < z_{\mathrm{phot}} < 1.2$. In this chapter we define as over-density

$$1+\delta = \frac{\Sigma}{\Sigma_{\mathrm{median}}} \tag{6.1}$$

with $\Sigma_{\mathrm{median}}$ being the median of the density field of a specific redshift slice. We used an adaptive kernel with variable size, with small kernel size for crowded regions and larger kernel size for sparser regions, around a typical width of 0.5 Mpc (characteristic size of X-ray clusters, see e.g. Finoguenov et al., 2007). For a more detailed description of the method, we refer to Darvish et al. (2015b, 2017). Having a pure density-based definition of the environment does not translate exactly into different physical regions (see e.g. Aragón-Calvo et al., 2010; Darvish et al., 2014). Nonetheless there are typical densities at which field ($\log_{10}(1+\delta) \lesssim 0.1$), filament ($0.1 \lesssim \log_{10}(1+\delta) \lesssim 0.6$), and cluster galaxies ($\log_{10}(1+\delta) \gtrsim 0.6$) dominate the population (see Chap. 5 for more details).

## 6.3 SPECTROSCOPIC PROPERTIES

To study the star formation activity levels of galaxies, we use three tracers present in our spectra (e.g. Balogh et al., 1999; Dressler et al., 2004; Oemler et al., 2009; Poggianti et al., 2009; Vergani et al., 2010; Mansheim et al., 2017b). The $\mathrm{H}_\delta$ line can be an indicative of a post-starburst phase ($\approx 100-1000$ Myr after the burst), if a strong absorption (typical of A stars, where hydrogen absorption is the strongest) is observed and no indication of on-going star formation (Couch & Sharples, 1987). The [OII] doublet in emission is linked to on-going star formation in the galaxy (e.g. Kewley et al., 2004). Finally, a measure of the flux break at 4000Å ($D4000$ and $D_n4000$, as defined by Bruzual 1983 and Balogh et al. 1999, respectively), traces the age of the galaxy

and also the stellar metallicity (especially for older systems) to a lesser degree. This break is produced by a combination of metal absorption on the atmosphere of old and cool stars and the lack of flux from young and hot OB stars (e.g. Poggianti & Barbaro, 1997) and so it is sensitive to the average age of the stellar population. All these indicators, when used together, can be used to distinguish actively star-forming, (post-) starburst, and old/passive galaxies since they should occupy different regions of the possible parameter space (e.g. Couch & Sharples, 1987; Balogh et al., 1999; Poggianti et al., 2009; Fritz et al., 2014).

### 6.3.1 Composite spectra

Co-adding spectra of galaxies binned by similar physical properties increases the signal-to-noise ratio and allows for a better determination of the median spectral properties of the sample in different regions of the parameter space that we aim to probe (e.g. Lemaux et al., 2010). We construct composite spectra by binning in stellar mass, over-density, and star formation rate.

To obtain a composite spectra we median combined (we obtain similar results with an average spectra) the set of normalized rest-frame spectra interpolated into a common wavelength grid. Using the redshift we have measured (see Sect. 6.2), we linearly interpolate the spectrum onto a common universal grid ($3250-4500$Å, $\Delta\lambda = 0.5$ Å pix$^{-1}$). We also obtain an error of the median spectra from the combination of the individual error spectra. We normalize each spectrum dividing it by the median flux measured at $4150-4350$Å. Finally, we obtain the composite spectra as the median flux per wavelength bin in the defined grid. We have repeated our analysis using different normalization schemes (blue-ward of 4000Å and with no normalization) and our results are qualitatively the same.

We have compared the derived parameters from the composite spectra with the median value for the population for which we have individual measurements ([OII] and $D_n4000$). In the case of [OII] emission, the composite spectra has systematically lower values for the line equivalent width (median difference of 3Å) when compared to the median of the population. This is explained by the fraction of galaxies with no individually measured [OII] emission that are included in the stack, lowering the strength of the emission. For $D_n4000$ the results we find a good agreement (median difference of 0.02) between the composite spectra and the median from individual measurements.

### 6.3.2 Spectral quantities

To be consistent with the classical notation, a negative equivalent width corresponds to a line in emission while positive values correspond to a line in absorption.

#### 6.3.2.1 [OII] EMISSION

To measure the [OII] we fit a double Gaussian to the doublet. The centre of each component is set to be $\lambda_1 = 3726.08 \pm 0.3$Å and $\lambda_2 = 3728.88 \pm 0.3$Å (a small shift in the line centre is allowed to account for our finite resolution and we allow for a systematic shift to the doublet to account for redshift uncertainties). We measure the flux and line equivalent widths by integrating over the best-fit models. For more details we refer the reader to Chap. 5 (see also Fig. 6.2, left panel).

#### 6.3.2.2 H$\delta$ IN EMISSION AND ABSORPTION

We fit the emission and absorption components of the H$\delta$ line by first fitting a single Gaussian to the absorption feature (whenever present) masking the $\pm$3Å around the central wavelength to avoid contamination by nebular emission. We then subtract the absorption model to the observed spectra and fit with a single Gaussian to the emission (see Fig. 6.2, right panel). We make this choice since we do not have enough signal-to-noise, even in some of the composite spectra (see Sect. 6.3.1), to perform simultaneous de-blending between the nebular emission and the stellar absorption component. In cases where one of the two components is much fainter than the other, the fitting of two simultaneous components fails to converge and is loosely constrained by a set of degenerate model combinations which produce the same combined result but for which the individual components are clearly not physically representative of the observed data (the sum of two symmetric components is degenerate against an equal multiplicative factor on the amplitude of individual components).

#### 6.3.2.3 CONTINUUM AND ERROR ESTIMATION

For all line fits we individually define two regions (one blue-ward, one red-ward of the line) with a width of 15 Å width ($\sim$3 times the spectral resolution) from which we estimate the median continuum level. Then the local continuum is defined as a straight line that goes through those two points (see e.g. Balogh et al., 1999; Lemaux et al., 2010; Mansheim et al., 2017b). To minimize the effect of a particular choice of windows from which we compute the continuum, we compute the median flux for 5 000 random shifts of $k$Å on the proposed interval, where $k$ is randomly drawn from a normal distribution centred at 0 and with a width of 5Å. Then the final estimate of the continuum is measured from the median of the 5 000 realizations.

To estimate the errors on the derived spectral quantities, we have randomly perturbed each composite spectra by its error, replacing the flux at each wavelength bin by a random value taken from a normal distribution centred on the observed flux and with $\sigma$ equal to the computed

error in that bin. We then fit our line models to the perturbed spectra to obtain a set of best-fit parameters. We have performed 10 000 realizations and derive the errors from the 16th and 84th percentiles of the distribution of best-fit values.

#### 6.3.2.4 4000Å BREAK

Apart from line measurements, we have also computed the strength of the break at 4000Å ($D4000$ and $D_n4000$ defined by Bruzual, 1983; Balogh et al., 1999, respectively). We automated the computation of these quantities by integrating the spectra over the red ($D4000$:4050-4250Å, $D_n4000$: 4000-4100Å) and blue ($D4000$: 3750-3950Å, $D_n4000$: 3850-3950Å) intervals and computing the ratio of those fluxes as

$$X4000 = \frac{\int_{\lambda_{r1}}^{\lambda_{r2}} f_\nu d\lambda}{\int_{\lambda_{b1}}^{\lambda_{b2}} f_\nu d\lambda} \tag{6.2}$$

where $X$ is either $D$ or $D_n$ depending on the integration limits of the red ($\lambda_{ri}$) and blue ($\lambda_{bi}$) intervals. When comparing both indices we find them to correlate well, with a median difference of $< 1\%$ and a spread of 30% on individual measurements. We opt to use for the remainder of the chapter the value of $D_n4000$ since it should be less affected by errors due to Poisson sampling and less affected by reddening (Balogh et al., 1999). Nevertheless our results are qualitatively the same regardless of which index we use. To avoid the contamination by emission lines in the integrated regions we mask 6Å regions around the [NeIII] and H$\zeta$ lines (see e.g. Fig. 6.10).

### 6.3.3 STELLAR POPULATION AGE ESTIMATES

Estimating a single representative stellar age for galaxies is not a trivial task due to their individual star formation histories. Nonetheless, we can obtain an estimate given a few set of assumptions. We will use the $D_n4000$ index as a proxy for age and obtain an estimate from a set of stellar population models described by Bruzual & Charlot (2003). We attempt to estimate an age based on a single stellar population (SSP), with the notation $t_{\rm SSP}$, which should trace the age of the last major burst that the galaxy had.

We note that the $D_n4000$ index depends not only on age but also on the stellar metallicity, especially for ages greater than 1 Gyr (e.g. Bruzual, 1983; Poggianti & Barbaro, 1997; Balogh et al., 1999). Since we do not have any independent way to estimate stellar metallicity for our dataset we chose to adopt an estimate for our sample based on a recent numerical simulation study by Ma et al. (2016) which parametrizes stellar metallicity as a function of stellar mass and redshift as:

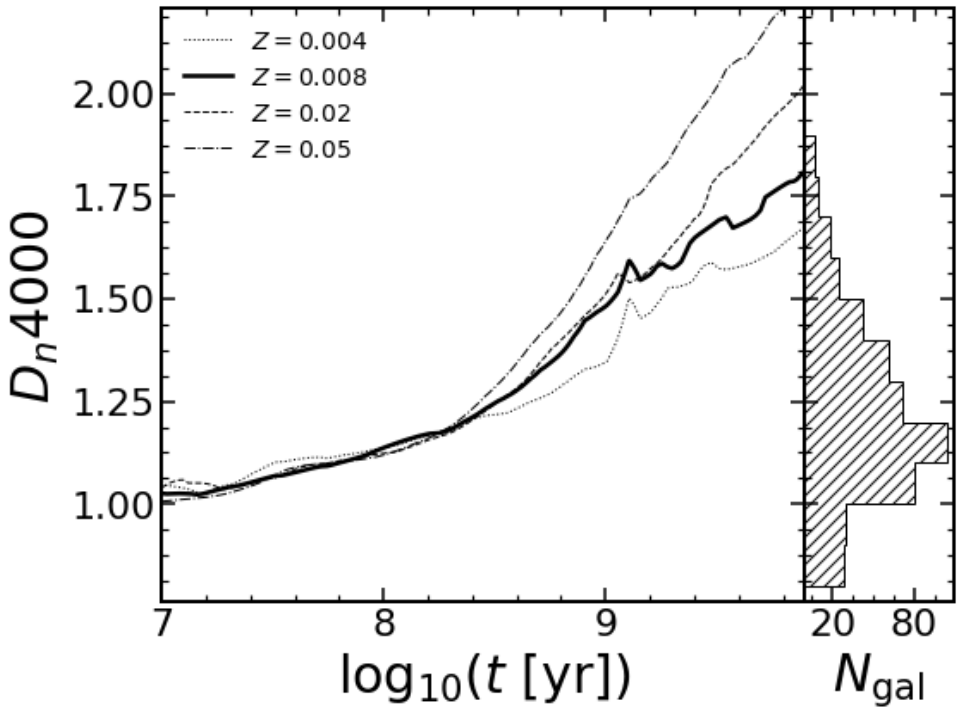


**Figure 6.3** The value of $D_n4000$ as a function of stellar age for a single stellar population from Bruzual & Charlot (2003) for four different stellar metallicities(we highlight as the dark solid line the expected stellar metallicity for our sample $Z = Z_{\odot}/2.5$, see Sect. 6.3.3). On the right panel we show the distribution of measured $D_n4000$ values for the galaxies in our sample.

$$\log_{10}\left(\frac{Z_{\star}}{Z_{\odot}}\right) = 0.40\left[\log_{10}\left(\frac{M_{\star}}{M_{\odot}}\right) - 10\right] + 0.67e^{-0.5z} - 1.04. \tag{6.3}$$

For the typical mass ($10^{10.5}M_{\odot}$) and redshift ($z = 0.84$) of our sample we get a stellar metallicity of $Z_{\star} \sim 0.008 = Z_{\odot}/2.5$. For a stellar mass of $10^{11.5}M_{\odot}$ we get $Z_{\star} \sim 0.02$ and for a stellar mass $10^{9.5}M_{\odot}$ we get $Z_{\star} \sim 0.003$. We show in Fig. 6.3 the age dependence of $D_n4000$ for 4 different metallicities spanning the expected range of our sample.

Assuming then a metallicity of $Z_{\odot}/2.5$ for an SSP based on Bruzual & Charlot (2003) models we measure $D_n4000$ as a function of stellar age and use the derived curve (see Fig. 6.3) to estimate stellar ages from our measurements of the 4000Å break. We stress that if galaxies have higher metallicities than our assumption, we underestimate the stellar age. If they have lower metallicities, we overestimate the stellar age.

## 6.4 Results

We explore the results on the spectral properties of our galaxies at $0.8 < z < 0.9$ highlighting both composite spectra and individual galaxies in this section. Our aim is to probe the influence

of key physical properties (stellar mass, environment, and SFR) on the median observed spectral properties of our sample. We note that with respect to H$\delta$ we have insufficient S/N on most galaxies to get robust measurements and we refrain from discussing that spectral feature in terms of individual galaxies.

We summarize in Fig. 6.4 (see also Appendix and Table 6.2) the properties of composite spectra on [OII] and H$\delta$ (both emission and absorption) line equivalent widths and $D_n4000$ at different stellar masses, over-densities, and SFRs. We stress that for samples not selected in stellar mass, we impose a minimum stellar mass limit of $10^{10}$M$_\odot$.

### 6.4.1 GLOBAL TRENDS ON THE SPECTROSCOPIC PROPERTIES

#### 6.4.1.1 STELLAR MASS

In terms of the [OII] line equivalent width (EW$_{[\rm OII]}$), we find in Fig. 6.4 a strong decrease with stellar mass, by a factor of $\sim 10$ in strength from the lowest ($9 < \log_{10}(M_\star/\mathrm{M}_\odot) < 9.5$) to the highest stellar mass bin ($\log_{10}(M_\star/\mathrm{M}_\odot) > 11$), which points to a decrease in sSFR with increasing stellar mass from $\sim 10^{-9}\mathrm{yr}^{-1}$ to $\sim 10^{-10}\mathrm{yr}^{-1}$ (a consequence of the main sequence of star-forming galaxies, see also Darvish et al., 2015a). We compare the results for individual galaxies and composite spectra with others available in the literature (Bridge et al., 2015; Cava et al., 2015; Darvish et al., 2015a). Our results are broadly consistent (in terms of the observed trends) with the literature which find a decrease in the absolute line equivalent width with increasing stellar mass. However, we find some discrepancies with Cava et al. (2015) and Bridge et al. (2015) in terms of the average value in bins of stellar mass that are likely related to the target selection in each work. In the case of Cava et al. (2015) they report consistently higher values of [OII] line equivalent width. However, their sources are selected through medium band filters down to equivalent widths of $\sim$15-20Å, which naturally explains their higher median values. As for the case of Bridge et al. (2015) they study a large field with blind spectroscopy and they exclude large equivalent width ($EW \gtrsim 40$Å) galaxies to avoid contamination by higher redshift interlopers (Ly$\alpha$ emitters), which can explain their observed lower equivalent widths. We find $EW_{[\rm OII]}$ values consistent with Darvish et al. (2015a), which had a similar observational setup as the VIS$^3$COS survey.

In the middle panels of Fig. 6.4 we show the measured equivalent width of the H$\delta$ emission and absorption for all composite spectra which allowed a measurement (some of them did not show any signs of absorption). The H$\delta$ absorption line equivalent width decreases with increasing stellar mass (from $\mathrm{EW}_{\mathrm{H}\delta} = 2.8 \pm 0.01$Åat $9.5 < \log_{10}(M_\star/\mathrm{M}_\odot) < 10$ down to $\mathrm{EW}_{\mathrm{H}\delta} = 0.8^{+0.14}_{-0.39}$Å at $\log_{10}(M_\star/\mathrm{M}_\odot) > 11$). The H$\delta$ emission line equivalent also correlates

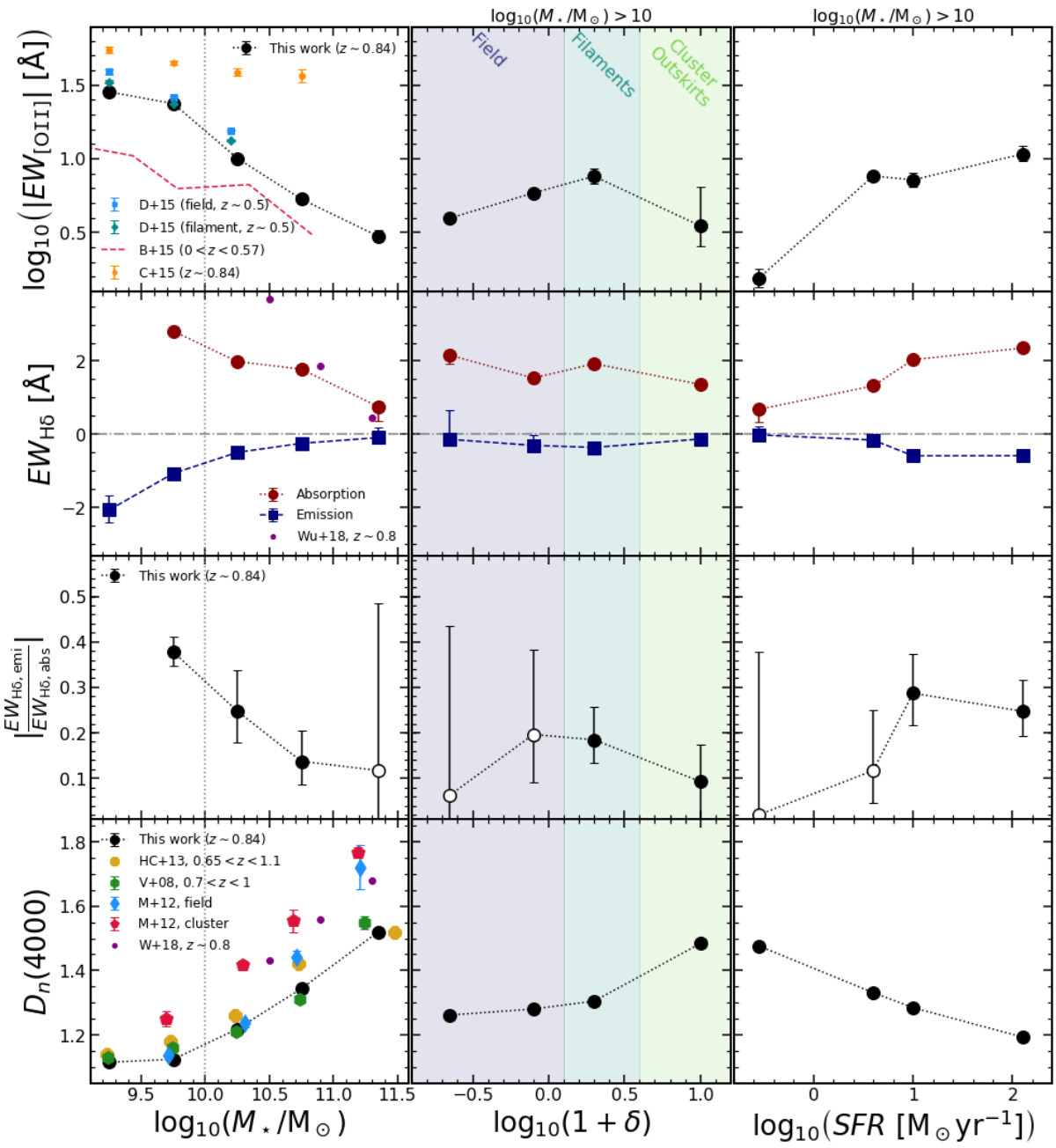


**Figure 6.4** The dependence of the three spectral features detailed in Sect. 6.3.2 (from top to bottom - [OII] equivalent width, H$\delta$ equivalent widths, and $D_n4000$) as a function of stellar mass (left), over-density (middle), and SED-derived SFR (right). We show our stellar mass completeness limit as a vertical dotted line in the left panels. We note that for bins not defined in stellar mass (middle and right panels), the composite spectra is built from galaxies with stellar mass greater than $10^{10}$M$_\odot$. Results from this chapter are shown as large and dotted line connected symbols with associated error bars (if the error bars are not seen, it implies an error smaller than the symbol size). When looking at trends with stellar mass, we see a decrease in [OII] and H$\delta$ emission (blue squares) and absorption (red circles) strength and an increase of the average age of the stellar population (traced by $D_n4000$). For trends with over-density, there is a peak in [OII] equivalent width at filament-like densities and H$\delta$ equivalent widths show little dependence on local density. There is also a clear trend for galaxies being older in higher density regions. Lastly both [OII] and H$\delta$ strength increase with SFR (excluding the most star-forming galaxies) and we see younger populations in galaxies with higher SFR, as expected. We compare our results to other surveys in the literature (Bridge et al., 2015; Darvish et al., 2015a; Cava et al., 2015; Wu et al., 2018; Hernán-Caballero et al., 2013; Vergani et al., 2008; Muzzin et al., 2012). In general we find similar trends to what is previously reported. For a more detailed discussion on the differences we refer to Sect. 6.4.2.1 and 6.4.2.2.

with stellar mass with stronger emission being found at lower stellar masses, dropping from $\mathrm{EW}_{\mathrm{H}\delta} = -2.1^{+0.39}_{-0.34}$Å at $9.0 < \log_{10}(M_\star/\mathrm{M}_\odot) < 9.5$ to a marginally non-existent emission component with $\mathrm{EW}_{\mathrm{H}\delta} = -0.1^{+0.28}_{-0.08}$Å at $\log_{10}(M_\star/\mathrm{M}_\odot) > 11$. When compared to the results by Wu et al. (2018) we see that there is also a decrease on their reported equivalent width with stellar mass but at a much steeper rate. We attribute the discrepancies to the different methods used to compute the line equivalent width. They use a spectral index defined by Worthey & Ottaviani (1997) which includes measures the line equivalent width on an emission subtracted/masked spectrum. We also show the dependence of the emission to absorption ratio of the equivalent widths as a proxy for the ratio of O to A stars. For its dependence with stellar mass we find that this ratio is the highest at stellar masses $9.5 < \log_{10}(M_\star/\mathrm{M}_\odot) < 10.0$ (ratio of $0.4 \pm 0.03$). It then decreases consistently towards higher stellar masses reaching $0.1^{+0.4}_{-0.1}$ at $\log_{10}(M_\star/\mathrm{M}_\odot) > 11$. This hints at a higher fraction of young stars in less massive systems.

The bottom panels of Fig. 6.4 show the dependence of the 4000Å break strength on the same quantities mentioned above. We find a strong correlation between $D_n4000$ with stellar mass, increasing from $D_n4000 = 1.12 \pm 0.01$ at $9 < \log_{10}(M_\star/\mathrm{M}_\odot) < 9.5$ to $D_n4000 = 1.52 \pm 0.006$ at $\log_{10}(M_\star/\mathrm{M}_\odot) > 11$. This trend points to more massive galaxies also having the older stellar populations. Our results are in general agreement with other studies in the literature targeting either clustered regions (GCLASS - Muzzin et al., 2012) or large field surveys (VVDS, SHARDS, LEGA-C - Vergani et al., 2008; Hernán-Caballero et al., 2013; Wu et al., 2018„ respectively). The trend with stellar mass is seen in all surveys. We find lower median $D_n4000$ at fixed stellar masses with respect to values reported by Muzzin et al. (2012) and Wu et al. (2018). We argue that this may be due to sample selection effects as these two surveys are selected in redder-bands (3.6$\mu$m and $K$-band, respectively) and these tend to be more effective at picking up older galaxies thus having higher values for $D_n4000$. We are in good agreement with Vergani et al. (2010) which is based on $I$-band selection, as is the VIS$^3$COS survey. We note that Hernán-Caballero et al. (2013) also select on 3.6$\mu$m but they measure $D_n4000$ on medium band data and they note in their study that doing so tends to decrease the value of $D_n4000$ with respect to a higher resolution spectrum.

#### 6.4.1.2 Local environment

Our analysis is restricted to stellar masses greater than $10^{10}\mathrm{M}_\odot$ and for this sub-sample there is little variation in the median stellar mass across the different bins ($\Delta\log_{10}(M_\star/\mathrm{M}_\odot) < 0.15$). We find an increase of $\mathrm{EW}_{[\mathrm{OII}]}$ from $-4.0 \pm 0.3$Å to $-7.6 \pm 0.9$Å from field to filament-like densities and then drops to $-3.5^{+2.1}_{-1.1}$Å at the highest densities. This is pointing to a slight increase of the sSFR at filament-like densities for galaxies more massive than $10^{10}\mathrm{M}_\odot$. We note that at the highest densities we have median $\mathrm{EW}_{[\mathrm{OII}]}$ comparable to that found a field-like densities. One might naively expect that at these densities the star formation to be lower than in the field.

However, these values can either be due a continuous in star formation decrease from galaxies which were forming more stars at filament-like densities, or to an increase of [OII] emission at cluster-like densities due to other ionizing sources (e.g. AGN).

Regarding the H$\delta$ line, we find a small decrease of the observed H$\delta$ absorption equivalent with increasing over-density, from $2.2^{+0.09}_{-0.24}$Å at $\log_{10}(1+\delta) < -0.3$ to $1.4 \pm 0.04$Å at the highest densities. For H$\delta$ emission, all our derived values for galaxies more massive than $10^{10}$M$_{\odot}$ are consistent with no dependence with over-density, having measured equivalent widths around $\sim$0.2Å. We find no significance on the results regarding the ratio between absorption and emission of H$\delta$. We tend to find an increase from low to intermediate densities and then a drop towards higher densities. However, we cannot exclude the null hypothesis of no dependence on over-density given our error bars.

Finally, we find an increase of $D_n4000$ towards higher densities. In low to intermediate density regions ($\log_{10}(1+\delta) < 0.5$) we find $D_n4000 \sim 1.27$ (corresponding to an SSP age of $0.4-0.5$ Gyr). The strength of the 4000Å break then increases at higher densities ($\log_{10}(1+\delta) > 0.5$), reaching $D_n4000 = 1.48 \pm 0.006$ (corresponding to an SSP age of 1 Gyr).

#### 6.4.1.3 STAR FORMATION RATE

Our analysis is restricted to stellar masses greater than $10^{10}$M$_{\odot}$, which probes a range of 3dex in SFR, and sub-samples selected in SFR should be somewhat independent of stellar mass. We find the [OII] equivalent width to increase with SFR for this sample. It increases from $-1.5 \pm 0.2$Å for the least star-forming galaxies ($\log_{10}(SFR) < 0.4$) up to $-10 \pm 1$Å in the most star-forming subset ($\log_{10}(SFR) > 1.2$). For the intermediate population we find an equivalent width of $\sim$-7Å.

Concerning the H$\delta$ absorption component, we find a consistent increase of the equivalent width with SFR, from $\mathrm{EW_{H\delta}} = 0.7^{+0.06}_{-0.35}$Å at $\log_{10}(\mathrm{SFR}\ [\mathrm{M_{\odot}yr^{-1}}]) < 0.4$ to $\mathrm{EW_{H\delta}} = 2.4^{+0.06}_{-0.03}$Å at $\log_{10}(\mathrm{SFR}\ [\mathrm{M_{\odot}yr^{-1}}]) > 1.2$. The H$\delta$ emission shows a correlation with SFR that closely mirrors what we find with [OII] emission with the line strength increasing from low to high SFRs (from $-0.0^{+0.24}_{-0.01}$Å to $-0.6^{+0.16}_{-0.13}$Å).

Finally, we observe a steady decrease in the value of $D_n4000$ from the lowest SFR bin ($D_n4000 = 1.48 \pm 0.005$ for $\log_{10}(SFR\ [\mathrm{M_{\odot}yr^{-1}}]) < 0.4$) to the highest SFR bin ($D_n4000 = 1.19 \pm 0.005$ for $\log_{10}(SFR\ [\mathrm{M_{\odot}yr^{-1}}]) > 1.2$). This is consistent with what is expected from the evolution of galaxies, since we expect a larger fraction of young stars in highly star-forming galaxies which decreases the value of $D_n4000$.

### 6.4.2 DISENTANGLING ENVIRONMENT AND STELLAR MASS EFFECTS

To disentangle the effects of stellar mass and environment we have explored our sample binned both in stellar mass and over-density bins. We chose the over-density bins in a ways that they should be representative of field (low-density), filament (intermediate-density), and cluster outskirts (high-density) regions (see Chap. 5 for more details). We show for individual galaxies and for composite spectra the influence of over-density in the observed spectroscopic properties in three different bins of stellar mass (chosen as a compromise for reasonable S/N for H$\delta$).

#### 6.4.2.1 EW$_{[OII]}$

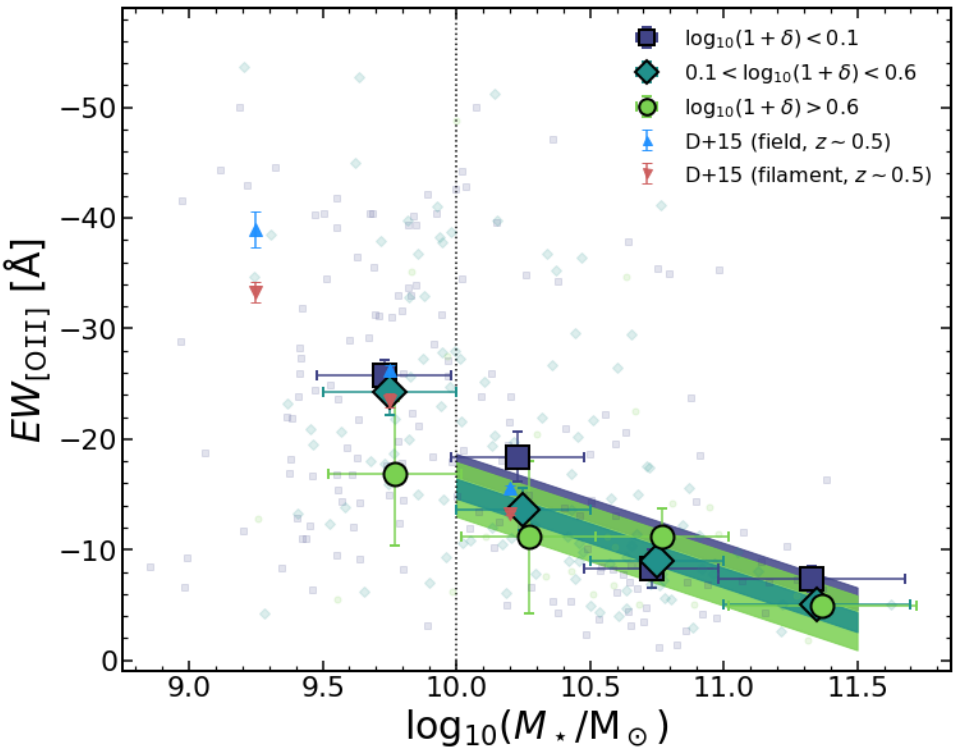


**Figure 6.5** We show the relation between [OII] equivalent width and stellar mass for the galaxies in our sample in three different bins of over-density. We compare our results (large green and dark blue symbols are the median of the population and the same smaller symbols represent individual measurements) with results from Darvish et al. (2015a) of filament/field galaxies, as small red/blue triangles, respectively. We show the best fit (with error estimate) from Eq. 6.4 for each density bin as shaded regions. Despite having different absolute values for the [OII] equivalent width, the trend with stellar mass is always the same. Higher stellar mass galaxies have weaker [OII] emission and this relation is seen in all over-density subsets.

We show in Fig. 6.5 the relation between [OII] line equivalent width and stellar mass for individual galaxies. We attempt to separate the effects of local density on this correlation and find that the correlation between [OII] line equivalent width and stellar mass is similar in all environments. We find similar gradients at all environments and fit a linear relation with a fixed

slope (the average of individually fitted slopes)[1] for all environments:

$$EW_{[\mathrm{OII}]} = 8.05 \times \log_{10}\left(M_{\star}/10^{10}\mathrm{M}_{\odot}\right) + b \tag{6.4}$$

we find the best fit values shown in Table 6.1. Line equivalent widths should be insensitive to dust if both continuum and line flux are being emitted from the same regions. We tentatively find a lower [OII] equivalent width with increasing density, but all relations are within $1\sigma$ uncertainties. This would likely point to galaxies having lower specific SFRs with increasing over-density, but larger samples are required to test this at a statistically significant level.

Concerning the results from composite spectra, we show in Fig. 6.7 an overall trend [OII] line equivalent width with stellar mass (as reported in Fig. 6.5) at each over-density bin. We show that [OII] depends on both the stellar mass and environment of galaxies. For lower stellar mass galaxies ($10 < \log_{10}(M_{\star}/\mathrm{M}_{\odot}) < 10.5$) we find a small decrease in $\mathrm{EW}_{[\mathrm{OII}]}$ with increasing local density. Intermediate mass galaxies ($10.5 < \log_{10}(M_{\star}/\mathrm{M}_{\odot}) < 11$) show a small rise in $\mathrm{EW}_{[\mathrm{OII}]}$ from field to filament-like regions and then a small decrease towards cluster-like regions. The most massive galaxies are consistent with no environmental effect on the [OII] emission.

#### 6.4.2.2 4000Å BREAK

The 4000Å break is a proxy for the age of the underlying stellar population (see Sect. 6.3.3). Under that assumption we find that at higher masses ($\log_{10}(M_{\star}/\mathrm{M}_{\odot}) > 10$) galaxies residing in high-density regions are typically older than their counterparts at lower density regions. We find that $D_n4000$ is 4% (lower stellar mass, $\sim$0.1 Gyr difference) to 23% (higher stellar mass, $\sim$2 Gyr difference) higher in high-density regions when compared to lower density regions, see Fig. 6.6. There is also an underlying correlation between stellar mass and $D_n4000$, with more massive galaxies having stronger flux breaks at 4000Å, thus being older (rising from $\sim 1.1$ to $\sim 1.35 - 1.65$ from lower to higher stellar masses, see also e.g. Vergani et al., 2008; Muzzin et al., 2012; Hernán-Caballero et al., 2013; Wu et al., 2018).

The relative difference between field and cluster galaxies shown by Muzzin et al. (2012) indicates a stronger break in higher density regions, although in their sample the difference between cluster and field galaxies becomes smaller with increasing stellar mass. We note, however, that the separation between field and cluster galaxies in Muzzin et al. (2012) is done by using the cluster centric radius (defined as the distance to the brightest cluster galaxy of each of their clusters). Their field sample is representative of a population of galaxies in-falling into the clusters and their cluster galaxies are drawn from a sample of rich clusters making a direct comparison not

[1] We made this choice since individual values for the slope are found to be similar and within the reported errors, and by doing so we can report the change in normalization independent of the slope of the relation.

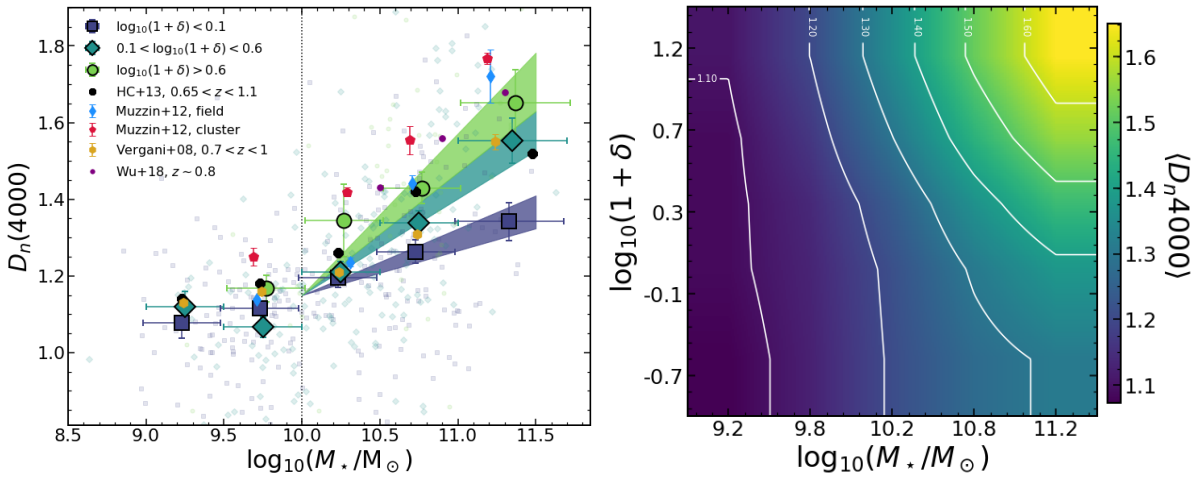


**Figure 6.6** $D_n4000$ as a function of stellar mass for three different over-density bins. The vertical dotted line shows the completeness limit of our survey. We show the best fit (with errors) from Eq. 6.5 for each density bin as shaded regions. We find an underlying correlation between stellar masses and $D_n4000$, with galaxies in the higher density regions showing systematically stronger breaks at intermediate to high stellar masses. The difference between low and high-density environments is larger at higher stellar masses. We compare with the results from GCLASS (Muzzin et al., 2012), from VVDS (Vergani et al., 2008), from SHARDS (Hernán-Caballero et al., 2013), and from LEGA-C (Wu et al., 2018) which also show the same trends. We also show here the dependence on both stellar mass and local density on $D_n4000$ in the right panel. This map is a smooth interpolation of the trends found in our sample.

straightforward. Thus we find that their field galaxies should correspond to filament-like densities as defined in our chapter and cluster galaxies likely correspond to higher densities than what we probe with the VIS$^3$COS survey.

Quantifying the rate of increase of $D_n4000$ with the linear model (we fix the y-intercept to the average of individual fits)[2]

$$D_n4000 = m \times \log_{10}\left(M_\star/10^{10}\mathrm{M}_\odot\right) + 1.15 \tag{6.5}$$

where the best fit values are summarized in Table 6.1.

**Table 6.1** Results of the linear fits $X = m \times \log_{10}(M_\star/10^{10}\mathrm{M}_\odot) + b$ to $\mathrm{EW}_{[\mathrm{OII}]}$ and $D_n4000$ that are shown in Figs. 6.5 and 6.6. We note that the slope is fixed for the [OII] related fits, and the y-intercept is fixed for the $D_n4000$ related fits.

| $X$ | $\log_{10}(1+\delta) < 0.1$ | | $0.1 < \log_{10}(1+\delta) < 0.6$ | | $\log_{10}(1+\delta) > 0.6$ | |
|---|---|---|---|---|---|---|
| | $m$ | $b$ | $m$ | $b$ | $m$ | $b$ |
| $\mathrm{EW}_{[\mathrm{OII}]}$ | [8.04] | $-17 \pm 1$ | [8.04] | $-16 \pm 1$ | [8.04] | $-15 \pm 2$ |
| $D_n4000$ | $0.14 \pm 0.02$ | [1.15] | $0.29 \pm 0.03$ | [1.15] | $0.37 \pm 0.05$ | [1.15] |

We confirm more clearly the trend reported on individual galaxies when looking at $D_n4000$ in the composite spectra (see Fig. 6.7). At fixed density, we see that $D_n4000$ increases from low to high

[2]We made this choice since individual values for the y-intercept are within the reported errors and by doing that we can report the change in gradient independent of the normalization of the relation.

stellar masses. At fixed stellar mass, we find that $D_n4000$ increases from low- to high-density environments. We also find that the difference between different stellar mass bins is increasing with increasing over-density. This translates into a $D_n4000$-stellar mass relation that is dependent on the local density, with higher density regions having the steeper slopes in contrast to flatter relations in field-like environments. This points to both stellar mass and environment having an impact on the stellar populations of galaxies, with higher density environments harbouring older galaxies at all stellar masses.

#### 6.4.2.3 H$\delta$ EMISSION AND ABSORPTION

We also find a dependence on stellar mass of the strength of the H$\delta$ emission with lower stellar mass galaxies having on average higher equivalent widths (see Fig. 6.7, Table 6.2). Within our estimated errors, we cannot pinpoint any dependence of the line strength with environment. Concerning the absorption component of H$\delta$ the results show a dependence on environment that depends itself on the stellar mass we consider. Lower stellar mass galaxies ($10 < \log_{10}(M_\star/\mathrm{M}_\odot) < 10.5$) have a decrease in the absorption strength from low- to high-density regions (from $2.5^{+0.04}_{-0.01}$Å to $0.8^{+0.3}_{-1.0}$Å). Intermediate stellar mass galaxies ($10.5 < \log_{10}(M_\star/\mathrm{M}_\odot) < 11$) show a small increase from low- to high-density regions (from 1.6±0.04Å to $1.7^{+0.13}_{-0.12}$Å), but consistent with no dependence with environment. At higher stellar masses, the absorption component has $0.0^{+0.4}_{-0.9}$Å at field-like densities, increases to $1.8^{+0.1}_{-0.03}$Å at intermediate densities and the decreases to $0.2^{+0.5}_{-0.8}$Å at the highest densities. Interestingly, at intermediate densities, the H$\delta$ absorption line has similar equivalent width at all stellar masses.

#### 6.4.2.4 ANTI-CORRELATION BETWEEN $D_n4000$ AND $\mathrm{EW}_{[\mathrm{OII}]}$

We show in Fig. 6.8 an anti-correlation between the strength of the 4000Å break (traced by $D_n4000$) and the [OII] line equivalent width which broadly traces the sSFR (Darvish et al., 2015a). The observed trend seems to be partially induced by a variation in stellar mass and we find that the most massive galaxies ($\log_{10}(M_\star/\mathrm{M}_\odot) > 11$) in intermediate- and high-density regions show an increase in $D_n4000$ while having similar [OII] line equivalent widths as lower density regions. We attempt at qualifying the correlation by fitting two linear models on two different stellar mass regimes

$$Y = \begin{cases} (-3.9 \pm 0.7) \times X + (5.8 \pm 0.9) & \text{if } 10 < M < 11 \\ (-0.8 \pm 0.2) \times X + (1.9 \pm 0.3) & \text{if } M > 11 \end{cases} \tag{6.6}$$

with $Y = \log_{10}(-\mathrm{EW}_{[\mathrm{OII}]})$, $X = D_n4000$, and $M = \log_{10}(M_\star/\mathrm{M}_\odot)$. This means a steeper slope

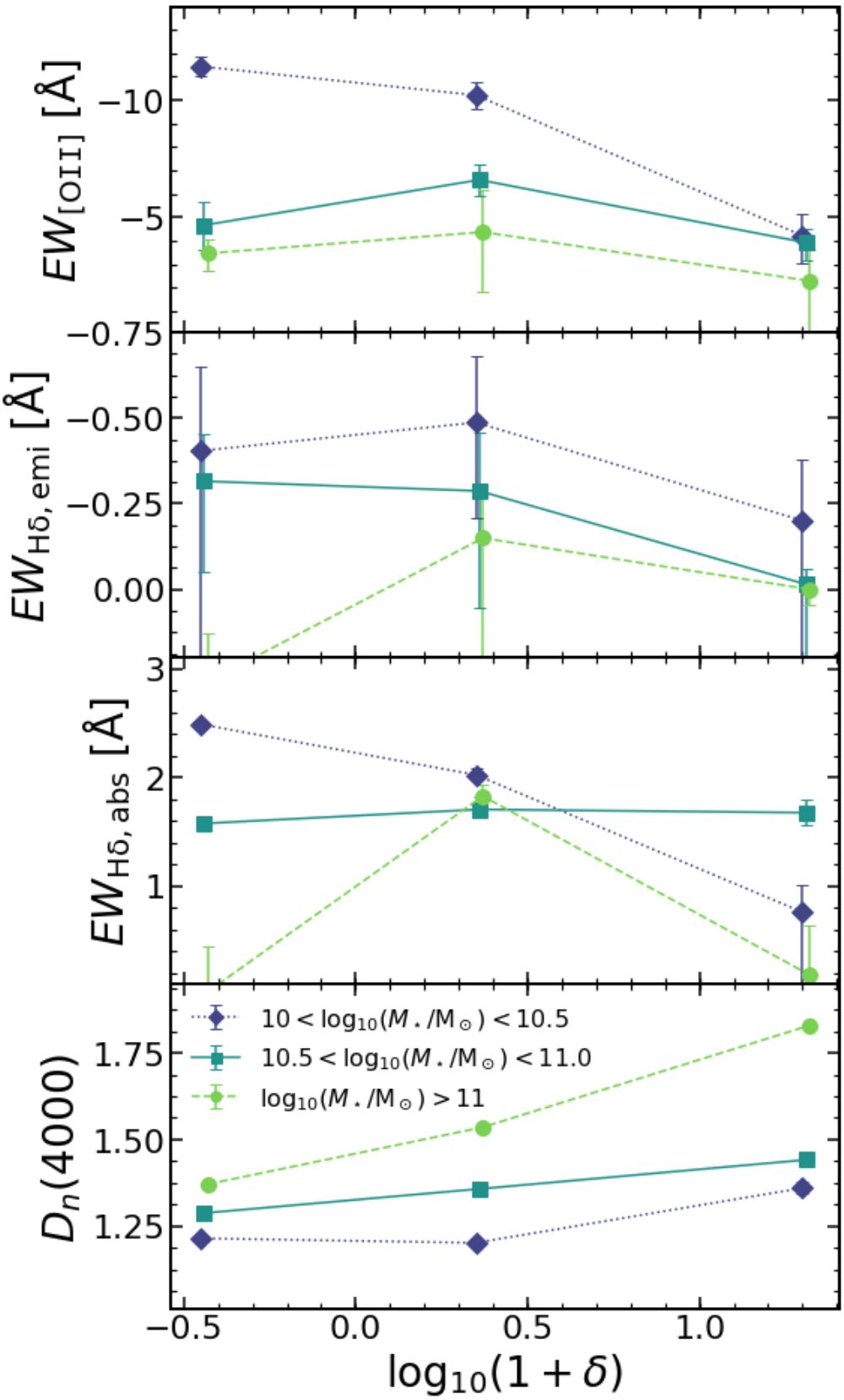


**Figure 6.7** The dependence of the three spectral indices detailed in Sect. 6.3.2 (from top to bottom - [OII] equivalent width, H$\delta$ equivalent width, and $D_n4000$) as a function of over-density in three stellar mass bins. This highlights the impact of both stellar mass and environment on the observed spectral properties of galaxies.

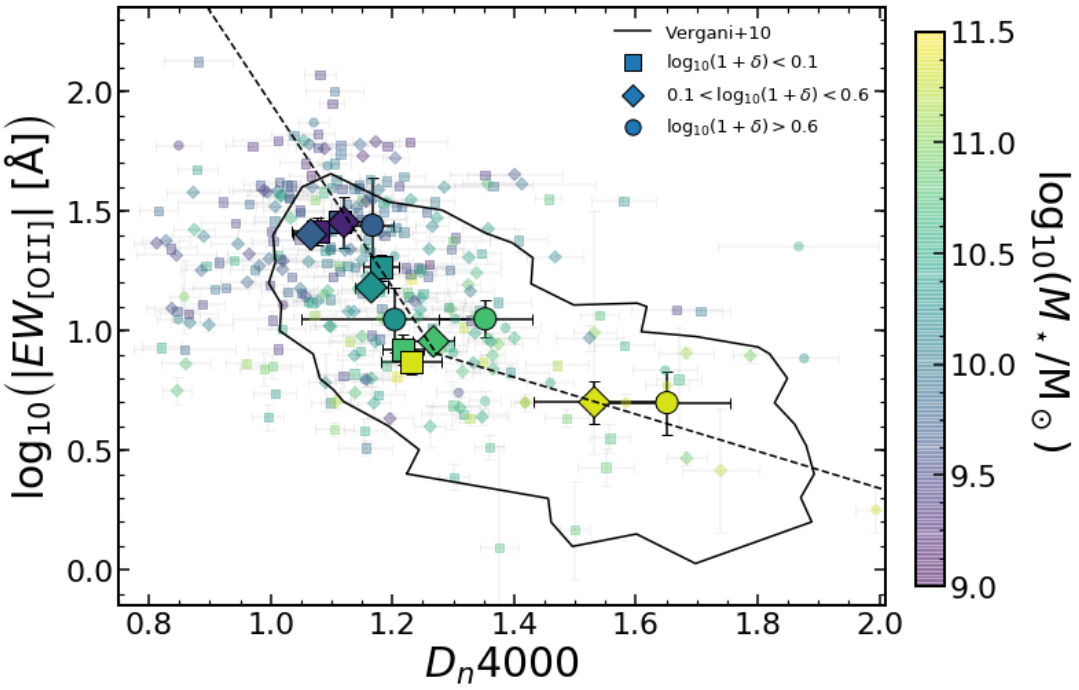


**Figure 6.8** Observed relation between $D_n4000$ and $\log_{10}(-EW_{[\mathrm{OII}]})$ for individual galaxies (small symbols) and median per stellar mass bin (large symbols), colour coded by their stellar mass. Different symbols correspond to different over-densities. The dashed lines are linear fits to the data of individual galaxies in two stellar mass subsamples (see text for details): the steeper slope is the fit for galaxies with $10 < \log_{10}(M_\star/\mathrm{M}_\odot) < 11$; the shallower slope is the fit for galaxies with $\log_{10}(M_\star/\mathrm{M}_\odot) > 11$. This highlights the underlying anti-correlation between the observed strength of the [OII] emission and the strength of the 4000Å break. We show as a black contour the location of 85% of the zCOSMOS sample at $0.48 < z < 1.2$ and with stellar masses greater than $10^{10}\mathrm{M}_\odot$ (Vergani et al., 2010).

for the less massive galaxies when compared to the one for the most massive galaxies. In the same figure we show as well the results from the median values (in bins of stellar mass and local environment) and we find that they follow the same relation as individual galaxies at all environments. We find that the departure from the lower stellar mass relation happens at lower stellar masses for higher density regions, with galaxies in field-like regions never departing from that relation.

This relation is qualitatively similar to what is reported for galaxies more massive than $10^{10}\mathrm{M}_\odot$ in zCOSMOS at $0.48 < z < 1.2$ by Vergani et al. (2010), although they only use this relation to compare the selection of star-forming, quiescent, and post-starburst galaxies. We interpret this relation as a combination of two phenomena. At lower stellar masses ($< 10^{11}\mathrm{M}_\odot$) it is likely a consequence of a declining sSFR that drives the decrease of [OII] equivalent width and an increase of $D_n4000$. At higher stellar masses we may have additional ionizing mechanisms (e.g. low luminosity AGN, pAGB stars) that boost the [OII] emission in galaxies dominated by older stellar populations and low sSFR. An alternative is that the most massive galaxies in richer environments simply have an evolved population or higher stellar metallicity that increases the strength of the 4000Å break.

### 6.4.3 STAR FORMATION ACTIVITY IN DIFFERENT ENVIRONMENTS

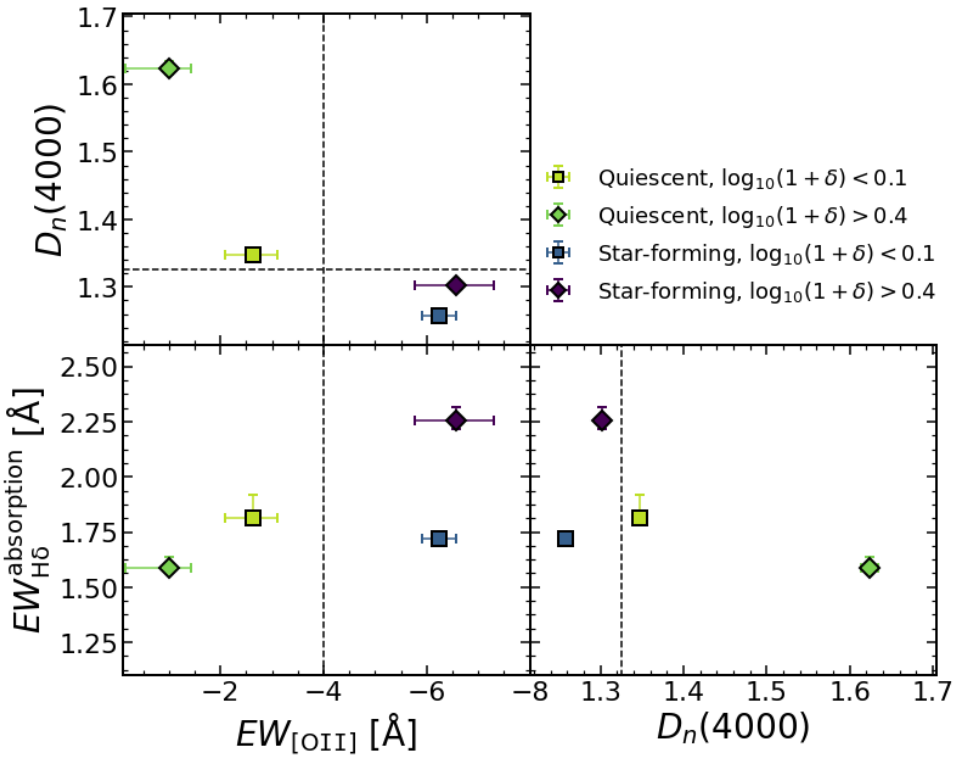


**Figure 6.9** We show the properties of composite spectra of quiescent and star-forming galaxies selected through their sSFR (separation at $\log_{10}(sSFR) = -11$, see also Chap. 5) in low- (diamonds) and high-density regions (squares). The dotted lines are for $D_n4000 = 1.325$ and $\mathrm{EW}_{[\mathrm{OII}]} = 4$Åand shown to guide the eye. We see that these two populations are separated in $D_n4000$ and $\mathrm{EW}_{[\mathrm{OII}]}$ and that we can also find some environmental effects within each population of galaxies. We find that it is in high-density regions that the quiescent and star-forming populations are more clearly separated.

Finally, we have also studied the composite spectra of quiescent and star-forming galaxies (separated at SED-derived $\log_{10}(sSFR) = -11$, see Chap. 5) in low -($\log_{10}(1+\delta) < 0.1$) and high-density ($\log_{10}(1+\delta) > 0.4$) environments and summarize our results in Fig. 6.9 (see also Table 6.2). We find that the two populations are separated clearly with $D_n4000$ and $\mathrm{EW}_{[\mathrm{OII}]}$. Overall, we also find that such difference is larger in high-density regions.

When focusing on H$\delta$ absorption strength, we see stronger absorption in star-forming galaxies in high-density regions than at lower densities. These results are indicative of star-forming galaxies in high-density regions having undergone a recent burst of star formation (or being a mix of normal star-forming galaxies with a post-starburst population). That scenario would explain similar observed [OII] equivalent widths but a $\sim 31\%$ increase in the H$\delta$ absorption strength and only a small $\sim 3\%$ increase in $D_n4000$ (see e.g. Balogh et al., 1999; Poggianti et al., 1999; Mansheim et al., 2017b). For field star-forming galaxies we find absorptions similar to that of quiescent galaxies. This might be due to a recent less bursty star formation history in quiescent and field star-forming galaxies.

From estimates using a single stellar population model with fixed stellar metallicity (see Sect.

6.3.3) we find that quenched galaxies in the densest regions are much older ($\sim$ 2.3 Gyr) than those in the field ($\sim$ 0.6 Gyr). We note that both quiescent samples in low- and high-density regions have similar stellar mass distributions, so we should not expect this to be a simple consequence of a mass-metallicity relation. For this population, we hypothesize that the differences that we see are a consequence of the time passed since the last episode of relevant star formation in the galaxy, with galaxies in high-density regions having quenched earlier. We may also expect that galaxies collapse earlier in the densest regions and thus these galaxies have likely formed their stars at earlier times than those in less dense regions. That would explain the higher values of $D_n4000$ and lower values of H$\delta$ absorption equivalent width for high-density quiescent galaxies, when compared to the lower density counterparts. Both these scenarios require that higher density environments ultimately (which might happen through bursts or in a continuous decline) depress star formation in galaxies.

We note, however, that a higher metallicity in high-density regions (e.g. Sobral et al., 2015b) could mitigate some of the observed differences. If we consider a metallicity of $2.5Z_{\odot}$ (6.25 times higher than the typical value at these redshifts) we would estimate an age of $\sim$ 0.9 Gyr for quiescent galaxies in high-density regions. Other studies find only marginal differences in gas-phase metallicity between field and cluster quiescent galaxies (e.g. Ellison et al., 2009, see also e.g. Cooper et al. 2008b; Darvish et al. 2015a; Sobral et al. 2016; Wu et al. 2017 for similar results on star-forming galaxies), also seen in stellar metallicity (e.g. Harrison et al., 2011), making it unlikely that a metallicity effect can explain the observed differences.

## 6.5 Discussion

Our results highlight that both stellar mass and environment play a role in the star formation history of galaxies. (as also reported by e.g. Iovino et al., 2010; Cucciati et al., 2010a; Peng et al., 2010b; Li et al., 2011; Davidzon et al., 2016; Darvish et al., 2016; Kawinwanichakij et al., 2017). We see in Fig. 6.7 that stellar mass influences the strength of the [OII] in all environments, showing weaker emission for the most massive galaxies, with stellar mass being the main driver of the observed changes. However, we see that the difference between populations of different stellar masses is affected by the environment. A similar result is also seen in H$\delta$ absorption, with field-like regions being the place where most differences are found (we note that for the most massive galaxies we find no evidence of emission or absorption in H$\delta$). This is also seen clearly in $D_n4000$ where the largest difference among galaxies with different stellar masses is now seen in cluster-like regions, decreasing gradually to filament and then field-like regions.

### 6.5.1 FILAMENT-ENHANCED STAR FORMATION

Figure 6.7 shows that for galaxies with stellar masses $10.5 < \log_{10}(M_\star/\mathrm{M}_\odot) < 11$ there is a small increase in the observed emission strength of [OII] at filament-like densities when compared to field and cluster regions (see also Fig. 6.4 for stacks with all galaxies more massive than $10^{10}\mathrm{M}_\odot$). This would translate to a slightly higher sSFR which might indicate a boost in star formation at these densities. While dust affects the observed flux of the [OII] line, the line equivalent width is mostly independent of dust extinction (assuming gas and stars have similar extinction). Different dust spatial distributions (e.g. star formation occurring in dusty regions within the galaxy) could also mimic the observed trend but there is no reason why this would preferentially affect galaxies in intermediate densities. Nevertheless, we would require resolved spatial maps on the distribution of star-forming regions in different environments which is out of the scope of this survey.

I show in Chap. 5 an increase of the quenched fraction of similar stellar mass galaxies at the defined transition between filament-like and cluster-like densities. Combining these results points to a scenario where environmental effects on the star formation of galaxies are more effective at lower stellar masses (e.g. Peng et al., 2012). Galaxies with higher stellar masses see their [OII] emission unaffected (or slightly suppressed) in filament-like regions with respect to field galaxies. This is compatible with a constant quenched fraction at these stellar masses seen in Chap. 5. This would support a scenario in which mass quenching mechanisms act to suppress star formation at these stellar masses and local environment has a negligible impact on star formation (e.g. Peng et al., 2010a), but more recent studies see a different picture for massive galaxies in dense environments (e.g. Darvish et al., 2016).

A scenario that is able to explain these results must account for an enhancement of star formation activity at intermediate densities and then some quenching mechanism that acts as galaxies move towards higher densities (which may be connected). This can be thought of as filaments being regions of higher probabilities for gas-rich galaxies to interact (e.g. Moss, 2006; Perez et al., 2009; Li et al., 2009; Tonnesen & Cen, 2012; Darvish et al., 2014; Malavasi et al., 2017) promoting compression of gas clouds and a peak in the SFR of the galaxy (e.g. Mihos & Hernquist, 1996; Kewley et al., 2006; Ellison et al., 2008; Gallazzi et al., 2009; Bekki, 2009; Owers et al., 2012; Roediger et al., 2014). Since we are looking at a superstructure composed of several sub-clusters, it is also possible that activity related to cluster-cluster interactions are capable of enhancing star formation as well (e.g. Stroe et al., 2014, 2015; Sobral et al., 2015b), although this might not always be the case (see e.g. Mansheim et al., 2017a).

### 6.5.2 Older population prevalence influenced by the environment

While we find in Fig. 6.4 that $D_n4000$ strongly correlates with stellar mass, we show in Fig. 6.7 that the strength of such correlation is strongly dependent on the environment. The fact that cluster galaxies have on average stronger 4000Å breaks was already reported in other studies (see e.g. Muzzin et al., 2012) but the environmental dependence of this relation was not as evident as we show here. This is likely related with the range of densities that we probe here which is complementary to the sample of Muzzin et al. (2012, targeting rich clusters and the galaxies around them).

To explain the observed trend we need the quenching timescale to be different at each environment (see also e.g. Rettura et al., 2010, 2011; Darvish et al., 2016). When looking at the most massive galaxies ($\log_{10}(M_\star/\mathrm{M}_\odot) > 11$) we find that they have older stellar populations in high-density regions when compared to the lower density region counterparts (8.5 Gyr compared to 0.6 Gyr at lower densities[3]). I show in Chap. 5 that, at these stellar masses, the quenched fraction is not changing with environment. To reproduce the observed trend then one would require that massive galaxies in clusters have been quenched for much longer than their field counterparts. This may be a consequence of denser regions having collapsed first and thus galaxies in such regions formed at earlier times. It is also consistent with the observed age difference for quenched galaxies in the field and cluster-like densities (0.6 and 2.3 Gyr, respectively). Such observations can be explained with the rate of in-fall gas fuelling new star formation episodes being dependent on the environment. This means that it is very difficult to get gas into massive galaxies inside dense regions, while in the filaments and fields, some gas should be able to funnel through, likely from minor mergers with gas rich satellites. We can recourse to mechanisms such as ram pressure stripping or tidal interactions or even starburst induced episodes on galaxies prior to entering galaxy clusters (see Sect. 6.5.1) that would basically prevent any gas from reaching the most massive galaxies, which are more prevalent in the cluster cores. Thus, massive galaxies in high-density regions must grow through mergers of gas poor galaxies (dry mergers, see e.g. Khochfar & Burkert, 2003; Khochfar & Silk, 2009; McIntosh et al., 2008; Lin et al., 2010; Davidzon et al., 2016) in order to build up their mass while maintaining an older stellar population. In this scenario, the dependence of the $D_n4000$-stellar mass on the environment is explained by the fraction of gas-rich galaxies that is available for merging at each density, being less common at higher densities. This is also in agreement to numerous reported trends of the quenched fraction (equivalent to the number of gas poor galaxies) with environment (Peng et al., 2010b; Cucciati et al., 2010a; Sobral et al., 2011; Muzzin et al., 2012; Darvish et al., 2016, Chap. 5).

As we move to stellar masses $10 < \log_{10}(M_\star/\mathrm{M}_\odot) < 11$, the impact of environment is less

[3]We note that this age estimate is based on an SSP with a metallicity of $Z_\odot/2.5$ (see Sect. 6.3.3). If we assume a solar metallicity, the estimated age would be 0.5 Gyr and 3.8 Gyr for low- and high-density regions, respectively.

pronounced (differences in $D_n4000$ between low- and high-density environments is smaller), although we still see slightly older stellar populations in higher density environments (0.6 Gyr compared to 0.3 Gyr at low-densities). In this case, we would require either that galaxies are still forming new stars or that, if they are quenched, it happened more recently. Since we observe a rise of the quenched fraction with local density for these stellar masses in Chap. 5, we would favour the latter scenario.

We note that our age estimates are made under the assumption of fixed stellar metallicity at all densities. However, we do not expect that metallicity differences are driving the trends we observe with $D_n4000$ as several studies find little impact of environment on metallicity (e.g. for gas-phase metallicity Ellison et al., 2009; Cooper et al., 2008b; Darvish et al., 2015a; Sobral et al., 2015b, 2016; Wu et al., 2017, and for stellar metallicity Harrison et al. 2011).

## 6.6 Conclusions

We have presented the spectroscopic properties of 466 galaxies in and around a $z \sim 0.84$ superstructure in the COSMOS field targeted with the VIS$^3$COS survey (Chap. 5). We explore the spectral properties of galaxies and relate those to their stellar mass and environment by measuring and interpreting [OII], H$\delta$, and $D_n4000$. We use [OII] equivalent width as a tracer of sSFR, H$\delta$ as a tracer of current episodes (from emission) or recent bursts (from absorption) of star formation, and $D_n4000$ as a tracer of the average age of the stellar population. We present results both on individual galaxies and on composite spectra to evaluate the relative importance of stellar mass and/or environment in the build-up of stellar populations in galaxies. Our main results are:

- We find that the strength of H$\delta$ absorption has an environmental dependence depending on the stellar mass. Lower stellar mass galaxies ($10.0 < \log_{10}(M_\star/\mathrm{M}_\odot) < 10.5$) show decreasing equivalent width with increasing over-density while intermediate stellar mass galaxies ($10.5 < \log_{10}(M_\star/\mathrm{M}_\odot) < 11$) show little dependence on environment. The higher stellar mass galaxies ($\log_{10}(M_\star/\mathrm{M}_\odot) > 11$) show the strongest absorption feature at intermediate over-densities.

- The [OII]$\lambda$3727 absolute line equivalent width decreases (from $28.4 \pm 0.4$Å to $3 \pm 0.3$Å) with increasing stellar mass. We observe this decrease in all environments which trend is mostly a consequence of the underlying main sequence of star-forming galaxies.

- We find $D_n4000$ to increase with increasing stellar mass in all environments and this relation is increasing more strongly in the highest densities. For stellar masses $10.0 < \log_{10}(M_\star/\mathrm{M}_\odot) < 10.5$ we see a small impact of the environment on the stellar age (0.3

Gyr to 0.6 Gyr, from low- to high-density regions). For the most massive galaxies ($\log_{10}(M_\star/\mathrm{M}_\odot) > 11$) the difference is much larger (0.6 Gyr to 8.5 Gyr[4]).

- There is an anti-correlation between $\log_{10}\left(-EW_{[\mathrm{OII}]}\right)$ and $D_n4000$ (also seen in e.g. Vergani et al., 2010) which is mostly a consequence of the underlying correlations of these quantities with stellar mass. We find that the most massive galaxies ($\log_{10}(M_\star/\mathrm{M}_\odot) > 11$) in intermediate- and high-density regions have higher $D_n4000$ while showing similar $\mathrm{EW}_{[\mathrm{OII}]}$ to lower density regions. This may hint at a different ionizing mechanism in high stellar mass galaxies operating in denser environments or be a consequence of older stellar populations residing in such regions.
- We find an increase in the [OII] equivalent width at intermediate-densities for intermediate stellar mass galaxies ($10.5 < \log_{10}(M_\star/\mathrm{M}_\odot) < 11$) which may point to episodes of enhanced star formation (more stars formed per stellar mass) on timescales around 10 Myr.

Based on our results on $D_n4000$, we hypothesize that the most massive galaxies ($\log_{10}(M_\star/\mathrm{M}_\odot) > 11$) have quenched earlier (by a few Gyr, depending on the stellar metallicity and assumed star formation history) in high-density environments than their field counterparts. Lower stellar mass galaxies ($10 < \log_{10}(M_\star/\mathrm{M}_\odot) < 11$) need to have quenched more recently at similar environments (or still have ongoing lower levels of star formation), since they have signs of younger stellar populations when compared to the most massive sample. The observed older stellar populations of massive galaxies in high-density environments point to a lack of recent episodes of significant star formation. This is compatible with a scenario where either all stars formed in-*situ* and earlier or they likely growth mechanism through dry merging events. In lower density environments they are either continuously forming new stars (at lower rates) or experiencing merging events with gas-rich galaxies fuelling new episodes of star formation. Such scenario is required to explain the dependence of $D_n4000$ on environment at these stellar masses.

## ACKNOWLEDGEMENTS

This work was supported by Fundação para a Ciência e a Tecnologia (FCT) through the research grant UID/FIS/04434/2013. APA, PhD::SPACE fellow, acknowledges support from the FCT through the fellowship PD/BD/52706/2014. DS acknowledges financial support from the Netherlands Organisation for Scientific research (NWO) through a Veni fellowship and from Lancaster University through an Early Career Internal Grant A100679. BD acknowledges financial support from NASA through the Astrophysics Data Analysis Program (ADAP), grant number NNX12AE20G, and the National Science Foundation, grant number 1716907. PNB is grateful for support from STFC (ST/M001229/1). IRS acknowledges support from the ERC

[4]We note that this age estimate is based on a single SSP. See Sect. 6.5.2.

Advanced Grant DUSTYGAL (321334), STFC (ST/P000541/1), and a Royal Society/Wolfson Merit award.

This work was only possible by the use of the following PYTHON packages: NumPy & SciPy (Walt et al., 2011; Jones et al., 2001), Matplotlib (Hunter, 2007), Astropy (Astropy Collaboration et al., 2013), and EzGal (Mancone & Gonzalez, 2012).

# APPENDIX

## DETAILED SPECTRAL STACK RESULTS

In this section we briefly describe some of the observed features in the composite spectra and refer any quantitative analysis to Sect. 6.3.2.

We show in Fig. 6.10 the composite spectra in bins of stellar mass. We observe a strong decrease in [OII] line flux from low- to high-stellar masses. We also see the relative strength of the two doublet lines changing with stellar mass (a quantitative analysis on the electron density estimates is subject of analysis in Chap. 8). We find a decrease of the emission strength of Balmer lines (H$\delta$, H$\varepsilon$, H$\zeta$, and H$\theta$) with increasing stellar mass. At the same time the prominence of the absorption features is increasingly noticeable at higher stellar masses. We also note the presence of [NeIII] emission in some spectra which will be the subject of a forthcoming paper based on the VIS$^3$COS survey.

In Fig.6.11 we show our findings of the stacked spectra in bins of over-density. In terms of the [OII] emission we find a decreasing line strength from low- to high-density regions (see also Chap. 5). In terms of the H$\delta$ line, we also see a dependence on local density. We find an increase of the absorption strength from low- to high-density and a decrease of the emission component.

Finally, in Fig. 6.12 we show the composite spectra binned by SFR. As expected, the [OII] emission is stronger for high-SFR galaxies. In terms of their H$\delta$ absorption, we see a stronger absorption in higher SFR galaxies.

**Table 6.2** Summary table with the results for all spectroscopic indices in composite spectra shown in this chapter. If only one variable is defined, it means that there is only a single selection for that row. Samples not selected in stellar mass in variables 1 and/or 2 have a minimum stellar mass limit of $10^{10}\mathrm{M}_{\odot}$. The last column shows the stellar age for a single stellar population from Bruzual & Charlot (2003) with stellar metallicity $Z = Z_{\odot}/2.5$ corresponding to the observed value of $D_n4000$. We opt not to show errors for the derived ages since the systematics due to our choice of metallicity and star formation history are much larger than those derived from observational errors on $D_n4000$.

| Variable 1 | Variable 2 | [OII] Å | $H\delta_{emi}$ Å | $H\delta_{abs}$ Å | $D_n4000$ | $t_{SSP}$ Gyr |
|---|---|---|---|---|---|---|
| $9.0 \leq \log_{10}(M/\mathrm{M}_{\odot}) < 9.5$ | - | $-28.4^{+0.4}_{-0.4}$ | $-2.1^{+0.39}_{-0.34}$ | $0.9^{+0.12}_{-0.57}$ | $1.12^{+0.011}_{-0.011}$ | 0.1 |
| $9.5 \leq \log_{10}(M/\mathrm{M}_{\odot}) < 10.0$ | - | $-23.7^{+0.2}_{-0.2}$ | $-1.1^{+0.09}_{-0.09}$ | $2.8^{+0.00}_{-0.01}$ | $1.12^{+0.003}_{-0.003}$ | 0.1 |
| $10.0 \leq \log_{10}(M/\mathrm{M}_{\odot}) < 10.5$ | - | $-10.1^{+0.2}_{-0.2}$ | $-0.5^{+0.18}_{-0.14}$ | $2.0^{+0.06}_{-0.05}$ | $1.22^{+0.004}_{-0.004}$ | 0.3 |
| $10.5 \leq \log_{10}(M/\mathrm{M}_{\odot}) < 11.0$ | - | $-5.3^{+0.4}_{-0.4}$ | $-0.2^{+0.12}_{-0.09}$ | $1.8^{+0.04}_{-0.03}$ | $1.34^{+0.004}_{-0.004}$ | 0.6 |
| $11.0 \leq \log_{10}(M/\mathrm{M}_{\odot}) < 11.7$ | - | $-3.0^{+0.3}_{-0.3}$ | $-0.1^{+0.28}_{-0.08}$ | $0.8^{+0.14}_{-0.39}$ | $1.52^{+0.006}_{-0.006}$ | 1.1 |
| $-1.0 \leq \log_{10}(1+\delta) < -0.3$ | - | $-4.0^{+0.3}_{-0.3}$ | $-0.1^{+0.80}_{-0.13}$ | $2.2^{+0.09}_{-0.24}$ | $1.26^{+0.007}_{-0.007}$ | 0.4 |
| $-0.3 \leq \log_{10}(1+\delta) < 0.1$ | - | $-5.9^{+0.3}_{-0.3}$ | $-0.3^{+0.28}_{-0.16}$ | $1.5^{+0.06}_{-0.05}$ | $1.28^{+0.005}_{-0.005}$ | 0.4 |
| $0.1 \leq \log_{10}(1+\delta) < 0.5$ | - | $-7.6^{+0.9}_{-0.9}$ | $-0.4^{+0.14}_{-0.10}$ | $1.9^{+0.07}_{-0.07}$ | $1.30^{+0.005}_{-0.005}$ | 0.5 |
| $0.5 \leq \log_{10}(1+\delta) < 1.5$ | - | $-3.5^{+2.1}_{-1.1}$ | $-0.1^{+0.11}_{-0.11}$ | $1.4^{+0.04}_{-0.00}$ | $1.48^{+0.006}_{-0.006}$ | 1.0 |
| $-1.5 \leq \log_{10}(SFR\,\mathrm{M}_{\odot}\mathrm{yr}^{-1}) < 0.4$ | - | $-1.5^{+0.2}_{-0.2}$ | $-0.0^{+0.24}_{-0.01}$ | $0.7^{+0.06}_{-0.35}$ | $1.48^{+0.005}_{-0.005}$ | 1.0 |
| $0.4 \leq \log_{10}(SFR\,\mathrm{M}_{\odot}\mathrm{yr}^{-1}) < 0.8$ | - | $-7.6^{+0.3}_{-0.3}$ | $-0.2^{+0.18}_{-0.09}$ | $1.3^{+0.10}_{-0.08}$ | $1.33^{+0.007}_{-0.006}$ | 0.5 |
| $0.8 \leq \log_{10}(SFR\,\mathrm{M}_{\odot}\mathrm{yr}^{-1}) < 1.2$ | - | $-7.2^{+0.8}_{-0.7}$ | $-0.6^{+0.17}_{-0.14}$ | $2.0^{+0.07}_{-0.05}$ | $1.28^{+0.007}_{-0.007}$ | 0.4 |
| $1.2 \leq \log_{10}(SFR\,\mathrm{M}_{\odot}\mathrm{yr}^{-1}) < 3.0$ | - | $-10.8^{+1.3}_{-1.1}$ | $-0.6^{+0.16}_{-0.13}$ | $2.4^{+0.06}_{-0.03}$ | $1.19^{+0.005}_{-0.005}$ | 0.2 |
| $-1.0 \leq \log_{10}(1+\delta) < 0.1$ | $10.0 \leq \log_{10}(M/\mathrm{M}_{\odot}) < 10.5$ | $-11.4^{+0.4}_{-0.4}$ | $-0.4^{+0.63}_{-0.24}$ | $2.5^{+0.04}_{-0.01}$ | $1.21^{+0.006}_{-0.006}$ | 0.3 |
| $-1.0 \leq \log_{10}(1+\delta) < 0.1$ | $10.5 \leq \log_{10}(M/\mathrm{M}_{\odot}) < 11.0$ | $-4.7^{+1.0}_{-1.0}$ | $-0.3^{+0.27}_{-0.14}$ | $1.6^{+0.04}_{-0.04}$ | $1.29^{+0.006}_{-0.007}$ | 0.4 |
| $-1.0 \leq \log_{10}(1+\delta) < 0.1$ | $11.0 \leq \log_{10}(M/\mathrm{M}_{\odot}) < 12.0$ | $-3.5^{+0.7}_{-0.6}$ | $0.3^{+0.08}_{-0.14}$ | $0.0^{+0.41}_{-0.90}$ | $1.37^{+0.009}_{-0.008}$ | 0.6 |
| $0.1 \leq \log_{10}(1+\delta) < 0.6$ | $10.0 \leq \log_{10}(M/\mathrm{M}_{\odot}) < 10.5$ | $-10.2^{+0.6}_{-0.6}$ | $-0.5^{+0.28}_{-0.19}$ | $2.0^{+0.06}_{-0.04}$ | $1.20^{+0.007}_{-0.007}$ | 0.2 |
| $0.1 \leq \log_{10}(1+\delta) < 0.6$ | $10.5 \leq \log_{10}(M/\mathrm{M}_{\odot}) < 11.0$ | $-6.6^{+0.7}_{-0.6}$ | $-0.3^{+0.34}_{-0.17}$ | $1.7^{+0.12}_{-0.04}$ | $1.36^{+0.006}_{-0.006}$ | 0.6 |
| $0.1 \leq \log_{10}(1+\delta) < 0.6$ | $11.0 \leq \log_{10}(M/\mathrm{M}_{\odot}) < 12.0$ | $-4.4^{+2.6}_{-1.8}$ | $-0.1^{+0.41}_{-0.13}$ | $1.8^{+0.11}_{-0.03}$ | $1.54^{+0.010}_{-0.010}$ | 1.2 |
| $0.6 \leq \log_{10}(1+\delta) < 2.0$ | $10.0 \leq \log_{10}(M/\mathrm{M}_{\odot}) < 10.5$ | $-4.2^{+1.2}_{-0.9}$ | $-0.2^{+0.89}_{-0.18}$ | $0.8^{+0.25}_{-0.97}$ | $1.36^{+0.016}_{-0.016}$ | 0.6 |
| $0.6 \leq \log_{10}(1+\delta) < 2.0$ | $10.5 \leq \log_{10}(M/\mathrm{M}_{\odot}) < 11.0$ | $-3.9^{+0.7}_{-0.6}$ | $-0.0^{+0.52}_{-0.04}$ | $1.7^{+0.13}_{-0.12}$ | $1.44^{+0.010}_{-0.010}$ | 0.8 |
| $0.6 \leq \log_{10}(1+\delta) < 2.0$ | $11.0 \leq \log_{10}(M/\mathrm{M}_{\odot}) < 12.0$ | $-2.3^{+2.2}_{-1.3}$ | $0.0^{+0.04}_{-0.00}$ | $0.2^{+0.46}_{-0.79}$ | $1.83^{+0.013}_{-0.012}$ | 8.5 |
| $\log_{10}(sSFR) < -11$ | $\log_{10}(1+\delta) < 0.1$ | $-2.6^{+0.6}_{-0.5}$ | $-0.1^{+0.74}_{-0.10}$ | $1.8^{+0.10}_{-0.02}$ | $1.35^{+0.009}_{-0.009}$ | 0.6 |
| $\log_{10}(sSFR) < -11$ | $\log_{10}(1+\delta) > 0.4$ | $-1.0^{+0.8}_{-0.4}$ | $0.1^{+0.27}_{-0.11}$ | $1.6^{+0.05}_{-0.02}$ | $1.62^{+0.010}_{-0.010}$ | 2.3 |
| $\log_{10}(sSFR) > -11$ | $\log_{10}(1+\delta) < 0.1$ | $-6.3^{+0.3}_{-0.3}$ | $-0.3^{+0.21}_{-0.14}$ | $1.7^{+0.03}_{-0.03}$ | $1.26^{+0.005}_{-0.005}$ | 0.4 |
| $\log_{10}(sSFR) > -11$ | $\log_{10}(1+\delta) > 0.4$ | $-6.6^{+0.8}_{-0.7}$ | $-0.4^{+0.20}_{-0.14}$ | $2.3^{+0.06}_{-0.04}$ | $1.30^{+0.006}_{-0.006}$ | 0.5 |
| Field | $10.0 \leq \log_{10}(M/\mathrm{M}_{\odot}) < 10.5$ | $-11.8^{+0.4}_{-0.4}$ | $-0.5^{+0.19}_{-0.14}$ | $2.7^{+0.02}_{-0.02}$ | $1.26^{+0.006}_{-0.006}$ | 0.3 |
| Field | $10.5 \leq \log_{10}(M/\mathrm{M}_{\odot}) < 11.0$ | $-5.8^{+0.8}_{-0.8}$ | $-0.1^{+0.86}_{-0.08}$ | $1.9^{+0.03}_{-0.07}$ | $1.29^{+0.007}_{-0.007}$ | 0.4 |
| Field | $11.0 \leq \log_{10}(M/\mathrm{M}_{\odot}) < 12.0$ | $-3.6^{+0.5}_{-0.5}$ | $0.9^{+0.04}_{-0.03}$ | $-0.7^{+12.26}_{-0.66}$ | $1.33^{+0.009}_{-0.009}$ | 0.5 |
| Filament | $10.0 \leq \log_{10}(M/\mathrm{M}_{\odot}) < 10.5$ | $-9.6^{+0.5}_{-0.5}$ | $-0.6^{+0.25}_{-0.18}$ | $1.8^{+0.10}_{-0.07}$ | $1.16^{+0.006}_{-0.006}$ | 0.1 |
| Filament | $10.5 \leq \log_{10}(M/\mathrm{M}_{\odot}) < 11.0$ | $-4.4^{+0.8}_{-0.7}$ | $-0.3^{+0.21}_{-0.15}$ | $1.6^{+0.06}_{-0.04}$ | $1.37^{+0.005}_{-0.005}$ | 0.6 |
| Filament | $11.0 \leq \log_{10}(M/\mathrm{M}_{\odot}) < 12.0$ | $-1.4^{+0.5}_{-0.4}$ | $-0.2^{+0.30}_{-0.14}$ | $1.3^{+0.08}_{-0.43}$ | $1.56^{+0.009}_{-0.009}$ | 1.2 |
| Cluster | $10.0 \leq \log_{10}(M/\mathrm{M}_{\odot}) < 10.5$ | $-5.0^{+1.9}_{-1.4}$ | $-0.1^{+1.39}_{-0.05}$ | $1.6^{+0.12}_{-1.19}$ | $1.38^{+0.026}_{-0.025}$ | 0.7 |
| Cluster | $10.5 \leq \log_{10}(M/\mathrm{M}_{\odot}) < 11.0$ | $-2.3^{+0.5}_{-0.4}$ | $-0.2^{+1.15}_{-0.17}$ | $2.2^{+0.07}_{-0.03}$ | $1.41^{+0.010}_{-0.010}$ | 0.7 |
| Cluster | $11.0 \leq \log_{10}(M/\mathrm{M}_{\odot}) < 12.0$ | $-1.9^{+0.9}_{-0.8}$ | $-0.1^{+0.61}_{-0.11}$ | $1.2^{+0.03}_{-0.39}$ | $1.84^{+0.017}_{-0.017}$ | 8.9 |

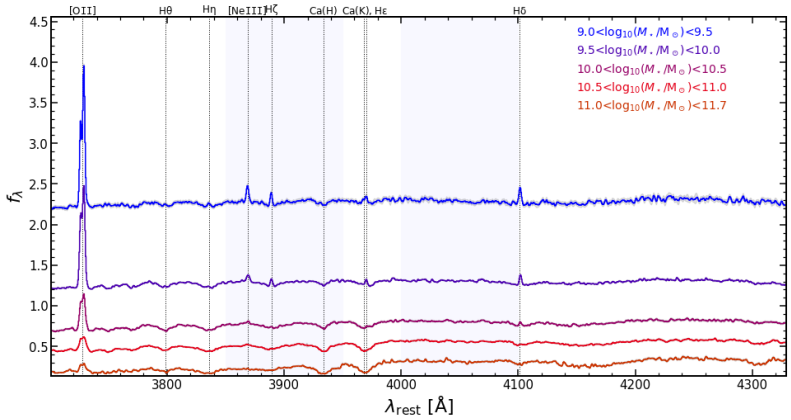


**Figure 6.10** Resulting median composite spectra normalized at 4150-4300Å and associated error (solid line + shaded region) in bins of stellar mass (high- to low-stellar mass from top to bottom). We apply a vertical offset for visualization purposes. We highlight with vertical lines the strongest features that we see on our spectra. The light grey vertical stripes show the spectral ranges which are used to compute $D_n4000$.

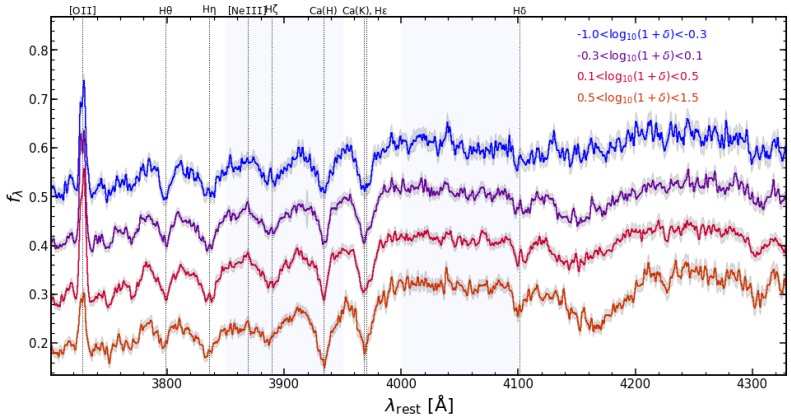


**Figure 6.11** Resulting median composite spectra stacks normalized at 4150-4300Å and associated error (solid line + shaded region) in bins of local over-density (high- to low-density regions from top to bottom) for galaxies with stellar masses greater than $10^{10}M_{\odot}$. We apply a vertical offset for visualization purposes. We highlight with vertical lines the strongest features that we see on our spectra. The light grey vertical stripes show the spectral ranges which are used to compute $D_n4000$.

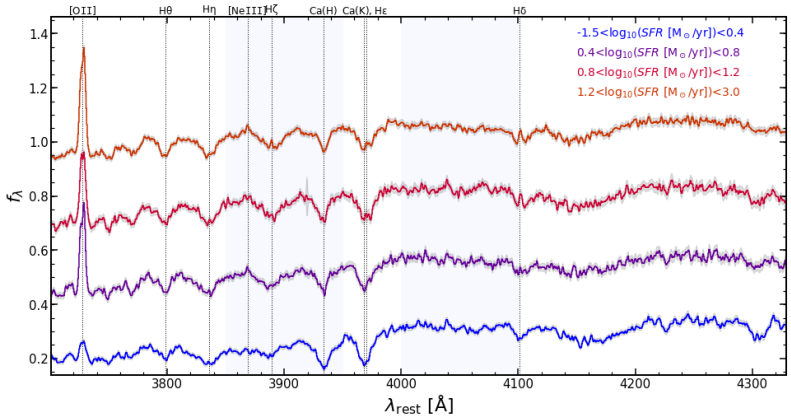


**Figure 6.12** Resulting median composite spectra normalized at 4150-4300Å and associated error (solid line + shaded region) in bins of star formation rate (low -to high-SFR from top to bottom) for galaxies with stellar masses greater than $10^{10}M_{\odot}$. We apply a vertical offset for visualization purposes. We highlight with vertical lines the strongest features that we see on our spectra. The light grey vertical stripes show the spectral ranges which are used to compute $D_n4000$.

# CHAPTER 7

## VIS$^3$COS: III. THE ROLE OF ENVIRONMENT ON GALAXY MORPHOLOGICAL TRANSFORMATIONS AT $Z \sim 0.8$

*We study the impact of local density on the morphology of quiescent and star-forming galaxies on a sample of* $\sim 500$ *galaxies with spectroscopic redshifts from the VIMOS Spectroscopic Survey of a Superstructure in COSMOS (VIS*$^3$*COS). We perform bulge-to-disk decomposition of the surface brightness profiles and find* $\sim 41 \pm 3\%$ *of* $> 10^{10}\mathrm{M}_{\odot}$ *galaxies to be best fit with two components. We complement our analysis with non-parametric morphology and qualitative visual classifications. We generally find that when splitting the sample in star-forming and quiescent sub-populations there are not statistically significant differences between low- and high-density regions. We do find, however, that quiescent galaxies are smaller, have higher Sérsic indices (for single profiles, around* $n \sim 4$*), and higher bulge-to-total light ratios (for decomposed profiles, around* $B/T \sim 0.5$*) when compared to star-forming counterparts (*$n \sim 1$ *and* $B/T \sim 0.3$*, for single and double profiles, respectively). We confirm these trends with non-parametric morphology finding quiescent galaxies to be smoother (lower asymmetry, lower* $M_{20}$*) and having most of their light over smaller areas (higher concentration and Gini coefficient) than star-forming galaxies. Considering our sample as a whole, we find evidence from visual classifications for the existence of a kind of "morphology-density relation" at* $z \sim 0.84$ *for galaxies more massive than* $10^{10}\mathrm{M}_{\odot}$*. This relation is much less evident (marginally significant) if we split our sample according to their star-forming activity. We find that the onset of the "morphology-density relation" is tightly coupled with the environmental dependence of the quenched fraction and hypothesize that the processes responsible for the quenching of star-formation must also affect the galaxy morphology on similar timescales.*

adapted from **Paulino-Afonso**, Sobral, D., Darvish, B. et al., in prep.

## 7.1 INTRODUCTION

In a ΛCDM Universe, galaxies form in dark matter halos when baryonic matter cools and collapses (e.g. White & Rees, 1978). This provides a hierarchical scenario where massive objects are formed through mergers of smaller entities. However, the exact details of galaxy formation

and evolution still elude our current understanding. The hierarchical nature of structure formation naturally produces different pathways of galaxy evolution based on the local density, as denser regions have higher probability of interactions which influence galaxy properties.

By studying samples of galaxies across different regions Dressler (1980) found a clear dichotomy in galaxy morphology when looking at low- (hereafter referred as field) and high-density (cluster) environments in the local Universe (see also e.g. Guzzo et al., 1997; Goto et al., 2003; Bamford et al., 2009; Skibba et al., 2009; Fasano et al., 2015). Galaxies in field environments are bluer, more star-forming and disk-like while galaxies in cluster environments are older, redder, less star-forming and elliptical (e.g. Dressler, 1984; Gómez et al., 2003; Boselli & Gavazzi, 2006; Kauffmann et al., 2004; Blanton & Moustakas, 2009; Deeley et al., 2017).

When studying higher redshifts, these differences with environment are found in intermediate ($z \lesssim 1$, e.g. Dressler et al., 1997; Treu et al., 2003; Postman et al., 2005; Capak et al., 2007b; van der Wel et al., 2007; Tasca et al., 2009; Kovač et al., 2010; Nantais et al., 2013a; Allen et al., 2016; Krywult et al., 2017) and high redshift ($z \gtrsim 1$, e.g. Grützbauch et al., 2011; Bassett et al., 2013a; Strazzullo et al., 2013; Allen et al., 2015) Universe. At these redshifts, observed galaxy sizes in each environment and grouped by morphological types show a dependence on environment at $z \sim 1-2$ (e.g. Papovich et al., 2012; Delaye et al., 2014; Mei et al., 2015) while in the intermediate to local Universe such differences are not found (e.g. Huertas-Company et al., 2013b; Kelkar et al., 2015) and also not seen in a proto-cluster at $z \sim 2$ (e.g. in rest-frame UV Peter et al., 2007). In terms of their light profiles it is expected that galaxies residing in the cluster environments might be more bulge-dominated (e.g. Goto et al., 2003; Poggianti et al., 2008; Skibba et al., 2012; Bluck et al., 2014). By comparing the different structures of galaxies observed in both field and cluster we can pinpoint the epoch of morphological diversification within denser environments with respect to that of the field population that seems to fade by $z \sim 2$ (e.g. Peter et al., 2007; Mortlock et al., 2015; Mei et al., 2015). Another key point in looking for morphological differences is to quantify the rate of interaction in each environment (e.g. Kampczyk et al., 2013; Pipino et al., 2014) and how it affects the observed properties.

The morphology-colour-density relation suggests that there is at least one physical mechanism that changes galaxy morphology as well as acts in suppression of the star-formation activity. Several processes have been proposed that include gas removal from the disk (e.g. Larson et al., 1980), ram pressure stripping from the intra-cluster medium (e.g. Gunn & Gott, 1972; Abramson et al., 2016), galaxy harassment through tidal forces (e.g. Moore et al., 1996) and eventual galaxy mergers (e.g. Burke & Collins, 2013). At the same time, there is a typical scale that is effective at quenching galaxies due to over-dense environments (e.g. Peng et al., 2010b, 2012).

In recent years, a major effort on understanding the onset of environmental differentiation of galaxies has been undertaken. By measuring galaxy sizes in field and cluster galaxies, separated by their star formation activity into quiescent and star-forming, several studies find quiescent

galaxies to show little difference in their extent $0 < z < 2$ (e.g. Papovich et al., 2012; Huertas-Company et al., 2013b,a; Cebrián & Trujillo, 2014; Newman et al., 2014; Kelkar et al., 2015; Allen et al., 2015, 2016; Saracco et al., 2017) while others find evidence for larger quiescent galaxies in cluster environments (e.g. Bassett et al., 2013a; Lani et al., 2013; Strazzullo et al., 2013; Delaye et al., 2014; Yoon et al., 2017). For star-forming galaxies, there is also not a clear trend with some studies finding little difference among cluster and field galaxies (e.g. Lani et al., 2013; Kelkar et al., 2015) and others finding larger star-forming galaxies in cluster environments (e.g. Cebrián & Trujillo, 2014; Tran et al., 2017, locally and at $z \sim 2$, respectively). Studies by Allen et al. (2015, 2016) show that star-forming galaxies are larger/smaller inside clusters at z$\sim$1/z$\sim$2, respectively, indicating an evolution of this particular population in the densest regions.

Quantifying the light distribution in galaxies with Sérsic (1968) profiles, Allen et al. (2016) find that at $z \sim 0.92$ star-forming galaxies are more likely found to have higher Sérsic indices than their field counterparts, but report no difference among quiescent galaxies. At $z \sim 1.6$, Bassett et al. (2013a) find no differences among star-forming galaxies but report shallower profiles (lower Sérsic index) for quiescent galaxies in a cluster environment. In terms of comparing star-forming and quiescent galaxies, the latter have higher Sérsic indices, indicative of a prevalence of elliptical or bulge-dominated galaxies in the red quiescent population (e.g. Bassett et al., 2013a; Morishita et al., 2014; Cerulo et al., 2017) which are also more common in higher density regions out to $z \sim 1$ (e.g. Dressler et al., 1997; Treu et al., 2003; Postman et al., 2005; Capak et al., 2007b; van der Wel et al., 2007; Tasca et al., 2009; Nantais et al., 2013a).

Differences in star-forming and quiescent galaxies can evolve through the morphological transformation of blue star-forming disk-dominated galaxies to redder quiescent and bulge-dominated (or pure elliptical) galaxies (e.g. through minor and major mergers De Lucia et al., 2011; Shankar et al., 2014). Observationally, we find a rise in the bulge-dominated fraction since $z \sim 3$ (e.g. Tasca et al., 2014; Bruce et al., 2014a; Margalef-Bentabol et al., 2016). And in the local Universe, there are hints that such morphological transformation are happening in higher density environments (e.g. Lackner & Gunn, 2013). Grossi et al. (2018) found that for a sample of H$\alpha$ selected galaxies galaxies tend to have more prominent bulges at higher density environments at $z \sim$0.4-0.8. However, we lack observations of the environmental dependence of the bulge prevalence at these redshifts for a continuum-selected sample.

In this chapter we aim at studying a sample of spectroscopically confirmed sources in and around a superstructure at $z \sim 0.84$ in the COSMOS field (Scoville et al., 2007) for which we have available high-resolution spectra covering [OII], the 4000Å break, and H$\delta$ (Paulino-Afonso et al., 2018b, Chap. 5). We aim to compare the morphological properties of star-forming and quiescent galaxies within dense environments and look for evidence or not of morphological transformations and its relation to star formation.

This chapter is organized as follows: in Sect. 7.2 we briefly explain the VIS$^3$COS survey, on which this analysis is based. Section 7.3 details the morphological measurements on the sources used in this chapter. In Sect. 7.4 we highlight some of the key results of our study in terms of galaxy stellar mass, star formation, and environment. In Sect. 7.5 we discuss our findings within the context of current galaxy formation and evolution literature. We end with Sect. 7.6 where we summarize the conclusions of this chapter. We use AB magnitudes, a Chabrier (Chabrier, 2003) initial mass function (IMF), and assume a ΛCDM cosmology with $H_0$=70 km s$^{-1}$Mpc$^{-1}$, $\Omega_M$=0.3 and $\Omega_\Lambda$=0.7. The physical scale at the redshift of the superstructure ($z \sim 0.84$) is 7.63 kpc/$''$.

## 7.2 Sample and data

### 7.2.1 The VIS$^3$COS survey

The VIMOS Spectroscopic Survey of a Superstructure in the COSMOS field (VIS$^3$COS) is based on a observing programme with the VIMOS instrument mounted at VLT/ESO to obtain high resolution spectroscopy down to the continuum level for galaxies in and around a large structure at $z \sim 0.84$ in the COSMOS field. The observations span an area of $21' \times 31'$ (9.6×14.1 Mpc) with an over-density of H$\alpha$ emitters (Sobral et al., 2011; Darvish et al., 2014) and three confirmed X-ray clusters (Finoguenov et al., 2007). This is the third chapter based on results from this survey and the full description of the data and derived physical quantities is presented in Chap. 5. We describe in this section a summary of the relevant information which is pertinent for this chapter.

We targeted galaxies from the Ilbert et al. (2009) catalogue which had $0.8 < z_{\rm phot,l} < 0.9$ (with $z_{\rm phot,l}$ being one of the upper or lower 99% confidence interval limit for each source) and being brighter than $i_{\rm AB} < 22.5$. The survey targeted a total of 971 sources with the VIMOS High-Resolution red grism (with the GG475 filter, $R \sim 2500$) using 6 overlapping VIMOS pointings to mitigate selection effects on higher density regions. Our choice of grism covers the 3400-4600Å rest-frame region at the redshift of the superstructure which have interesting spectral features such as [OII] $\lambda$3726,$\lambda$3729 (partially resolved doublet), the 4000 Å break and H$\delta$.

We have computed the spectroscopic redshifts from the extracted 1D spectra using SpecPro (Masters & Capak, 2011). The redshift determination is based on a set of prominent spectral features: [OII], H+K absorption, G-band, some Fe lines and H$\delta$. We have obtained successful spectroscopic redshifts for 696 galaxies, of which 490 have confirmed spectroscopic redshifts within our primary redshift selection ($0.8 < z < 0.9$).

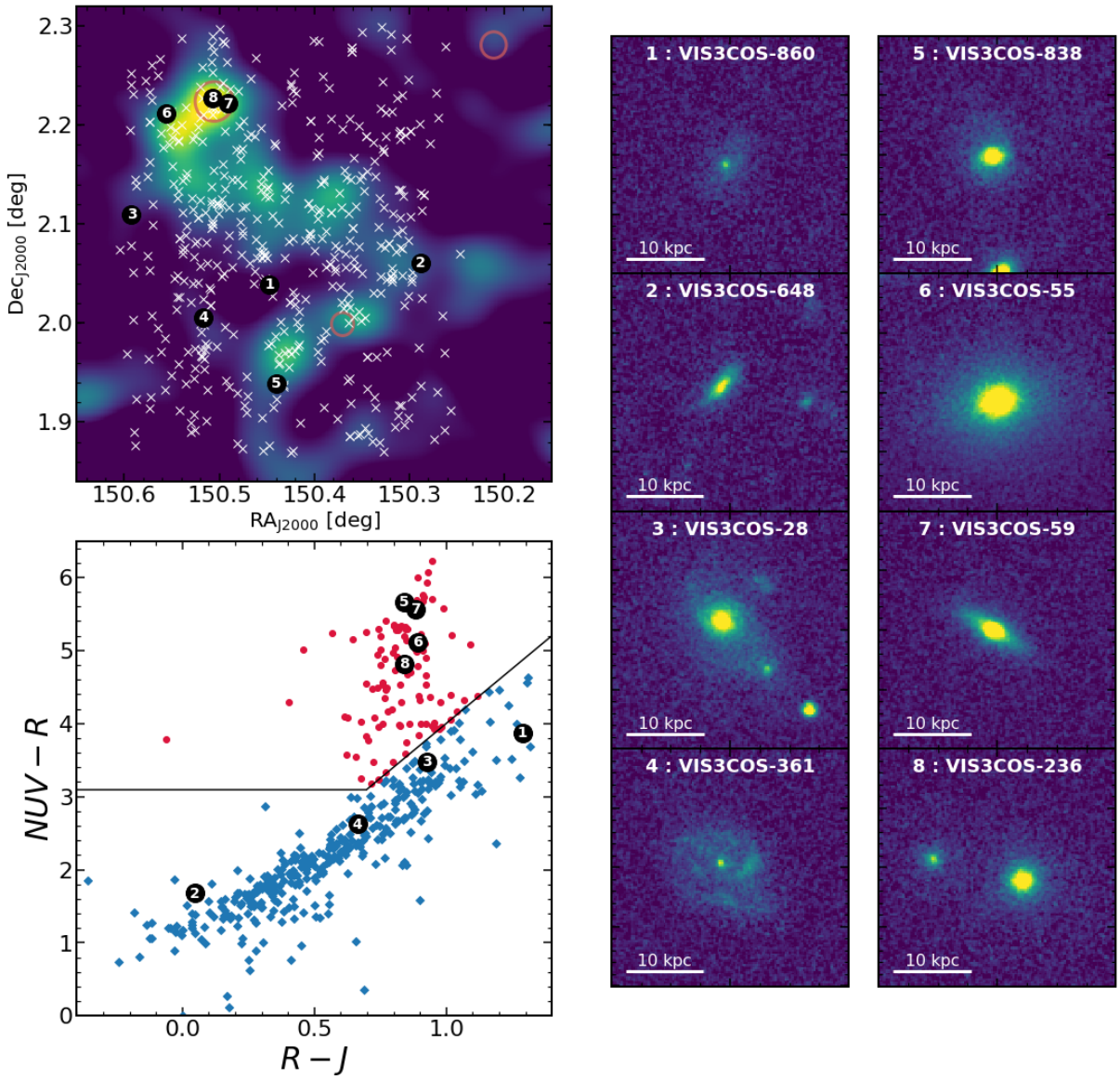


**Figure 7.1** An overview of the VIS$^3$COS survey showing the galaxy over-density and targeted galaxies at $0.8 < z < 0.9$ with spectroscopic redshifts (white crosses) along with location of known X-ray clusters (empty red circles, Finoguenov et al., 2007) (top left); the NUVrJ diagram for galaxies in our survey, with the separation between quiescent (red circles) and star-forming (blue diamonds) as defined by Ilbert et al. (2013) shown as a solid line (bottom left); and examples of HST/ACS F814W $4'' \times 4''$ images (Koekemoer et al., 2007) of eight of our targets (panels on the right). We highlight the position of these 8 galaxies with large numbered black circles in the left panels.

With the knowledge of the spectroscopic redshift we can improve on existing physical quantity measurements. We obtain stellar masses and star formation rates (SFR) from running MAGPHYS (da Cunha et al., 2008) with spectral models were constructed from the stellar libraries by Bruzual & Charlot (2003) on the set of photometric bands from near-UV to near-IR from the COSMOS2015 catalogue (Laigle et al., 2016). The dust is modelled based on the Charlot & Fall (2000) prescription.

We also use in this chapter a measurement of local over-density based on the cosmic density field value at the position of each target. We use the density estimation of Darvish et al.

(2014, 2017) which is constructed from a $K_s$ magnitude-limited sample based on the Ilbert et al. (2013) photometric redshift catalogue. The density field was computed for a $\sim 1.8\,\mathrm{deg}^2$ area in COSMOS over a large redshift interval ($0.05 < z_{\mathrm{phot}} < 3.2$). In this chapter, we define over-density as

$$1 + \delta = \frac{\Sigma}{\Sigma_{\mathrm{median}}} \tag{7.1}$$

with $\Sigma_{\mathrm{median}}$ being the median of the density field at the redshift of the galaxy. For a detailed description of the density estimation method we refer to Darvish et al. (2014, 2017).

The final sample studied in this chapter is selected to be at $0.8 < z < 0.9$ (matching our target selection) and has a total of 490 galaxies spanning a large diversity of stellar masses and environments across ∼10 Mpc. We show an overview of the main properties of the sample and survey in Fig. 7.1. We note also that we are probing both the star-forming and the quiescent population within this region (defined from the NUVrJ diagram, see e.g. Ilbert et al., 2013).

### 7.2.2 Imaging data

Since this structure was detected in the COSMOS field we base our morphological measurements on data from the HST/ACS F814W COSMOS survey (Scoville et al., 2007; Koekemoer et al., 2007). These images have a typical PSF FWHM of $\sim 0.09''$, a pixel scale of $0.03''$/pixel, and a limiting point-source depth AB(F814W) = 27.2 (5 $\sigma$). At the redshift of the superstructure, these images probe the rest-frame $B$-band galaxy morphology with sub-kpc resolution.

We use $10'' \times 10''$cut-outs (corresponding to square images with a $\sim$ 76 kpc side at the redshift of the superstructure) centred on the target position. To account for the PSF, we use the HST/ACS PSF profiles that were created with TinyTim (Krist, 1995) models and described by Rhodes et al. (2006, 2007).

## 7.3 Morphological characterization of the sample

Quantitative morphological analysis has complemented visual classification of images in the past decades. There are two main groups of morphological characterization: parametric modelling of the surface brightness profiles (e.g. de Vaucouleurs, 1959; Sérsic, 1968; Simard, 1998; Simard et al., 2011; Peng et al., 2002, 2010a; de Souza et al., 2004) and non-parametric quantitative morphology (e.g. Abraham et al., 1994, 2003; Bershady et al., 2000; Conselice et al., 2000a; Conselice, 2003; Papovich et al., 2003; Lotz et al., 2004; Law et al., 2007; Freeman et al., 2013;

Pawlik et al., 2016). Each method has its own strengths and drawbacks and the choice is usually related to a particular scientific question. Parametric models are more effective in getting a description of the light profile to get galaxy size estimates (e.g. Blanton et al., 2003; Trujillo et al., 2007; van der Wel et al., 2014; Wuyts et al., 2011) and to perform bulge-disk profile decomposition (e.g. de Souza et al., 2004; Tasca et al., 2009; Simard et al., 2011; Meert et al., 2013; Bruce et al., 2014a,b; Lang et al., 2014; Margalef-Bentabol et al., 2016; Gao & Ho, 2017; Dimauro et al., 2018). Whereas non-parametric methods are used often to identify irregularities in galaxies as signatures of past or ongoing mergers (e.g. Lotz et al., 2008; Conselice et al., 2009; Conselice & Arnold, 2009; Freeman et al., 2013; Pawlik et al., 2016). We are interested in both the estimation of galaxy interactions and the build-up of galactic bulges in dense environments and so we use a combination of both methods, along with visual classification to have a complete perspective on the impact of environment on galaxy morphology.

### 7.3.1 PARAMETRIC MODELLING OF GALAXIES

The retrieval of structural parameters based on Sérsic (1968) profiles is done using the publicly available GALFIT (Peng et al., 2002, 2010a), a stand-alone program aimed at two-dimensional decomposition of light profiles through model fitting. We also use SEXTRACTOR (Bertin & Arnouts, 1996) to provide initial guesses for each galaxy model and to produce binary images to mask all neighbour objects that might affect the fit. This method follows closely the procedures defined in Paulino-Afonso et al. (2017) and Paulino-Afonso et al. (2018c). We add on that method by fitting all galaxies with two models: a single Sérsic profiles and a combination of an exponential disk with a central Sérsic profile to account for the existence of a bulge. We chose to do so since we are dealing with an already evolved population of galaxies and at a resolution where sub-structures are resolved (see e.g. Tasca et al., 2009).

We are free to choose a model with as many components as one wants to fit every galaxy. However, to get physically meaningful results from fitting galaxy images one should take caution with over-fitting the data by choosing models that are too complex when compared to what is needed to fit the actual data. There have been some statistical criteria to decide whether or not a complex model should be used (e.g. Simard et al., 2011; Kelvin, 2012; Meert et al., 2013; Bruce et al., 2014b; Margalef-Bentabol et al., 2016). The Bayesian Information criterion, e.g. used by Bruce et al. (2014b) and Kelvin (2012), is a measure of how good a model fits the data which. In the case of nested models it penalizes those with the higher number of free parameters. It is described by

$$BIC = \chi^2 + k\ln(N) \tag{7.2}$$

where $\chi^2$ is the measure of the global goodness of the fit given by GALFIT, $k$ is the number of the free parameters of the model we are considering and $N$ is the number of contributing data points to the analysis of the model which is taken to be the area, in pixels, of the object one is considering. Given two models we can compute the difference in this estimator with

$$\Delta BIC = BIC_c - BIC_s = (\chi^2_c - \chi^2_s) + (k_c - k_s)\ln(N) \tag{7.3}$$

where $s$ and $c$ denote the simple (one profile) and complex (bulge+disk) models, respectively. The preferred model is that with the lower BIC value. In a strict sense, if $\Delta BIC < 0$ then the complex model is to be chosen over the simplest one. However to be sure that the complex model is more than just simply marginally better than a single profile, a stricter rule is usually applied: $\Delta BIC < -10$ (Kelvin, 2012).

### 7.3.2 Non-parametric quantitative morphology

The indices for non-parametric morphology that we have implemented allow us to get additional structural indicators that can extract morphological information from galaxies with the need to assume any model. These include the CAS system (Conselice et al., 2000a; Conselice, 2003, see also Abraham et al. 1994 and Bershady et al. 2000), the G-$M_{20}$ system (Lotz et al., 2004, see also Abraham et al. 2003). The two latter indices are computed over the segmentation map of the galaxy which is computed as the group of a minimum of 10 connected pixels above $3\sigma$ that are closest to the object coordinates. These indices are commonly used to detect disturbed galaxy light profiles associated with on-going galaxy mergers (e.g. Conselice, 2003; Lotz et al., 2004, 2008; Conselice et al., 2009; Conselice & Arnold, 2009).

The concentration index $C$ is defined as the ratio of the 80% to the 20% curve of growth radii within 1.5 times the Petrosian (1976, $r_p$) radius for a parameter $\eta = 0.2$. With that radius we compute the flux using elliptical apertures centred on the light-weighted centre of the galaxy up to which 20% and 80% of the light is contained. Then we compute $C$ via:

$$C = 5\log\left(\frac{r_{80}}{r_{20}}\right). \tag{7.4}$$

This parameter allows to separate between concentrated objects such as ellipticals from more extended sources such as spirals or irregulars. Using this definition the values of $C$ range from about 2 to 5, where $C > 4$ usually indicates spheroidal like systems, $3 < C < 4$ disk galaxies and the lower values of $C$ are from low surface brightness objects or sometimes from multi-component systems (see e.g. Conselice, 2003).

The asymmetry index $A$ measures the strength of non axis-symmetric features of an image $I$ by comparing it to a 180 degrees rotated version of itself, $I^{180}$. Since we expect asymmetric features on irregular galaxies usually associated with galaxy-galaxy interactions, this index is very useful to identify on-going galaxy mergers. It also correlates with on-going star formation as individual star-forming regions in a larger galaxy can also produce asymmetric flux distributions (Bershady et al., 2000; Conselice et al., 2000a; Conselice, 2003). We compute the index $A$ as

$$A = \frac{\sum_{i,j} |I_{i,j} - I_{i,j}^{180}|}{\sum_{i,j} I_{i,j}} - B_{180}, \tag{7.5}$$

where $I_{i,j}$ is the intensity at the pixel (i,j) and $B_{180}$ is the intensity of the background asymmetries. The centre around which the image is rotated is an important parameter and there are difficulties in having a well defined galaxy centre. We follow the method of Conselice et al. (2000a) and iterate the centre position following a gradient-step approach starting from the light-weighted centre to find the local minimum of $A$ within the segmentation map. To compute $B_{180}$ we use the median of 100 different sky patches of the same size of the image on which we compute $A$ and extracted from regions around the object of interest.

The Gini coefficient, $G$, measures the concentration of light within the pixels belonging to the galaxy's segmentation map. There is some correlation between $G$ and $C$ simply because more concentrated galaxies tend to have their light distributed over a small number of pixels therefore leading to high values of $G$ and $C$. Reversely, low and shallow surface brightness profiles tend to have their light more equally distributed leading to lower values of $G$ and $C$. However, the Gini coefficient will differ from the Concentration parameter in those cases where there is a concentration of high flux pixels away from the projected centre of the galaxy (e.g. multi-clump galaxy). This index is derived from the Lorenz curve which is a rank ordered cumulative distribution function of a galaxy's pixel values:

$$L(p) = \frac{1}{\bar{X}} \int_0^p F^{-1}(u) du, \tag{7.6}$$

where $F(u)$ is the cumulative distribution function, $p$ is the percentage of the fainter pixels normalized and $\bar{X}$ is the mean pixel flux. The Gini coefficient is then defined as the ratio of the curve $L(p)$ and the equality curve $L(p) = p$. In a discrete population it can be computed as

$$G = \frac{1}{2\bar{X}n(n-1)} \sum_{i,j}^{n} |X_i - X_j|, \tag{7.7}$$

where $n$ is the number of pixels of the galaxy. $G = 0$ if all the pixels have the same non-zero flux and $G = 1$ if all the flux is contained in one pixel. An efficient way to compute this coefficient is to first sort the pixels of the galaxy in increasing order of flux an then compute simply

$$G = \frac{1}{\bar{X}n(n-1)} \sum_{i}^{n} (2i - n - 1) X_i. \tag{7.8}$$

Since this coefficient takes into account all pixels of the object, it is very sensitive to the segmentation map associated with the galaxy (see Lotz et al., 2004). The inclusion of background flux will increase the value of $G$ while not taking into account low surface brightness pixels will decrease its value. We note that direct comparison to other results in the literature needs to be done with caution, as different definitions of the segmentation map can yield different Gini values for the same galaxies. While this affects the absolute value of $G$ any relative comparison within our sample is valid since it is all computed using the same definition for the segmentation map.

The index $M_{20}$ is also a measure of light concentration. However, being independent of a specific definition of centre or on having elliptical/circular apertures is less sensitive to asymmetries in the light profile. It is thus a more robust measure for galaxies with multiple bright clumps within a single segmentation map. The total second order moment $M_{tot}$ is computed by summing the flux in each pixel $I_i$ multiplied by the squared distance to the centre of the galaxy. In this case, the centre of the galaxy is that which minimizes $M_{tot}$:

$$M_{tot} = \sum_{i}^{n} I_i[(x_i - x_c)^2 + (y_i - y_c)^2]. \tag{7.9}$$

The index $M_{20}$ is then the normalized sum of the brightest 20% pixels values taken from a list of intensity sorted values in a descending order

$$M_{20} = \log_{10}\left(\frac{\sum_{i}^{N} I_i[(x_i - x_c)^2 + (y_i - y_c)^2]}{M_{tot}}\right) \tag{7.10}$$

with the sum considering the pixels that obey $\sum I_i < 0.2 I_{tot}$ where $I_{tot}$ is the total flux of the galaxy inside the segmentation map region. We normalize by $M_{tot}$ so that this parameter is independent of either total flux or galaxy size.

### 7.3.3 Visual classification

The classification of galaxies into different categories has been done extensively since the first extragalactic images were recorded in photographic plates (e.g. Hubble, 1926, 1930; de Vaucouleurs, 1959; van den Bergh, 1976; Nair & Abraham, 2010; Baillard et al., 2011; Buta et al., 2015; Kartaltepe et al., 2015). This is a time-consuming task if one wishes to carry out on large samples and has the problem of not being reproducible and subject to individual bias.

More recently, citizen science project Galaxy Zoo (Lintott et al., 2008) has combined more that 200 000 classifiers to produce a reliable catalogue of visual classifications (Lintott et al., 2011; Willett et al., 2013, 2017). We use in this chapter the data release of Galaxy Zoo containing the classifications for Hubble Space Telescope images, fully described by Willett et al. (2017). Out of 490 galaxies within our sample at $0.8 < z < 0.9$ we find a match for 447 objects.

To create subsets of different morphological types (elliptical, disk, or irregular, see e.g. Paulino-Afonso et al., 2018c) we use mainly the results from the first and second tiers (Willett et al., 2017, Fig. 4). Briefly, the user is presented with a colour image and is asked to answer a set of pre-defined questions. The first question is to categorize the galaxy into one of three categories: smooth, features, or star/artefact. If a smooth morphology is chosen, the user is then asked to classify the shape into completely round, in between, or cigar-shaped. If on the other hand the user classifies the galaxies has having features then it should classify the galaxy as being clumpy or not. Usually disk galaxies are classified as non-clumpy featured galaxies. At the end of the process all users are asked if they find anything odd (e.g. rings, tails, asymmetries, mergers, disturbed galaxies) which can be used to identify irregular galaxies. The final results for each galaxy are given as the fraction of users that have answered each given possibility. To map the user classifications to our defined categories we use the following criteria:

- Elliptical - $f_{\rm smooth} > 0.50$ and $f_{\rm odd} < 0.5$ and $f_{\rm cigar-shaped} < 0.5$;
- Disk - $f_{\rm features} > 0.23$[1] and $f_{\rm clumpy} < 0.5$ and $f_{\rm odd} < 0.5$ or $f_{\rm smooth} > 0.50$ and $f_{\rm odd} < 0.5$ and $f_{\rm cigar-shaped} > 0.5$;
- Irregular - $f_{\rm odd} > 0.5$ or $f_{\rm features} > 0.23$ and $f_{\rm clumpy} > 0.5$.

We note that due to the nature of the multi-tier classifications a galaxy may be classified in more than one category. For e.g., an elliptical galaxy in a pair could be both classified as elliptical or irregular under our assumptions.

## 7.4 Galaxy morphology across stellar mass, environment, and star-formation

We group galaxies in three different samples based on the local density to trace objects which should be representative of field ($\log_{10}(1+\delta) < 0.1$), filament ($0.1 < \log_{10}(1+\delta) < 0.5$), and cluster galaxies ($\log_{10}(1+\delta) > 0.5$) based on the relation of the cosmic web environment with over-density (see Chap. 5). We also explore the differences between two different populations: star-forming and quiescent.

[1] As suggested by Willett et al. (2017, see Table 11) when considering fractions on second tier questions.

Of the 490 galaxies at $0.8 < z < 0.9$ we have successfully fit either a one or two-component model to 470 galaxies (96%). The remaining 20 galaxies have failed to converge. We have a total of 173 galaxies for which their best-fit is a bulge+disk model. Considering only galaxies with stellar masses greater than $10^{10}\mathrm{M}_{\odot}$ we find a fraction of $\sim 41 \pm 3\%$ of two-component systems. This is in agreement with the reported two-component model fraction of $35 \pm 6\%$ at $z \sim 1$ by Margalef-Bentabol et al. (2016) for a field sample of $\log_{10}(M_{\star}/M_{\odot}) > 10$ galaxies.

### 7.4.1 GALAXY SIZES

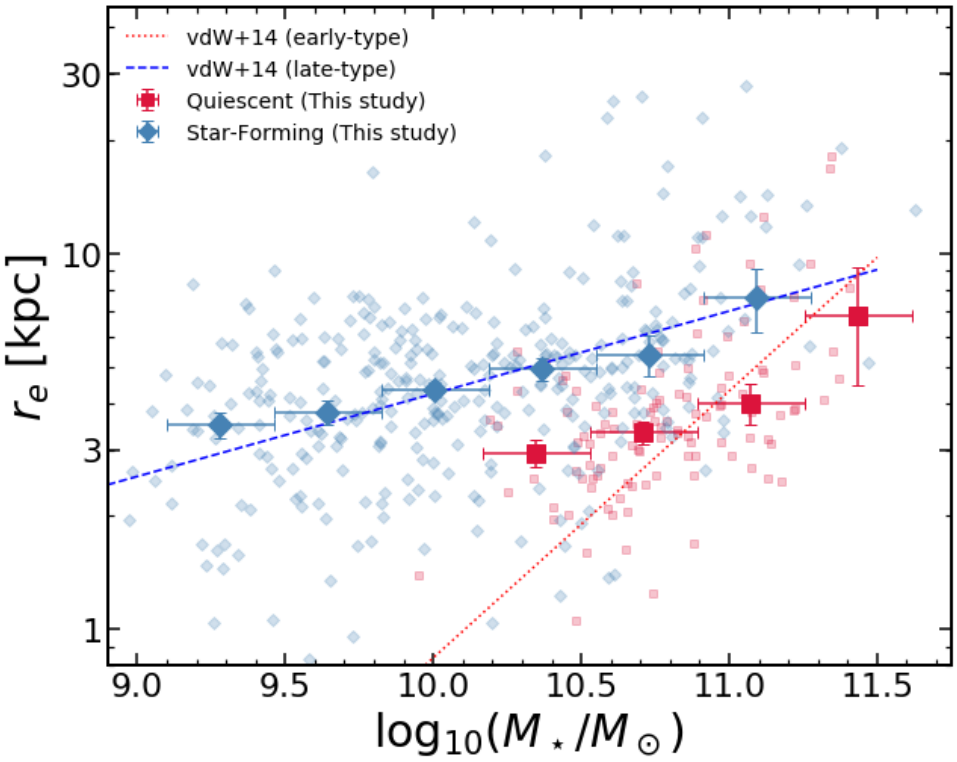


**Figure 7.2** The stellar-mass size relation for all galaxies in our sample, divided in the quiescent (red squares) and the star-forming (blue diamonds) subsamples. Horizontal error bars delimit the stellar mass bins. We also show the derived relation for a large sample at similar redshifts for late-type (blue dashed line) and early-type (red dotted line) derived by van der Wel et al. (2014). We find very good agreement between our sample and a magnitude-limited sample at these redshifts, indicating that our sample is representative of the larger population in terms of sizes and stellar masses.

We show in Fig. 7.2 (top panel) the relation between the median galaxy size (measured as the effective radius) as a function of stellar mass for quiescent and star-forming galaxies. In the case of galaxies best fit with a bulge+disk model we have two parameters for the size of each component. To compare the extent of these objects to the single Sérsic models we assume in that case that the size of the galaxy is traced by the size of its disk component. We find a good agreement to a large field sample at similar redshifts (van der Wel et al., 2014) which means that galaxies in this over-dense region in the COSMOS have similar sizes at fixed stellar mass.

We have attempted to split each population in three local density bins and find no significant differences in galaxy size between low- and high-density regions within our sample, both for star-forming and quiescent galaxies. This is in agreement with studies in the literature that find little difference between field and cluster galaxies at $0 < z < 2$ (e.g. Papovich et al., 2012; Huertas-Company et al., 2013b; Lani et al., 2013; Cebrián & Trujillo, 2014; Newman et al., 2014; Kelkar et al., 2015; Allen et al., 2015, 2016; Saracco et al., 2017).

### 7.4.2 Prominence of galactic bulges

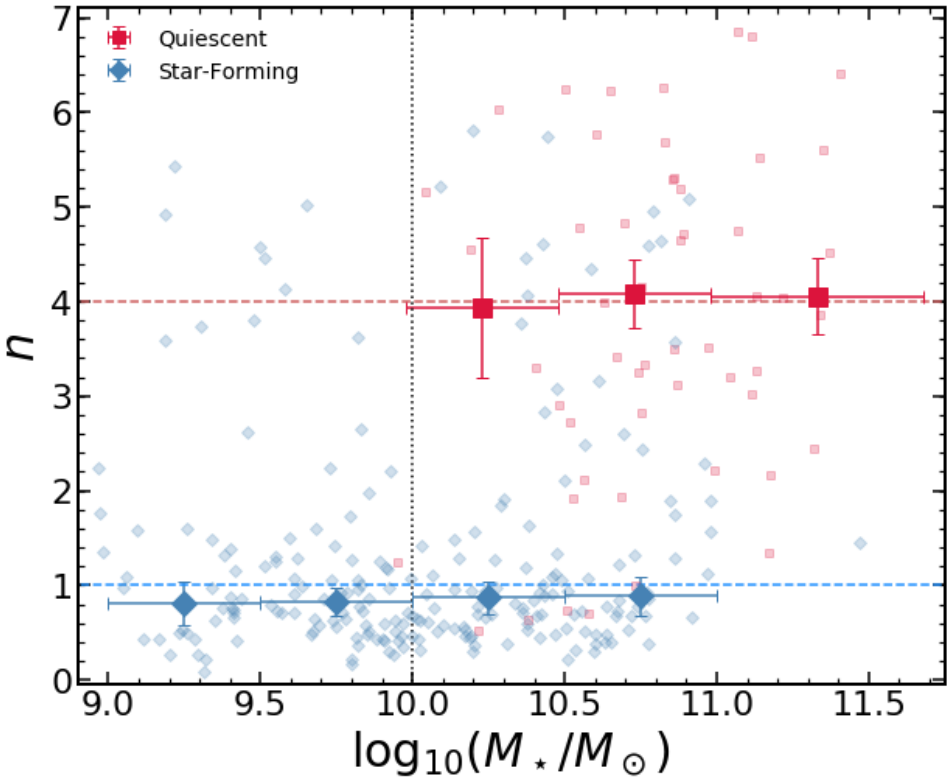


**Figure 7.3** Sérsic index as a function of stellar mass for galaxies best fit by a single Sérsic profile. We show star-forming (blue diamonds) and quiescent (red squares) separately. The median (and corresponding error) is shown with large symbols. Horizontal error bars delimit the stellar mass bins. We show as horizontal dashed lines the values for an exponential disk (blue, $n = 1$) and a classical elliptical (red, $n = 4$) profiles. The vertical dotted line highlights the stellar mass completeness of our survey. We find star-forming and quiescent galaxies to align with the classical expectations at lower redshifts, with quiescent galaxies having profiles typical of ellipticals and star-forming galaxies those of typical disks.

We explore the impact of stellar mass on the steepness of the light profiles in galaxies in star-forming and quiescent galaxies. We show in Fig. 7.3 the median Sérsic index for all galaxies best-fit with a single Sérsic profile. We find that quiescent galaxies have similar Sérsic indices at all stellar masses greater than $10^{10}\mathrm{M}_{\odot}$, and is the typical value for classical ellipticals $n \sim 4$. For star-forming galaxies we also find no dependence on stellar mass of the median value of $n$, with a typical value around $n \sim 1$, characteristic of exponential disks. We attempt to split further

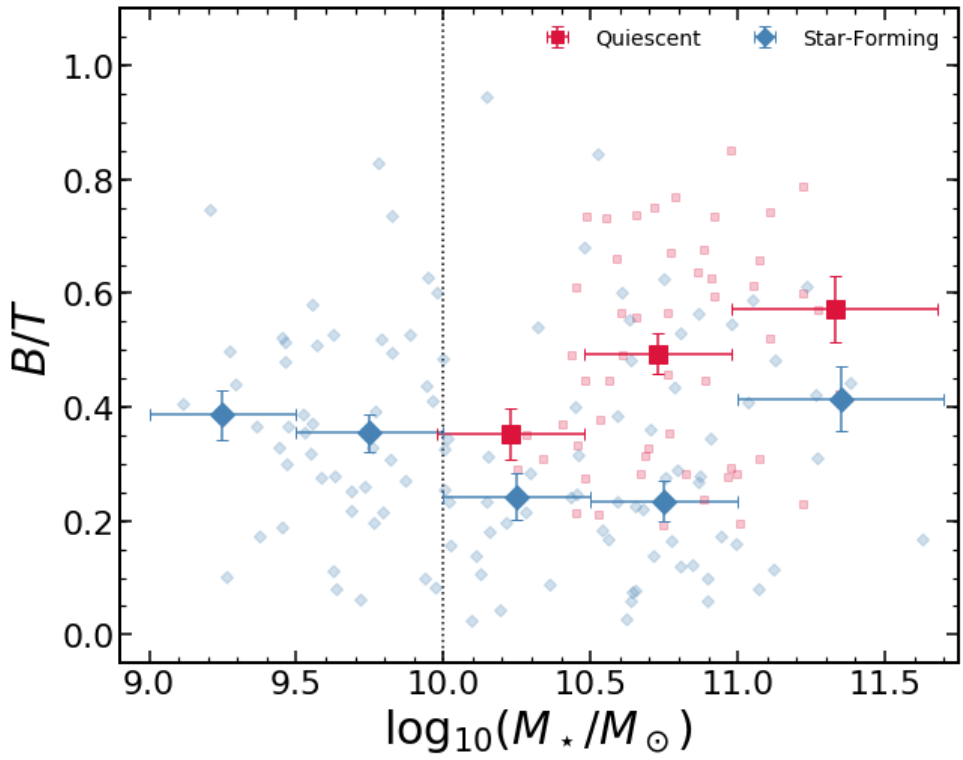


**Figure 7.4** Bulge-to-total light ratio as a function of stellar mass. We find quiescent galaxies to have slightly more prominent bulges than star-forming galaxies at similar stellar masses.

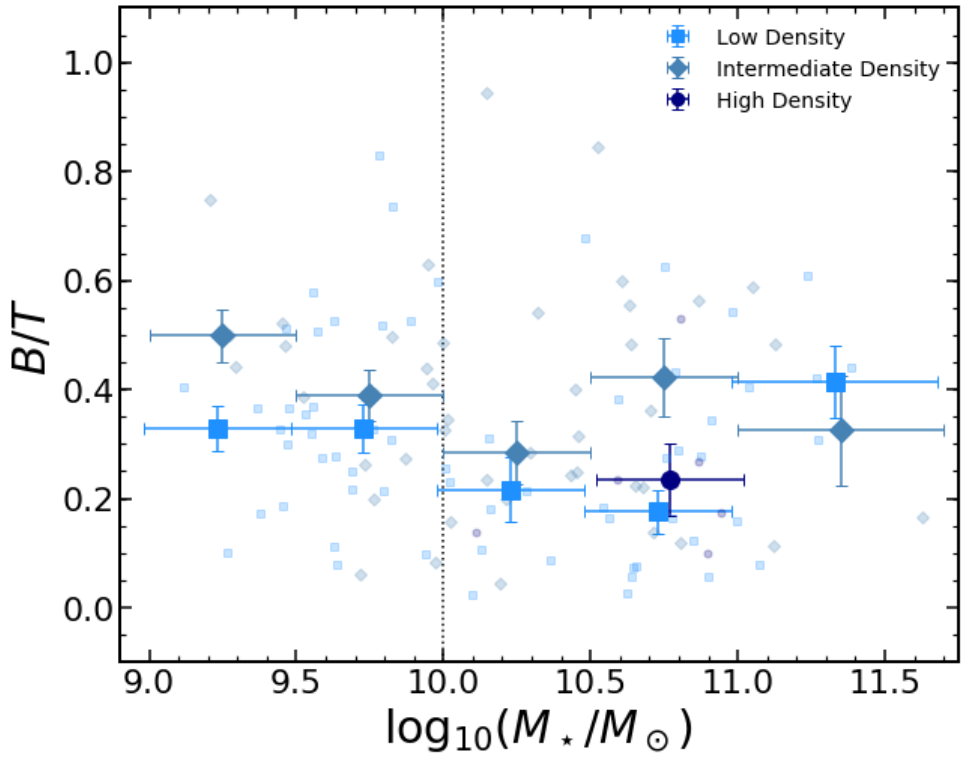


**Figure 7.5** Bulge-to-total light ratio of star-forming galaxies as a function of stellar mass for three over-density bins. We find hints for environmental influence on the $B/T$ of star-forming galaxies, with them being more prominent bulges in intermediate density environments at all stellar masses lower than $10^{11}\mathrm{M}_{\odot}$.

our sample in over-density bins, to explore the impact of environment on galaxy morphology, and find no statistical difference for samples in different environments both for star-forming and quiescent galaxies.

We show in Fig. 7.4 the median bulge-to-total light ratio ($B/T$) for galaxies best-fit with a two-component model in our sample splitting in stellar mass and over-density bins. Considering star-forming galaxies we find it to slightly decrease with stellar mass (from $B/T = 0.38 \pm 0.04$ at $9 < \log_{10}(M_\star/M_\odot) < 9.5$ to $B/T = 0.23 \pm 0.03$ at $10.5 < \log_{10}(M_\star/M_\odot) < 11$) and then an increase towards higher stellar masses reaching $B/T = 0.41 \pm 0.05$ at $\log_{10}(M_\star/M_\odot) > 11$. For quiescent galaxies we find a rise in the median $B/T$ with stellar mass. It increases from $B/T = 0.35 \pm 0.04$ at $10 < \log_{10}(M_\star/M_\odot) < 10.5$ to $B/T = 0.57 \pm 0.06$ at $\log_{10}(M_\star/M_\odot) > 11$.

We further explore any environmental dependence on the median value of $B/T$ and find no statistical difference in the case of quiescent galaxies. For star-forming galaxies, we show in Fig. 7.5 that the bulge is slightly more prominent in intermediate-density environments when compared to lower density counterparts at stellar masses lower than $10^{11}\mathrm{M}_\odot$. We stress that we do not have enough star-forming galaxies in high-density regions to establish a comparison to the densest regions we probe with our survey.

### 7.4.3 A MODEL-INDEPENDENT APPROACH TO CONFIRM THE MORPHOLOGY TRENDS

As detailed in Sect. 7.3.2, there are a number of quantities that can describe the light profiles of galaxies without the assumption of a physical model. We show in Fig. 7.6 the properties of star-forming and quiescent galaxies as a function of stellar mass. At first glance we find that quiescent galaxies have higher concentration indices than star-forming galaxies at all stellar masses. We also find a dependence on stellar mass (from $\sim 10^{10.25}\mathrm{M}_\odot$ to $\sim 10^{11.25}\mathrm{M}_\odot$) for both populations, with higher stellar mass galaxies having higher concentration values. In quiescent galaxies the median value of $C$ rises from $3.29 \pm 0.05$ up to $3.64 \pm 0.09$ and in star-forming galaxies it rises from $2.54 \pm 0.05$ to $3.0 \pm 0.1$. We note that despite having lower concentration values than those reported for ellipticals and spirals observed at lower redshift (Conselice, 2003, 4.4 for ellipticals and 3.1-3.9 for spirals) we find that quiescent galaxies having higher concentration values is indicative of them having elliptical or bulge-dominated morphologies.

We also show in Fig. 7.6 the median asymmetry of galaxy light profiles. On a global trend, we find that neither star-forming nor quiescent galaxies asymmetry is correlated with its stellar mass. Considering galaxies above our stellar mass completeness limit ($10^{10}\mathrm{M}_\odot$), we find quiescent galaxies to have lower asymmetry ($A \sim 0.05 - 0.06$) than star-forming galaxies ($A \sim 0.10 - 0.12$) at all stellar masses. This difference in asymmetry values is consistent with the difference between ellipticals and spirals in the local Universe (e.g. Conselice, 2003). This difference in asymmetry

indicates that quiescent galaxies have smoother light profiles when compared to star-forming galaxies, which usually means that star-forming galaxies have a clumpier light profile consistent with patches of HII regions within the galaxy's extent.

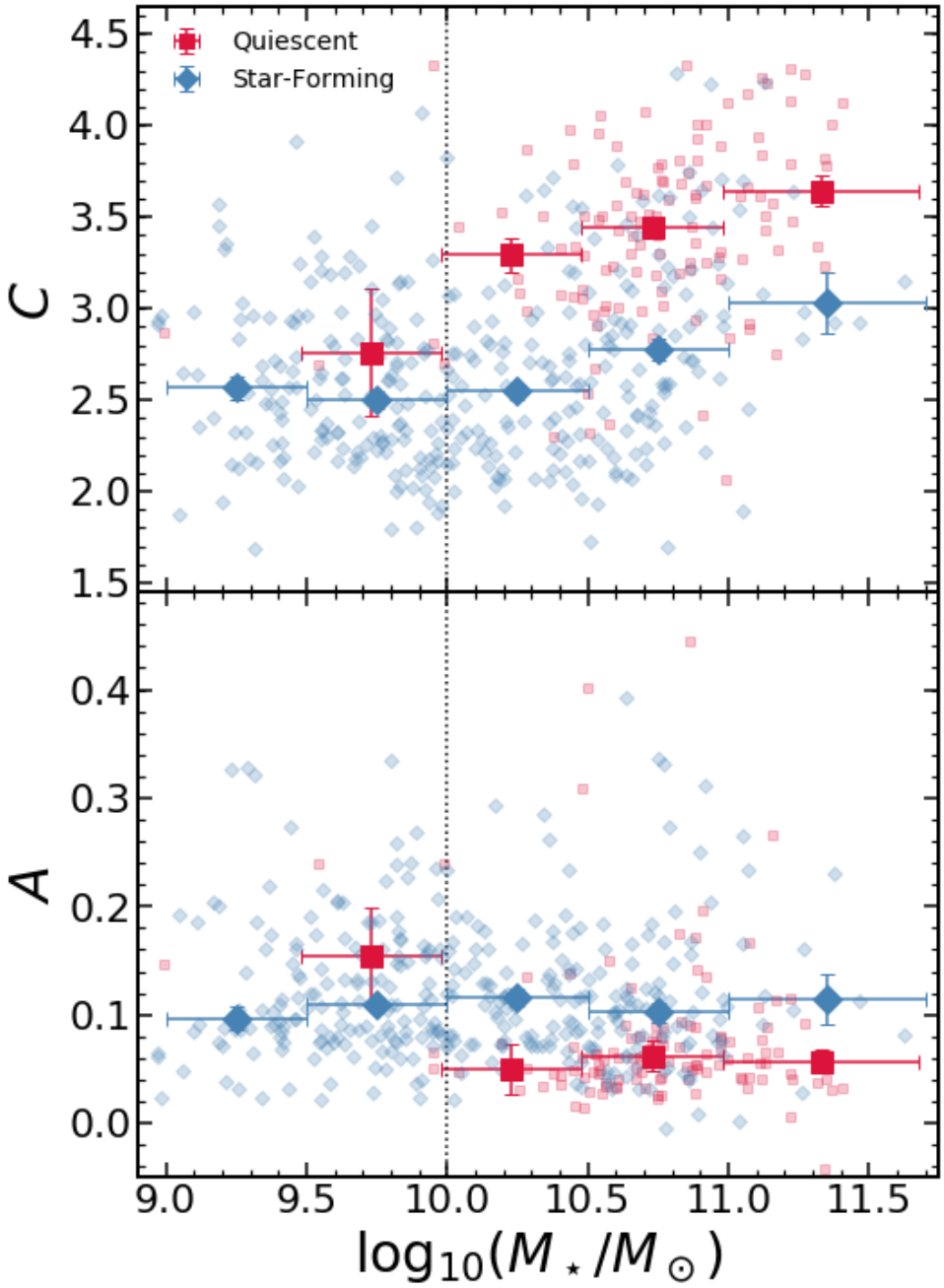


**Figure 7.6** Light concentration (top) and image asymmetry (bottom) as a function of stellar mass. We find quiescent galaxies to have higher concentration of light than star-forming galaxies at similar stellar masses. We also find quiescent galaxies to have less disturbed profiles at stellar masses greater than $10^{10}M_{\odot}$.

In Fig. 7.7 we show the results of a different set of morphology diagnostics highlight the median value for star-forming and quiescent galaxies. We find that quiescent galaxies have a higher percentage of their light concentrated on a smaller area (higher Gini coefficient) when compared to star-forming galaxies at similar stellar masses. Considering galaxies with stellar masses above $10^{10}M_{\odot}$, we find a small increase in $G$ for quiescent galaxies (from $0.49 \pm 0.02$ to $0.52 \pm 0.01$)

and a steeper increase for star-forming galaxies (from $0.30 \pm 0.01$ to $0.37 \pm 0.02$). When considering the value of $M_{20}$, which measures the concentration of the brightest regions and is sensitive to the existence of multiple clumps, we find a global trend for galaxies with high stellar mass to have lower values of $M_{20}$ (higher concentration of the brightest regions, irrespective of clumpy sub-structures). We also find quiescent galaxies to have higher flux concentration when compared to star-forming galaxies of similar stellar masses. The combination of these two quantities highlights the difference between quiescent galaxies having a higher concentration of their flux and less likely to have clumpy substructures, when contrasted to their star-forming counterparts.

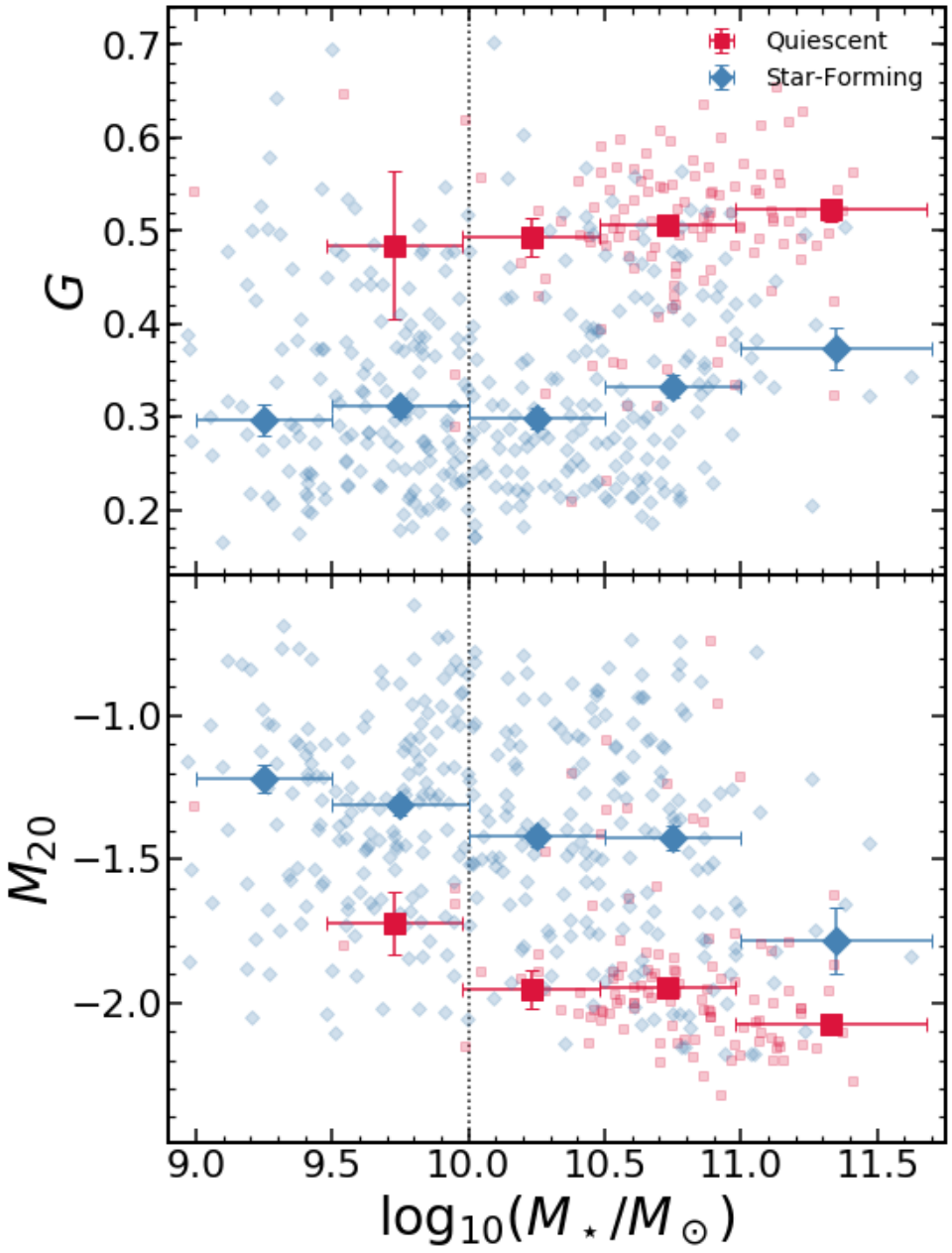


**Figure 7.7** Gini coefficient (top) and moment of light (bottom) as a function of stellar mass. We find quiescent galaxies to have their light concentrated on a smaller area (higher value of $G$) than star-forming galaxies at similar stellar masses. We also find quiescent galaxies to be smoother (lower values of $M_{20}$) at all stellar masses.

We stress that we have attempted to split both populations in different bins of local density and find no statistically significant differences among different environments for each subsample. The trends reported in this section all hint at quiescent galaxies having morphologies characteristic of elliptical (or bulge-dominated) light profiles whereas star-forming galaxies resemble more exponential disks with a small degree of clumpiness/asymmetry in their light profiles. It is thus an independent assessment of galaxy morphology which confirms the trends we find with profile fitting in Sect. 7.4.2.

### 7.4.4 LOCAL DENSITY IMPACT ON VISUAL MORPHOLOGY

We have defined in Sect. 7.3.3 three different morphological classes based on GalaxyZoo classifications of HST data. In this section we explore the impact of local density on the fraction of galaxies for each of the defined classes: ellipticals, disks, and irregulars. We restrict our analysis to galaxies more massive than $10^{10}M_{\odot}$ (our completeness limit) and opt not to show results on the stellar mass dependence of this fraction since we find all classes to be roughly consistent with no stellar mass dependence, given our error bars. We show instead the influence of local environment to explore the existence of a morphology-density relation within our sample at $z \sim 0.84$.

We show in Fig. 7.8 the differences in the fraction of observed morphologies for massive galaxies in our sample. At the lower densities (field- and filament-like regions) we find similar fractions of disks and elliptical galaxies ($\sim$48%). As we move towards higher density regions we find an increase in the fraction of elliptical galaxies (up to $75 \pm 24\%$) and a strong decline in the fraction of disk galaxies (down to $13 \pm 7\%$). The fraction of galaxies classified as irregular is roughly constant at $\sim 16-18\%$. This result hints at an established morphology-density relation at the redshifts of our sample.

We note, however, that we showed in the previous subsections that if we split our sample in star-forming and quiescent populations we find little effect of local environment on quantitative morphology. We also explore here the fraction of each class for these two populations in Fig. 7.9.

For quiescent galaxies we find that the fraction of ellipticals dominates at all environments and we observe no change with local density (nearly constant fraction at $\sim$80%). For quiescent galaxies with disk morphology we find a constant fraction in field- and filament-like densities ($\sim$35%) and then a drop higher densities (down to $7 \pm 5\%$). We find that quiescent galaxies with irregular morphologies at $\sim$7% at lower density regions and then a rise to $21 \pm 10\%$ in the highest density bin, surpassing the fraction of disks at these densities.

For star-forming galaxies we find disk morphologies to be the most common class at all densities

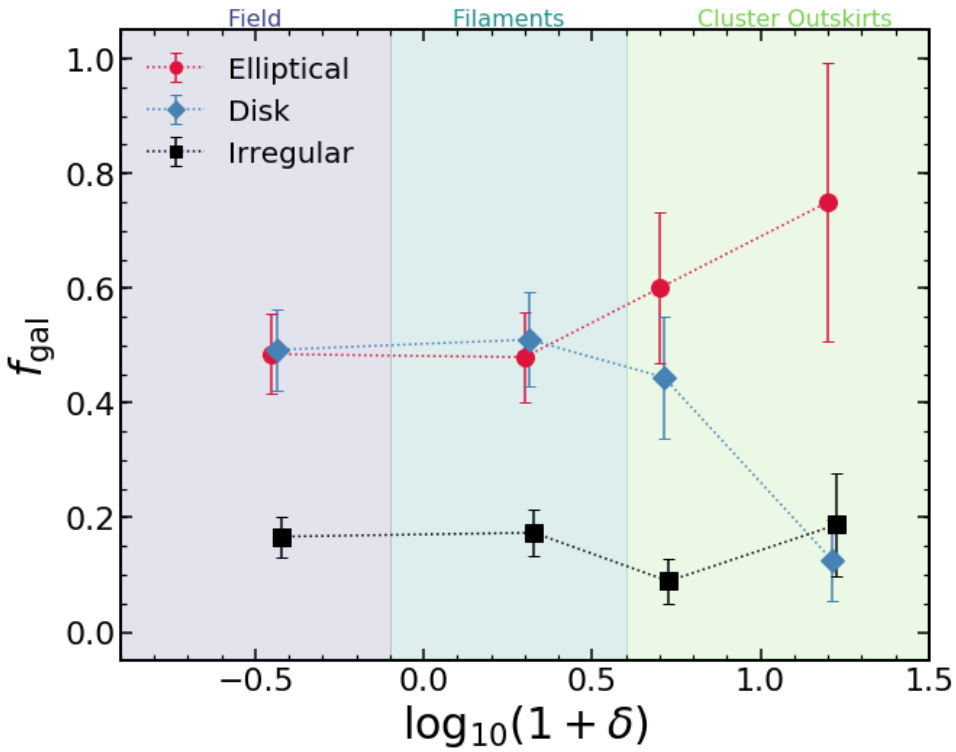


**Figure 7.8** The fraction of galaxies more massive than $10^{10}M_{\odot}$ of a given galaxy morphology (see Sect. 7.3.3) as a function of local density. We show as coloured vertical regions the likely association between local density and density regions. We note that we find no differences between field-like and filament-like densities. We do find a rise in the fraction of ellipticals and a decline of disk-like morphologies towards the densest regions.

(∼60%) with little change across different densities. For star-forming ellipticals we find a nearly constant fraction for the three lower density bins (at ∼30%) and then a rise to $50 \pm 15\%$ at the highest density bin. We also find a decrease on the fraction of irregular galaxies from field- and filament-like regions (∼20%) down to 0% at the highest density bin in the sample.

## 7.5 Discussion

We have studied galaxy morphology on sample of ∼500 spectroscopically confirmed galaxies in and around a superstructure in COSMOS at $z \sim 0.84$. We have found that when split in star-forming and quiescent galaxies we find little difference across environments.

### 7.5.1 Environmental dependence predicted from the quiescent fraction

We have shown in Sect. 7.4 that when split into star-forming and quiescent sub-samples we find little dependence on local density for a morphological indicators (both quantitative and

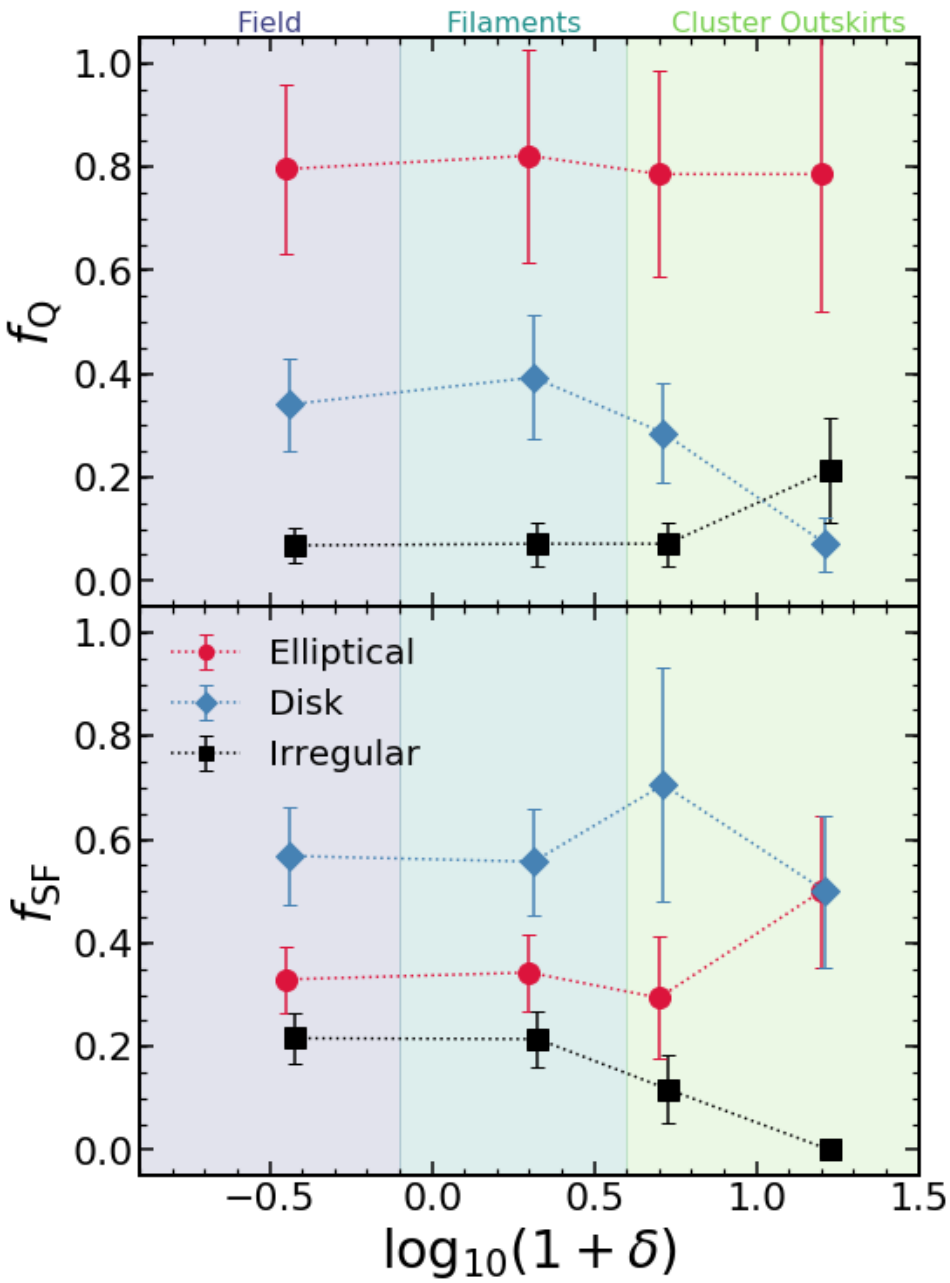


**Figure 7.9** The fraction of galaxies more massive than $10^{10}M_{\odot}$ of a given galaxy morphology (see Sect. 7.3.3) as a function of local density for quiescent (top) and star-forming (bottom) galaxies. We show as coloured vertical regions the likely association between local density and density regions. For quiescent galaxies we see a constant fraction of elliptical galaxies with density and a increase in irregular morphologies at the expense of disk galaxies in the densest regions. For star-forming galaxies we might find a small trend in the densest bin with an increase in ellipticals and a decline in disk galaxies, but our results are consistent with no influence of environment. We note that due to the multi-tier classification a galaxy might fit in more than one category (see Sect. 7.3.3).

qualitative). But we also show (see e.g. Fig. 7.8) that we find a morphology-density relation when considering the full sample. We can then try to explain the change with density as a change in the fraction of each population that contributes at each environment. We show in Fig. 7.10 the dependence of the quiescent fraction for galaxies more massive than $10^{10}M_{\odot}$ (see also Paulino-Afonso et al., 2018b) and find that it strongly increases from intermediate to high density

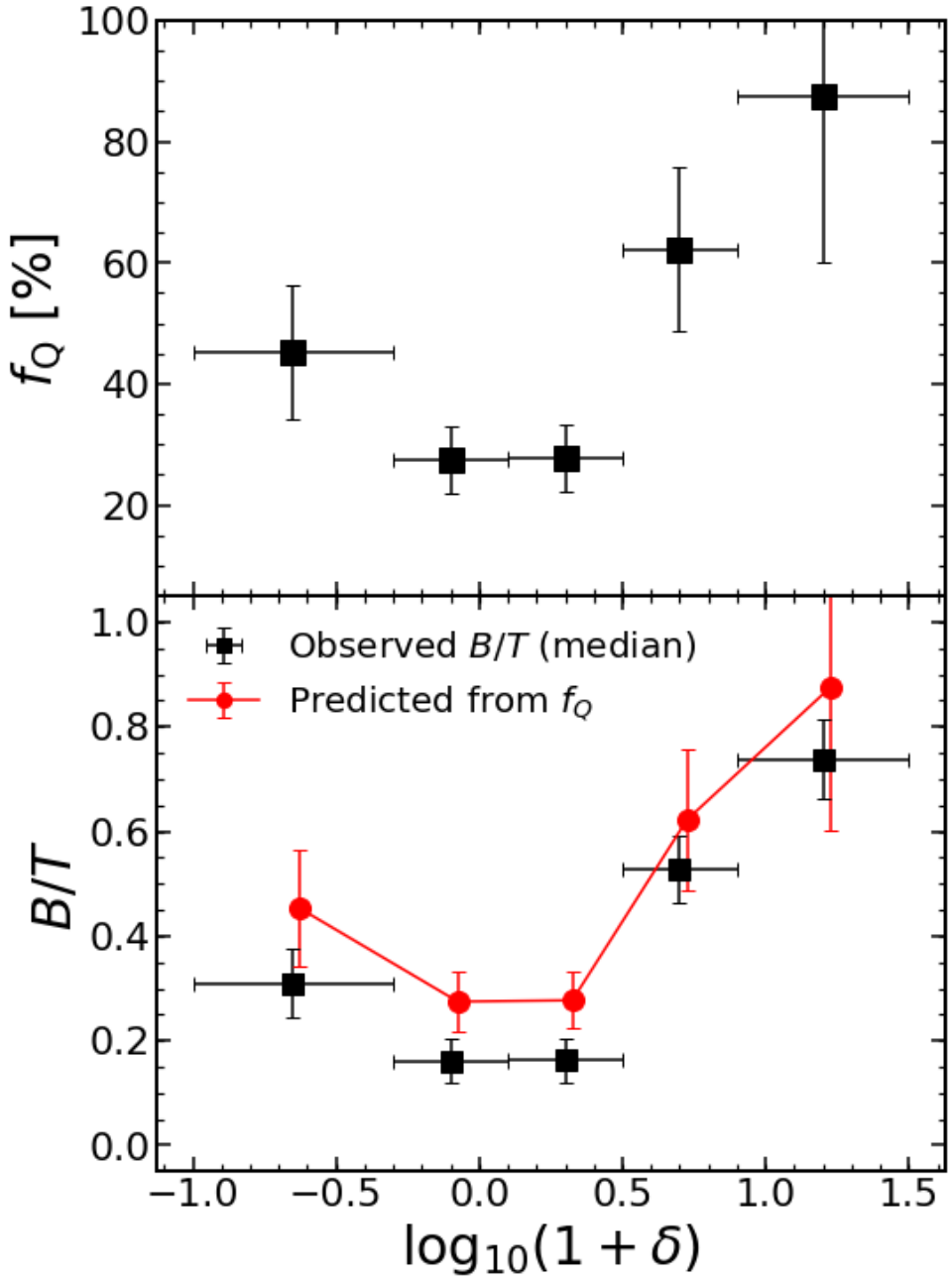


**Figure 7.10** Top: The fraction of galaxies more massive than $10^{10}M_{\odot}$ classified as quiescent as a function of local density. Bottom: The predicted (red circles) and observed (black squares) values of the bulge-to-total light ratio. The predicted values are based on a simple model (see Sect. 7.5.1) that predicts environmental dependence of any property based on the fraction of quiescent/star-forming galaxies in different environments. We find a good agreement between predicted and observed values, indicating that the perceived environmental effect of galaxy morphology is tightly correlated with the fraction of each population.

regions.

If we assume a simple model, considering two populations with average properties $x$, we can described the environmental dependence as a function of the fraction of e.g. quiescent galaxies $f_Q$:

$$x = \frac{x_{\rm SF} N_{\rm SF} + x_{\rm Q} N_{\rm Q}}{N_{\rm T}} = x_{\rm SF}(1 - f_Q) + x_{\rm Q} f_Q. \tag{7.11}$$

We can then use this to predict the expected values of any property if the fraction of quiescent objects is the driving influence of the observed environmental dependence. For example, we can derive the median $B/T$ as a function of environment assuming that star-forming galaxies have $B/T = 0$ (exponential disks) and quiescent galaxies have $B/T = 1$ (classical ellipticals). To compute the median properties for our observations we also assign a value of $B/T$ for galaxies best-fit with a single Sérsic profile ($B/T = 0$ if $n < 2.5$ and $B/T = 1$ if $n > 2.5$). We show in the bottom panel of Fig. 7.10 the resulting prediction compared to the median observed values of $B/T$. Overall, we find a good agreement between the observed and the predicted value from our very simple model. This is a strong argument in favour of having the morphology-density relation being tightly correlated with the fraction of quiescent/star-forming galaxies in different environments.

### 7.5.2 Morphology-density relation at $z \sim 0.84$

There are studies that show evidence for a correlation between morphology and environment up to $z \sim 1$ (e.g. Tasca et al., 2009). We find that such relation is also present in our sample (see Fig. 7.8). However, we also show that the impact of local density on the galaxy structure among galaxies of similar colours is negligible. What we find is consistent with the fraction of red/blue galaxies changing with environment and morphology tracing that change as well (see Fig. 7.10).

The differences in galaxy morphology for quiescent and star-forming galaxies has long been studied and established up to $z \sim 1$ (e.g. Strateva et al., 2001; Bamford et al., 2009; Mignoli et al., 2009; Wuyts et al., 2011; Whitaker et al., 2015; Krywult et al., 2017). And there are complimentary studies that the environmental dependence of galaxy morphology is tightly correlated with colour (Poggianti et al., 2008; Skibba et al., 2009; Bait et al., 2017). This confirms our findings that when splitting our sample in colour space, the dependence with environment vanishes (see also e.g. Papovich et al., 2012; Huertas-Company et al., 2013a,b; Lani et al., 2013; Cebrián & Trujillo, 2014; Newman et al., 2014; Kelkar et al., 2015; Allen et al., 2015, 2016; Saracco et al., 2017). The existence of such correlation hints at a coherent transformation both in colour and morphology for galaxies in different environments. This is already seen in some studies targeting green valley galaxies (with colours in-between the red sequence and the blue cloud) where morphologies in-between exponential disks and classical ellipticals are found (e.g. Mendez et al., 2011; Gu et al., 2018; Coenda et al., 2018). However, a difference in colour does not always translate to a difference in morphology for these sources (e.g. Schawinski et al., 2014) and both internal and external processes are required to explain such

evolution across the green valley (e.g. Kelvin et al., 2018; Nogueira-Cavalcante et al., 2018).

### 7.5.3 Bulge growth in higher density environments

One subtle effect of environment on star-forming galaxies seems to be linked to the growth of the galactic bulge (see Fig. 7.5). Although being mostly within $1\sigma$ from lower density environments, we do find a systematic brighter bulge on star-forming galaxies in intermediate-density environments[2] (at stellar masses $10^9 - 10^{11}\mathrm{M}_\odot$).

It is possible that the growth of the inner bulge is induced by a higher rate of interactions characteristic of intermediate-density environments, since several studies point to major and minor mergers as mechanisms for bulge growth (e.g. Eliche-Moral et al., 2006; Hopkins et al., 2010; Querejeta et al., 2015; Brooks & Christensen, 2016). And we find in the local Universe that merger induced star-formation is important (e.g. Lambas et al., 2012; Ellison et al., 2013; Scudder et al., 2015) which can account at the same time for the change in galaxy colour (see also e.g. Ellison et al., 2018) and structure required to explain the observations in our study.

## 7.6 Conclusions

We study the influence of environment on galaxy morphology on a sample of $\sim 500$ galaxies with spectroscopic redshifts in and around a superstructure in the COSMOS field. We present our results based on bulge-disk decomposition of light profiles, non-parametric morphology and visual classification. We study separately star-forming and quiescent galaxies selected in the NUVrJ colour space. We find little dependence on environment for each of the studied sub-samples. A summary of our results is found below:

- We find a fraction of $41 \pm 3\%$ of galaxies more massive than $10^{10}\mathrm{M}_\odot$ with a disk+bulge structure.
- Quiescent galaxies are smaller than their star-forming counterparts at similar stellar masses.
- Galaxies best-fit with a single profile show a clear morphology-colour dichotomy. Quiescent galaxies median Sérsic indices comparable to classical ellipticals ($n \sim 4$) and star-forming galaxies show profiles close to exponential disks ($n \sim 1$).
- We confirm this differences in light profiles with non-parametric morphology. Quiescent galaxies have smoother profiles (lower asymmetry and $M_{20}$) and have more concentrated

[2] We stress that we do not find enough star-forming galaxies in the higher density environments in our sample to make statistical assertions.

light profiles (higher concentration and Gini coefficient) than star-forming galaxies.

- We find evidence for the existence of a morphology-density relation at $z \sim 0.84$ when looking at the sample as a whole, but less pronounced when splitting in the two sub-samples.
- The existence of any environmental dependence of galaxy morphology is tightly correlated with the dependence of the quenched fraction on local density.

Based on our results we argue that both colour and morphology are affected by environment and this is manifested through a varying fraction of blue disks to red ellipticals from low- to high-densities. Such tight correlation between star formation and morphology implies that physical mechanisms responsible for regulating star formation must also act in changing the morphology of galaxies.

# CHAPTER 8

## VIS$^3$COS: IV. IS THERE A DEPENDENCE OF THE ELECTRON DENSITY WITH ENVIRONMENT AND/OR STELLAR MASS?

*We use high-resolution spectroscopic observations from the VIS$^3$COS survey to estimate the electron density ($n_e$) for a sample of galaxies in and around a superstructure at $z \sim 0.84$ in the COSMOS field. We measure $N_e$ from the [OII] doublet ratio. We find that for massive galaxies ($10.75 < \log_{10}(M_\star/\mathrm{M}_\odot) < 11.5$) the electron densities rises from low- to high-densities (from $n_e \sim 100$ cm$^{-3}$ to $n_e \sim 1000$ cm$^{-3}$, respectively). However, for intermediate stellar mass galaxies the electron density is found to decrease with increasing environmental density, in agreement with Darvish et al. (2015a). We also find that quiescent galaxies in the field have electron densities much higher than star-forming galaxies in similar environments. We hypothesize that high electron densities are not produced by star-forming processes in HII regions.*

adapted froma **Paulino-Afonso**, Sobral, D., Darvish, B. et al., in prep.

## 8.1 INTRODUCTION

We find that in the local Universe, some observed properties of galaxies (e.g. morphology, colours) are influenced by the environment they reside in.(e.g. Oemler, 1974; Dressler, 1980, 1984; Balogh et al., 2004; Kauffmann et al., 2004; Baldry et al., 2006; Bamford et al., 2009). And it is though that the main influence of local density on galaxy evolution is linked to the fraction of star-forming/quiescent galaxies as a function of environment (e.g. Lewis et al., 2002; Gómez et al., 2003; Hogg et al., 2004; Best, 2004; Kodama et al., 2004; Peng et al., 2010b; Cucciati et al., 2010a; Sobral et al., 2011; Muzzin et al., 2012; Darvish et al., 2014, 2016; Cohen et al., 2017). And when studying the properties of the subset of star-forming galaxies, many studies find that their properties, when directly linked to star formation (e.g. star formation rate - SFR, line equivalent widths, star formation main sequence), seem to not depend on local density (but it is still not a settled argument, see e.g. Peng et al., 2010b; Iovino et al., 2010; Wijesinghe et al., 2012; Muzzin et al., 2012; Koyama et al., 2013, 2014; Hayashi et al., 2014; Darvish et al.,

2014, 2015a, 2016).

However, there are a number of recent studies that find other properties to be influenced by the environment. On one hand, there are reports that metallicity is slightly higher in high-density environments at (e.g. Kulas et al., 2013; Shimakawa et al., 2015b; Sobral et al., 2015b). One other quantity that has be found to vary with environment is the electron density ($n_e$) at $z \sim 0.2-0.5$ (e.g. Sobral et al., 2015b; Darvish et al., 2015a). We note that both Sobral et al. (2015b) and Darvish et al. (2015a) target a merging cluster and large scale filaments, which are dynamically active regions. At higher redshift ($z \sim 2$), Kewley et al. (2016) find no difference in electron density with environment.

Measurements of the electron density are based on single component doublets from a single atom species which have different collisional level transitions (e.g. Osterbrock, 1989; Sanders et al., 2016). The flux ratio between the two components of the line doublet is therefore a consequence of the density of free electrons available for collision. Typical rest-frame optical lines used to probe this physical quantity are [OII] $\lambda$3726,$\lambda$3729 and [SII] $\lambda$6716,$\lambda$6731 ( e.g. Seaton & Osterbrock, 1957; Canto et al., 1980; Pradhan et al., 2006; Lehnert et al., 2009; Hainline et al., 2009; Bian et al., 2010; Krabbe et al., 2014; Masters et al., 2014; Shirazi et al., 2014; Darvish et al., 2015a; Shimakawa et al., 2015a; Sanders et al., 2016; Kewley et al., 2016; Kashino et al., 2017; Kaasinen et al., 2017). By measuring $n_e$ we are able to probe the inter-stellar medium (ISM) pressure of regions producing ionizing photons, namely HII regions (e.g. Lehnert et al., 2009).

Most studies of high redshift galaxies ($1 \lesssim z \lesssim 3$) show that typical electron densities were higher in the past by factors of $5-10$ (Masters et al., 2014; Shirazi et al., 2014; Sanders et al., 2016; Kashino et al., 2017; Kaasinen et al., 2017). Though some studies argue that this increase in the ISM pressure is related to an increase in star formation, and that differences between low and high redshift are mainly due to selection of galaxies with different SFRs (e.g. Shimakawa et al., 2015b; Kaasinen et al., 2017). However, not all studies find this correlation to be clear (e.g. Darvish et al., 2015a). Other studies link an increase in electron density to galaxy-galaxy interactions, finding that galaxies are more likely to have higher $n_e$ if they are undergoing tidal interactions (e.g. Krabbe et al., 2014).

In this chapter we use a large spectroscopic survey (VIS$^3$COS - Paulino-Afonso et al., 2018b, Chap. 5) targeting a large superstructure in the COSMOS field. The spectral coverage includes the [OII] doublet and allows for a statistical study of the variation of the electron density in a wide range of environments at $z \sim 0.84$. Aside from that, we will also be able to link high ($z > 1$) and low ($z < 0.1$) redshift observations, by providing measurements of electron density at an intermediate redshift.

This chapter is organized as follows: in Sect. 8.2 we give an overview of the VIS$^3$COS survey and derived measurements. Section 8.3 we describe our measurement of [OII] fluxes and our

estimation of electron density. In Sect. 8.4 we summarize our results on the dependence of electron density on stellar mass, environment, and star formation. In Sect. 8.5 we discuss our findings within the context of current galaxy formation and evolution literature. We use AB magnitudes (Oke & Gunn, 1983), a Chabrier (Chabrier, 2003) initial mass function (IMF), and assume a ΛCDM cosmology with $H_0$=70 km $s^{-1}$Mpc$^{-1}$, $\Omega_M$=0.3 and $\Omega_\Lambda$=0.7. The physical scale at the redshift of the superstructure ($z \sim 0.84$) is 7.63 kpc/″.

## 8.2 THE VIS$^3$COS SURVEY

The VIMOS Spectroscopic Survey of a Superstructure in the COSMOS field (VIS$^3$COS) is based on a high-resolution spectroscopic survey of galaxies in and around a large structure at $z \sim 0.84$ in the COSMOS field. The target structure covers a region $21' \times 31'$ ($9.6 \times 14.1$ Mpc) with three confirmed X-ray clusters (Finoguenov et al., 2007) and a large-scale over-density of H$\alpha$ emitters (Sobral et al., 2011; Darvish et al., 2014). For more details on the description of the survey we refer to Chap. 5.

The target selection was done using the Ilbert et al. (2009) catalogue and selecting galaxies brighter than $i_{AB} < 22.5$ and with photometric redshifts in the interval $0.8 < z_{phot} < 0.9$. Observations were carried out with the GG475 filter of VIMOS ($R \sim 2500$), covering a rest-frame region 3400-4600Å at the redshift of the structure. This wavelength coverage allows us to probe spectral features such as [OII] $\lambda$3726,$\lambda$3729 (partially resolved doublet), the 4000 Å break, and H$\delta$.

We measured spectroscopic redshifts on the 1D spectra with the SPECPRO (Masters & Capak, 2011) tool. We used a large set of prominent spectral features (e.g. [OII], H+K absorption, G-band, some Fe lines, and H$\delta$) to determine the redshift of each galaxy. We obtained a total of 696 spectroscopic redshifts of which 490 were in the selection range ($0.8 < z < 0.9$).

Using our spectroscopic redshift as prior information, we have re-fit the spectral energy distribution of all galaxies in the sample. We used MAGPHYS (da Cunha et al., 2008) to obtain new estimates of stellar masses and star formation rates (SFR) with a range of models built from the stellar libraries described by Bruzual & Charlot (2003) and with a dust modelled with the prescription by Charlot & Fall (2000). We used photometric measurements from near-UV to near-IR available in the COSMOS2015 catalogue (Laigle et al., 2016).

To estimate the local density associated with each galaxy, we use the cosmic density fields computed by Darvish et al. (2014, 2017). These density estimations were done based on a mass-complete sample with good quality photometric redshifts spanning $0.1 < z_{phot} < 1.2$ over an area of $\sim 1.8\,\mathrm{deg}^2$. We define over-density as

$$1 + \delta = \frac{\Sigma}{\Sigma_{\rm median}}, \tag{8.1}$$

where $\Sigma_{\rm median}$ is the median of the density at the galaxy's redshift. We refer to Darvish et al. (2014, 2017) for a detailed description of the method.

To summarize, we have a final sample of 490 galaxies with spectroscopic redshifts within $0.8 < z < 0.9$ that spans a large range in both stellar mass, and environments (see Fig. 8.1).

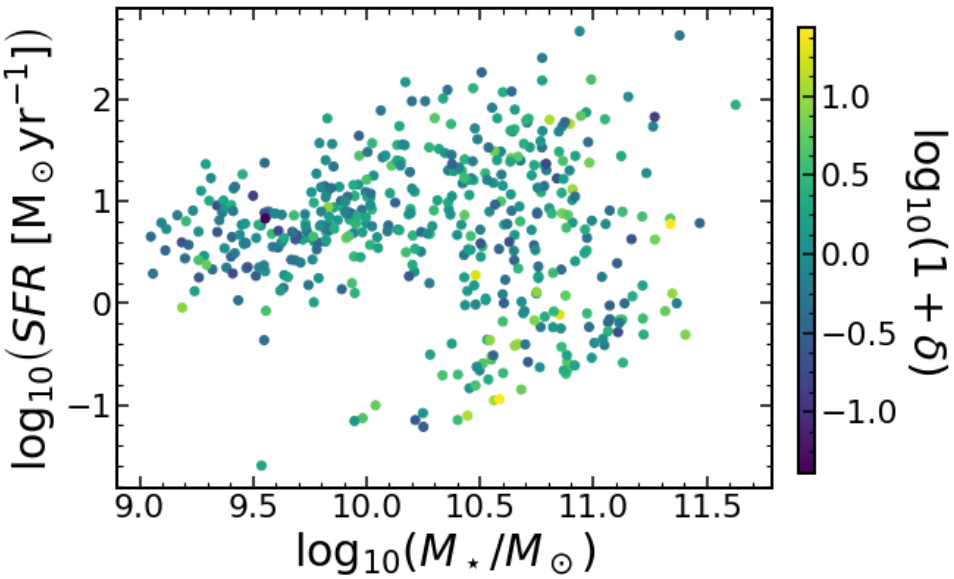


**Figure 8.1** The stellar mass-SFR relation for our sample, colour-coded with the local density for each target galaxy. The vertical dotted line highlights the approximate stellar mass completeness limit of our sample.

## 8.3 Estimating electron density from [OII]

One useful diagnostic we can use to probe the electron density of the star-forming regions in galaxies is the ratio between the flux of the two components of the [OII] doublet ( e.g. Seaton & Osterbrock, 1957; Canto et al., 1980; Pradhan et al., 2006; Darvish et al., 2015a; Sanders et al., 2016; Kaasinen et al., 2017). The relation between the measured ratio and the electron density is dependent on the gas temperature. To test this dependence we have used the package PyNeb (Luridiana et al., 2015), which allows for the estimation of physical conditions from measurements of emission lines. We show in Fig. 8.2, the estimated dependence of the electron density estimation on gas temperature. We find that when the temperature is above $\sim$ 1000 K, the dependence on temperature is very shallow. Since we have no independent measurement for the temperature (e.g. Peimbert, 1967; Garnett, 1992; Hägele et al., 2006), we translate our measured values of this ratio into predicted electron densities we use the parametrization by Sanders et al. (2016, assuming an electron temperature of $T_e = 10000$ K)

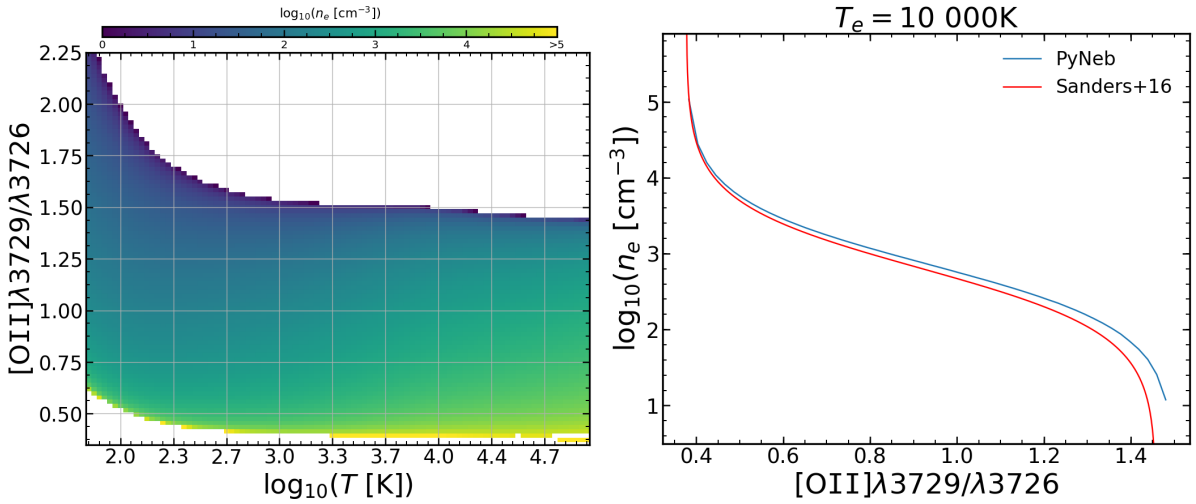


**Figure 8.2** Left: the predicted electron density given a measured doublet ratio and a gas temperature. We show that for $T > 1000$ K, the electron density estimate is rather independent of temperature. Right: he estimated electron density from the measured doublet ratio, assuming a gas temperature of 10 000 K.

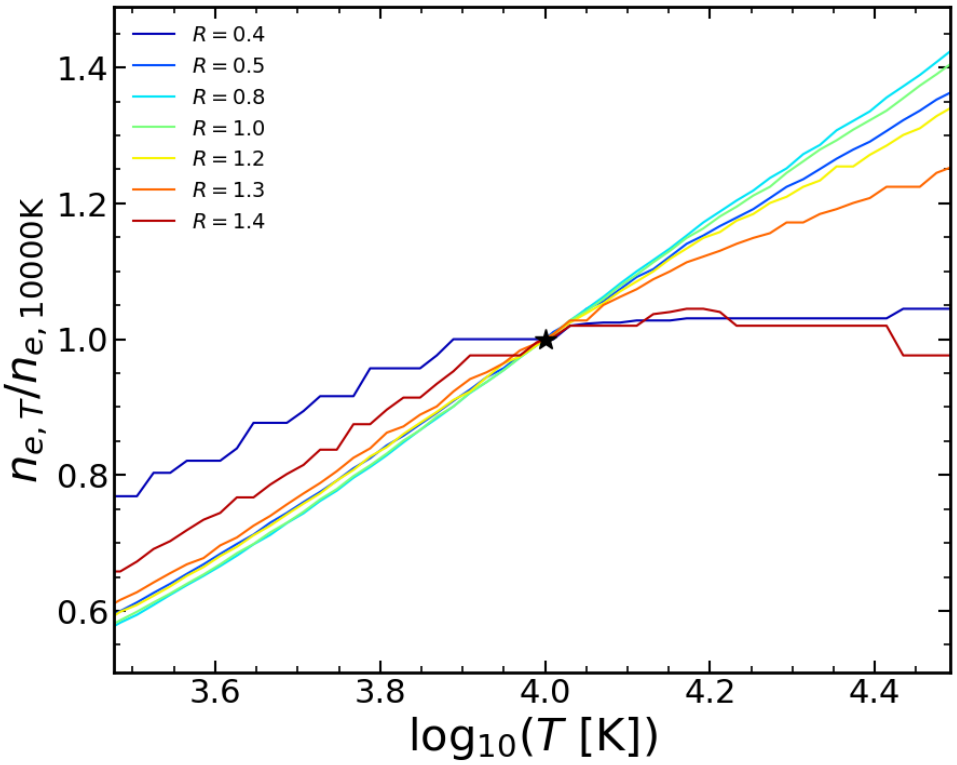


**Figure 8.3** Dependence of inferred electron density on temperature for fixed doublet ratios. We report the relative difference with respect to the reference temperature T=10 000 K, highlighted as a black star. We find an uncertainty of at most ∼40% on the inferred value of $n_e$ for temperatures in the range 3000 K < $T$ < 30000 K.

$$n_e\ [\mathrm{cm}^{-3}] = \frac{cR - ab}{a - R} \tag{8.2}$$

with $R$ =[OII]$\lambda$3729/$\lambda$3726 and $a, b$ ,and $c$ fixed parameters with values 0.3771, 2468, and 638.4, respectively. We show in Fig. 8.3 the difference of the inferred ratio as a function of

the temperature with respect to the reference value of 10 000 K we use here. We find that the inferred electron density is overestimated if the temperature is lower and underestimated if the temperature is higher (with the exception of the two extremes on the derived ratio, where $n_e$ is independent of temperature for $T >$10 000 K). We find that our estimates of the electron density have an uncertainty of $\sim$40% at most in the 3000 K < $T$< 30000 K temperature range. We note that uncertainties due to our assumption of the gas temperature are typically of the same order of magnitude than those derived from the measurements.

### 8.3.1 FLUX MEASUREMENTS

To obtain flux measurements of emission lines from our spectra, we interactively iterate through the entire dataset and zoom to a window of 100 Å around [OII] $\lambda$3726,$\lambda$3729. We define two regions of $\sim$ 15 Å (one blue-ward, one red-ward of the line) from which we estimate the median continuum level. Then the local continuum is defined as a straight line that goes through those points. To fit the doublet we use a combination of two Gaussian models through the functional form:

$$f(\lambda) = A_1 \exp\left[-\frac{(\lambda-\lambda_1)^2}{2\sigma^2}\right] + A_2 \exp\left[-\frac{(\lambda-\lambda_2)^2}{2\sigma^2}\right], \tag{8.3}$$

with 3 free parameters: $A_1$,$A_2$, and $\sigma$. The parameters $A_1$ and $A_2$ are the amplitudes of each component, $\sigma$ is the width of each Gaussian component. The centre of each component is fixed to be $\lambda_1 = 3726.08 \pm 0.3$Å and $\lambda_2 = 3728.88 \pm 0.3$Å (we allow for a small shift in the line centre that is of the size of the resolution element of the spectra). To estimate the line properties we use the information on the error spectra and perturb each flux at all wavelengths considered for the fitting by drawing a random number on the observed value and with a width that is equal to its error. We run this exercise 50 000 times and then estimate the errors on the line fit by taking the 16th and 84th percentile of the distribution in each free parameter.

Given that we impose that both components have similar widths, the flux ratio is simply $A_2/A_1$. We test the impact that line blending may have on our estimate of $R$ by simulating 100 000 spectra with various line widths. We find that for our galaxies we should have a typical error of 5% on $R$ due to this effect. We estimate that for our most massive galaxies, where the blending effect should be more severe, we are still able to recover the value of $R$ to within $\lesssim$ 10%. We detail the results of our simulations in Sect. 8.3.2.

### 8.3.2 Resolving the [OII] doublet in simulated spectra

To test our ability of recovering the value of the doublet ratio $R$ that we use to estimate the electron density in our stacked spectra we have performed a test on 100 000 simulated spectra. We simulate spectra by creating a double Gaussian function with both components having the same randomly distributed value of FWHM between 0.7 Å and 7 Å, with $R$ between 0.3 and 1.6 and an offset of the line centres of $\pm$0.15 Å. We then add noise to the spectra based on the average noise properties of our stacked profiles. Finally, we fit our model to this simulated spectra and test our recovery of the input doublet ratio as a function of line width to test for the impact of line blending in our measurements.

We show our results on Fig. 8.4 where we find that we are able to recover the input value of $R$ on average for all simulated spectra with no systematic effects. We show that the typical error on $R$ is around 5% at the lowest values of input FWHM, decreases to 4% at FWHM $\sim$ 2.4Å and then steadily increases up to 15% at FWHM $\sim$ 7Å. We use the results on the simulation to add in quadrature to the estimated error of $R$ given the FWHM of the measured line.

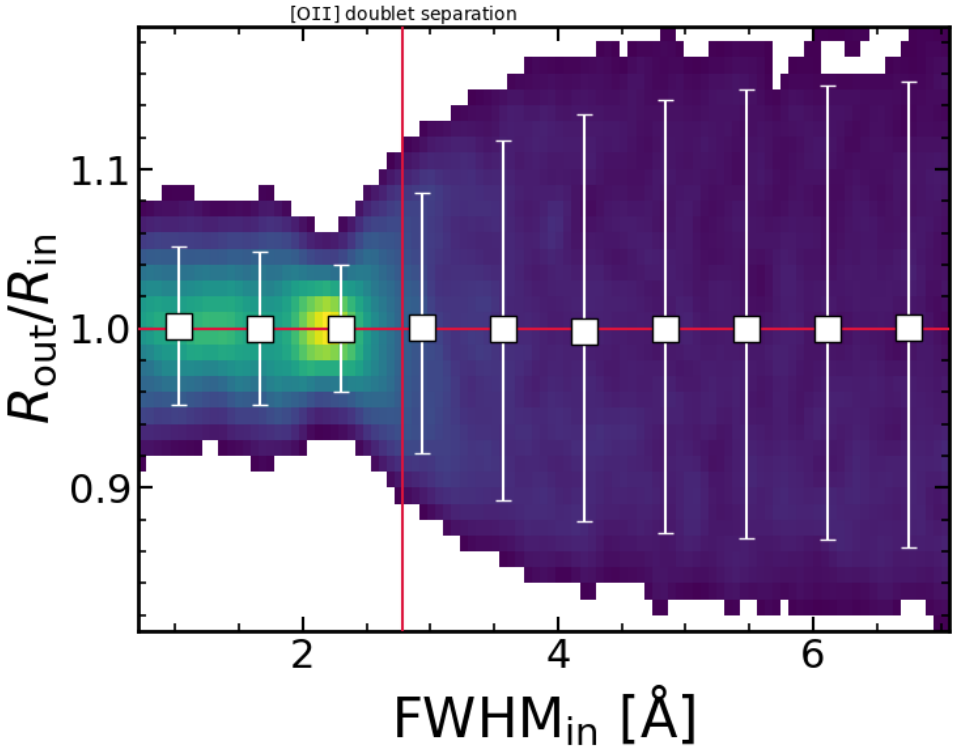


**Figure 8.4** Results on the recovered value of $R$ as a function of the input FWHM of both components for 100 000 realizations. White squares show the median fraction in bins of FWHM and the error bars show the 16th and 84th percentile of that bin. The red horizontal and vertical lines show the position of perfect recovery and the nominal doublet separation, respectively. The colour bar encodes the number of galaxies at each plot position.

### 8.3.3 SPECTRAL STACKS

To increase the S/N on the obtained spectra and investigate details on the spectral properties of galaxies as a function of their stellar mass and local density, we have performed stacking of individual galaxy spectra. Our stacking method can be summarized as a median, interpolated, and normalized spectra. For each set of spectra we start by shifting the spectrum to its rest-frame wavelengths using the redshift we have measured. Then we linearly interpolate the spectra onto a common universal grid (3250-4500 Å, $\Delta\lambda = 0.3$ Å/pixel). We normalize each spectrum to the mean flux measured from 4150-4350 ÅL̇astly, we median combine all spectra by taking the median flux at each wavelength. We estimate that our typical errors in the spectroscopic redshift measurements are on the order of $\sim 0.0005$, which translates to an error of $\sim 1$ Å, comparable to our spectral resolution at $z \sim 0.8$. Thus, our stacking should not smear the lines enough to affect the measurements on the [OII] $\lambda$3726,$\lambda$3729 doublet.

## 8.4 RESULTS

Throughout this section, our measure of environment is quantified by $\delta$ (see Eq. 8.1). For a broad comparison between different environments, we defined as lower density galaxies residing in $\log_{10}(1+\delta) < 0.1$ and as higher density galaxies residing in regions with $\log_{10}(1+\delta) > 0.4$.

### 8.4.1 INDIVIDUAL STACKS

Since some trends are difficult to see when showing all stacked spectra in a single panel due to line cluttering, we show in this section all the stacked spectra individually in Fig. 8.5 (in bins of stellar mass), 8.6 (in bins of over-density), and 8.7 (in bins of SFR). All results are also summarized in Table 8.1. We show in Fig. 8.6 and 8.7 stacked spectra in a grid of density and stellar mass bins and density and star formation activity bins, respectively.

### 8.4.2 THE DEPENDENCY OF ELECTRON DENSITY ON STELLAR MASS, SFR AND ENVIRONMENT

We have converted our measured line ratios of the [OII] doublet into electron densities using Eq. 8.2. We show in Fig. 8.10 our results. First, we find that our galaxies are typically found in regions of low electron density ($10\ \mathrm{cm}^{-3} \lesssim n_e \lesssim 300\ \mathrm{cm}^{-3}$). When compared against stellar

**Table 8.1** Summary of [OII] properties from the stacked spectra. Equivalent widths (EW) are in units of Å. Fluxes are in units of $10^{-18}$erg s$^{-1}$cm$^{-2}$. The third column shows the $R$ =[OII]$\lambda$3729/$\lambda$3726, which represents the doublet ratio used as a proxy for the electron density.

| Range | EW([OII]) | Flux([OII]) | $R$ |
|---|---|---|---|
| $9.0 < \log_{10}(M_\star/M_\odot) < 9.4$ | $-35.4^{+0.4}_{-0.4}$ | $8.3^{+0.01}_{-0.01}$ | $1.46^{+0.07}_{-0.07}$ |
| $9.4 < \log_{10}(M_\star/M_\odot) < 9.8$ | $-20.7^{+0.2}_{-0.2}$ | $4.9^{+0.01}_{-0.01}$ | $1.45^{+0.06}_{-0.06}$ |
| $9.8 < \log_{10}(M_\star/M_\odot) < 10.3$ | $-18.9^{+0.2}_{-0.2}$ | $4.0^{+0.01}_{-0.01}$ | $1.43^{+0.06}_{-0.06}$ |
| $10.3 < \log_{10}(M_\star/M_\odot) < 10.7$ | $-6.9^{+0.3}_{-0.2}$ | $1.4^{+0.01}_{-0.01}$ | $1.16^{+0.10}_{-0.10}$ |
| $10.7 < \log_{10}(M_\star/M_\odot) < 11.7$ | $-4.0^{+0.2}_{-0.2}$ | $0.8^{+0.01}_{-0.01}$ | $1.09^{+0.08}_{-0.08}$ |
| $-1.0 < \log_{10}(1+\delta) < -0.3$ | $-11.7^{+0.2}_{-0.2}$ | $2.6^{+0.01}_{-0.01}$ | $1.59^{+0.07}_{-0.07}$ |
| $-0.3 < \log_{10}(1+\delta) < 0.1$ | $-12.8^{+0.2}_{-0.2}$ | $2.8^{+0.01}_{-0.01}$ | $1.26^{+0.05}_{-0.05}$ |
| $0.1 < \log_{10}(1+\delta) < 0.5$ | $-10.4^{+0.4}_{-0.4}$ | $2.1^{+0.01}_{-0.01}$ | $1.23^{+0.08}_{-0.08}$ |
| $0.5 < \log_{10}(1+\delta) < 0.9$ | $-5.6^{+0.3}_{-0.3}$ | $1.1^{+0.01}_{-0.01}$ | $1.15^{+0.09}_{-0.09}$ |
| $0.9 < \log_{10}(1+\delta) < 1.5$ | $-2.5^{+1.1}_{-0.8}$ | $0.5^{+0.03}_{-0.02}$ | $1.31^{+0.47}_{-0.34}$ |
| $-1.0 < \log_{10}\left(SFR\ [\mathrm{M}_\odot\mathrm{yr}^{-1}]\right) < 0.4$ | $-3.6^{+0.3}_{-0.3}$ | $0.7^{+0.01}_{-0.01}$ | $1.02^{+0.08}_{-0.08}$ |
| $0.4 < \log_{10}\left(SFR\ [\mathrm{M}_\odot\mathrm{yr}^{-1}]\right) < 0.8$ | $-15.2^{+0.2}_{-0.2}$ | $3.3^{+0.01}_{-0.01}$ | $1.47^{+0.06}_{-0.06}$ |
| $0.8 < \log_{10}\left(SFR\ [\mathrm{M}_\odot\mathrm{yr}^{-1}]\right) < 1.2$ | $-17.6^{+0.2}_{-0.2}$ | $3.9^{+0.01}_{-0.01}$ | $1.45^{+0.06}_{-0.06}$ |
| $1.2 < \log_{10}\left(SFR\ [\mathrm{M}_\odot\mathrm{yr}^{-1}]\right) < 3.0$ | $-12.1^{+0.4}_{-0.4}$ | $2.5^{+0.01}_{-0.01}$ | $1.36^{+0.10}_{-0.10}$ |

mass, we find an approximately flat relation with $n_e \sim 10$ cm$^{-3}$ at $\log_{10}(M_\star/\mathrm{M}_\odot) < 10.3$ and then an increase of $n_e$ by an order of magnitude for higher stellar masses ($n_e \sim 300$ cm$^{-3}$).

When investigating the dependency on local over-density, we find a rather consistent value of $n_e \sim 100-300$ cm$^{-3}$ for all bins but the lowest density one. When considering densities below $\log_{10}(1+\delta) < 1$, we see an increase of electron density from low- to high-density regions. We are unable to pinpoint a value of electron density in the densest region in our analysis (but we find an upper limit of $n_e \lesssim 500$ cm$^{-3}$).

We also show in Fig. 8.10 the electron density as a function of the host SFR (see also Fig. 8.7 where we show each stacked spectrum). As already stated above, our electron density measurements ($\lesssim 100$ cm$^{-3}$) are consistent with no relation with SFR for the values above $\sim 2.5\mathrm{M}_\odot\mathrm{yr}^{-1}$. We note that galaxies with the lowest SFR in our sample (below that threshold), have a markedly different estimate of the doublet ratio, consistent with them having higher electron densities ($\sim 500$ cm$^{-3}$).

When comparing our results for different stellar mass regimes, we find two opposing trends (see Fig. 8.11). For intermediate mass galaxies ($10 < \log_{10}(M_\star/\mathrm{M}_\odot) < 10.75$) we find similar results to those found by Darvish et al. (2015a) for a pilot study at $z \sim 0.5$. At low-density regions, the electron density is higher and then there is a drop at the highest densities. We are able to expand that study to much lower projected galaxy densities and confirm similar values for $n_e$ across all low density regions for this stellar mass range. When looking at galaxies with higher

stellar masses ($\log_{10}(M_\star/\mathrm{M}_\odot) > 10.75$) we find a somewhat inverted trend with over-density. In low-density regions, the electron density is similar to what is found at lower masses but the value of $n_e$ increases for higher density regions. At the densest regions probed in our study, we find a difference greater than one order of magnitude. These results portray a scenario where low- and intermediate-density environments have little impact on the observed electron densities, but in high-density environments, we find evidence for environmental and stellar mass dependence of the measured electron density.

We have also stacked all quiescent and star-forming galaxies with $\log_{10}(M_\star/\mathrm{M}_\odot) > 10$ in the low- and high-density bins defined in Sect. 8.4 ($\log_{10}(1+\delta) < 0.1$ and $\log_{10}(1+\delta) > 0.4$, respectively). Our choice of bins is driven by the low number (64) of quiescent galaxies in our sample which require the better S/N to get a fair estimate of the electron density, given that their [OII] emission is much fainter when compared to star-forming galaxies, as one should expect. On the low-density regions we find that quiescent galaxies have one order of magnitude higher electron densities ($n_e = 1708^{+799}_{-496}$ cm$^{-3}$) when compared to the star-forming population at similar redshifts ($n_e = 186^{+75}_{-64}$ cm$^{-3}$). In high-density regions we can only estimate the electron density of star-forming galaxies and we find that they have $n_e = 222^{+116}_{-92}$ cm$^{-3}$.

When attempting to quantify the difference of different cosmic web environments as a function of stellar mass (see Fig. 8.12) the picture is not as clear. Overall, cluster galaxies do not distinguish themselves from field or filament galaxies at all stellar masses due to their larger error bars. As for the difference between filament and field galaxies, we do find that between $9.5 < \log_{10}(M_\star/\mathrm{M}_\odot) < 10.5$, field galaxies have on average higher electron densities, qualitatively consistent with the results by Darvish et al. (2015a). At higher stellar masses, field and filament galaxies have consistent values of $R$ ($n_e$) within their error bars. At lower stellar masses ($\log_{10}(M_\star/\mathrm{M}_\odot) < 9.5$), field galaxies have higher values of $R$ and consequently lower electron densities. As an overall trend at all cosmic web environments, we find that higher stellar masses translate into higher electron densities. We note that when comparing to the field galaxy sample of Darvish et al. (2015a) at $9.5 < \log_{10}(M_\star/\mathrm{M}_\odot) < 10$, we find the largest difference between our results and theirs. This is likely caused by different estimators of the value of $R$ since they allow for $\sigma$ to be different for each of the components and we do not (our choice is driven by the lower S/N of our data) and a potentially larger ratio between the two line widths would explain our different results.

## 8.5 DISCUSSION AND CONCLUSIONS

### 8.5.1 IMPACT OF ENVIRONMENT ON THE ELECTRON DENSITY

To infer more detailed properties we have stacked our spectra and derived average electron density values for different regions. We find that galaxies in our sample have typical electron densities around $10-300$ cm$^{-3}$. This range is fully consistent with values reported in the local Universe as well as at $z\sim2-3$ (see e.g. Shirazi et al., 2014; Steidel et al., 2014; Kewley et al., 2016; Kaasinen et al., 2017). If we take our sample as a subset of the population at these redshifts (since we are sampling from low- to high-density regions in a broad interval of stellar masses), we can predict the average electron density of galaxies. We have stacked all galaxies with stellar masses $\log_{10}(M_\star/\mathrm{M}_\odot)>10$ and we find a value of $n_e\approx275$ cm$^{-3}$, which is consistent with those reported at higher redshift but higher than what is reported in the local Universe (see e.g. Shirazi et al., 2014; Steidel et al., 2014; Kewley et al., 2016; Kaasinen et al., 2017). This likely means that the star-forming regions of the galaxies in our sample are forming in denser pockets of gas. Nevertheless, we would require a larger survey spanning a larger redshift interval to pinpoint any evolution that is independent of selection effects (see e.g. Kaasinen et al., 2017). Our results are also consistent with the most recent measurements by Epinat et al. (2017) in a galaxy group at $z\sim0.7$. They report a value of $R=1.4\pm0.1$ for their 6 galaxies, of which 5 are below $\log_{10}(M_\star/\mathrm{M}_\odot)=10$, which is the same we get for $\log_{10}(M_\star/\mathrm{M}_\odot)\sim9-10$ (see Fig. 8.10).

One interesting trend we find is the dependence of the electron density on the local over-density (see Fig. 8.11). We find similar results at $z\sim0.5$ reported by Darvish et al. (2015a) for the same stellar masses (lower electron densities in higher density environments) and a reverse trend for higher stellar masses. At $z\sim2$, Kewley et al. (2016) finds no dependence of electron density on galaxy density, but they do not probe regions in the same high-density regime where the differences are evident and only have a small sample of 13 star-forming galaxies. Therefore, we are also consistent with their results considering a nearly constant electron density for low- to intermediate-density regions.

Overall, we tend to find a small dependence of the values of electron density with environment as found in a $z\sim2$ cluster (Kewley et al., 2016). We find some dependence of $n_e$ on the stellar mass and star formation activity of galaxies from a particular subset of the population. This influence is seen at $\log_{10}(M_\star/\mathrm{M}_\odot)>10.75$ in high-density regions, above the typical stellar masses probed by Darvish et al. (2015a) and Sanders et al. (2016), which find little dependence of $n_e$ on the stellar mass. We also find that quiescent galaxies in lower density regions have higher electron densities than their star-forming counterparts. Since, by definition, quiescent galaxies have low SFRs, we need additional ionizing mechanisms that are not related to the

presence of HII regions to explain the observed [OII] emission. We may also be influenced by the electron temperature of the ionized regions which can lead to under or over estimation of the electron densities, depending on the metal richness of the targets (e.g. Sanders et al., 2016).

The ionizing mechanism that controls the electron density in each galaxy can have diverse natures: hot bubbles around star-forming regions (e.g. Osterbrock, 1989), low luminosity AGN (e.g. Kauffmann et al., 2003; Kewley et al., 2006) or hot and evolved post asymptotic giant branch stars (pAGBs, e.g. Binette et al., 1994). While we cannot say for sure what is boosting the electron densities in the densest environments at high stellar masses, there can be a range of explanations. Either there is a non-negligible number of massive star-forming galaxies that have dense HII regions, or there are warm and dense gas clouds ionized by pAGB stars or low luminosity AGNs that produced the observed [OII] emission and allows us to measure electron densities. The first scenario could decrease the gas cloud densities by stripping less massive galaxies of its gas, which would translate into lower electron densities in high-density environments as we report in Fig. 8.11 (see also Darvish et al., 2015a). In that same scenario, more massive galaxies would keep their gas reservoirs (and probably increase their quantity by stripping gas from smaller galaxies) producing higher gas density regions as we see in Fig. 8.11. The alternative scenario would be the case for galaxies similar to samples in the lower redshift Universe, which show extended low-ionization emission compatible with a ionization field powered by a widespread hot and evolved population (see e.g. Singh et al., 2013; Gomes et al., 2016; Belfiore et al., 2016, 2017). This last scenario is likely the explanation to why we see higher electron densities in quiescent galaxies when compared to star-forming galaxies in similar density regions.

The local measurements of electron densities is also related to measurements of the strength of the magnetic fields of galaxies (e.g. Murgia et al., 2004; Frick et al., 2011; Beck, 2015; Ideguchi et al., 2017). We highlight that having accurate values for the electron density, preferentially from spatially resolved spectral maps, can help us pinpoint the strength of magnetic fields in individual galaxies outside our own.

### 8.5.2 SUMMARY

We have presented in this chapter an overview of effects of stellar mass and environment on the electron density (as measured from [OII]$\lambda$3729/[OII]$\lambda$3726)) of galaxies in the the VIS$^3$COS survey. We report on trends with environment of electron densities. Our main findings are summarizes as follows:

- We measure electron densities of $\sim 1000\,\mathrm{cm}^{-3}$ for the most massive galaxies ($\log_{10}(M_\star/\mathrm{M}_\odot) > 10.75$) in the densest regions, higher than what we measure at lower density regions ($n_e \sim 100\ \mathrm{cm}^{-3}$). We find an inverted trend for intermediate stellar mass galaxies

$(10 < \log_{10}(M_\star/\mathrm{M}_\odot) < 10.75)$ where the electron densities drops to $n_e \sim 10$ cm$^{-3}$ in the densest regions we probe in this study.

- We find that in low-density regions ($\log_{10}(\delta) < 0.1$), quiescent galaxies have one order of magnitude higher electron densities than their star-forming counterparts ($n_e \sim 1000, 100$ cm$^{-3}$, respectively).
- When comparing galaxies in different environment regions (field, filament and cluster) we find little dependence of $n_e$ on the cosmic web environment.

However, we cannot infer any generalized trends with time or environment due to the lack of measurements of $n_e$ across large patches of the sky (to minimize cosmic variance) and at different epochs (to infer evolution). Further surveys of different structures (or large fields) at these and other redshifts are needed to clarify if and when environment plays a role on determining the properties of galaxies. Independent measurements of inter stellar medium properties, namely the electron temperature, we allow for better estimates of the electron densities, measured from light tracing different ionizing mechanisms.

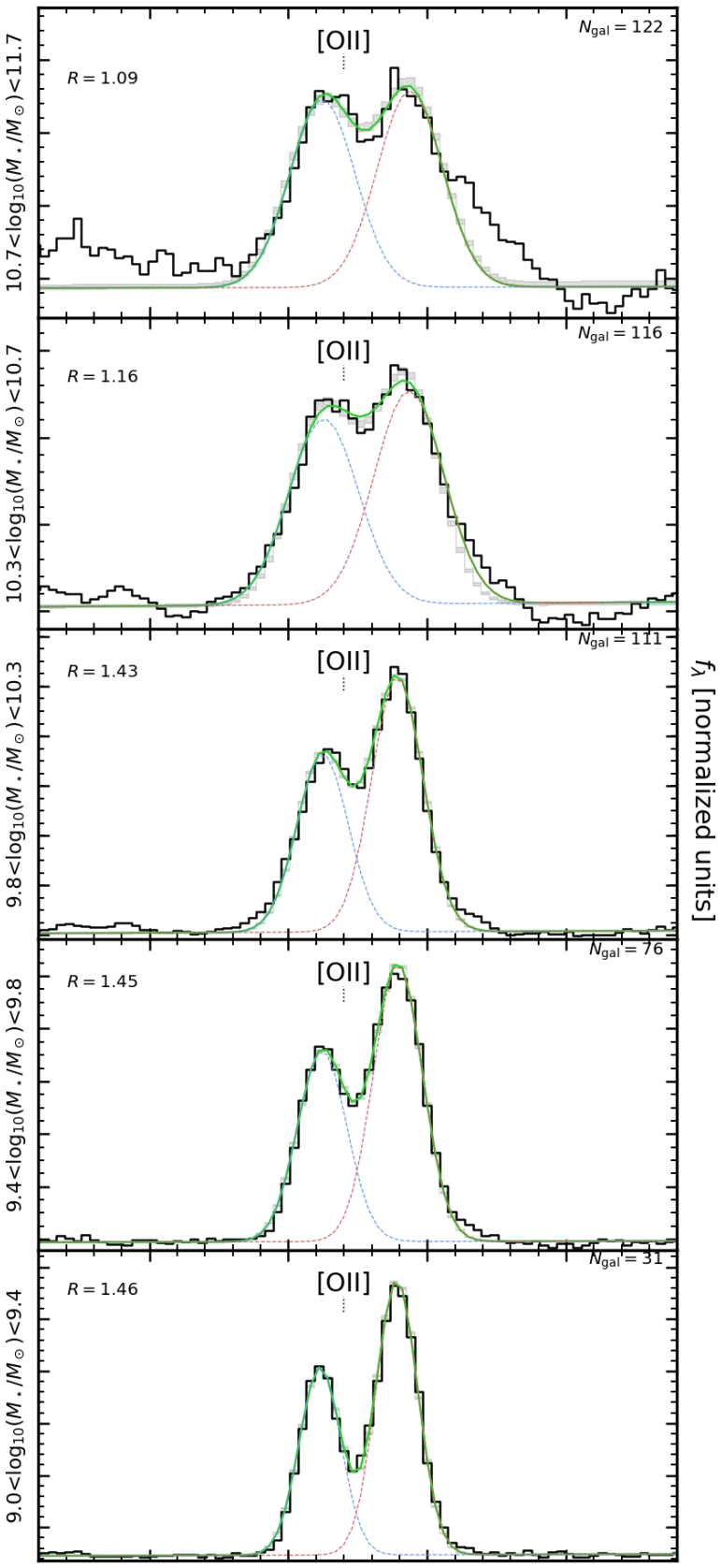


**Figure 8.5** Resulting spectral stacks (solid black line) in bins of stellar mass (low to high stellar mass from top to bottom) around the [OII] doublet. We show in green the best fit doublet model with each component shown as blue and red dashed lines. The shaded grey area represents the typical error on the fit of the spectra at each wavelength computed from the 16th and 84th percentiles of 50 000 realizations of perturbing the spectra by its error.

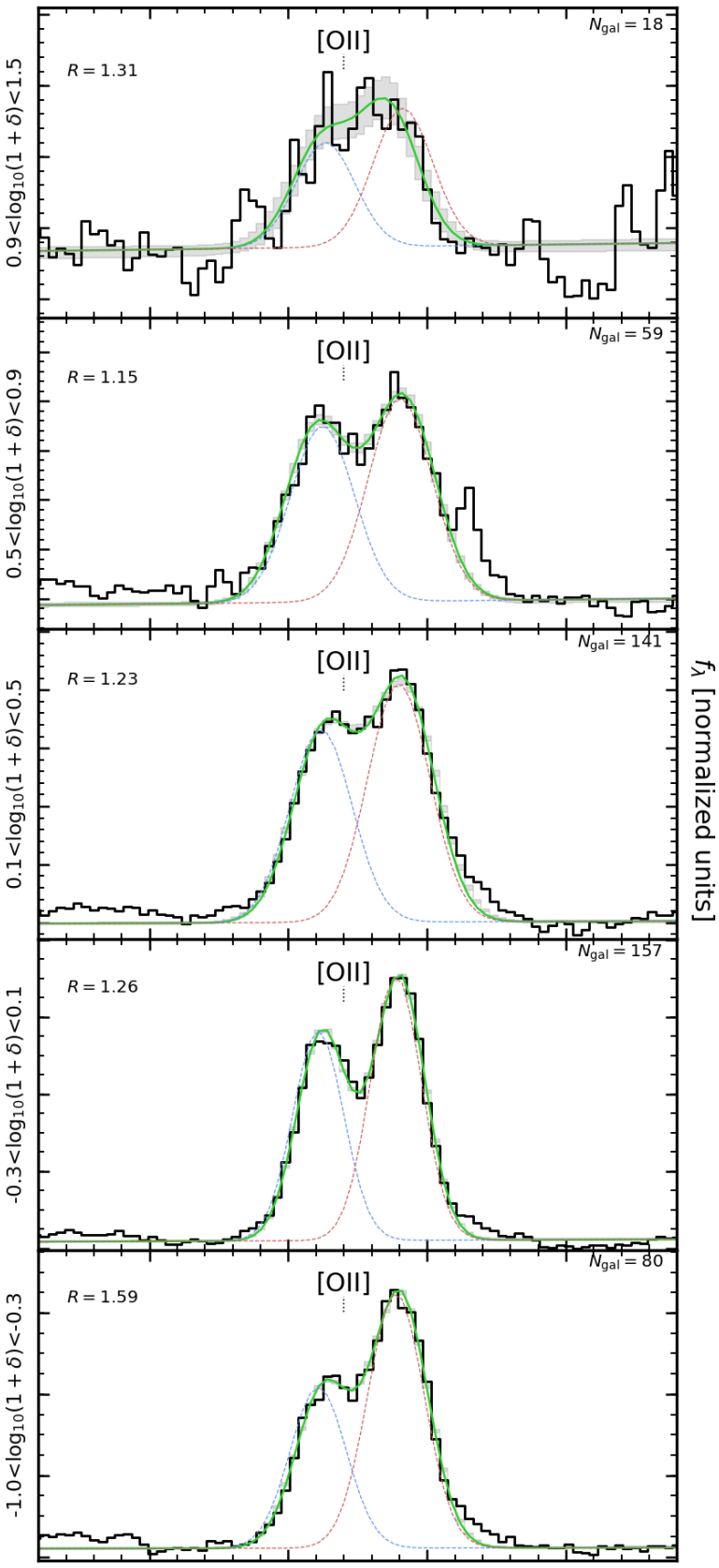


**Figure 8.6** Resulting spectral stacks (solid black line) in bins of over-density (low- to high-density from top to bottom) around the [OII] doublet. We show in green the best fit doublet model with each component shown as blue and red dashed lines. The shaded grey area represents the typical error on the fit of the spectra at each wavelength computed from the 16th and 84th percentiles of 50 000 realizations of perturbing the spectra by its error.

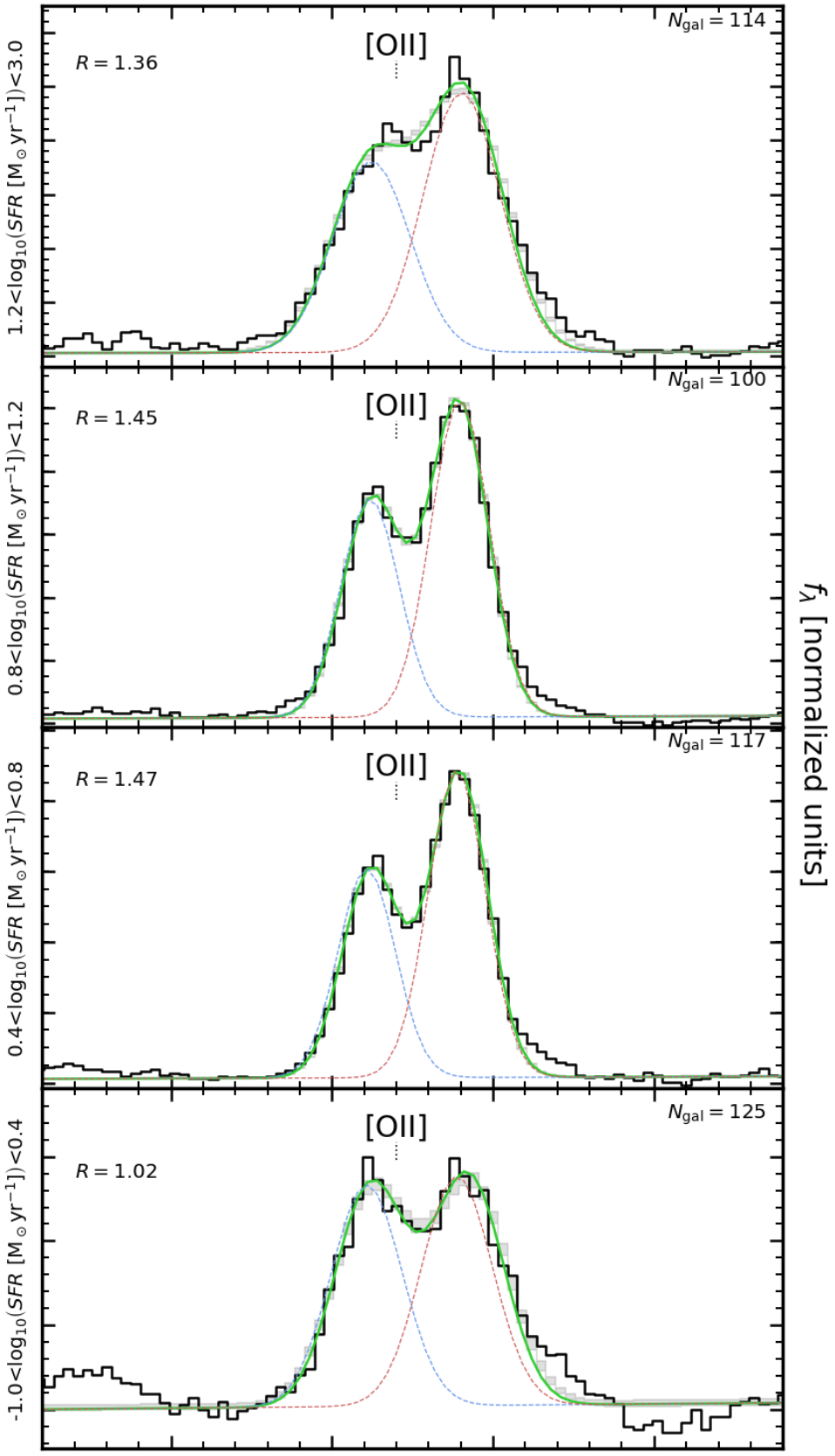


**Figure 8.7** Resulting spectral stacks (solid black line) in bins of SFR (low to high SFR from top to bottom) around the [OII] doublet. We show in green the best fit doublet model with each component shown as blue and red dashed lines. The shaded grey area represents the typical error on the fit of the spectra at each wavelength computed from the 16th and 84th percentiles of 50 000 realizations of perturbing the spectra by its error.

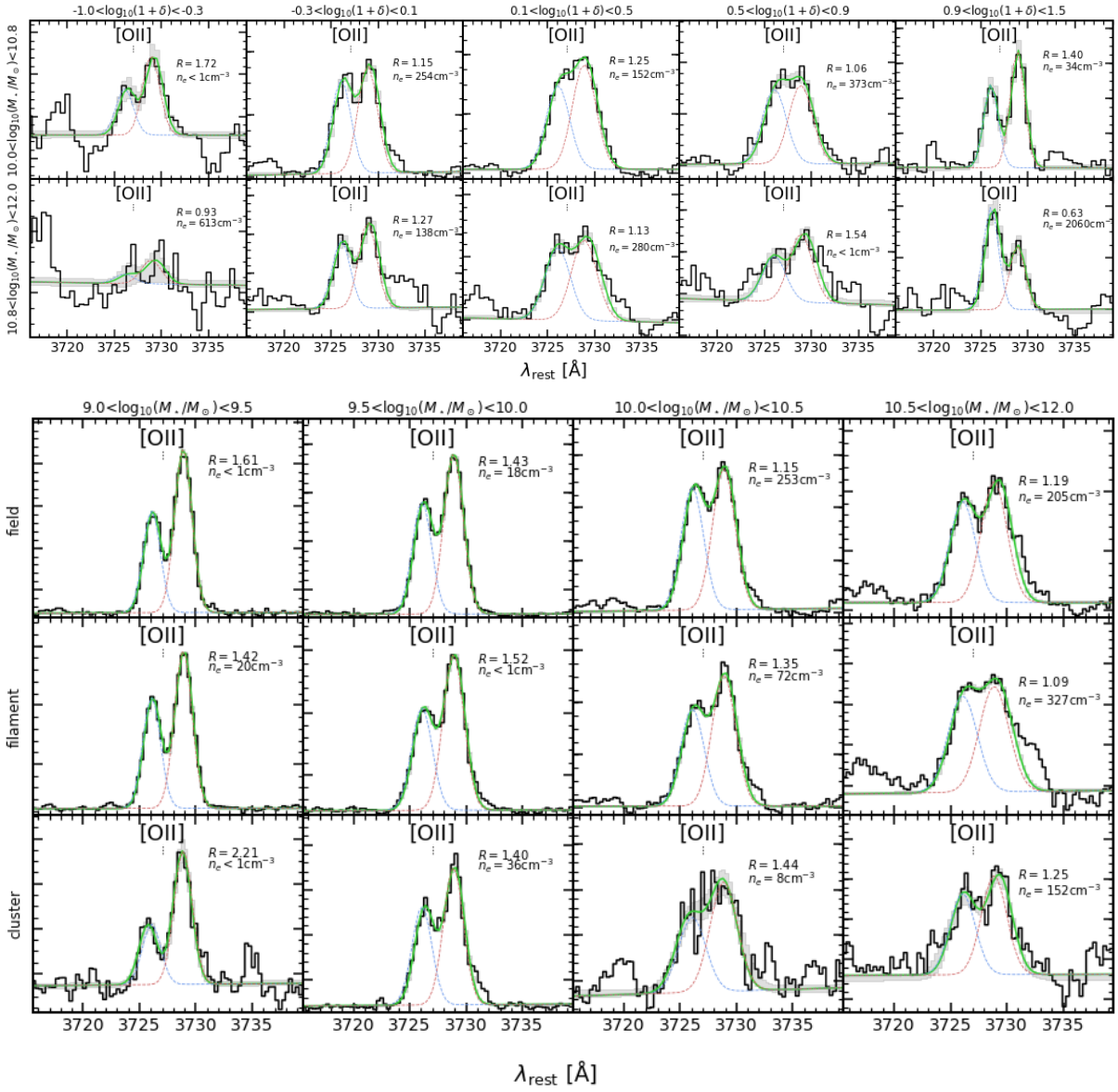


**Figure 8.8** Top: results of stacked spectra in a two bins of stellar mass and different density regions. Bottom: results of stacked spectra in a grid of stellar masses and different cosmic web environments as defined in Darvish et al. (2014). We show in green the best fit doublet model with each component shown as blue and red dashed lines. The shaded grey area represents the typical error on the fit of the spectra at each wavelength computed from the 16th and 84th percentiles of 50 000 realizations of perturbing the spectra by its error.

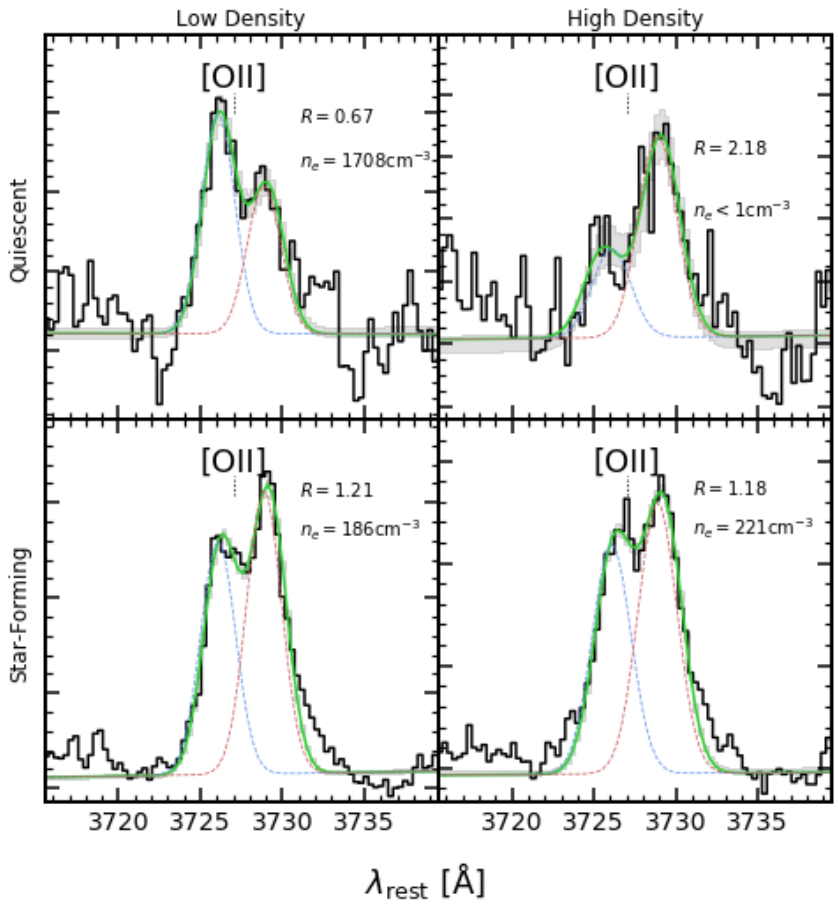


**Figure 8.9** Results of stacked spectra for the quiescent and star-forming populations in the low- and high-density bins defined in Sect. 8.4. We show in green the best fit doublet model with each component shown as blue and red dashed lines. The shaded grey area represents the typical error on the fit of the spectra at each wavelength computed from the 16th and 84th percentiles of 50 000 realizations of perturbing the spectra by its error. We note that we are not able to measure the value of $R$ reliably for the quiescent galaxies in the high-density regions.

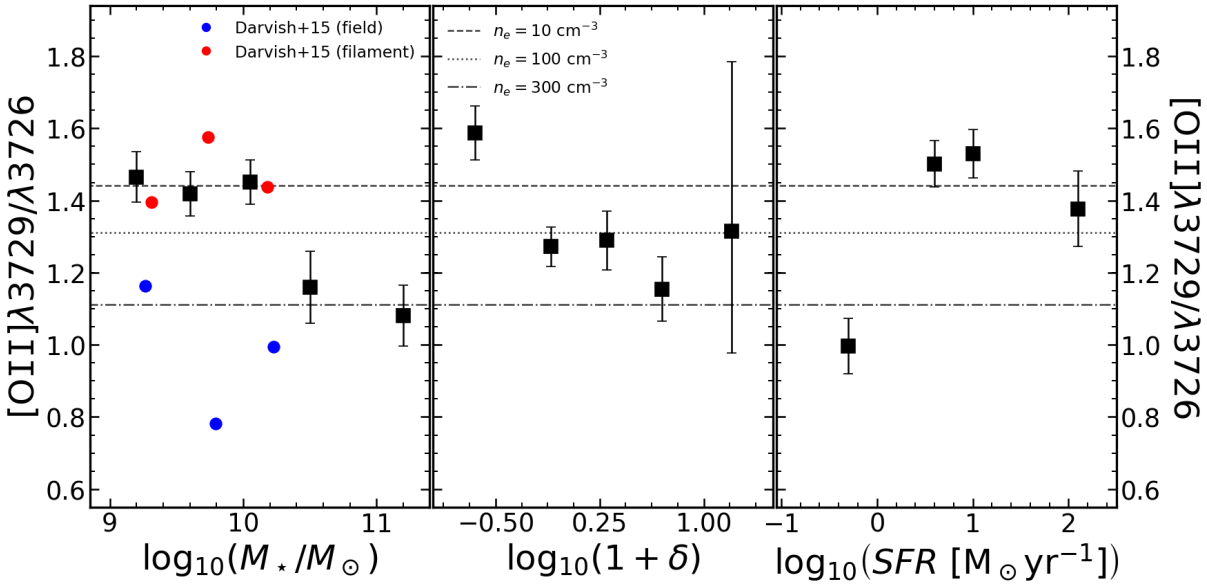


**Figure 8.10** Line intensity ratio between the two components of the [OII] doublet as a function of stellar mass (left), local density (middle), and SFR (right). Horizontal lines show the predicted electron density as derived by Eq. 8.2 assuming an electron temperature $T_e = 10000$ K.

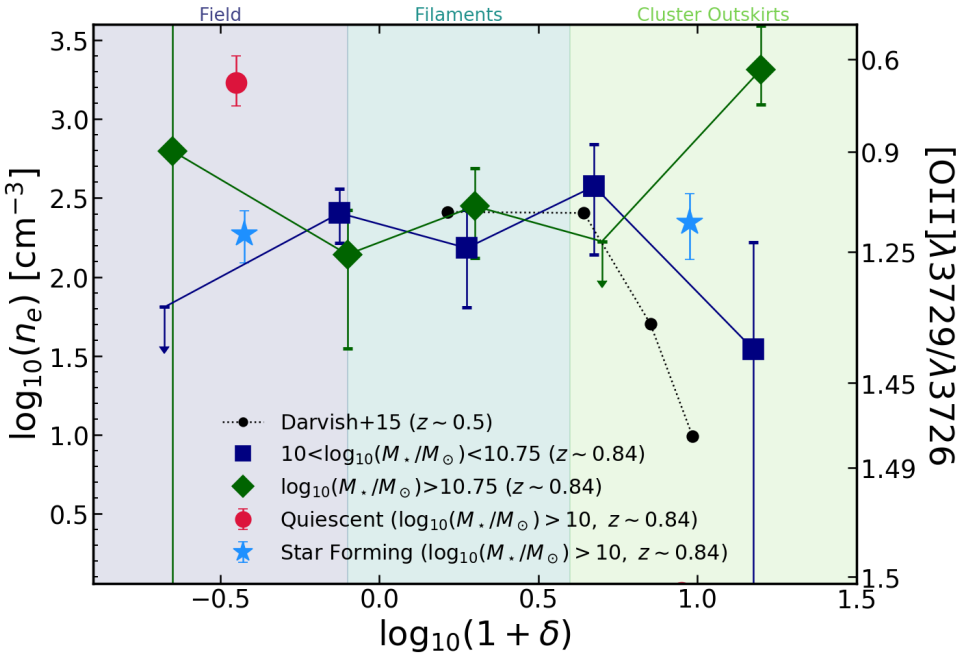


**Figure 8.11** The estimated electron density as derived by Eq. 8.2 assuming an electron temperature $T_e = 10000$ K as a function of local over-density for two different stellar mass bins, and also for stacks of quiescent and star-forming galaxies. For some spectra we are only able to pinpoint the upper limits (drawn as arrows) on the electron density. We show the results for a dataset at $z \sim 0.5$ (Darvish et al., 2015a).

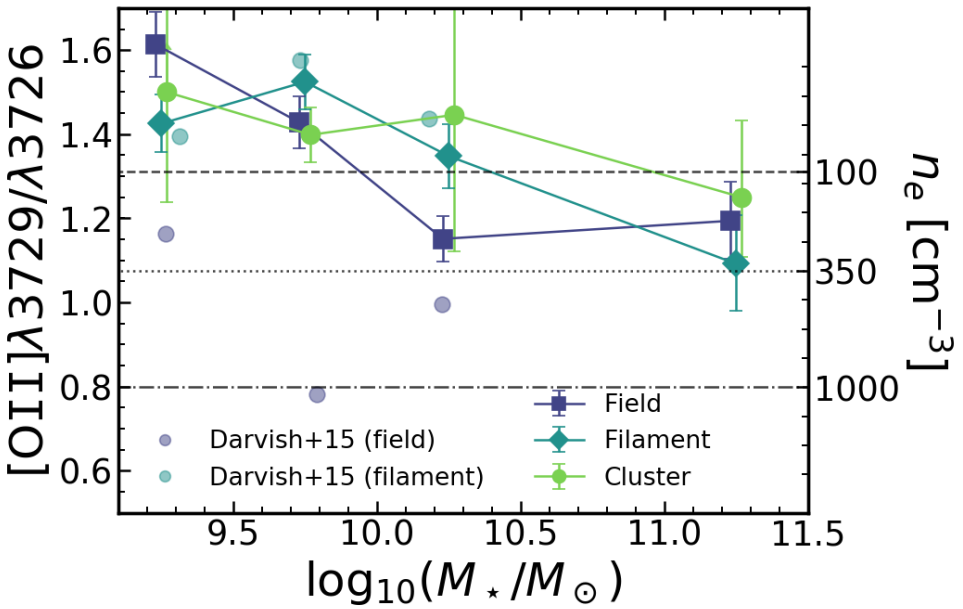


**Figure 8.12** Line intensity ratio between the two components of the [OII] doublet as a function of stellar mass in three environments. Horizontal lines show the predicted electron density as derived by Eq. 8.2, assuming an electron temperature $T_e = 10000$ K.

This page intentionally contains only this sentence.

# CHAPTER 9

## CONCLUSIONS AND FUTURE WORK

I have presented throughout this thesis some analysis linked to galaxy evolution across cosmic time, with a special emphasis on galaxy morphology. I have shown in Chap. 2 that galaxies selected to be star-forming due to their emission in H$\alpha$ are typically characterized by exponential disk profiles and their sizes increased by a factor of $\sim 2-3$ in the past $\sim$11 Gyr ($0 \lesssim z \lesssim 2$). I have also tested the impact of surface brightness dimming on the profiles of these galaxies and I found that the expected luminosity evolution can counterbalance this cosmological dimming and the structural parameters as derived from profile fitting are not hugely affected. Galaxy show differences smaller than 5% while Sérsic indices are underestimated by $\sim$20%. By combining my results with a previous work based on the same sample and done at redder wavelengths (probing the older stars), I find that these types of galaxies should grow from inside-out. This explains the growth of the star-forming areas while older stellar populations remain unchanged during the same period.

I have then expanded the morphological analysis towards higher redshifts ($2 \lesssim z \lesssim 6$) using Ly$\alpha$ to select large samples of star-forming in Chap. 3 and 4 (since H$\alpha$ moves out of the observable region at $z \gtrsim 2.5$). I find that LAEs are remarkably similar in morphology across this $\sim$3 Gyr period. They have typically compact morphologies, with light profiles close to exponential disks and average sizes around $\sim$1 kpc. I also find that the variation of morphology among LAEs is correlated with their observed emission. Galaxies with brighter lines are on average larger and stronger line equivalent widths correspond to the smaller galaxies in our sample. When compared to lower redshift H$\alpha$-selected galaxies (as studied in Chap. 2) at a similar epoch, I find LAEs to be smaller by a factor of $\sim$2 than the typical SFGs. By comparing to other samples studied by different groups, I confirm that below $z \lesssim 4$, LAEs have different sizes than UV-selected samples. This is a good indicator that typical LAEs should be characteristically young objects and correspond to a phase of galaxy evolution. In this scenario, we should have more LAEs when the Universe was younger as the fraction of young objects are forced to increase due to the

limited age of the Universe at that epoch, which is consistent with numerous findings by other groups. Additionally, by studying a particular sample of bright LAEs in the epoch of reionization, I find that clumpy morphologies seem ubiquitous among galaxies with strong Ly$\alpha$ emission.

Since time is not the only driver of galaxy evolution, I have dedicated Chap. 5 through 8 to the study of the environmental impact on the galactic properties. This analysis studies a superstructure at $z \sim 0.84$ and makes use of high-resolution spectroscopy in the rest-frame optical-blue and high-resolution imaging. With a large sample of $\sim$500 galaxies spanning both in stellar mass and local density, I was able to test the impact of both on galaxy star formation and morphology. I find that the environment influences star formation but not for all galaxies. The most massive galaxies ($> 10^{10.75} M_{\odot}$) see no effect of local density, while lower stellar mass galaxies show a decrease in the star formation towards higher density environments. This change in the average star formation can be explained by an increasing number of quiescent galaxies found at high densities. I also find tentative evidence for an increase in star formation in intermediate-density environments (filaments) for galaxies of intermediate stellar masses ($\sim 10^{10.5} M_{\odot}$). Additionally, the average age of the stellar populations of galaxies seems to be also affected by the environment they reside in with older galaxies being found in higher density regions and this effect is stronger the more massive the galaxies are. I also show in Chap. 7 that a kind of morphology-density relation is already in place at $z \sim 0.84$ for this superstructure. However, this relation disappears if we separate galaxies by their typical star formation and it is simply a consequence of the changing fraction of quiescent galaxies with local density. This means that processes that affect star formation must also affect morphology during similar timescales. Finally, the study of interstellar medium pressure through the measurement of electron density shows again that environmental influence depends on the stellar mass of the galaxy. More massive galaxies show increased electron density at high-density regions in contrast to lower stellar mass counterparts which show lower electron densities in those environments. This can potentially be explained by different sources of ionizing photons being produced in both samples, but further observations are required to confirm this scenario.

The future on galaxy evolution studies will benefit greatly from access to optical rest-frame data at high-resolution from space in deep (JWST) and wide (Euclid, WFIRST) surveys. This will be combined with the powerful next-generation of extremely large telescopes that will have first light in the coming decade. By having synergies between several instruments we will be able to probe the galaxy population across a large luminosity/stellar mass range while also using wide surveys to map accurately the large-scale structure of the Universe, which will provide us a better window to study galaxy evolution across time and space.

On a shorter time-scale, wide-field surveys such as DES and HETDEX can provide the first glimpse into the era of large-area sky surveys. For example, by working as a de-facto low-resolution wide-field integral field unit, the HETDEX survey will be able to detect millions of Ly$\alpha$ emitters at $1.9 < z < 3.5$ over an area of 434 deg$^2$. Such unprecedented survey area

with spectroscopic coverage will provide key advancements on the distribution of Ly$\alpha$ on large scales, tracing the cosmic web as well as probing to exquisite precision the luminosity function of LAEs in the bright regime. Due to its wide-ranging capabilities, one will also be able to open a new window into very rare and luminous LAEs which are excellent targets for follow-up with other instruments to understand the physical properties of such sources. One can then compare these rare LAEs to those being now found at the epoch of re-ionization and provide insight into the physics of Ly$\alpha$ escape at $z \sim 2-3$. After careful calibration and combination with other large area ground-based surveys with photometric counterparts one will also be able to trace populations of CIII] emitters at $0.8 < z < 1.9$ and [OII] emitters at $z < 0.5$, complementing current narrow-band surveys targeting these galaxies with strong emission lines. As a tracer of large-scale structure, this survey instrument will also be able to identify dozens of dense regions of the Universe (proto-clusters) which are the precursors of today's massive galaxy clusters. The largest overdensities will be excellent follow-up targets for current and upcoming facilities to probe the regime of formation of massive clusters and assess the impact on galaxy properties during the build-up phase of the densest regions in the Universe and pinpoint the epoch where environmental effects become a dominant process for shaping galaxy evolution.

I have now more interesting questions to answer than those I started with at the beginning of this project. The analysis presented in this thesis shed some light on the intervening processes of galactic evolution but there is much more to be discovered. Since time is limited and I cannot dedicate myself to the many unsolved problems that I realized but not tackle during the limited time for this project, I can only hope that this thesis can inspire others to keep searching for answers in this ever-changing Universe.

This page intentionally contains only this sentence.

# ACKNOWLEDGEMENTS

I am grateful for the help of my supervisor, David Sobral, for guiding me through the tortuous path of a PhD and for giving me the opportunity to do research on the different projects that I present in this thesis. I am also grateful to all the collaborators who, at some point during this past 4 years, have contributed with help and fruitful discussions to make this thesis as it is: José Afonso, Philip Best, Fernando Buitrago, João Calhau, Benham Darvish, Alex Forshaw, Andrea Johnson, Jorryt Matthee, Joanna Merrick, Sara Pérez, Bruno Ribeiro, Sérgio Santos, Oliver Sheldon, Ian Smail, and Andra Stroe.

I would like to thank the support from the Fundação para a Ciência e a Tecnologia (FCT) through the fellowship PD/BD/52706/2014.

This page intentionally contains only this sentence.

# BIBLIOGRAPHY


Abazajian, K. N. et al. 2009, ApJS, 182, 543, 0812.0649
Abraham, R. G., Valdes, F., Yee, H. K. C., & van den Bergh, S. 1994, ApJ, 432, 75
Abraham, R. G., van den Bergh, S., Glazebrook, K., Ellis, R. S., Santiago, B. X., Surma, P., & Griffiths, R. E. 1996, ApJS, 107, 1
Abraham, R. G., van den Bergh, S., & Nair, P. 2003, ApJ, 588, 218, astro-ph/0301239
Abramson, A., Kenney, J., Crowl, H., & Tal, T. 2016, AJ, 152, 32, 1604.01883
Acquaviva, V., Vargas, C., Gawiser, E., & Guaita, L. 2012, ApJ, 751, L26, 1111.6688
Ahn, C. P. et al. 2012, ApJS, 203, 21, 1207.7137
Akiyama, M., Minowa, Y., Kobayashi, N., Ohta, K., Ando, M., & Iwata, I. 2008, ApJS, 175, 1, 0709.2714
Alavi, A. et al. 2016, ApJ, 832, 56, 1606.00469
Albrecht, A., & Steinhardt, P. J. 1982, Phys. Rev. Lett., 48, 1220
Allen, R. J., Kacprzak, G. G., Glazebrook, K., Tran, K.-V. H., Spitler, L. R., Straatman, C. M. S., Cowley, M., & Nanayakkara, T. 2016, ApJ, 826
Allen, R. J. et al. 2015, ApJ, 806
Alpher, R. A., Bethe, H., & Gamow, G. 1948, Physical Review, 73, 803
Andredakis, Y. C., Peletier, R. F., & Balcells, M. 1995, MNRAS, 275, 874
Arago, F., & Barral, J. A. 1854, Astronomie populaire
Aragón-Calvo, M. A., van de Weygaert, R., & Jones, B. J. T. 2010, MNRAS, 408, 2163, 1007.0742
Arnouts, S. et al. 2013, A&A, 558, A67, 1309.0008
Astropy Collaboration et al. 2013, A&A, 558, A33, 1307.6212
Atek, H., Kunth, D., Schaerer, D., Mas-Hesse, J. M., Hayes, M., Östlin, G., & Kneib, J.-P. 2014, A&A, 561, A89, 1308.6577
Atek, H. et al. 2010, ApJ, 723, 104, 1005.4068
Bacon, R. et al. 2015, A&A, 575, A75, 1411.7667
Baillard, A. et al. 2011, A&A, 532, A74, 1103.5734
Bait, O., Barway, S., & Wadadekar, Y. 2017, MNRAS, 471, 2687
Baldry, I. K., Balogh, M. L., Bower, R. G., Glazebrook, K., Nichol, R. C., Bamford, S. P., & Budavari, T. 2006, MNRAS, 373, 469, astro-ph/0607648
Ball, N. M., Loveday, J., & Brunner, R. J. 2008, MNRAS, 383, 907, astro-ph/0610171
Balogh, M. et al. 2004, MNRAS, 348, 1355, astro-ph/0311379
Balogh, M. L., Couch, W. J., Smail, I., Bower, R. G., & Glazebrook, K. 2002, MNRAS, 335, 10, astro-ph/0203334
Balogh, M. L. et al. 2014, MNRAS, 443, 2679, 1406.4528
Balogh, M. L., Morris, S. L., Yee, H. K. C., Carlberg, R. G., & Ellingson, E. 1999, ApJ, 527, 54, astro-ph/9906470
Balogh, M. L., Navarro, J. F., & Morris, S. L. 2000, ApJ, 540, 113, astro-ph/0004078
Bamford, S. P. et al. 2009, MNRAS, 393, 1324, 0805.2612
Barden, M., Jahnke, K., & Häußler, B. 2008, ApJS, 175, 105, 0812.1022
Bassett, R. et al. 2013a, ApJ, 770, 58, 1305.0607
——. 2013b, ApJ, 770, 58, 1305.0607
Beck, R. 2015, A&A Rev., 24, 4, 1509.04522
Beers, T. C., Flynn, K., & Gebhardt, K. 1990, AJ, 100, 32
Behrens, C., & Braun, H. 2014, A&A, 572, A74, 1410.3733
Bekki, K. 2009, MNRAS, 399, 2221, 0907.4409
Belfiore, F. et al. 2017, MNRAS, 466, 2570, 1609.01737
——. 2016, MNRAS, 461, 3111, 1605.07189
Bershady, M. A., Jangren, A., & Conselice, C. J. 2000, AJ, 119, 2645, astro-ph/0002262
Bertin, E. 2006, in Astronomical Society of the Pacific Conference Series, Vol. 351, Astronomical Data Analysis Software and Systems XV, ed. C. Gabriel, C. Arviset, D. Ponz, & S. Enrique, 112
Bertin, E., & Arnouts, S. 1996, A&AS, 117, 393
Bertin, E., Mellier, Y., Radovich, M., Missonnier, G., Didelon, P., & Morin, B. 2002, in Astronomical Society of the

Pacific Conference Series, Vol. 281, Astronomical Data Analysis Software and Systems XI, ed. D. A. Bohlender, D. Durand, & T. H. Handley, 228
Best, P. N. 2004, MNRAS, 351, 70, astro-ph/0402523
Bian, F. et al. 2010, ApJ, 725, 1877, 1004.4318
Binette, L., Magris, C. G., Stasińska, G., & Bruzual, A. G. 1994, A&A, 292, 13
Birnboim, Y., & Dekel, A. 2003, MNRAS, 345, 349, astro-ph/0302161
Birnboim, Y., Dekel, A., & Neistein, E. 2007, MNRAS, 380, 339, astro-ph/0703435
Blanton, M. R., Eisenstein, D., Hogg, D. W., Schlegel, D. J., & Brinkmann, J. 2005a, ApJ, 629, 143, astro-ph/0310453
Blanton, M. R. et al. 2003, ApJ, 594, 186, arXiv:astro-ph/0209479
Blanton, M. R., Kazin, E., Muna, D., Weaver, B. A., & Price-Whelan, A. 2011, AJ, 142, 31, 1105.1960
Blanton, M. R., Lupton, R. H., Schlegel, D. J., Strauss, M. A., Brinkmann, J., Fukugita, M., & Loveday, J. 2005b, ApJ, 631, 208, astro-ph/0410164
Blanton, M. R., & Moustakas, J. 2009, ARA&A, 47, 159, 0908.3017
Blanton, M. R. et al. 2005c, AJ, 129, 2562, astro-ph/0410166
Bluck, A. F. L., Mendel, J. T., Ellison, S. L., Moreno, J., Simard, L., Patton, D. R., & Starkenburg, E. 2014, MNRAS, 441, 599
Blumenthal, G. R., Faber, S. M., Primack, J. R., & Rees, M. J. 1984, Nature, 311, 517
Bond, N. A., Gawiser, E., Gronwall, C., Ciardullo, R., Altmann, M., & Schawinski, K. 2009, ApJ, 705, 639, 0907.2235
Bond, N. A., Gawiser, E., Guaita, L., Padilla, N., Gronwall, C., Ciardullo, R., & Lai, K. 2012, ApJ, 753, 95, 1104.2880
Bond, N. A., Gawiser, E., & Koekemoer, A. M. 2011, ApJ, 729, 48, 1010.1525
Boselli, A., Cortese, L., Boquien, M., Boissier, S., Catinella, B., Gavazzi, G., Lagos, C., & Saintonge, A. 2014, A&A, 564, A67, 1402.0326
Boselli, A., & Gavazzi, G. 2006, PASP, 118, 517, astro-ph/0601108
Bottrell, C., Torrey, P., Simard, L., & Ellison, S. L. 2017, MNRAS, 467, 2879
Bournaud, F. 2016, Galactic Bulges, 418, 355, 1503.07660
Bournaud, F. et al. 2014, ApJ, 780, 57, 1307.7136
Bouwens, R. J., Illingworth, G. D., Blakeslee, J. P., Broadhurst, T. J., & Franx, M. 2004, ApJ, 611, L1, astro-ph/0406562
Bouwens, R. J. et al. 2015, ApJ, 803, 34, 1403.4295
Bower, R. G., Benson, A. J., Malbon, R., Helly, J. C., Frenk, C. S., Baugh, C. M., Cole, S., & Lacey, C. G. 2006, MNRAS, 370, 645, astro-ph/0511338
Bowler, R. A. A. et al. 2015, MNRAS, 452, 1817, 1411.2976
Bowler, R. A. A., Dunlop, J. S., McLure, R. J., & McLeod, D. J. 2017, MNRAS, 466, 3612, 1605.05325
Bridge, J. S. et al. 2015, ApJ, 799, 205, 1411.6015
Bromm, V., & Yoshida, N. 2011, ARA&A, 49, 373, 1102.4638
Brooks, A., & Christensen, C. 2016, in Galactic Bulges, Vol. 418, 317
Brown, T. et al. 2017, MNRAS, 466, 1275, 1611.00896
Bruce, V. A. et al. 2014a, MNRAS, 444, 1001
——. 2014b, MNRAS, 444, 1660
Bruzual, A. G. 1983, ApJ, 273, 105
Bruzual, G., & Charlot, S. 2003, MNRAS, 344, 1000, astro-ph/0309134
Bryant, J. J. et al. 2015, MNRAS, 447, 2857, 1407.7335
Buitrago, F., Trujillo, I., Conselice, C. J., Bouwens, R. J., Dickinson, M., & Yan, H. 2008, ApJ, 687, L61, 0807.4141
Buitrago, F., Trujillo, I., Conselice, C. J., & Häußler, B. 2013, MNRAS, 428, 1460, 1111.6993
Bundy, K. et al. 2015, ApJ, 798, 7, 1412.1482
Burgarella, D. et al. 2013, A&A, 554, A70, 1304.7000
Burke, C., & Collins, C. A. 2013, MNRAS, 434, 2856, 1307.1702
Buta, R. J. et al. 2015, ApJS, 217, 32, 1501.00454
Canto, J., Meaburn, J., Theokas, A. C., & Elliott, K. H. 1980, MNRAS, 193, 911
Caon, N., Capaccioli, M., & D'Onofrio, M. 1993, MNRAS, 265, 1013, astro-ph/9309013
Capak, P., Abraham, R. G., Ellis, R. S., Mobasher, B., Scoville, N., Sheth, K., & Koekemoer, A. 2007a, The Astrophysical Journal Supplement Series, 172, 284
Capak, P. et al. 2007b, ApJS, 172, 99, 0704.2430
Cardamone, C. et al. 2009, MNRAS, 399, 1191, 0907.4155
Carollo, C. M. et al. 2013, ApJ, 773, 112, 1302.5115
Cassata, P. et al. 2010, ApJ, 714, L79, 0911.1158
——. 2013, ApJ, 775, 106, 1303.2689
——. 2011, A&A, 525, A143, 1003.3480
——. 2015, A&A, 573, A24, 1403.3693
Catalán-Torrecilla, C. et al. 2015, A&A, 584, A87, 1507.03801
Cava, A. et al. 2015, ApJ, 812, 155, 1507.07939
Cebrián, M., & Trujillo, I. 2014, MNRAS, 444, 682
Cerulo, P. et al. 2017, MNRAS, 472, 254
Chabrier, G. 2003, ApJ, 586, L133, astro-ph/0302511

Charlot, S., & Fall, S. M. 2000, ApJ, 539, 718, astro-ph/0003128
Cimatti, A. et al. 2008, A&A, 482, 21, 0801.1184
Clauwens, B., Schaye, J., Franx, M., & Bower, R. G. 2018, MNRAS, 478, 3994
Coenda, V., Martínez, H. J., & Muriel, H. 2018, MNRAS, 473, 5617
Cohen, S. A., Hickox, R. C., Wegner, G. A., Einasto, M., & Vennik, J. 2017, ApJ, 835, 56, 1612.04813
Combes, F., García-Burillo, S., Braine, J., Schinnerer, E., Walter, F., & Colina, L. 2013, A&A, 550, A41, 1209.3665
Conselice, C. J. 2003, ApJS, 147, 1, arXiv:astro-ph/0303065
——. 2014, ARA&A, 52, 291, 1403.2783
Conselice, C. J., & Arnold, J. 2009, MNRAS, 397, 208, 0904.4250
Conselice, C. J., Bershady, M. A., & Jangren, A. 2000a, ApJ, 529, 886, arXiv:astro-ph/9907399
Conselice, C. J., Gallagher, J. S., Calzetti, D., Homeier, N., & Kinney, A. 2000b, AJ, 119, 79, astro-ph/9910382
Conselice, C. J., Yang, C., & Bluck, A. F. L. 2009, MNRAS, 394, 1956, 0812.3237
Cooper, M. C. et al. 2008a, MNRAS, 383, 1058, 0706.4089
Cooper, M. C., Tremonti, C. A., Newman, J. A., & Zabludoff, A. I. 2008b, MNRAS, 390, 245
Coppin, K. E. K. et al. 2012, ApJ, 749, L43, 1203.0007
Cortese, L. et al. 2010, A&A, 518, L49, 1005.3055
Couch, W. J., & Sharples, R. M. 1987, MNRAS, 229, 423
Cox, T. J., Jonsson, P., Primack, J. R., & Somerville, R. S. 2006, MNRAS, 373, 1013, astro-ph/0503201
Crain, R. A. et al. 2015, MNRAS, 450, 1937, 1501.01311
Croton, D. J. et al. 2006, MNRAS, 365, 11, astro-ph/0508046
Cucciati, O. et al. 2017, A&A, 602, A15, 1611.07049
——. 2010a, A&A, 524, A2, 1007.3841
——. 2006, A&A, 458, 39, astro-ph/0603202
——. 2010b, A&A, 520, A42, 0911.3740
——. 2014, A&A, 570, A16, 1403.3691
Curtis, H. D. 1920, Journal of the Royal Astronomical Society of Canada, 14, 317
Curtis-Lake, E. et al. 2016, MNRAS, 457, 440, 1409.1832
da Cunha, E., Charlot, S., & Elbaz, D. 2008, MNRAS, 388, 1595, 0806.1020
Daddi, E. et al. 2005, ApJ, 626, 680, astro-ph/0503102
Darvish, B., Martin, C., Gonçalves, T. S., Mobasher, B., Scoville, N. Z., & Sobral, D. 2018, ArXiv e-prints, 1801.02618
Darvish, B., Mobasher, B., Martin, D. C., Sobral, D., Scoville, N., Stroe, A., Hemmati, S., & Kartaltepe, J. 2017, ApJ, 837, 16, 1611.05451
Darvish, B., Mobasher, B., Sobral, D., Hemmati, S., Nayyeri, H., & Shivaei, I. 2015a, ApJ, 814, 84, 1510.05009
Darvish, B., Mobasher, B., Sobral, D., Rettura, A., Scoville, N., Faisst, A., & Capak, P. 2016, ApJ, 825, 113, 1605.03182
Darvish, B., Mobasher, B., Sobral, D., Scoville, N., & Aragon-Calvo, M. 2015b, ApJ, 805, 121, 1503.07879
Darvish, B., Sobral, D., Mobasher, B., Scoville, N. Z., Best, P., Sales, L. V., & Smail, I. 2014, ApJ, 796, 51, 1409.7695
Davidzon, I. et al. 2016, A&A, 586, A23
Davies, J. I., Phillipps, S., Cawson, M. G. M., Disney, M. J., & Kibblewhite, E. J. 1988, MNRAS, 232, 239
De Lucia, G., Fontanot, F., Wilman, D., & Monaco, P. 2011, MNRAS, 414, 1439
de Souza, R. E., Gadotti, D. A., & dos Anjos, S. 2004, ApJS, 153, 411, astro-ph/0404103
de Vaucouleurs, G. 1948, Annales d'Astrophysique, 11, 247
——. 1959, Handbuch der Physik, 53, 275
Deeley, S. et al. 2017, MNRAS, 467, 3934
Dekel, A., & Cox, T. J. 2006, MNRAS, 370, 1445, astro-ph/0603497
Dekel, A., & Krumholz, M. R. 2013, MNRAS, 432, 455, 1302.4457
Dekel, A., Sari, R., & Ceverino, D. 2009, ApJ, 703, 785, 0901.2458
Delaye, L. et al. 2014, MNRAS, 441, 203, 1307.0003
Delgado-Serrano, R., Hammer, F., Yang, Y. B., Puech, M., Flores, H., & Rodrigues, M. 2010a, A&A, 509, A78, 0906.2805
——. 2010b, A&A, 509, A78, 0906.2805
Dicke, R. H., & Peebles, P. J. E. 1979, in General Relativity: An Einstein centenary survey, 504–517
Dicke, R. H., Peebles, P. J. E., Roll, P. G., & Wilkinson, D. T. 1965, ApJ, 142, 414
Dickinson, H. et al. 2018, ApJ, 853, 194
Dijkstra, M., & Kramer, R. 2012, MNRAS, 424, 1672, 1203.3803
Dimauro, P. et al. 2018, ArXiv e-prints, 1803.10234
Draine, B. T. 2004, in The Cold Universe, Saas-Fee Advanced Course 32, Springer-Verlag, 308 pages, 129 figures, Lecture Notes 2002 of the Swiss Society for Astronomy and Astrophysics (SSAA), Springer, 2004. Edited by A.W. Blain, F. Combes, B.T. Draine, D. Pfenniger and Y. Revaz, ISBN 354040838x, p. 213, ed. A. W. Blain, F. Combes, B. T. Draine, D. Pfenniger, & Y. Revaz, 213, astro-ph/0304488
Dressler, A. 1980, ApJ, 236, 351
——. 1984, ARA&A, 22, 185
Dressler, A., & Gunn, J. E. 1983, ApJ, 270, 7
Dressler, A. et al. 1997, ApJ, 490, 577, astro-ph/9707232
Dressler, A., Oemler, Jr., A., Poggianti, B. M., Smail, I., Trager, S., Shectman, S. A., Couch, W. J., & Ellis, R. S. 2004, ApJ, 617, 867, astro-ph/0408490

Driver, S. P. et al. 2009, Astronomy and Geophysics, 50, 5.12, 0910.5123
Dunlop, J. S. 2013, in Astrophysics and Space Science Library, Vol. 396, Astrophysics and Space Science Library, ed. T. Wiklind, B. Mobasher, & V. Bromm, 223
Duval, F., Schaerer, D., Östlin, G., & Laursen, P. 2014, A&A, 562, A52, 1302.7042
Efstathiou, G. 2000, MNRAS, 317, 697, astro-ph/0002245
Efstathiou, G., & Silk, J. 1983, Fund. Cosmic Phys., 9, 1
Eggen, O. J., Lynden-Bell, D., & Sandage, A. R. 1962, ApJ, 136, 748
Ehlert, S. et al. 2014, MNRAS, 437, 1942, 1310.5711
Einasto, J., Saar, E., Kaasik, A., & Chernin, A. D. 1974, Nature, 252, 111
Elbaz, D. et al. 2007, A&A, 468, 33, astro-ph/0703653
Eliche-Moral, M. C., Balcells, M., Aguerri, J. A. L., & González-García, A. C. 2006, A&A, 457, 91
Ellison, S. L., Catinella, B., & Cortese, L. 2018, MNRAS, 478, 3447
Ellison, S. L., Mendel, J. T., Patton, D. R., & Scudder, J. M. 2013, MNRAS, 435, 3627, 1308.3707
Ellison, S. L., Patton, D. R., Simard, L., & McConnachie, A. W. 2008, AJ, 135, 1877, 0803.0161
Ellison, S. L., Simard, L., Cowan, N. B., Baldry, I. K., Patton, D. R., & McConnachie, A. W. 2009, MNRAS, 396, 1257
Elmegreen, D. M., Elmegreen, B. G., & Sheets, C. M. 2004, ApJ, 603, 74, astro-ph/0401364
Epinat, B. et al. 2017, ArXiv e-prints, 1710.11225
Erb, D. K., Shapley, A. E., Pettini, M., Steidel, C. C., Reddy, N. A., & Adelberger, K. L. 2006, ApJ, 644, 813, astro-ph/0602473
Erfanianfar, G. et al. 2016, MNRAS, 455, 2839, 1511.01899
Fabian, A. C. 2012, ARA&A, 50, 455, 1204.4114
Fan, X. 2016, Is Lyman Alpha Emitter CR7 Powered by a Direct Collapse Black Hole?, HST Proposal
Fasano, G. et al. 2015, MNRAS, 449, 3927
Ferguson, H. C. et al. 2004, ApJL, 600, L107, astro-ph/0309058
Ferrero, I. et al. 2017, MNRAS, 464, 4736
Finkelstein, S. L., Rhoads, J. E., Malhotra, S., & Grogin, N. 2009, ApJ, 691, 465, 0806.3269
Finkelstein, S. L. et al. 2015, ApJ, 810, 71, 1410.5439
Finoguenov, A. et al. 2007, ApJS, 172, 182, astro-ph/0612360
Foreman-Mackey, D., Hogg, D. W., Lang, D., & Goodman, J. 2013, PASP, 125, 306, 1202.3665
Forster Schreiber, N. 2011, Constraints on the Mass Assembly and Early Evolution of z 2 Galaxies: Witnessing the Growth of Bulges and Disks, HST Proposal
Franx, M., van Dokkum, P. G., Schreiber, N. M. F., Wuyts, S., Labbé, I., & Toft, S. 2008, ApJ, 688, 770, 0808.2642
Freeman, P. E., Izbicki, R., Lee, A. B., Newman, J. A., Conselice, C. J., Koekemoer, A. M., Lotz, J. M., & Mozena, M. 2013, MNRAS, 1306.1238
Frick, P., Sokoloff, D., Stepanov, R., & Beck, R. 2011, MNRAS, 414, 2540, 1102.4316
Friedmann, A. 1922, Zeitschrift fur Physik, 10, 377
Fritz, J. et al. 2014, A&A, 566, A32, 1402.4131
Fujita, Y. 1998, ApJ, 509, 587, astro-ph/9807120
Fumagalli, M. et al. 2014, ApJ, 796, 35, 1308.4132
Furlong, M. et al. 2015, ArXiv e-prints, 1510.05645
Gabor, J. M., Davé, R., Finlator, K., & Oppenheimer, B. D. 2010, MNRAS, 407, 749, 1001.1734
Gallazzi, A. et al. 2009, ApJ, 690, 1883, 0809.2042
Gamow, G. 1946, Physical Review, 70, 572
——. 1948, Nature, 162, 680
Gao, H., & Ho, L. C. 2017, ApJ, 845, 114, 1709.00746
Garn, T., & Best, P. N. 2010, MNRAS, 409, 421, 1007.1145
Garnett, D. R. 1992, AJ, 103, 1330
Gawiser, E. et al. 2007, ApJ, 671, 278, 0710.2697
——. 2006, ApJ, 642, L13, astro-ph/0603244
Geach, J. E., Smail, I., Best, P. N., Kurk, J., Casali, M., Ivison, R. J., & Coppin, K. 2008, MNRAS, 388, 1473, 0805.2861
Geach, J. E., Smail, I., Moran, S. M., Treu, T., & Ellis, R. S. 2009, ApJ, 691, 783
Genel, S. et al. 2014, MNRAS, 445, 175, 1405.3749
Genzel, R. et al. 2008, ApJ, 687, 59, 0807.1184
Giavalisco, M., Livio, M., Bohlin, R. C., Macchetto, F. D., & Stecher, T. P. 1996, AJ, 112, 369
Giovanelli, R., & Haynes, M. P. 1985, ApJ, 292, 404
Gomes, J. M. et al. 2016, A&A, 585, A92, 1511.00744
Gómez, P. L. et al. 2003, ApJ, 584, 210, astro-ph/0210193
Goto, T., Yamauchi, C., Fujita, Y., Okamura, S., Sekiguchi, M., Smail, I., Bernardi, M., & Gomez, P. L. 2003, MNRAS, 346, 601, astro-ph/0312043
Graham, A. W. 2001, AJ, 121, 820, astro-ph/0011256
Graham, A. W., & Driver, S. P. 2005, PASA, 22, 118, astro-ph/0503176
Grazian, A. et al. 2012, A&A, 547, A51, 1208.0506
Gronke, M., Bull, P., & Dijkstra, M. 2015, ApJ, 812, 123, 1506.03836
Gronke, M., Dijkstra, M., McCourt, M., & Oh, S. P. 2016, ApJ, 833, L26, 1611.01161
Gronke, M., Dijkstra, M., McCourt, M., & Peng Oh, S. 2017, A&A, 607, A71

Gronwall, C., Bond, N. A., Ciardullo, R., Gawiser, E., Altmann, M., Blanc, G. A., & Feldmeier, J. J. 2011, ApJ, 743, 9, 1005.3006
Grossi, M., Fernandes, C. A. C., Sobral, D., Afonso, J., Telles, E., Bizzocchi, L., Paulino-Afonso, A., & Matute, I. 2018, MNRAS, 475, 735
Grützbauch, R., Chuter, R. W., Conselice, C. J., Bauer, A. E., Bluck, A. F. L., Buitrago, F., & Mortlock, A. 2011, MNRAS, 412, 2361
Gu, Y., Fang, G., Yuan, Q., Cai, Z., & Wang, T. 2018, ApJ, 855, 10
Guaita, L. et al. 2011, ApJ, 733, 114, 1101.3017
——. 2015, A&A, 576, A51, 1501.02387
Gunn, J. E., & Gott, III, J. R. 1972, ApJ, 176, 1
Guo, Y. et al. 2015, ApJ, 800, 39, 1410.7398
——. 2009, MNRAS, 398, 1129, 0901.1150
Guth, A. H. 1981, Phys. Rev. D, 23, 347
Guzzo, L., Strauss, M. A., Fisher, K. B., Giovanelli, R., & Haynes, M. P. 1997, ApJ, 489, 37
Hägele, G. F., Pérez-Montero, E., Díaz, Á. I., Terlevich, E., & Terlevich, R. 2006, MNRAS, 372, 293
Hagen, A. et al. 2014, ApJ, 786, 59, 1403.4935
——. 2016, ApJ, 817, 79, 1512.03063
Hainline, K. N., Shapley, A. E., Kornei, K. A., Pettini, M., Buckley-Geer, E., Allam, S. S., & Tucker, D. L. 2009, ApJ, 701, 52, 0906.2197
Hansen, M., & Oh, S. P. 2006, MNRAS, 367, 979, astro-ph/0507586
Harrison, C. D., Colless, M., Kuntschner, H., Couch, W. J., de Propris, R., & Pracy, M. B. 2011, MNRAS, 413, 1036
Hashimoto, T. et al. 2015, ApJ, 812, 157, 1504.03693
Hathi, N. P. et al. 2016, A&A, 588, A26, 1503.01753
Hathi, N. P., Malhotra, S., & Rhoads, J. E. 2008, ApJ, 673, 686, 0709.0520
Hayashi, M. et al. 2014, MNRAS, 439, 2571, 1401.3919
Hayes, M. et al. 2010, Nature, 464, 562, 1002.4876
Hayes, M., Schaerer, D., Östlin, G., Mas-Hesse, J. M., Atek, H., & Kunth, D. 2011, ApJ, 730, 8, 1010.4796
Henriques, B. M. B., White, S. D. M., Thomas, P. A., Angulo, R., Guo, Q., Lemson, G., Springel, V., & Overzier, R. 2015, MNRAS, 451, 2663, 1410.0365
Henry, A., Scarlata, C., Martin, C. L., & Erb, D. 2015, ApJ, 809, 19, 1505.05149
Hernán-Caballero, A. et al. 2013, MNRAS, 434, 2136, 1306.5581
Hibbard, J. E., & Vacca, W. D. 1997, AJ, 114, 1741, astro-ph/9707275
Hogg, D. W. et al. 2004, ApJ, 601, L29, astro-ph/0307336
Holmberg, E. 1958, Meddelanden fran Lunds Astronomiska Observatorium Serie II, 136, 1
Hopkins, A. M., Connolly, A. J., & Szalay, A. S. 2000, AJ, 120, 2843
Hopkins, P. F. et al. 2010, ApJ, 715, 202, 0906.5357
Huang, K.-H., Ferguson, H. C., Ravindranath, S., & Su, J. 2013, ApJ, 765, 68, 1301.4443
Hubble, E. 1929, Proceedings of the National Academy of Science, 15, 168
Hubble, E. P. 1925, Popular Astronomy, 33, 252
——. 1926, ApJ, 64, 321
——. 1930, ApJ, 71
——. 1936, Realm of the Nebulae
Huertas-Company, M. et al. 2016, MNRAS, 462, 4495, 1606.04952
——. 2013a, MNRAS, 428, 1715
——. 2015a, ApJ, 809, 95, 1506.03084
——. 2015b, ApJ, 809, 95, 1506.03084
Huertas-Company, M., Shankar, F., Mei, S., Bernardi, M., Aguerri, J. A. L., Meert, A., & Vikram, V. 2013b, ApJ, 779, 29, 1212.4143
Hunter, J. D. 2007, Computing In Science & Engineering, 9, 90
Ichikawa, T., Kajisawa, M., & Akhlaghi, M. 2012, MNRAS, 422, 1014, 1202.1138
Ideguchi, S., Tashiro, Y., Akahori, T., Takahashi, K., & Ryu, D. 2017, ApJ, 843, 146, 1701.00315
Ideue, Y. et al. 2009, ApJ, 700, 971, 0905.3982
Ilbert, O. et al. 2009, ApJ, 690, 1236, 0809.2101
——. 2013, A&A, 556, A55, 1301.3157
——. 2010, ApJ, 709, 644, 0903.0102
Iovino, A. et al. 2010, A&A, 509, A40, 0909.1951
——. 2016, A&A, 592, A78, 1606.06185
Izotov, Y. I., Guseva, N. G., & Thuan, T. X. 2011, ApJ, 728, 161, 1012.5639
Jiang, L. et al. 2013, ApJ, 773, 153, 1303.0027
Jones, E., Oliphant, T., Peterson, P., et al. 2001, SciPy: Open source scientific tools for Python, [Online; accessed 2016-03-23]
Kaasinen, M., Bian, F., Groves, B., Kewley, L. J., & Gupta, A. 2017, MNRAS, 465, 3220, 1611.01166
Kamionkowski, M., & Kovetz, E. D. 2016, Annual Review of Astronomy and Astrophysics, 54, 227
Kampczyk, P. et al. 2013, ApJ, 762
Karim, A. et al. 2011, ApJ, 730, 61, 1011.6370
Kartaltepe, J. S. et al. 2015, ApJS, 221, 11, 1401.2455

Kashino, D. et al. 2017, ApJ, 835, 88
Kauffmann, G. et al. 2003, MNRAS, 346, 1055, astro-ph/0304239
Kauffmann, G., White, S. D. M., Heckman, T. M., Ménard, B., Brinchmann, J., Charlot, S., Tremonti, C., & Brinkmann, J. 2004, MNRAS, 353, 713, astro-ph/0402030
Kawamata, R., Ishigaki, M., Shimasaku, K., Oguri, M., & Ouchi, M. 2015, ApJ, 804, 103, 1410.1535
Kawinwanichakij, L. et al. 2017, ApJ, 847, 134, 1706.03780
Kelkar, K., Aragón-Salamanca, A., Gray, M. E., Maltby, D., Vulcani, B., De Lucia, G., Poggianti, B. M., & Zaritsky, D. 2015, MNRAS, 450, 1246, 1503.08225
Kelvin, L. S. 2012, in IAU General Assembly Special Session 3 Galaxy Evolution Through Secular Processes, Beijing, China
Kelvin, L. S. et al. 2018, MNRAS, 477, 4116
Kennicutt, R. C., & Evans, N. J. 2012, ARA&A, 50, 531, 1204.3552
Kennicutt, Jr., R. C. 1998, ARA&A, 36, 189, astro-ph/9807187
Kereš, D., Katz, N., Davé, R., Fardal, M., & Weinberg, D. H. 2009a, MNRAS, 396, 2332, 0901.1880
Kereš, D., Katz, N., Fardal, M., Davé, R., & Weinberg, D. H. 2009b, MNRAS, 395, 160, 0809.1430
Kereš, D., Katz, N., Weinberg, D. H., & Davé, R. 2005, MNRAS, 363, 2, astro-ph/0407095
Kewley, L. J., Geller, M. J., & Barton, E. J. 2006, AJ, 131, 2004, astro-ph/0511119
Kewley, L. J., Geller, M. J., & Jansen, R. A. 2004, AJ, 127, 2002, astro-ph/0401172
Kewley, L. J. et al. 2016, ApJ, 819, 100, 1506.07525
Khochfar, S., & Burkert, A. 2003, ApJ, 597, L117, astro-ph/0303529
Khochfar, S., & Silk, J. 2009, MNRAS, 397, 506, 0809.1734
Khosroshahi, H. G., Wadadekar, Y., & Kembhavi, A. 2000, ApJ, 533, 162, astro-ph/9911402
Khostovan, A. A., Sobral, D., Mobasher, B., Best, P. N., Smail, I., Stott, J. P., Hemmati, S., & Nayyeri, H. 2015, MNRAS, 452, 3948, 1503.00004
Khostovan, A. A., Sobral, D., Mobasher, B., Smail, I., Darvish, B., Nayyeri, H., Hemmati, S., & Stott, J. P. 2016, MNRAS, 463, 2363, 1604.02456
Kobayashi, M. A. R. et al. 2016, ApJ, 819, 25, 1601.05878
Kocevski, D. D., Lemaux, B. C., Lubin, L. M., Shapley, A. E., Gal, R. R., & Squires, G. K. 2011, ApJ, 737, L38, 1011.1495
Kodama, T., Balogh, M. L., Smail, I., Bower, R. G., & Nakata, F. 2004, MNRAS, 354, 1103, astro-ph/0408037
Kodama, T., Smail, I., Nakata, F., Okamura, S., & Bower, R. G. 2001, ApJ, 562, L9
Koekemoer, A. M. et al. 2007, ApJS, 172, 196, astro-ph/0703095
Konno, A., Ouchi, M., Nakajima, K., Duval, F., Kusakabe, H., Ono, Y., & Shimasaku, K. 2016, ApJ, 823, 20, 1512.01854
Konno, A. et al. 2014, ApJ, 797, 16, 1404.6066
Kormendy, J. 2013, Secular Evolution in Disk Galaxies, ed. J. Falcón-Barroso & J. H. Knapen, 1
Kormendy, J., & Kennicutt, Jr., R. C. 2004, ARA&A, 42, 603, astro-ph/0407343
Kornei, K. A., Shapley, A. E., Erb, D. K., Steidel, C. C., Reddy, N. A., Pettini, M., & Bogosavljević, M. 2010, ApJ, 711, 693, 0911.2000
Kovač, K. et al. 2014, MNRAS, 438, 717, 1307.4402
Kovač, K. et al. 2010, ApJ, 718, 86
Koyama, S. et al. 2017, ApJ, 847, 137, 1708.09672
Koyama, Y., Kodama, T., Shimasaku, K., Hayashi, M., Okamura, S., Tanaka, I., & Tokoku, C. 2010, MNRAS, 403, 1611, 0912.2786
Koyama, Y. et al. 2008, MNRAS, 391, 1758, 0809.2795
Koyama, Y., Kodama, T., Tadaki, K.-i., Hayashi, M., Tanaka, I., & Shimakawa, R. 2014, ApJ, 789, 18, 1405.4165
Koyama, Y. et al. 2013, MNRAS, 434, 423, 1302.5315
Krabbe, A. C., Rosa, D. A., Dors, O. L., Pastoriza, M. G., Winge, C., Hägele, G. F., Cardaci, M. V., & Rodrigues, I. 2014, MNRAS, 437, 1155, 1310.7910
Kriek, M. et al. 2015, ApJS, 218, 15, 1412.1835
Krist, J. 1995, in Astronomical Society of the Pacific Conference Series, Vol. 77, Astronomical Data Analysis Software and Systems IV, ed. R. A. Shaw, H. E. Payne, & J. J. E. Hayes, 349
Krywult, J. et al. 2017, A&A, 598
Kulas, K. R. et al. 2013, ApJ, 774, 130, 1306.6334
Kusakabe, H., Shimasaku, K., Nakajima, K., & Ouchi, M. 2015, ApJ, 800, L29, 1411.1615
Lackner, C. N., & Gunn, J. E. 2013, MNRAS, 428, 2141
Lai, K. et al. 2008, ApJ, 674, 70, 0710.3384
Laigle, C. et al. 2016, ApJS, 224, 24, 1604.02350
Lake, E., Zheng, Z., Cen, R., Sadoun, R., Momose, R., & Ouchi, M. 2015, ApJ, 806, 46, 1502.01349
Lambas, D. G., Alonso, S., Mesa, V., & O'Mill, A. L. 2012, A&A, 539, A45, 1111.2291
Lang, P. et al. 2014, ApJ, 788, 11, 1402.0866
Lani, C. et al. 2013, MNRAS, 435, 207
Larson, R. B., Tinsley, B. M., & Caldwell, C. N. 1980, ApJ, 237, 692
Laursen, P., Duval, F., & Östlin, G. 2013, ApJ, 766, 124, 1211.2833
Law, D. R., Steidel, C. C., Erb, D. K., Pettini, M., Reddy, N. A., Shapley, A. E., Adelberger, K. L., & Simenc, D. J. 2007, ApJ, 656, 1, arXiv:astro-ph/0610693
Law, D. R., Steidel, C. C., Shapley, A. E., Nagy, S. R., Reddy, N. A., & Erb, D. K. 2012, ApJ, 759, 29, 1206.6889

Le Fèvre, O. et al. 2003, in Proc. SPIE, Vol. 4841, Instrument Design and Performance for Optical/Infrared Ground-based Telescopes, ed. M. Iye & A. F. M. Moorwood, 1670–1681
Le Fèvre, O. et al. 2015, A&A, 576, A79, 1403.3938
Lee, S.-K., Im, M., Kim, J.-W., Lotz, J., McPartland, C., Peth, M., & Koekemoer, A. 2015, ApJ, 810, 90, 1508.01294
Lehnert, M. D., Le Tiran, L., Nesvadba, N. P. H., van Driel, W., Boulanger, F., & Di Matteo, P. 2013, A&A, 555, A72, 1304.7734
Lehnert, M. D., Nesvadba, N. P. H., Le Tiran, L., Di Matteo, P., van Driel, W., Douglas, L. S., Chemin, L., & Bournaud, F. 2009, ApJ, 699, 1660, 0902.2784
Lemaître, G. 1927, Annales de la Societe; Scientifique de Bruxelles, 47, 49
Lemaux, B. C. et al. 2014, A&A, 572, A41, 1403.4230
Lemaux, B. C., Lubin, L. M., Shapley, A., Kocevski, D., Gal, R. R., & Squires, G. K. 2010, ApJ, 716, 970, 1003.1780
Lewis, I. et al. 2002, MNRAS, 334, 673, astro-ph/0203336
Li, C., Kauffmann, G., Jing, Y. P., White, S. D. M., Börner, G., & Cheng, F. Z. 2006, MNRAS, 368, 21, astro-ph/0509873
Li, C. et al. 2015, ApJ, 804, 125, 1502.07040
Li, I. H. et al. 2011, MNRAS, 411, 1869, 1010.1447
Li, I. H., Yee, H. K. C., & Ellingson, E. 2009, ApJ, 698, 83, 0904.0831
Lilly, S. et al. 1998, ApJ, 500, 75, astro-ph/9712061
Lilly, S. J., Le Fevre, O., Hammer, F., & Crampton, D. 1996, ApJ, 460, L1, astro-ph/9601050
Lilly, S. J. et al. 2007, ApJS, 172, 70, astro-ph/0612291
Lin, L. et al. 2010, ApJ, 718, 1158, 1001.4560
Linde, A. D. 1982, Physics Letters B, 108, 389
Lintott, C. et al. 2011, MNRAS, 410, 166, 1007.3265
Lintott, C. J. et al. 2008, MNRAS, 389, 1179, 0804.4483
Liske, J. et al. 2015, MNRAS, 452, 2087, 1506.08222
Lotz, J. M. et al. 2008, ApJ, 672, 177, astro-ph/0602088
Lotz, J. M., Primack, J., & Madau, P. 2004, AJ, 128, 163, arXiv:astro-ph/0311352
Lubin, L. M., Gal, R. R., Lemaux, B. C., Kocevski, D. D., & Squires, G. K. 2009, AJ, 137, 4867, 0809.2092
Lupton, R., Gunn, J. E., Ivezić, Z., Knapp, G. R., & Kent, S. 2001, in Astronomical Society of the Pacific Conference Series, Vol. 238, Astronomical Data Analysis Software and Systems X, ed. F. R. Harnden, Jr., F. A. Primini, & H. E. Payne, 269, astro-ph/0101420
Luridiana, V., Morisset, C., & Shaw, R. A. 2015, A&A, 573, A42, 1410.6662
Ly, C., Lee, J. C., Dale, D. A., Momcheva, I., Salim, S., Staudaher, S., Moore, C. A., & Finn, R. 2011, ApJ, 726, 109, 1011.2759
Ma, X., Hopkins, P. F., Faucher-Giguère, C.-A., Zolman, N., Muratov, A. L., Kereš, D., & Quataert, E. 2016, MNRAS, 456, 2140
Madau, P., & Dickinson, M. 2014, ARA&A, 52, 415, 1403.0007
Malavasi, N. et al. 2017, MNRAS, 465, 3817, 1611.07045
Malavasi, N., Pozzetti, L., Cucciati, O., Bardelli, S., & Cimatti, A. 2016, A&A, 585, A116, 1509.08964
Malhotra, S., Rhoads, J. E., Finkelstein, S. L., Hathi, N., Nilsson, K., McLinden, E., & Pirzkal, N. 2012, ApJ, 750, L36, 1106.2816
Mallery, R. P. et al. 2012, ApJ, 760, 128, 1208.6031
Mancone, C. L., & Gonzalez, A. H. 2012, Publications of the Astronomical Society of the Pacific, 124, 606
Mansheim, A. S., Lemaux, B. C., Dawson, W. A., Lubin, L. M., Wittman, D., & Schmidt, S. 2017a, ApJ, 834, 205, 1611.07040
Mansheim, A. S. et al. 2017b, MNRAS, 469, L20, 1705.03468
Margalef-Bentabol, B., Conselice, C. J., Mortlock, A., Hartley, W., Duncan, K., Ferguson, H. C., Dekel, A., & Primack, J. R. 2016, MNRAS, 461, 2728, 1606.07405
Martin, C. L., & Sawicki, M. 2004, ApJ, 603, 414, astro-ph/0310839
Mas-Ribas, L., Dijkstra, M., Hennawi, J. F., Trenti, M., Momose, R., & Ouchi, M. 2017, ApJ, 841, 19, 1703.02593
Masters, D., & Capak, P. 2011, PASP, 123, 638, 1103.3222
Masters, D. et al. 2014, ApJ, 785, 153, 1402.0510
Matsuda, Y. et al. 2011, MNRAS, 410, L13, 1010.2877
——. 2012, MNRAS, 425, 878, 1204.4934
Matthee, J., Sobral, D., Best, P., Smail, I., Bian, F., Darvish, B., Röttgering, H., & Fan, X. 2017a, MNRAS, 471, 629, 1702.04721
Matthee, J., Sobral, D., Darvish, B., Santos, S., Mobasher, B., Paulino-Afonso, A., Röttgering, H., & Alegre, L. 2017b, MNRAS, 472, 772, 1706.06591
Matthee, J., Sobral, D., Gronke, M., Paulino- Afonso, A., Stefanon, M., & Röttgering, H. 2018, ArXiv e-prints, arXiv:1805.11621, 1805.11621
Matthee, J., Sobral, D., Oteo, I., Best, P., Smail, I., Röttgering, H., & Paulino-Afonso, A. 2016, MNRAS, 458, 449, 1602.02756
Matthee, J., Sobral, D., Santos, S., Röttgering, H., Darvish, B., & Mobasher, B. 2015, MNRAS, 451, 400, 1502.07355
McCarthy, P. J. et al. 1999, ApJ, 520, 548, astro-ph/9902347
McIntosh, D. H., Guo, Y., Hertzberg, J., Katz, N., Mo, H. J., van den Bosch, F. C., & Yang, X. 2008, MNRAS, 388, 1537, 0710.2157
McKee, C. F., & Ostriker, E. C. 2007, Annual Review of Astronomy and Astrophysics, 45, 565, 0707.3514

Meert, A., Vikram, V., & Bernardi, M. 2013, MNRAS, 433, 1344, 1211.6123
Mei, S. et al. 2015, ApJ, 804, 117, 1403.7524
Mendez, A. J., Coil, A. L., Lotz, J., Salim, S., Moustakas, J., & Simard, L. 2011, ApJ, 736, 110
Merritt, D. 1984, ApJ, 276, 26
Messier, C. 1781, Catalogue des Nébuleuses et des Amas d'Étoiles (Catalog of Nebulae and Star Clusters), Tech. rep.
Mignoli, M. et al. 2009, A&A, 493, 39
Mihos, J. C., & Hernquist, L. 1996, ApJ, 464, 641, astro-ph/9512099
Misner, C. W. 1968, ApJ, 151, 431
Miyazaki, S. et al. 2002, PASJ, 54, 833, astro-ph/0211006
Mo, H., van den Bosch, F., & White, S. 2010, Galaxy Formation and Evolution (Cambridge University Press)
Mok, A. et al. 2013, MNRAS, 431, 1090, 1302.2562
——. 2016, MNRAS, 456, 4384, 1512.05768
Möllenhoff, C., & Heidt, J. 2001, A&A, 368, 16
Momose, R. et al. 2014, MNRAS, 442, 110, 1403.0732
Moore, B., Katz, N., Lake, G., Dressler, A., & Oemler, A. 1996, Nature, 379, 613, astro-ph/9510034
Moore, B., Lake, G., & Katz, N. 1998, ApJ, 495, 139, astro-ph/9701211
Moorwood, A. F. M., van der Werf, P. P., Cuby, J. G., & Oliva, E. 2000, A&A, 362, 9, astro-ph/0009010
Moriondo, G., Giovanardi, C., & Hunt, L. K. 1998, A&AS, 130, 81, astro-ph/9802144
Morishita, T., Ichikawa, T., & Kajisawa, M. 2014, ApJ, 785, 18, 1402.5752
Mortlock, A. et al. 2015, MNRAS, 447, 2, 1411.3339
——. 2013, MNRAS, 433, 1185, 1305.2204
Mosleh, M., Williams, R. J., & Franx, M. 2013, ApJ, 777, 117, 1302.6240
Mosleh, M., Williams, R. J., Franx, M., & Kriek, M. 2011, ApJ, 727, 5, 1011.3042
Moss, C. 2006, MNRAS, 373, 167, astro-ph/0608672
Mulroy, S. L., McGee, S. L., Gillman, S., Smith, G. P., Haines, C. P., Démoclès, J., Okabe, N., & Egami, E. 2017, MNRAS, 472, 3246, 1708.05971
Murgia, M., Govoni, F., Feretti, L., Giovannini, G., Dallacasa, D., Fanti, R., Taylor, G. B., & Dolag, K. 2004, A&A, 424, 429, astro-ph/0406225
Muzzin, A. et al. 2013, ApJS, 206, 8, 1303.4410
——. 2012, ApJ, 746, 188, 1112.3655
Naab, T., & Ostriker, J. P. 2017, Annual Review of Astronomy and Astrophysics, 55, 59
Nair, P. B., & Abraham, R. G. 2010, ApJS, 186, 427, 1001.2401
Nakata, F., Bower, R. G., Balogh, M. L., & Wilman, D. J. 2005, MNRAS, 357, 679, astro-ph/0412064
Nantais, J. B., Flores, H., Demarco, R., Lidman, C., Rosati, P., & Jee, M. J. 2013a, A&A, 555
Nantais, J. B., Rettura, A., Lidman, C., Demarco, R., Gobat, R., Rosati, P., & Jee, M. J. 2013b, A&A, 556, A112, 1306.3431
Nelson, E. J. et al. 2016, ApJ, 828, 27
Neufeld, D. A. 1991, ApJ, 370, L85
Newman, A. B., Ellis, R. S., Andreon, S., Treu, T., Raichoor, A., & Trinchieri, G. 2014, ApJ, 788
Nilsson, K. K., Östlin, G., Møller, P., Möller-Nilsson, O., Tapken, C., Freudling, W., & Fynbo, J. P. U. 2011, A&A, 529, A9, 1009.0007
Noeske, K. G. et al. 2007, ApJ, 660, L43, astro-ph/0701924
Nogueira-Cavalcante, J. P., Gonçalves, T. S., Mené ndez-Delmestre, K., & Sheth, K. 2018, MNRAS, 473, 1346
Oemler, Jr., A. 1974, ApJ, 194, 1
Oemler, Jr., A., Dressler, A., Kelson, D., Rigby, J., Poggianti, B. M., Fritz, J., Morrison, G., & Smail, I. 2009, ApJ, 693, 152, 0812.4405
Oesch, P. A. et al. 2010, ApJL, 709, L21, 0909.5183
——. 2016, ApJ, 819, 129, 1603.00461
Oh, S. et al. 2014, ApJ, 790, 43, 1406.3059
Oke, J. B., & Gunn, J. E. 1983, ApJ, 266, 713
Ono, Y. et al. 2013, ApJ, 777, 155, 1212.3869
——. 2012, ApJ, 744, 83, 1107.3159
Opik, E. 1922, ApJ, 55, 406
Osterbrock, D. E. 1989, Astrophysics of gaseous nebulae and active galactic nuclei
Östlin, G. et al. 2014, ApJ, 797, 11, 1409.8347
Ostriker, J. P., Peebles, P. J. E., & Yahil, A. 1974, ApJ, 193, L1
Oteo, I., Sobral, D., Ivison, R. J., Smail, I., Best, P. N., Cepa, J., & Pérez-García, A. M. 2015, MNRAS, 452, 2018, 1506.02670
Ouchi, M. 2010, Determining the Physical Nature of a Unique Giant Lya Emitter at z=6.595, HST Proposal
Ouchi, M. et al. 2013, ApJ, 778, 102, 1306.3572
——. 2018, PASJ, 70, S13, 1704.07455
——. 2009, ApJ, 696, 1164, 0807.4174
——. 2008, ApJS, 176, 301, 0707.3161
——. 2010, ApJ, 723, 869, 1007.2961
Overzier, R. A. et al. 2008, ApJ, 673, 143, astro-ph/0601223
Owers, M. S., Couch, W. J., Nulsen, P. E. J., & Randall, S. W. 2012, ApJ, 750, L23, 1204.1052

Oyarzún, G. A., Blanc, G. A., González, V., Mateo, M., & Bailey, III, J. I. 2017, ApJ, 843, 133, 1706.01886
Papovich, C. et al. 2012, ApJ, 750, 93, 1110.3794
Papovich, C., Giavalisco, M., Dickinson, M., Conselice, C. J., & Ferguson, H. C. 2003, ApJ, 598, 827, astro-ph/0308386
Parsa, S., Dunlop, J. S., McLure, R. J., & Mortlock, A. 2016, MNRAS, 456, 3194, 1507.05629
Partridge, R. B., & Peebles, P. J. E. 1967, ApJ, 147, 868
Patel, S. G., Holden, B. P., Kelson, D. D., Illingworth, G. D., & Franx, M. 2009, ApJ, 705, L67, 0910.0837
Paulino-Afonso, A., Sobral, D., Buitrago, F., & Afonso, J. 2017, MNRAS, 465, 2717, 1611.05039
Paulino-Afonso, A., Sobral, D., Darvish, B., Ribeiro, B., Stroe, A., Best, P., Afonso, J., & Matsuda, Y. 2018a, in Press, arXiv:1805.07371, 1805.07371
——. 2018b, ArXiv e-prints, arXiv:1805.07371, 1805.07371
Paulino-Afonso, A. et al. 2018c, MNRAS, 476, 5479
Pawlik, M. M., Wild, V., Walcher, C. J., Johansson, P. H., Villforth, C., Rowlands, K., Mendez-Abreu, J., & Hewlett, T. 2016, MNRAS, 456, 3032, 1512.02000
Peebles, P. J., & Ratra, B. 2003, Reviews of Modern Physics, 75, 559, astro-ph/0207347
Peebles, P. J. E. 1982, ApJ, 263, L1
Peimbert, M. 1967, ApJ, 150, 825
Peng, C. Y., Ho, L. C., Impey, C. D., & Rix, H.-W. 2002, AJ, 124, 266, arXiv:astro-ph/0204182
——. 2010a, AJ, 139, 2097, 0912.0731
Peng, Y.-j. et al. 2010b, ApJ, 721, 193, 1003.4747
Peng, Y.-j., Lilly, S. J., Renzini, A., & Carollo, M. 2012, ApJ, 757, 4, 1106.2546
Pentericci, L. et al. 2013, A&A, 552, A111, 1302.2861
Pentericci, L., Grazian, A., Fontana, A., Salimbeni, S., Santini, P., de Santis, C., Gallozzi, S., & Giallongo, E. 2007, A&A, 471, 433, astro-ph/0703013
Penzias, A. A., & Wilson, R. W. 1965, ApJ, 142, 419
Perez, J., Tissera, P., Padilla, N., Alonso, M. S., & Lambas, D. G. 2009, MNRAS, 399, 1157, 0904.2851
Pérez-González, P. G., Trujillo, I., Barro, G., Gallego, J., Zamorano, J., & Conselice, C. J. 2008, ApJ, 687, 50, 0807.1069
Perlmutter, S. et al. 1998, Nature, 391, 51, astro-ph/9712212
Peter, A. H. G., Shapley, A. E., Law, D. R., Steidel, C. C., Erb, D. K., Reddy, N. A., & Pettini, M. 2007, ApJ, 668, 23, 0706.2865
Petrosian, V. 1976, ApJL, 209, L1
Petty, S. M., de Mello, D. F., Gallagher, III, J. S., Gardner, J. P., Lotz, J. M., Mountain, C. M., & Smith, L. J. 2009, AJ, 138, 362, 0904.4433
Pipino, A. et al. 2014, ApJ, 797
Pirzkal, N., Malhotra, S., Rhoads, J. E., & Xu, C. 2007, ApJ, 667, 49, astro-ph/0612513
Planck Collaboration et al. 2016a, A&A, 594, A1
——. 2016b, A&A, 594, A13, 1502.01589
——. 2018a, ArXiv e-prints, arXiv:1807.06209, 1807.06209
——. 2018b, ArXiv e-prints, arXiv:1807.06205, 1807.06205
Poggianti, B. M. et al. 2009, ApJ, 693, 112, 0811.0252
Poggianti, B. M., & Barbaro, G. 1997, A&A, 325, 1025, astro-ph/9703067
Poggianti, B. M. et al. 2008, ApJ, 684, 888, 0805.1145
Poggianti, B. M., Smail, I., Dressler, A., Couch, W. J., Barger, A. J., Butcher, H., Ellis, R. S., & Oemler, Jr., A. 1999, ApJ, 518, 576, astro-ph/9901264
Poggianti, B. M. et al. 2006, ApJ, 642, 188, astro-ph/0512391
Popesso, P. et al. 2011, A&A, 532, A145, 1104.1094
Postman, M. et al. 2005, ApJ, 623, 721
Pradhan, A. K., Montenegro, M., Nahar, S. N., & Eissner, W. 2006, MNRAS, 366, L6, astro-ph/0510099
Puchwein, E., & Springel, V. 2013, MNRAS, 428, 2966, 1205.2694
Querejeta, M., Eliche-Moral, M. C., Tapia, T., Borlaff, A., Rodríguez-Pérez, C., Zamorano, J., & Gallego, J. 2015, A&A, 573, A78, 1409.5126
Rauch, M. et al. 2008, ApJ, 681, 856, 0711.1354
Ravindranath, S. et al. 2004, ApJL, 604, L9, astro-ph/0401483
——. 2006, ApJ, 652, 963, astro-ph/0606696
Reddy, N. A., & Steidel, C. C. 2009, ApJ, 692, 778, 0810.2788
Reddy, N. A., Steidel, C. C., Pettini, M., Adelberger, K. L., Shapley, A. E., Erb, D. K., & Dickinson, M. 2008, ApJS, 175, 48, 0706.4091
Rettura, A. et al. 2011, ApJ, 732, 94, 1103.0265
——. 2010, ApJ, 709, 512, 0806.4604
Rhoads, J. E., Malhotra, S., Dey, A., Stern, D., Spinrad, H., & Jannuzi, B. T. 2000, ApJ, 545, L85, astro-ph/0003465
Rhodes, J. D., Massey, R., Albert, J., Taylor, J. E., Koekemoer, A. M., & Leauthaud, A. 2006, in The 2005 HST Calibration Workshop: Hubble After the Transition to Two-Gyro Mode, ed. A. M. Koekemoer, P. Goudfrooij, & L. L. Dressel, 21, astro-ph/0512170
Rhodes, J. D. et al. 2007, ApJS, 172, 203, astro-ph/0702140
Ribeiro, B. et al. 2017, A&A, 608, A16
——. 2016, A&A, 593, A22, 1602.01840

Roberts, M. S., & Haynes, M. P. 1994, ARA&A, 32, 115
Roberts, M. S., & Rots, A. H. 1973, A&A, 26, 483
Robertson, B. E., Ellis, R. S., Dunlop, J. S., McLure, R. J., & Stark, D. P. 2010, Nature, 468, 49, 1011.0727
Rodríguez del Pino, B. et al. 2017, MNRAS, 467, 4200, 1701.06483
Roediger, E., Brüggen, M., Owers, M. S., Ebeling, H., & Sun, M. 2014, MNRAS, 443, L114, 1405.1033
Rubin, V. C., Ford, W. K., J., & Thonnard, N. 1978, ApJ, 225, L107
——. 1980, ApJ, 238, 471
Salim, S. et al. 2007, ApJS, 173, 267, 0704.3611
Salpeter, E. E. 1955, ApJ, 121, 161
Sánchez, S. F. et al. 2012, A&A, 538, A8, 1111.0962
Sandage, A. 1961, The Hubble atlas of galaxies
Sanders, R. L. et al. 2016, ApJ, 816, 23, 1509.03636
Santos, J. S. et al. 2013, MNRAS, 433, 1287, 1305.1938
——. 2014, MNRAS, 438, 2565, 1312.1694
Santos, S., Sobral, D., & Matthee, J. 2016, MNRAS, 1606.07435
Saracco, P., Gargiulo, A., Ciocca, F., & Marchesini, D. 2017, A&A, 597
Schaerer, D. 2003, A&A, 397, 527, astro-ph/0210462
Schawinski, K. et al. 2014, MNRAS, 440, 889
Schaye, J. et al. 2015, MNRAS, 446, 521, 1407.7040
Schmidt, B. P. et al. 1998, ApJ, 507, 46, astro-ph/9805200
Scoville, N. et al. 2007, ApJS, 172, 38, astro-ph/0612306
——. 2013, ApJS, 206, 3, 1303.6689
Scudder, J. M., Ellison, S. L., Momjian, E., Rosenberg, J. L., Torrey, P., Patton, D. R., Fertig, D., & Mendel, J. T. 2015, MNRAS, 449, 3719
Seaton, M. J., & Osterbrock, D. E. 1957, ApJ, 125, 66
Serra, P. et al. 2012, MNRAS, 422, 1835, 1111.4241
Sérsic, J. L. 1968, Atlas de galaxias australes
Shankar, F. et al. 2014, MNRAS, 439, 3189
Shapley, A. E., Steidel, C. C., Pettini, M., & Adelberger, K. L. 2003, ApJ, 588, 65, astro-ph/0301230
Shen, S., Mo, H. J., White, S. D. M., Blanton, M. R., Kauffmann, G., Voges, W., Brinkmann, J., & Csabai, I. 2003, MNRAS, 343, 978, astro-ph/0301527
Shibuya, T., Ouchi, M., & Harikane, Y. 2015, ApJS, 219, 15, 1503.07481
Shibuya, T., Ouchi, M., Kubo, M., & Harikane, Y. 2016, ApJ, 821, 72, 1511.07054
Shibuya, T. et al. 2014a, ApJ, 788, 74, 1402.1168
Shibuya, T., Ouchi, M., Nakajima, K., Yuma, S., Hashimoto, T., Shimasaku, K., Mori, M., & Umemura, M. 2014b, ApJ, 785, 64, 1401.1209
Shim, H., Colbert, J., Teplitz, H., Henry, A., Malkan, M., McCarthy, P., & Yan, L. 2009, ApJ, 696, 785, 0902.0736
Shimakawa, R. et al. 2018, MNRAS, 473, 1977, 1708.06369
——. 2015a, MNRAS, 451, 1284, 1411.1408
Shimakawa, R., Kodama, T., Tadaki, K.-i., Hayashi, M., Koyama, Y., & Tanaka, I. 2015b, MNRAS, 448, 666, 1406.5219
Shirazi, M., Brinchmann, J., & Rahmati, A. 2014, ApJ, 787, 120, 1307.4758
Simard, L. 1998, in Astronomical Society of the Pacific Conference Series, Vol. 145, Astronomical Data Analysis Software and Systems VII, ed. R. Albrecht, R. N. Hook, & H. A. Bushouse, 108
Simard, L., Mendel, J. T., Patton, D. R., Ellison, S. L., & McConnachie, A. W. 2011, ApJS, 196, 11, 1107.1518
Singh, R. et al. 2013, A&A, 558, A43, 1308.4271
Siudek, M. et al. 2017, A&A, 597, A107
Skibba, R. A. et al. 2009, MNRAS, 399, 966, 0811.3970
——. 2012, MNRAS, 423, 1485
Slipher, V. M. 1915, Popular Astronomy, 23, 21
Smail, I., Ivison, R. J., Kneib, J.-P., Cowie, L. L., Blain, A. W., Barger, A. J., Owen, F. N., & Morrison, G. 1999, MNRAS, 308, 1061, astro-ph/9905246
Snyder, G. F. et al. 2015, MNRAS, 454, 1886
Sobral, D. 2016, The hosts of the early ionized bubbles: the nature and diversity of the most luminous Lyman-alpha emitters at z 6-7, HST Proposal
Sobral, D. et al. 2009, MNRAS, 398, 75, 0901.4114
Sobral, D., Best, P. N., Smail, I., Geach, J. E., Cirasuolo, M., Garn, T., & Dalton, G. B. 2011, MNRAS, 411, 675, 1007.2642
Sobral, D., Best, P. N., Smail, I., Mobasher, B., Stott, J., & Nisbet, D. 2014, MNRAS, 437, 3516, 1311.1503
Sobral, D. et al. 2017, MNRAS, 466, 1242, 1609.05897
——. 2015a, MNRAS, 451, 2303, 1502.06602
——. 2018a, MNRAS, 477, 2817, 1802.10102
Sobral, D., Santos, S., Matthee, J., Paulino-Afonso, A., Ribeiro, B., Calhau, J., & Khostovan, A. A. 2018b, MNRAS, 1712.04451
Sobral, D., Smail, I., Best, P. N., Geach, J. E., Matsuda, Y., Stott, J. P., Cirasuolo, M., & Kurk, J. 2013a, MNRAS, 428, 1128, 1202.3436
Sobral, D., Stroe, A., Dawson, W. A., Wittman, D., Jee, M. J., Röttgering, H., van Weeren, R. J., & Brüggen, M. 2015b, MNRAS, 450, 630, 1503.02076

Sobral, D., Stroe, A., Koyama, Y., Darvish, B., Calhau, J., Afonso, A., Kodama, T., & Nakata, F. 2016, MNRAS, 458, 3443, 1603.00462
Sobral, D. et al. 2013b, ApJ, 779, 139, 1310.3822
Soille, P. J., & Ansoult, M. M. 1990, Signal Processing, 20, 171
Somerville, R. S., & Davé, R. 2015, ARA&A, 53, 51, 1412.2712
Somerville, R. S., Hopkins, P. F., Cox, T. J., Robertson, B. E., & Hernquist, L. 2008, MNRAS, 391, 481, 0808.1227
Sparke, L., & Gallagher, J. 2007, Galaxies in the Universe: An Introduction (Cambridge University Press)
Springel, V. et al. 2005, Nature, 435, 629, astro-ph/0504097
Stark, D. P. 2016, ARA&A, 54, 761
Stark, D. P., Ellis, R. S., & Ouchi, M. 2011, ApJ, 728, L2, 1009.5471
Steidel, C. C., Adelberger, K. L., Giavalisco, M., Dickinson, M., & Pettini, M. 1999, ApJ, 519, 1, astro-ph/9811399
Steidel, C. C., Giavalisco, M., Pettini, M., Dickinson, M., & Adelberger, K. L. 1996, ApJ, 462, L17, astro-ph/9602024
Steidel, C. C. et al. 2014, ApJ, 795, 165, 1405.5473
Stott, J. P., Sobral, D., Smail, I., Bower, R., Best, P. N., & Geach, J. E. 2013a, MNRAS, 430, 1158, 1212.4834
——. 2013b, MNRAS, 430, 1158, 1212.4834
Stott, J. P. et al. 2014, MNRAS, 443, 2695, 1407.1047
——. 2016, MNRAS, 457, 1888, 1601.03400
Straatman, C. M. S. et al. 2015, ApJ, 808, L29, 1506.01380
Strateva, I. et al. 2001, AJ, 122, 1861
Strazzullo, V. et al. 2013, ApJ, 772, 118, 1305.3577
Stroe, A., & Sobral, D. 2015, MNRAS, 453, 242, 1507.02687
Stroe, A. et al. 2015, MNRAS, 450, 646, 1410.2891
Stroe, A., Sobral, D., Matthee, J., Calhau, J., & Oteo, I. 2017a, ArXiv e-prints, 1703.10169
——. 2017b, ArXiv e-prints, 1704.01124
Stroe, A., Sobral, D., Paulino-Afonso, A., Alegre, L., Calhau, J., Santos, S., & van Weeren, R. 2017c, MNRAS, 465, 2916, 1611.03512
Stroe, A., Sobral, D., Röttgering, H. J. A., & van Weeren, R. J. 2014, MNRAS, 438, 1377, 1311.6812
Swinbank, A. M., Smail, I., Sobral, D., Theuns, T., Best, P. N., & Geach, J. E. 2012a, ApJ, 760, 130, 1209.1396
Swinbank, A. M., Sobral, D., Smail, I., Geach, J. E., Best, P. N., McCarthy, I. G., Crain, R. A., & Theuns, T. 2012b, MNRAS, 426, 935, 1209.1395
Tadaki, K.-i. et al. 2012, MNRAS, 423, 2617, 1204.1165
Taniguchi, Y. et al. 2015, PASJ, 67, 104, 1510.00550
——. 2009, ApJ, 701, 915
——. 2007, ApJS, 172, 9, astro-ph/0612295
Tasca, L. A. M. et al. 2009, A&A, 503, 379, 0906.4556
——. 2014, A&A, 565, A10, 1303.4400
Taylor-Mager, V. A., Conselice, C. J., Windhorst, R. A., & Jansen, R. A. 2007, ApJ, 659, 162, astro-ph/0612558
Tolman, R. C. 1930, Proceedings of the National Academy of Science, 16, 511
Tonnesen, S., & Cen, R. 2012, MNRAS, 425, 2313, 1111.0636
Toomre, A., & Toomre, J. 1972, ApJ, 178, 623
Trainor, R. F., Strom, A. L., Steidel, C. C., & Rudie, G. C. 2016, ApJ, 832, 171, 1608.07280
Tran, K.-V. H. et al. 2017, ApJ, 834, 101
——. 2010, ApJ, 719, L126, 1005.5126
Tremonti, C. A. et al. 2004, ApJ, 613, 898, astro-ph/0405537
Treu, T., Ellis, R. S., Kneib, J.-P., Dressler, A., Smail, I., Czoske, O., Oemler, A., & Natarajan, P. 2003, ApJ, 591, 53, astro-ph/0303267
Trujillo, I., Conselice, C. J., Bundy, K., Cooper, M. C., Eisenhardt, P., & Ellis, R. S. 2007, MNRAS, 382, 109, 0709.0621
Trujillo, I. et al. 2006a, ApJ, 650, 18, astro-ph/0504225
——. 2006b, ApJ, 650, 18, astro-ph/0504225
Trujillo, I., Graham, A. W., & Caon, N. 2001, MNRAS, 326, 869, astro-ph/0102393
van den Bergh, S. 1960, ApJ, 131, 215
——. 1976, ApJ, 206, 883
van der Wel, A. et al. 2014, ApJ, 788, 28, 1404.2844
——. 2007, ApJ, 670, 206, 0707.2787
——. 2016, ApJS, 223, 29, 1603.05479
van Dokkum, P. G. et al. 2011, ApJ, 743, L15, 1108.6060
——. 2010, ApJ, 709, 1018, 0912.0514
Venemans, B. P. et al. 2005, A&A, 431, 793, astro-ph/0501259
Vergani, D. et al. 2008, A&A, 487, 89, 0705.3018
——. 2010, A&A, 509, A42, 0909.1968
Verhamme, A., Dubois, Y., Blaizot, J., Garel, T., Bacon, R., Devriendt, J., Guiderdoni, B., & Slyz, A. 2012, A&A, 546, A111, 1208.4781
Verhamme, A., Orlitová, I., Schaerer, D., Izotov, Y., Worseck, G., Thuan, T. X., & Guseva, N. 2017, A&A, 597, A13, 1609.03477
Viero, M. P. et al. 2012, MNRAS, 421, 2161, 1008.4359

Villar, V., Gallego, J., Pérez-González, P. G., Pascual, S., Noeske, K., Koo, D. C., Barro, G., & Zamorano, J. 2008, ApJ, 677, 169, 0712.4150
Vogelsberger, M. et al. 2014, Nature, 509, 177, 1405.1418
Wagoner, R. V., Fowler, W. A., & Hoyle, F. 1967, ApJ, 148, 3
Walt, S. v. d., Colbert, S. C., & Varoquaux, G. 2011, Computing in Science & Engineering, 13, 22
Weedman, D. W., & Huenemoerder, D. P. 1985, ApJ, 291, 72
Weinzirl, T. et al. 2011, ApJ, 743, 87, 1107.2591
Whitaker, K. E. et al. 2015, ApJ, 811, L12, 1508.04771
Whitaker, K. E., van Dokkum, P. G., Brammer, G., & Franx, M. 2012, ApJ, 754, L29, 1205.0547
White, S. D. M. et al. 2005, A&A, 444, 365, astro-ph/0508351
White, S. D. M., & Rees, M. J. 1978, MNRAS, 183, 341
Wijesinghe, D. B. et al. 2012, MNRAS, 423, 3679, 1205.3368
Willett, K. W. et al. 2017, MNRAS, 464, 4176, 1610.03068
——. 2013, MNRAS, 435, 2835, 1308.3496
Williams, R. J., Quadri, R. F., Franx, M., van Dokkum, P., & Labbé, I. 2009, ApJ, 691, 1879, 0806.0625
Williams, R. J., Quadri, R. F., Franx, M., van Dokkum, P., Toft, S., Kriek, M., & Labbé, I. 2010, ApJ, 713, 738, 0906.4786
Willott, C. J. et al. 2013, AJ, 145, 4, 1202.5330
Windhorst, R. A. et al. 2002, ApJS, 143, 113, astro-ph/0204398
Wisnioski, E. et al. 2015, ApJ, 799, 209, 1409.6791
Wisotzki, L. et al. 2016, A&A, 587, A98, 1509.05143
Wolf, C. et al. 2009, MNRAS, 393, 1302
Worthey, G., & Ottaviani, D. L. 1997, ApJS, 111, 377
Wu, P.-F. et al. 2018, ArXiv e-prints, 1802.06799
Wu, P.-F., Zahid, H. J., Hwang, H. S., & Geller, M. J. 2017, MNRAS, 468, 1881
Wuyts, S. et al. 2011, ApJ, 742, 96, 1107.0317
Xue, R. et al. 2017, ApJ, 837, 172, 1611.03510
Yan, L., McCarthy, P. J., Freudling, W., Teplitz, H. I., Malumuth, E. M., Weymann, R. J., & Malkan, M. A. 1999, ApJ, 519, L47, astro-ph/9904427
Yan, R., Newman, J. A., Faber, S. M., Konidaris, N., Koo, D., & Davis, M. 2006, ApJ, 648, 281, astro-ph/0512446
Yang, H., Malhotra, S., Gronke, M., Rhoads, J. E., Dijkstra, M., Jaskot, A., Zheng, Z., & Wang, J. 2016, ApJ, 820, 130, 1506.02885
Yoon, Y., Im, M., & Kim, J.-W. 2017, ApJ, 834
Zheng, Z., Cen, R., Weinberg, D., Trac, H., & Miralda-Escudé, J. 2011, ApJ, 739, 62, 1010.3017
Zwicky, F. 1933, Helvetica Physica Acta, 6, 110
——. 1937, ApJ, 86, 217